Zirconocene-based Magnesium and Zinc Hydride Complexes

by Michael James Butler

September 2017

Department of Chemistry
Imperial College London

A thesis submitted for Doctorate of Philosophy

Thesis Abstract

Interest in heterobimetallic complexes stems from the promise they hold as precursors to materials, reagents in synthesis, and as new catalysts. The thesis begins by presenting the TM–H–M linkage (TM = transition metal; M = Mg, Zn, Al, Ga) and organising the full catalogue of examples for its developed understanding.

The β-diketiminate/(trihydrido)zirconocene complexes of Mg and Zn (**^{D}Mg•Zr** and **^{D}Zn•Zr**) are reported, creating a Mg, Zn, Al series. The Zr–H–Zn linkage is hitherto unknown, and Zr–H–Mg has not been reported without support from alkyne or alkene bridging ligands. The new complexes show very little evidence of bridge cleavage to form the mononuclear complexes under 363 K. Such dissociation is facile in the aluminium system (**^{M}Al•Zr**) down to 193 K. The bridging unit is probed further using ^{1}H NMR spectroscopy and DFT calculations: a 'cog' mechanism is established for the chemical exchange process between terminal and bridging hydride in both the Mg and Zn analogues. This exchange, and M^{II}/Zr dissociation, are found to be easier with **^{D}Zn•Zr**.

The reactivity differences in the M/Zr series are investigated with regards to alkene isomerisation. In the case of tightly-bound **^{D}Mg•Zr** (and the easily dissociating **^{M}Al•Zr**), only the catalytic isomerisation of cycloocta-1,5-diene to cycloocta-1,3-diene is effected. However, the slightly weaker-bound **^{D}Zn•Zr** reacts with either cyclooctadiene to give a new Zr–H–Zn complex that includes a bridging cyclo*octyne* ligand. It is proposed that **^{D}Zn•Zr** has the ability to dissociate to give a spectator Zn hydride fragment and the Zr centre that is active for the on-metal isomerisation, before later recombination. Tightly-bound **^{D}Mg•Zr** gives the (*E*)-selective isomerisation of terminal alkenes to internal positions with a high ratio of alkene:alkane products across a number of substrates – **^{M}Al•Zr** gives larger amounts of alkane by-products, and **^{D}Zn•Zr** is not an active catalyst.

For
Peter, Susan,
the shoplifters of the world,
and HXO.

Declaration of Originality

The work contained within this thesis was performed at Imperial College London between September 2013 and October 2016. Unless stated otherwise, through cited reference or other acknowledgement, it is entirely my own work and has not been previously submitted for a degree at this, or any other university.

Copyright Declaration

The copyright of this thesis rests with the author and is made available under a Creative Commons Attribution Non-Commercial No Derivative licence. Researchers are free to copy, distribute or transmit the thesis on the condition that they attribute it, that they do not use if for commercial purposes and that they do not alter, transform or build upon it. For any reuse or redistribution, researchers must make clear to others the licence terms of this work.

Acknowledgements

Dr Mark R. Crimmin is an alien – the sort of man who built the Pyramids, only for conspiracy theorists in later millennia to deduce an extra-terrestrial agency. I have had the pleasure of being but one of those pyramids, perhaps the 'difficult second pyramid', built on shifting sands and from fallible materials. There is of course very little entropic chance that I would have been capable of building myself. Therefore, sincerely, I shall forever be indebted to him.

Thank you for always being a good sport, for teaching me Occam's razor and the importance of Story, and showing me the humbling feats which are achievable when one is truly in love with one's work.

Mythology states that every architect of the ancient period needs a slave labour work force, and O, what a work force. Of course there is Peter Haycock and Andrew White of the NMR and XRD services respectively. Thanks for all the long slogs where the results were of no significance to you; and thanks for kindling my interest in cryptic crosswords and raglan sweaters. Nonetheless, I still wish a plague on both your football clubs. But then there is the absolute lowest and most dutiful caste of slaves, the Crimmin Group, selected so appositely by Mark to complement and support each other when his own brand of academic zealotry fails. Adi, David, Olga, Sam, Alex, Wenyi, Andy, Clare, Bryan, Tom, Martí and Greg: thank you for being such a well-rounded bunch of nerds, for doing all the tough jobs in the lab and office, for your academic bequests, and for your unique recreational habits. May your Schlenk lines be blessèd, and your gloveboxes sealed with a kiss.

***

Speaking of airtight boxes, there is no doubt that the production of this thesis would have been in some ways smoother if it were written in a one-man capsule in near-earth orbit, with an infinite supply of egg custard tarts. Yet, it is a truth universally acknowledged, that a single man in desire of egg custard tarts, must be in want of a life. As such, I would like to give unending thanks to all the friends that have, over the past four years, frustrated my endeavours with welcome distractions and interruptions. You stopped me losing my mind when I needed it most. Thanks to my family for giving me belief and money, the dead ones equally. Thanks to the state & population of the UK, for (amongst other things) your indulgence.

One person has made far more sacrifices than anyone during the writing of this thesis. In fact, I only made the grave mistake of beginning the bloody thing because she wasn't around. Jade Huang, see you afterwards.

Contents

Thesis Abstract	i
Declaration of Originality	iii
Copyright Declaration	iii
Acknowledgements	iv
List of Abbreviations	x
Key for Important Labelled Compounds	xi

CHAPTER 1 – INDRODUCTION

Magnesium, Zinc, Aluminium and Gallium Hydride Complexes of the Transition Metals 1

1.1 INTRODUCTION	2
1.2 σ-COMPLEXES (TM←H–M)	4
1.3 OXIDATIVE ADDITION (H–TM–M)	8
1.4 LOW-VALENT MAIN GROUP LIGANDS FROM DEHYDROGENATION (TM←M)	10
1.5 HYDRIDE-BRIDGED LEWIS ADDUCTS (TM–H→M)	12
1.5.1 Late Transition Metal Adducts	12
1.5.2 Early Transition Metal Adducts	14
1.6 MULTIPLY-BRIDGED (TM–H_n–M, n > 1) COMPLEXES	16
1.6.1 Rare Earth Metal Adducts	16
1.6.2 Group 4 Metal Adducts	17
1.6.3 Late Transition Metal Adducts	20
1.7 DISCUSSION	23
1.7.1 Structure and Bonding	23
1.7.1.1 Sigma-Complexes and Oxidative Addition	23
1.7.1.2 Multiply-bridged Hydride Complexes	26
1.7.2 Reactivity	27
1.7.3 Potential in Catalysis	29
1.8 APPENDIX	31
1.9 REFERENCES	32

CHAPTER 2
Characterisation of (Hydrido)Zirconocene Complexes of Magnesium, Zinc and Aluminium

38

2.1 INTRODUCTION		39
2.1.1	***Aims***	40
2.2 SYNTHESIS & GROUND STATE CHARACTERISATION		42
2.2.1	***Preparation***	42
2.2.2	***Structural Characterisation***	42
2.2.2.1	Single-Crystal X-ray Diffraction	42
2.2.2.2	Structure by Density Functional Theory	45
2.2.2.3	Structure by NMR Characterisation	47
2.3 CHARACTERISATION OF STRUCTURAL INTEGRITY		50
2.3.1	***Relative Stabilities***	50
2.3.1.1	Experimental Studies	50
2.3.1.2	Theoretical Studies	54
2.3.2	***Hydride Exchange Phenomena***	55
2.3.2.1	NMR Studies	55
2.3.2.2	Theoretical Studies on the Exchange Mechanism	59
2.4 STOICHIOMETRIC REACTIVITY		63
2.4.1	***C–F bond Cleavage of Pentafluorobenzene***	63
2.4.2	***Crossover with an Oxazirconacycle Fragment***	66
2.4.3	***Purity***	69
2.4.3.1	^{1}H NMR	70
2.4.3.2	Colour	71
2.4.3.3	Quantitative Analysis	72
2.5 CONCLUSIONS		73
2.5.1	***Future Work***	74
2.5.1.1	Inert Bond Cleavage (C–F / C–O)	74
2.6 EXPERIMENTAL		76
2.6.1	***General***	76
2.6.1.1	Data Treatment & Equations	76

2.6.1.2 Materials 76
2.6.2 Synthesis and Characterisation of the Bimetallic Hydride Complexes 78
2.6.2.1 Preparative-Scale Synthesis 78
2.6.2.2 NMR-scale Experiments 80
2.6.3 X-ray Crystallography 84
2.6.3.1 Data and Parameters 84
2.6.3.2 Comments on the Structures of the Heterobimetallic Complexes 85
2.6.4 DFT Studies 87
2.6.4.1 Calculated Structures 87
2.7 REFERENCES 88

CHAPTER 3
Isomerisation of Cyclooctadiene to Cyclooctyne with a Zinc/Zirconium Heterobimetallic Complex 91

3.2 INTRODUCTION 92
3.1.1 *Alkynes and Dienes in Isomerisation* 92
3.1.1.1 Background 92
3.1.1.2 Mechanisms of Alkyne/Diene Isomerisation 93
3.1.1.3 Aims 95
3.2 RESULTS 96
3.2.1 Cyclooctadiene Isomerisation Reactions 96
3.2.2 Structural Analysis of the Cyclooctene Adduct 97
3.2.2.1 Experimental Data 98
3.2.2.2 Density Functional Theory Calculations 100
3.2.3 Stability of the Metallacyclopropene 101
3.2.3.1 Theoretical Studies on Stability 101
3.2.3.2 Experimental Stability and Reactivity 105
3.2.4 Mechanistic Studies 107
3.2.4.1 Substrate Scope 107
3.2.4.2 Reaction Kinetics 108
3.2.4.3 Mechanistic Probes and Control Experiments 111

3.3 MECHANISTIC DISCUSSION AND DFT STUDIES 115
3.3.1 Mechanistic Discussion and DFT Studies 115
3.3.2 C(sp²)–H Cleavage Theoretical Investigation 117
3.3.3 Selectivity and By-products 119
3.3.3.1 By-Products 119
3.3.3.2 Heterobimetallic Effect with Zinc 121
3.4 CONCLUSIONS 122
3.4.1 *Future Work* 122
3.4.1.1 Theoretical Studies 122
3.4.1.2 Diene/Alkyne Variation 122
3.4.1.3 Experimental Work on Zr 123
3.4.1.4 Heterobimetallic Effects with Al/Zr and Mg/Zr Systems 123
3.4.1.5 Wider Work 124
3.5 EXPERIMENTAL 125
3.5.1 General 125
3.5.1.1 Materials 125
3.5.2 Preparative-Scale Synthesis 125
3.5.2.1 NMR-scale Catalysis 127
3.5.2.2 NMR-scale Reactions 129
3.5.3 DFT Studies 137
3.5.4 X-ray Crystallography Studies 140
3.5.4.1 Data and Parameters 140
3.6 REFERENCES 142

CHAPTER 4
(E)-Selective Alkene Isomerisation Catalysis with a Magnesium/Zirconium Heterobimetallic Complex 146

4.1 INTRODUCTION TO ALKENE ISOMERISATION 147
4.2 RESULTS 149
4.2.1 Alkene Isomerisation 149
4.2.2 Mechanistic Studies 151
4.2.2.1 Metal Hydride Insertion-elimination Mechanism 151

4.2.2.2 π-Allyl Hydride Mechanism 153
4.2.2.3 Monometallic Catalyst and the Origin of Selectivity 157
4.2.2.4 Kinetic Analysis for the Mg/Zr Catalyst 158
4.3 DISCUSSION 163
4.3.1 Mechanistic Proposal for the Mg/Zr Catalyst 163
4.3.1.1 On-cycle Mechanism 163
4.3.1.2 Pre-catalyst Activation 164
4.3.2 Autocatalysis 165
4.3.2.1 Allylbenzene 165
4.3.2.2 Allyltrimethylsilane 166
4.3.2.3 Origin of Autocatalyst 166
4.3.3 General Mechanistic Summary 167
4.4 CONCLUSION 168
4.5 FUTURE WORK 169
4.5.1 ^{D}Mg•Zr & ^{D}Mg•14 169
4.5.2 Experimental Issues 169
4.5.3 Existence and Identity of cat* 170
4.5.3.1 Synthesis of **cat*** Candidates 170
4.5.3.2 **^{D}Mg•Zr**/Allylbenzene: controls and traps for **cat*** 171
4.5.3.3 Mg and Zn Systems 172
4.6 EXPERIMENTAL 173
4.6.1 General 173
4.6.2 Preparative-Scale Synthesis 173
4.6.3 NMR-Scale Reactions 175
4.6.3.1 Catalyic Experiments (for Table 4.1) 175
4.6.3.2 Mechanistic Controls 181
4.6.3.3 Kinetics of Alkene Isomerisation Catalysis 187
4.6.4 X-ray Crystallography 190
4.6.5 DFT Studies 192
4.7 REFERENCES 193

5 Supporting Information 196

5.1 DFT DATA 196

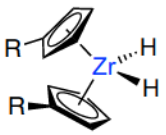
5.2 NMR DATA 199

List of Abbreviations

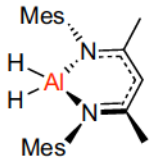
2,6-xylyl	2,6-Dimethylphenyl
Ar	Aromatic group
BDI	β-Diketimininato
BINAP	2,2'-bis(diphenylphosphino)-1,1'-binaphthyl
cat.	Catalyst
Cp*	Permethylcyclopentadienyl, η^5-C_5Me_5
COD	Cyclooctadiene
Cy	Cyclohexyl
D	Deuterium, ^2H
Dipp	2,6-Di-*iso*-propylphenyl
DFT	Density functional theory
E	Element
fsr	Formal shortness ratio
FTIR	Fourier transform infrared spectroscopy
Ln	Lanthanide
M	Main group metal
Mes	2,4,6-Trimethylphenyl
NBO	Natural bond order
NMR	Nuclear magnetic resonance
NOESY	Nuclear Overhauser effect spectroscopy
NPA	Natural population analysis
ox. addn.	Oxidative addition
Pin	Pinacolato
pK_a	Acid dissociation constant
QTAIM	Quantum theory of atoms in molecules
red. elim.	Reductive elimination
ref.	Reference
T_c	Temperature of coalescence
THF	Tetrahydrofuran
TM	Transition Metal, including the lanthanides
TMEDA	*N,N,N',N'*-Tetramethylethylenediamine
TS	Transition state
VT	Variable-temperature
WBI	Wiberg bond index

Key for Important Labelled Compounds

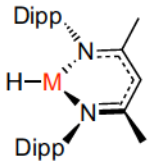
Nota bene: Literature compounds are numbered as simple Arabic numerals within Chapter 1, but in the following chapters they are given the prefix "**1.**" – *i.e.* **80** becomes **1.80** in chapters 2–4.



R = H: **Zr**
R = Me: **Zr'**

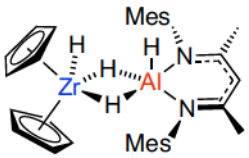


^{M}1

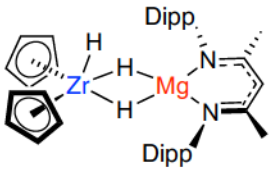


M = Mg: **^{D}2**
M = Zn: **^{D}3**

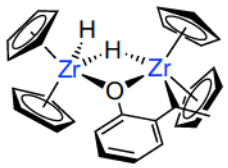
^{M}Al•Zr



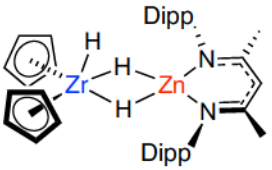
^{D}Mg•Zr

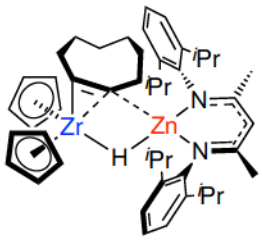


Zr•8

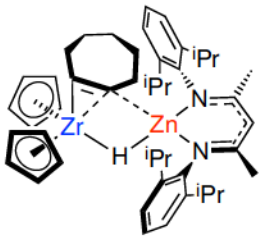


^{D}Zn•Zr

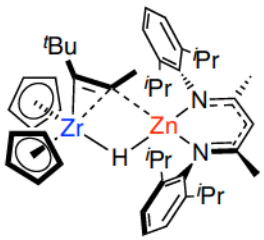




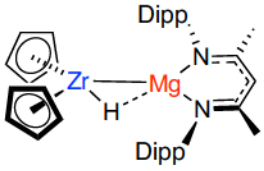
^{D}Zn•10



^{D}Zn•11



^{D}Zn•12

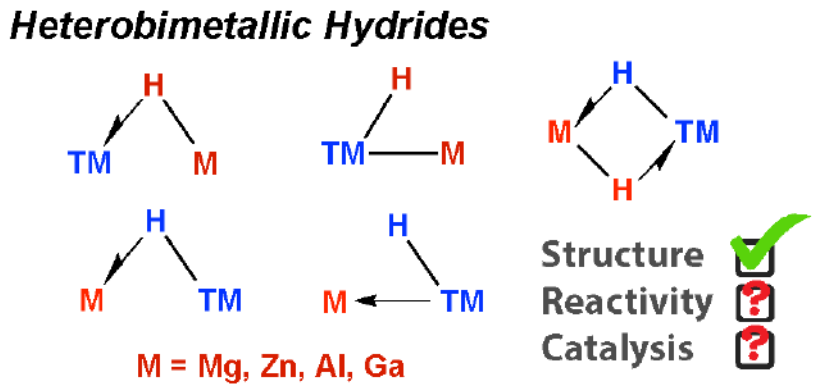


^{D}Mg•14

"In a way, literature is truer than life … On paper, you say exactly and completely what you feel. How easy it is to break things off on paper!"

Simone de Beauvoir, *The Mandarins*

Chapter 1 – Introduction
Magnesium, Zinc, Aluminium and Gallium Hydride Complexes of the Transition Metals



The preparation and applications of heterobimetallic complexes continue to occupy researchers in the fields of organometallic, main group, and coordination chemistry. This interest stems from the promise these complexes hold as precursors to materials, reagents in synthesis and as new catalysts. This chapter organises the state-of-the-art understanding of the TM–H–M linkage (TM = transition metal; M = Mg, Zn, Al, Ga). It discusses the structure and bonding in these complexes, their known reactivity, and their largely unrealised potential in catalysis.

Parts of this chapter have been published:

M. J. Butler and M. R. Crimmin, *Chem. Commun.*, 2017, **53**, 1348–1365.

1.1 INTRODUCTION

The catalytic practices of C–H bond functionalisation, dehydrocoupling (for hydrogen storage), hydroboration and hydrosilylation are all attractive prospects for the future chemical economy. The modern development in these methodologies continues to be enhanced by the perception of borane and silane σ-complexes as intermediates in reaction mechanisms (Figure 1.1).

A σ-complex can be described as an η^2-binding of the σ-E–H bond to a transition metal centre (E = C, Si, B, H).[1,2] Along with dihydrogen complexes,[3-6] σ-silanes are the most comprehensively studied type of this bonding mode.[7-12] While the latter appear as potential intermediates in alkene hydrosilylation via the Chalk–Harrod mechanism,[13,14] the former bear significance for a range of industrially relevant hydrogenation reactions.[15,16] In C–H borylation, stabilisation of catalytic intermediates by a TM–H–B interaction has been supported by significant experimental mechanistic studies.[17-19]

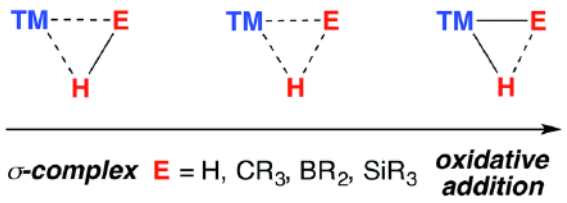


Figure 1.1. The continuum between σ-complex and oxidative addition for the coordination of E–H bonds to a transition metal.

A 3-centre 2-electron interaction, the η^2-ligation of E–H to TM can be viewed within the Dewar-Chatt-Duncanson model and interpreted as a combination of: i) donation of the σ-electrons in the E–H bond to a vacant orbital on the transition metal and ii) back-donation from the metal into the σ^*-orbital of the same E–H bond. The resulting σ-E–H adduct represents an intermediate along the oxidative addition reaction coordinate (Figure 1.1) – part of a continuum of bonding descriptions between free E–H and E–TM–H. It is clear that the nature of the bonding in TM–H–E containing complexes is a tuneable property, being a consideration of the symmetry and energy of the frontier orbitals of the transition metal fragment along with the substituents on, and nature of, E.

A fundamental question that arises when considering this model, is: what happens when C, B and Si are replaced by metallic main group elements such as Mg, Zn, Al, or Ga? The increased ionic contribution within the TM–H–M interaction will necessarily give another dimension to the bonding description. As with silicon, the ability of these elements to expand their coordination sphere leads to the possibility of forming additional bonding interactions with existing ligands on the TM fragment. Furthermore, for the heavier group 13 elements the formation of low-valent M^I ligands through manifestation of the inert-pair effect becomes an

important consideration.

The TM–H–M motif is one way of adjoining two metal centres bearing at least one reactive hydride ligand (Figure 1.2a). This motif can also be obtained by coordinating a transition metal hydride to a neutral main group metal fragment (Figure 1.2b), and multiply bridged species formed by a combination of the two aforementioned donor-acceptor interactions (Figure 1.2c).

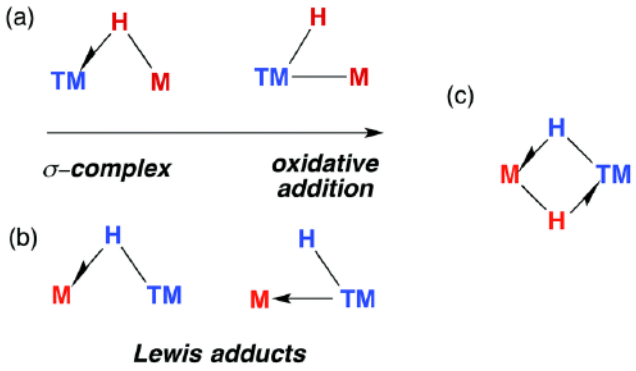


Figure 1.2. (a) The continuum for addition of M–H to a transition metal. (b) Lewis adducts between a TM hydride and M, (c) combination of interactions.

Herein is surveyed the known heterobimetallic complexes of transition metal and main group hydrides. The coordination chemistry of heterobimetallic transition metal hydrides,[20-22] and of Al, Ga, In and Zn-based ligands at a transition metal centre have been summarised previously.[23-26] To focus the discourse, a loose definition of 'heterobimetallic hydride complexes' is employed. The complexes mostly fit these criteria: (a) crystallographically characterised; (b) 1:1 ratio of transition:main group metal; (c) the absence of TM···TM interactions; (d) a hydride ligand in a bridging role. The survey is arranged: TM←H–M, TM–H→M, TM–H_n–M (n > 1).

The half-arrow notation and covalent bond classification advocated by Green, Green and Parkin are used to represent the TM–H–M 3-centre 2-electron interactions.[11] This formalism is employed as an organisational principle not as an absolute interpretation of the bonding within TM–H–M units. The line drawings are constructed from the perspective of the transition metal coordination environment in order to represent charge neutral species rather than an accurate representation of the bonding within the TM–H–M group. The literature survey is followed by discussion of the "continuum" of bonding descriptions, reactivity and the potential these complexes hold for catalysis.

1.2 σ-Complexes (TM←H–M)

The Crimmin group has reported **1**, a Zn congener of structurally related σ-alane complexes (Figure 1.3).[27] The binding of the zinc hydride to the Cu^{I} centre is weak and reversible. In toluene or benzene solution, an equilibrium exists between the heterobimetallic complex and the η^2-arene complex of Cu^{I}. The electronic structure of the three-centre linkage has been investigated by DFT calculations. The analysis suggests that the formal L donation of the M–H σ-bond to the 4s orbital on Cu^{I} is accompanied by weak Cu→M back-donation into the M–H σ^*-orbital (see Discussion, section 1.7.1.1). In combination, the data allow **1** to be described as a weakly bound σ-complex.

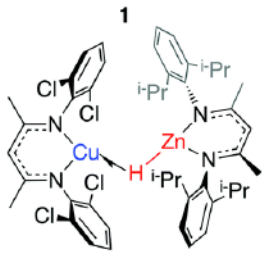


Figure 1.3. A σ-zincane complex of Cu^{I}

Coordination of Al–H bonds to Cu^{I} has also been examined; complexes possessing four-coordinate and five-coordinate aluminium centres have been isolated (Figure 1.4, **2** and **3**). The binding of Cu–H–Al is again weak and reversible based on solution NMR studies and crossover experiments. In DFT calculations, the coordination of exogenous ligands to the Cu^{I} fragment was found be increasingly exergonic across the series C_6F_6 < H–B < H–Si < C_6H_6 < H–Zn < H–Al – a trend that is manifest in the experimental data.[27]

In **2** the Cu···Al vector lies outside of the H–Al–H wedge – the only example of this structural feature in main group metal σ-complexes.[27] The 'lee side' coordination of the Al–H bond and very long intermetallic distance in **2** are notable. For comparison, σ-complexes of HBpin (pinacolborane) or HBcat (catecholborane) show different coordination geometries to those of four-coordinate boranes BH_3•EMe_3 (E = N, P).[28,29] The discrepancy has been rationalised by disruption of the TM···B back-donation due to the absence of a vacant acceptor orbital of suitable energy in BH_3•EMe_3, be it the boron p-orbital or the σ^*-orbital of the B–H bond.[28] While steric factors are undoubtedly important, a similar effect may explain the solid state structures of **2** and **3**. DFT calculations are consistent with reduced back-donation from d^{10} Cu^{I} into the Al–H σ^*-orbital of the five-coordinate species when compared to the four-coordinate analogue.[27] Higher nuclearity species containing Cu–H–Al interactions are known and the

intermetallic cluster $[(Cp^*AlCu)_6H_4]$ has been obtained from reaction of $[Cp^*Al]_4$ with $[Ph_3PCuH]_6$.[30]

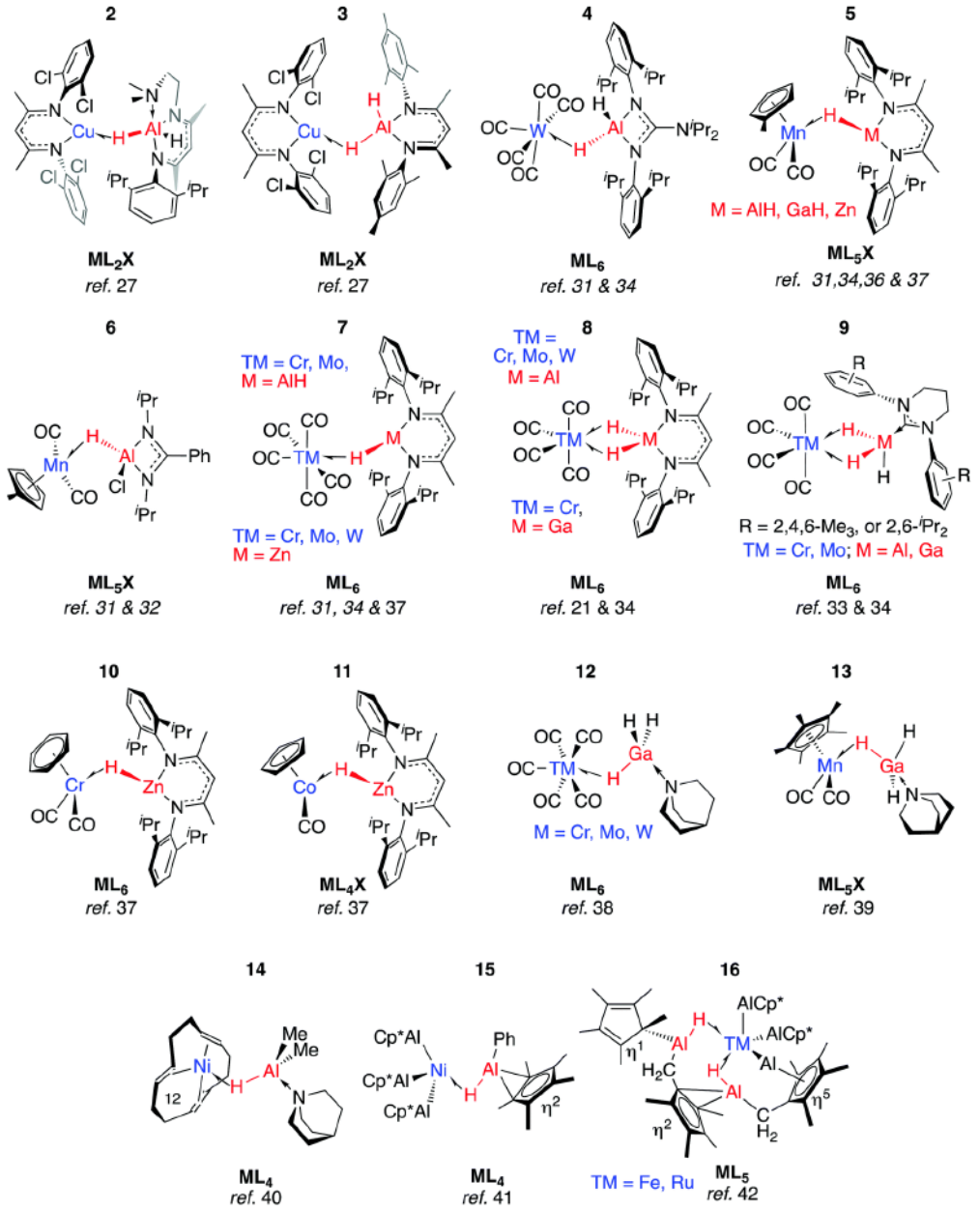


Figure 1.4. σ-Alane, σ-gallane and σ-zincane complexes of late TM.

Aldridge and co-workers pioneered this area of research and have isolated a series of σ-alane and σ-gallane complexes of groups 6 and 7 transition metal carbonyl complexes.[31-35] Like **2** and **3**, the structures of **4**–**7** contain σ-Al–H adducts and derive from ligand exchange reactions, in this case from the parent metal carbonyl under either thermal or photochemical conditions. Four-electron, η^2:η^2-coordination of H–Al–H (**8**–**9**) requires a 14-electron transition metal fragment, $\{M(CO)_4\}$ and necessitates displacement of two ligands from ML_6 starting materials.[31,33,36] Complexes **7-Cr/Al** and **8-Cr/Al** have not been separated and, like their heavier congeners, **7-Mo/Al** and **8-Mo/Al** were isolated in an approximate 9:1 mixture with the

minor component containing the η^2:η^2-coordination mode.[34] The adduct **8-W/Al** could not be obtained by photoejection of CO from [$W(CO)_6$] and was finally obtained under thermal conditions using [$W(CO)_4$(1,5-COD)] as a precursor (COD = cyclooctadiene).[34] The M···Al distance in **8-W/Al** is shorter than would be expected based on the lighter members of the series, presumably due to a tighter binding of the σ-alane to the more expanded 5d orbitals of W. In contrast to the W analogue, **8-Cr/Al** may be formed directly upon heating **7-Cr/Al**: Eyring analysis and the first order kinetics of this reaction have led Aldridge and co-workers to suggest it proceeds by an associative pathway.[34]

All TM–H–Al heterobimetallic complexes characterised by Aldridge and co-workers show slow exchange between the bridging and terminal hydride ligands on the NMR timescale at ambient temperature.[31-34,36] From structural and spectroscopic evaluation of these complexes (**4**–**9**), it appears that back-donation into the M–H σ* orbital is negligible. Whilst the close TM···M contacts are short enough to hint at TM–M interaction (especially in **9-Ga**), the four-membered ring imparted by the η^2:η^2-coordination mode in **8**–**9** demands such a short contact.[33] The weaker nature of the Ga–H bonds (*cf.* Al–H) means **8-Ga** is only a minor product of the reaction of the corresponding gallane with [$M(CO)_4$(1,5-COD)] as this species is unstable with respect to dihydrogen elimination (see section 1.4).[36]

Although the coordination chemistry of Zn–H–TM and Mg–H–TM groups remains underdeveloped when compared to the aluminium analogues, the group has recently reported a series of σ-zincane complexes of closely related transition metal carbonyl fragments. Ligand exchange reactions readily occur under photochemical conditions and **5-Zn**, **7-Zn**, **10**–**11** have been isolated and crystallographically characterised.[37]

Ueno and co-workers provided evidence that the η^2:η^2-coordination mode is not necessary for the stabilisation of σ-gallanes, and reported **12** and **13**.[38,39] These complexes were formed from displacement of THF or CO from group 6 transition metal carbonyl complexes by GaH_3•quinuclidine. While there is little account for TM···Ga interactions in **12**, **12-W** again contains a shorter TM···Ga separation than what would be reasoned from inspection of the solid state structures **12-Cr** and **12-Mo**.[38,39] Complex **13** is noticeably similar to **6** in terms of the TM–H–M parameters. In both cases, the $Cp_{centroid}$–Mn–H–M torsion angle is near 90° allowing for overlap of the M–H σ*-orbital with the HOMO of the Mn fragment. There are also similarities to the first reported example of a σ-alane complex. Formally a Ni^0 species possessing a triene ligand and a coordinated alane, **14** contains an unsupported Ni–Al–H linkage that survives the substitution of the tridentate ligand with three equivalents of CO to form [$(CO)_3Ni(\mu$-H)$AlMe_2$•quinuclidine].[40]

An alternative approach to TM–H–Al groups has been discovered by Fischer and co-workers. Addition of $[Cp^*Al]_4$ to transition metals with labile ligands is proposed to generate intermediates of the form $[TM(AlCp^*)_n]$ (n = 4–6) which react further, effecting the inter- or

intramolecular C–H activation of arenes or alkanes.[41,42] Complexes **15**–**16** (Figure 1.4) are formed through this route and possess geometries that are consistent with the σ-alanes described above. For example, the Al–H distance in **15** of 1.76(3) Å lies within the range for established σ-alanes. While **16** possesses elongated Al–H distances ranging from 1.88(8) to 1.89(7) Å, these are perhaps shorter than the > 2.0 Å separation required to suggest oxidative addition (*vide infra*). The latter may be described as a complex containing stretched σ-alane ligands with an Al–H–TM geometry somewhere between coordination and oxidative addition.

1.3 Oxidative Addition (H–TM–M)

The Crimmin group has reported the thermal reaction of M–H bonds (M = Al, Zn, Mg) with $[Cp^*Rh(H)_2(SiEt_3)_2]$ to form **17** and **18**,[43] a reaction that is believed to proceed through the 16-electron intermediate $\{Cp^*RhH(SiEt_3)\}$. These species are different to the σ-complexes described above and data are consistent with the product of oxidative addition (Figure 1.5).

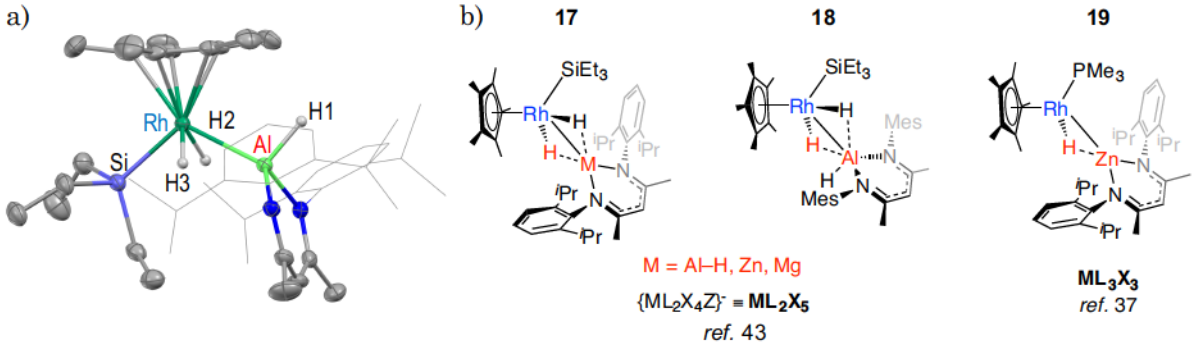


Figure 1.5. a) The crystal structure of **17-Al**. Selected bond lengths [Å]: Rh(1)–Si(1) 2.3668(7), Rh(1)-Al(1) 2.4579(7), Al(1)–H(1) 1.51(2), Al(1)–H(2) 2.13(3), Al(1)–H(3) 2.22(3), Rh–H(2), 1.47(3), Rh–H(3) 1.53(3). b) Oxidative addition (hydride transfer) of M–H bonds to a Rh complex

In all cases the TM–M distances are within the sum of covalent radii and the M···H distances stretch to well beyond 2.0 Å. Moreover the four-legged piano-stool geometry around the Rh centre, including the *trans*-relation of the hydride ligands, is conserved when compared with silyl and boryl analogues, $[Cp^*Rh(H)_2(SiEt_3)(X)]$ (X = $SiEt_3$, Bpin). The description of **19** as an oxidative addition product is supported by the significant $^1J_{Rh-H}$ value of 40.2 Hz and terminal ν(Rh–H) frequency of 1966 cm^{-1}. The calculated charges (NBO analysis) on Rh are significant for only the Zn and Mg analogues. As such, while these Zn and Mg complexes could be described as oxidative addition products, hydride transfer to form an "ate-complex" is also a fair description.[43]

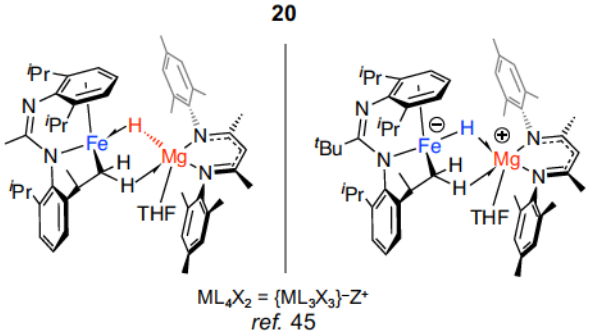


Figure 1.6. Hydride transfer to form a tightly bound ion-pair, complex **20**.[46]

The structure of **17-Al**, an analogue of **18** that incorporates more sterically demanding substituents on the β-diketiminate ligand, shows a geometry with familiar *trans*-disposed

hydrides, short TM–Al distance and long Al···H distances (Figure 1.5). Reaction of **18-Zn** with an excess of PMe_3 under photochemical conditions leads to the elimination of an equivalent of silane and formation of **19**. This latter heterobimetallic complex again contains a short TM–M distance and a M···H separation of greater than > 2.1 Å.[37]

Mindiola and co-workers have isolated a related Fe–H–Mg complex, albeit as a minor component of a mixture formed upon reaction of EtMgCl with an iron chloride precursor.[44] Complex **20** (Figure 1.6) also results from C–H activation of the ligand.[45] Whilst it could be assigned as an σ-Mg–H complex of Fe the long Mg···H distance and short Fe–H separation make this debatable. It is arguably closer to an ate-complex formed by a tightly bound $\{Fe–H\}^- \rightarrow Mg^+$ ion-pair. Although both **20** and **17–19** can be described as the products of hydride transfer the key difference is that the latter are formed from addition of the M–H bond to the TM centre and contain a defined and quantifiable TM–M bond.

1.4 Low-Valent Main Group Ligands from Dehydrogenation (TM←M)

The products of oxidative addition of M–H bonds to transition metals may only be intermediates on a path to coordinated low-valent fragments (M = Al, Ga). As the main group is descended, not only does the reduced M–H bond strength result in easier M–H "bond activation", but the manifestation of the inert pair effect means the lower common oxidation state becomes increasingly stable.

Two examples of the generation of Al^{I} ligands by the dehydrogenation of aluminium dihydride precursors in the coordination sphere of a transition metal have been reported. The products of these reactions retain an undeniable H···Al interaction. The photochemical elimination of $HSiEt_3$ from **18** leads to the dimer **21** (Figure 1.7).[43] Complex **21** contains a $\{Rh_2Al_2H_4\}$ core. Supporting the argument for Al^{I} is the deviation of the alumocycle from planarity, suggestive of decreased π-donation by the N atoms into the 3p orbital of Al. This allows for Al^{I} to act as both a Z- and L-type ligand with respect to Rh.[43] Structurally related intermetallic compounds containing $\{Pt_2Ga_2H_4\}$,[46] $\{Ru_2GaH_2\}$,[47] $\{Ru_2Ga_2H_4\}$,[48] $\{Ru_2Al_2H_4\}$,[48] $\{Co_2H_2Al_2\}$,[49] $\{Rh_2Zn_2H_2\}$ groups are all known,[50,51] as are higher nuclearity species in which multiple main group fragments act as ligands for the transition metal (see 1.8 Appendix, Figure 1.25).[52-57] The work on cluster complexes supported by organozinc, organoaluminum and organogallium ligands has been reviewed before.[23-26]

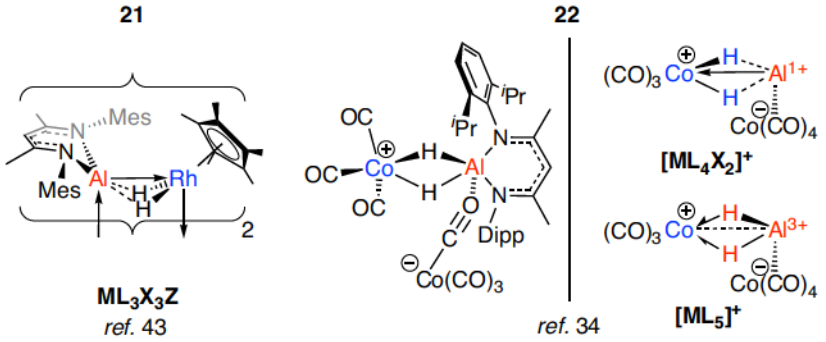


Figure 1.7. Generation of Al^{I} ligands from addition of aluminium dihydrides to TM

Coordination of a related aluminium dihydride to a 14-electron $\{Co^{I}(CO)_3\}^{+}$ synthon gives **22** (Figure 1.7).[34] This latter species appears to be a product of simultaneous addition of both Al–H bonds to Co. The bridging Al···H distances of 1.92(3)–1.98(3) Å in **22** are comparable to those found in the oxidative addition products **17-Al** or **18** of 2.0–2.2 Å, but are longer than those found in σ-complexes of the same aluminium species which typically range from 1.6–1.8 Å. As with **21,** the aluminium centre receives additional electron density, here by end-on coordination of an isocarbonyl ligand of the formally anionic $\{Co(CO)_4\}$ moiety. The electronic structure of

22 lies somewhere between the *bis* σ-complex and the dehydrogenated Co^{III}/Al^{I} species (Figure 1.7).

Complexation of gallanes to late transition metal carbonyl complexes (TM = Cr, Mo, W, Mn, Fe, Co) has been shown to lead to the formation of Ga^{I} ligands (Figure 1.8). Overall, the gallium L-type ligand effectively replaces a carbonyl ligand. The process includes spontaneous or photo-induced extrusion of dihydrogen (see Discussion, Figure 1.23).[34,36] Complexes **23** and **24** are formed from addition of gallanes to $[(\eta^5\text{-}C_5H_4Me)Mn(CO)_3]$ and $[TM(CO)_n]$ (TM = Cr, Mo, W, n = 6; TM = Fe, n = 5) precursors. A H–TM–Ga–H intermediate is proposed, from which 1,2-elimination of dihydrogen occurs.

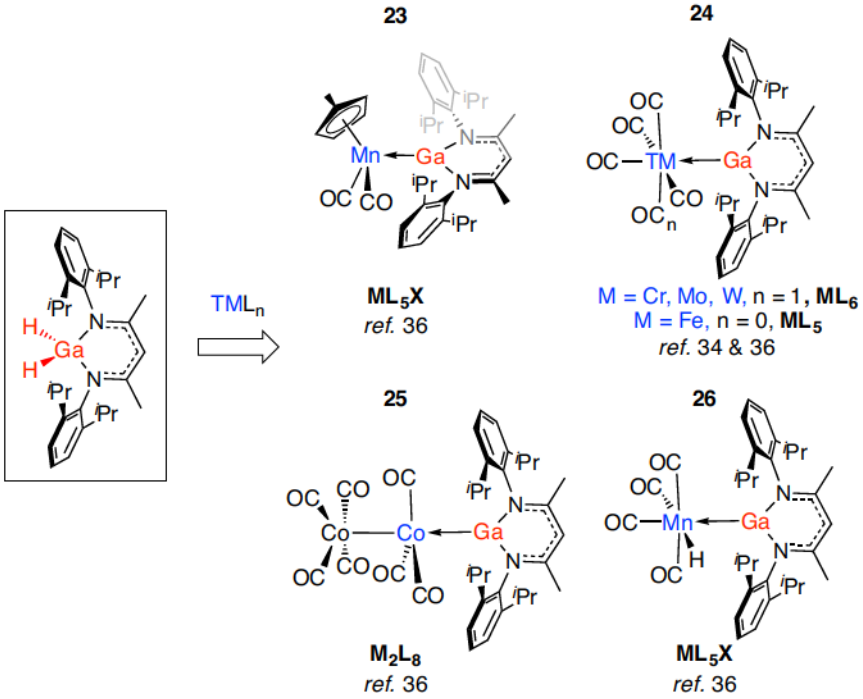


Figure 1.8. Generation of Ga^{I} ligands from addition of gallium dihydrides to TM

Reactions employing 34-electron carbonyl complexes $[Mn_2(CO)_{10}]$ or $[Co_2(CO)_8]$ in place of the 18-electron $[M(CO)_n]$ complexes proceed similarly. For Co, oxidative addition of the Ga–H bond is followed by H_2 elimination across the TM–M bond to give **25**. For Mn, oxidative addition is followed by reductive elimination of $H\text{–}TM(CO)_4$ and α-migration of the remaining hydride from Ga to Mn to form **26**.[36] The pre-migration intermediate – a Mn–Ga–H moiety – finds experimental support from the work of the groups of both Driess and Fischer who have reported complexes containing Fe←Ga–H,[58] and TM←M–H moieties (TM = Cr, Mo, Zn; M = Al, Ga).[59-61]

1.5 Hydride-Bridged Lewis Adducts (TM–H→M)

1.5.1 Late Transition Metal Adducts

Lewis acidic main group metal centres *without* hydride substituents may be coordinated by transition metal hydrides in two different ways: i) through a direct metal–metal interaction from donation of d-electrons of the TM to the main group metal (Z-type ligand) or ii) through 3-centre 2-electron hydride bridges of the form TM–H→M (Figure 1.2b). Elimination reactions may result from these adducts (Figure 1.9). For alkane (or arene) elimination to occur, the pK_a of the hydride must be low enough and the metal alkyl (or aryl) basic enough.

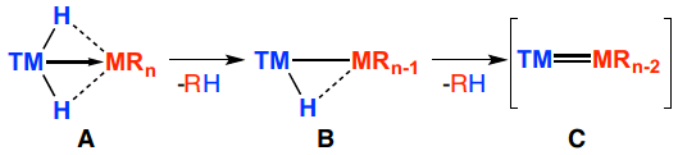


Figure 1.9. Alkane and arene elimination from Lewis acid-base adducts.

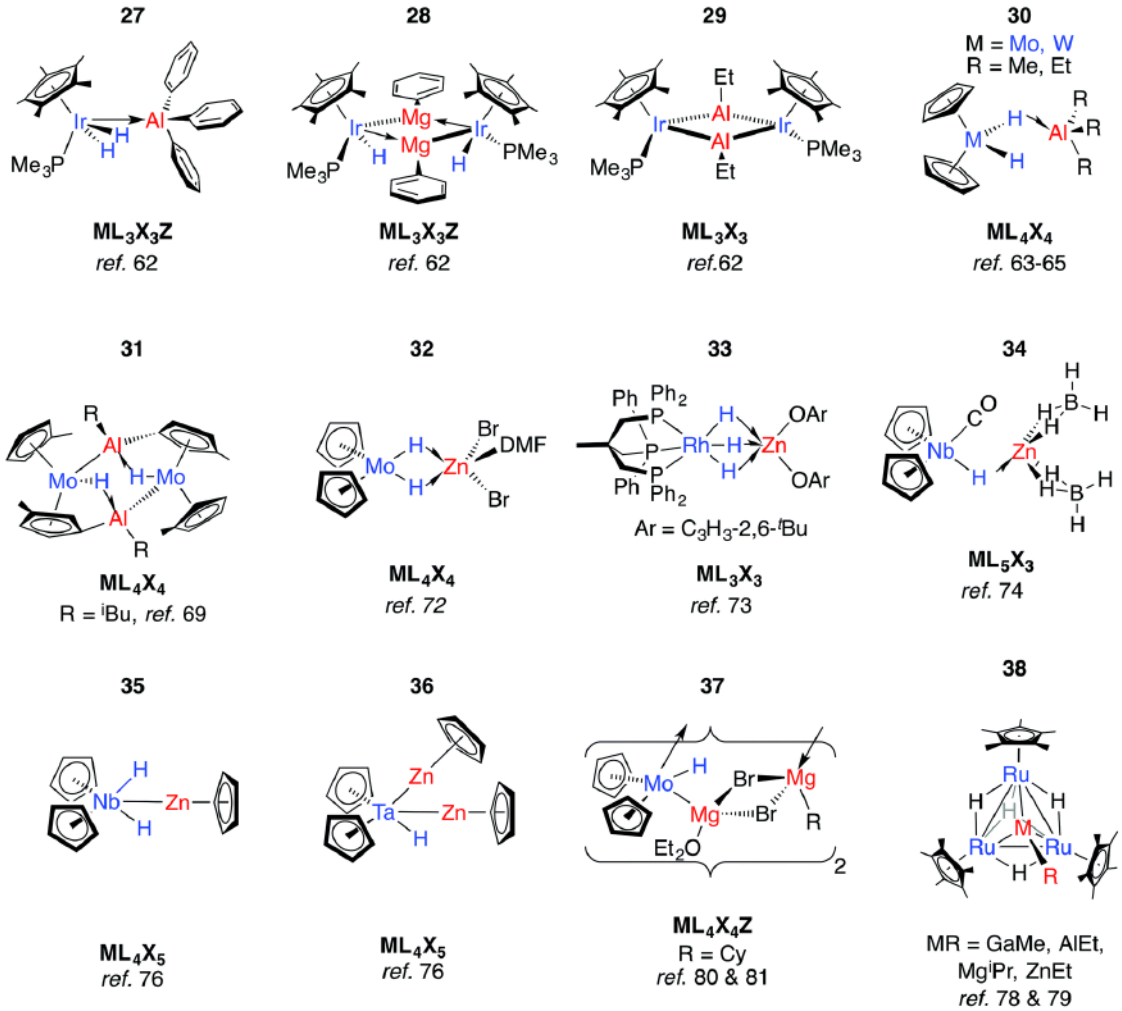


Figure 1.10. Late transition metal adducts.

For example, Andersen and Bergman have reported the reaction of $[Cp^*Ir(H)_2(PMe_3)]$ with a series of organo-aluminium and -magnesium compounds (Figure 1.10).[62] Coordination of Ph_3Al to form **27** results in the widening of the H–Ir–H angle by 20° and signifies dominant TM–M bonding. Adduct **27** is representative of bonding situation **A**. In contrast, the reaction of $[Cp^*Ir(H)_2(PMe_3)]$ with $Ph_2Mg(THF)_2$ eliminates benzene and forms **28**, while that with $AlEt_3$ eliminates two equiv. of ethane and yields the dimeric species $[Cp^*IrPMe_3(\mu\text{-}AlEt)]_2$, **29**. These TM–M products are dimeric examples of **B** and **C** respectively. Both **28** and **29** activate CO_2, giving $[Cp^*Ir(PMe_3)CO]$ as the TM-containing product.[62]

The TM···M distances in **27**–**29** are in the range of the sum of the covalent radii, and the coordination at iridium in **27** is such that the Ir–Al bond is distorted away from the IrH_2 plane by 37°.[62] The geometries contrast with those of **30-W** and **30-Mo**. First reported by Wailes *et al.*[63] and Storr *et al.*,[64] **30-W** has been characterised by X-ray diffraction and analysed by DFT methods.[65,66] While the current understanding is that the two metals interact through a single hydride bridge to Al, there is limited data to support a non-negligible TM→M donation. Firstly, the HOMO on the TM fragment is calculated to be a metal-localised d-orbital-type suitable for electron donation. Secondly, the BX_3 (X = F, Cl) adducts of the same TM fragments were calculated with the boron atom lying outside of the H–TM–H wedge.[66]

Although the gallium and boron analogues of **30** are yet to be isolated, ^{1}H NMR data for a $GaMe_3/[Cp_2WH_2]$ admixture shows likely equilibrium between free compounds and a weakly bound adduct.[67] These data are consistent with the known acceptor strength of the Lewis acids $AlMe_3 > GaMe_3 > BMe_3$. Rhenium analogues of **30** were discovered by Wailes *et al.* using the metallocene $[Cp_2ReH]$.[63] The potential for reversible H/D exchange between the hydrides and protons of the cyclopentadienyl ring of **30-W** has been highlighted and proposed to occur by a mechanism involving anchimeric assistance.[65] Non-reversible intramolecular deprotonation of the cyclopentadienyl ligands is also well established, and often leads to high nuclearity species such as complex **31**.[68-71]

When $[Cp_2MoH_2]$ was treated with ethylzinc bromide, **32** was isolated and presumed to derive from $ZnBr_2$ formed from a Schlenk-type equilibrium.[72] An $\eta^2{:}\eta^2$-bonding mode of the Mo hydrides is implied by the narrowing of the MoH_2 wedge upon adduct formation, data that contrast those of **27**. A similar adduct, **33**, is formed from addition of a *bis*-aryloxy zinc solvate to a Rh trihydride complex.[73]

Reaction of a mixture of $NbCl_5$, sodium cyclopentadienyl and zinc powder in THF under an atmosphere of CO, and subsequent treatment with $NaBH_4$, gives **34**.[74] The metal···metal distance in **34** is just within the sum of the covalent radii and there is a shift of the ν(CO) absorption upon coordination of the Lewis acid relative to $[Cp_2Nb(CO)H]$ (1910 to 1960 cm^{-1}). Both findings mark a significant Nb→Zn interaction. In contrast, only a small shift in the ν(CO) absorption is seen upon reaction of $[Cp_2NbH(CO)]$ with $AlEt_3$.[75] Based on significant changes

to the hydride resonance observed by ^{1}H NMR data, the coordination of $AlEt_3$ in $[Cp_2Nb(L)H{\bullet}AlEt_3]$ (L = CO, C_2H_2, PMe_3) is proposed to occur through a μ-hydride ligand rather than a direct metal···metal interaction. Related reactions between a 1:1 mixture of $[Cp_2NbH_3]$ or $[Cp_2TaH_3]$ and $[Cp_2Zn]$ do not lead to adduct formation but cyclopentadiene elimination and formation of new species **35** and **36** both of which contain TM–Zn bonds.[76,77] Tebbe and co-workers reported the d^1 complex $[(Cp_2NbH_2)_2Zn]$ from the 1:2 reaction of Et_2Zn with $[Cp_2NbH_3]$.[75] Higher nuclearity species **36**–**38** have been isolated from reactions of ruthenium polyhydride complexes or $[Cp_2MoH_2]$ with main group alkyls (Figure 1.10).[78-81] Their data show no signs of hydride interaction with the main group metals.

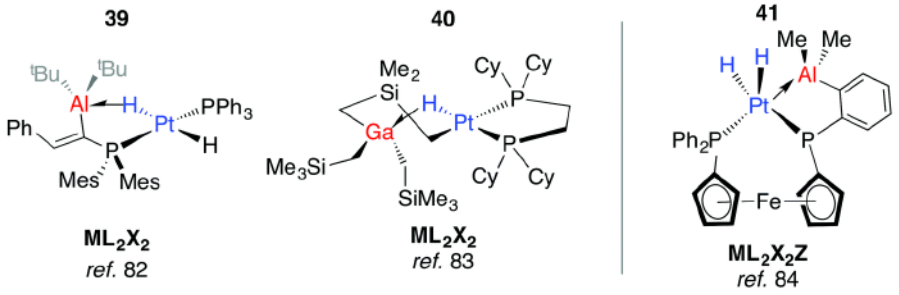


Figure 1.11. Adducts from H_2 or C–H addition across a Pt→Al Bond.

In more recent work, Bourissou, Uhl and co-workers have shown that hydrogenation of an intramolecularly coordinated Pt→Al adduct leads to the heterobimetallic hydride **39** (Figure 1.11). [82] Calculations suggest that H_2 addition occurs across the Pt→Al bond. There is precedent for this intramolecular coordination mode: Fischer and co-workers have reported the gallium adduct **40**.[83] Related hydrogenation reactions of platinium diene complexes either bearing a Z-type Al ligand or in the presence of Ga^I co-ligands lead to the formation of heterobimetallic complexes bearing terminal hydride ligands on the transition metal (see Appendix, Figure 1.25).[46,84] For example, **41** is formed upon hydrogenation of a Pt···norbornadiene precursor; it is currently unclear if the Pt→Al moiety plays a role in dihydrogen activation (Figure 1.11).[84]

1.5.2 Early Transition Metal Adducts

Relevant to Ziegler-Natta polymerisation, Zr–H→Al Lewis acid-base interactions have been known for some time.[85] Coordinatively saturated, d^0 heterobimetallic complexes may be formed by coordination of the parent hydride to a Lewis acid. For example, **42** was suggested by Wailes and co-workers based on ^{1}H NMR experiments as early as 1972.[67] Crystallographic characterisation of related adducts **43** and **44** containing inter- and intramolecular Zr–H–Al moieties was later reported.[86,87] While there is less data for hafnium, the adduct **45** has been reported and is notable for the location of the Al centre outside of the H–Hf–H wedge. The

position of the hydrides are unusual when compared to related group 4 metallocenes as is the 16-electron configuration of Hf.[88] For group five analogues, [Cp_2TaH_3•MEt_n] forms irreversibly for M = Al, Ga (n = 3) but reversibly for Zn (n = 2).[75] Solid state infrared spectroscopy and X-ray diffraction data for a related complex, **46**, are consistent with formation of an adduct containing two Ta–H→Zn linkages forming an $\eta^2{:}\eta^2$-coordination mode, although NMR data suggest that only one bridging hydride is retained in solution (Figure 1.12).[89]

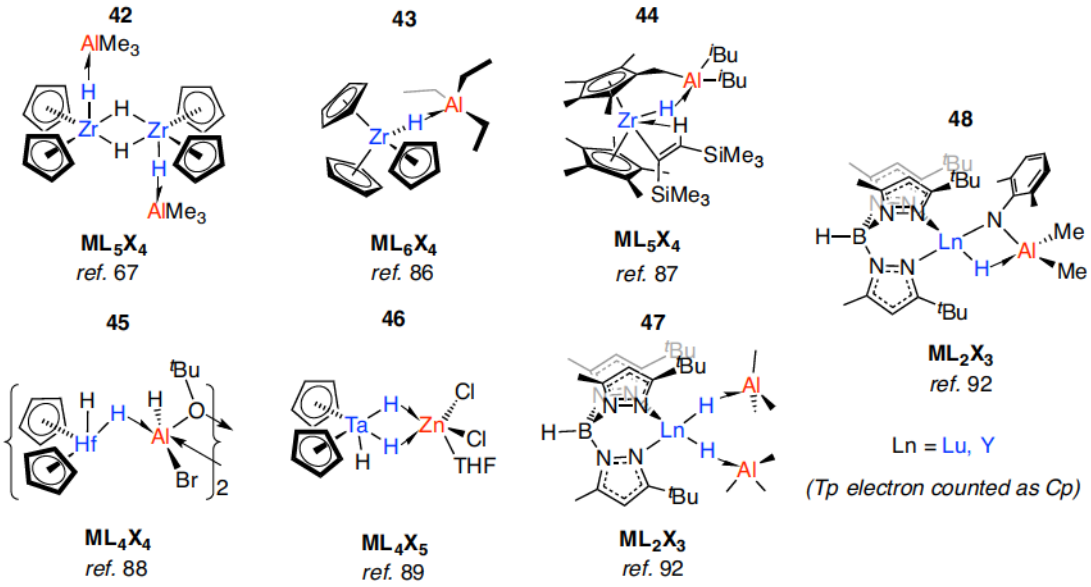


Figure 1.12. Early TM / main group adducts.

Anwander *et al*. have investigated the reactions of yttrium and lutetium alkyl and amide complexes with aluminium hydrides.[90-93] For example, lanthanide hydride bonds in **47** are capped and stabilised by Lewis acidic aluminium sites.[92] This motif is not unique to **47**, and X-ray data has been collected on monomeric [$Cp_2Lu(\mu$-H)•AlH_3•NEt_3],[94] and dimeric [Cp*Y(Me)(μ-H)$AlMe_2$(μ-H)]$_2$.[95] Despite the coordinated Lewis acid, **47** displays reactivity consistent with a terminal hydride; deprotonation of 2,6-dimethylaniline gave complex **48**. Here, the imide linker supports an intramolecular Ln–H→Al interaction (Figure 1.12).[92]

1.6 Multiply-Bridged (TM–H_n–M, n > 1) Complexes

1.6.1 Rare Earth Metal Adducts

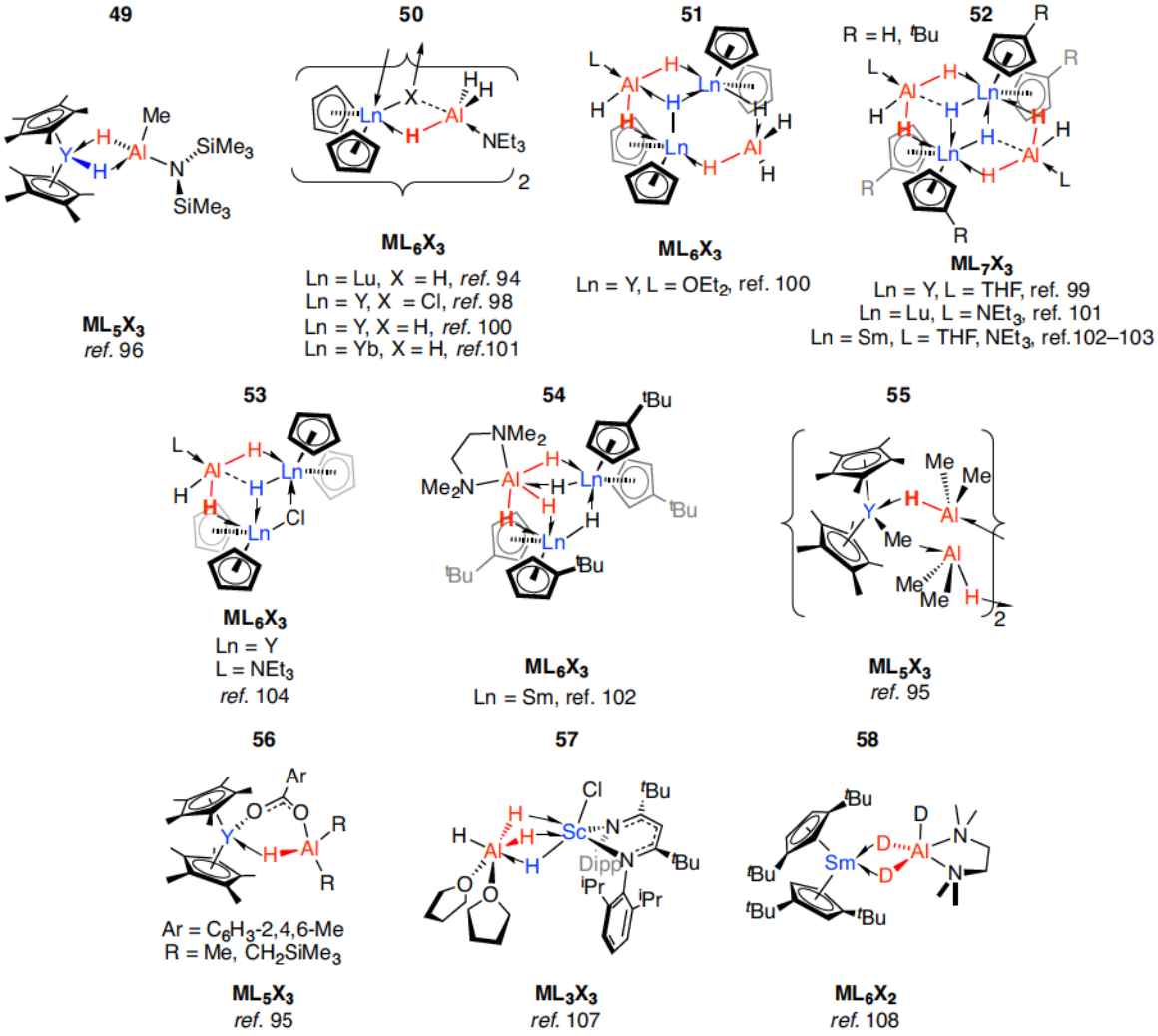


Figure 1.13. Coordination of aluminium hydrides to rare earth metal centres.

$[(C_5Me_5)_2YMe(THF)]$ reacts with $HAl\{N(SiMe_3)_2\}_2$ allowing trapping of μ-H_2-bridged **49**.[96] The alane in this complex is strongly bound and addition of donor, including chelating, ligands could not effect separation of the heterobimetallic complex. The coordination mode in **49** is pre-dated by those found in **50**–**54** reported by Bulychev and co-workers in the 1980s.[94,97-105] In these latter complexes, the Al fragment and hydride source derive from either $LiAlH_4$ or AlH_3•L (L = NEt_3, THF, OEt_2), and either the chloride or hydride ligands take up μ^3-coordination modes. Amongst the complexes $[Cp_2YH•AlH_3L]_2$ (**50**), the Y···Al distances decrease, and Al–H stretching frequencies increase, across the series L = Et_2O < THF < NEt_3. The five-coordinate

Al centres found in these complexes are notably different to the borate analogues, where the boron atom does not engage in coordination numbers higher than four, and solvation occurs at the rare earth metal centre (Figure 1.13).[106]

Alanes react with yttrocene hydride or carboxylate complexes to form Y←H–Al adducts (**55**–**56**).[95] While investigating the salt metathesis of a β-diketiminato-supported Sc dichloride complex with $LiAlH_4$, Piers and co-workers isolated the alane adduct, **57**.[107] In **57**, both metals are six coordinate, and this is the only time a $(\mu\text{-H})_3$ bridging motif is seen in the absence of a late TM. Heterobimetallic hydrides of rare earth metals are not limited to those in which the heavy metal is in the +3 oxidation state. Bulychev *et al.* found that $[(1,3\text{-}^{t}Bu_2\text{-}C_5H_3)_2Sm^{II}]$ partially decomposes into an octanuclear aggregate of Sm^{III} and alane, when treated with AlH_3 in the presence of TMEDA. Upon substitution of the alane for AlD_3, however, **58** may be isolated: an apparent effect of isotopic substitution.[108]

1.6.2 Group 4 Metal Adducts

In understanding the role of methylaluminoxane in polymerization catalysis,[109] Bercaw, Brintzinger and others have reported NMR studies on hydride-bridged Zr/Al oligomers, trimers and dimers in solution (**59**–**60**).[85,110-112] They concluded that binuclear structures of type **60** are only produced for *ansa*-metallocenes and inclusion of a terminal Me ligand on Zr causes decomposition. Cationic Zr- and Hf-analogues are known.[113-115] It has been shown that $\{Zr(\mu\text{-H})_3Al_2\}^+$ reacts reversibly with $AlMe_3$ or $ClAl^{i}Bu_2$ to give dimethyl- or dichloro-bridged Zr/Al species (Figure 1.14).[114]

An early example of a Zr–H–Al complex was published in 1997 by Raston and co-workers.[116] Structurally and synthetically, **61** is a logical extension of the work of Bulychev *et al.* (*vide supra*). These species are poorly soluble in all common organic solvents but THF, and require stabilisation by a base. Power and Wehmschulte added a super bulky aryl group (**62**) improving solubility and eradicating the need for base stabilisation.[117] Base-free complexes have also been reported by Stephan and colleagues.[118] NMR data and calculations for the monomers **62** suggest both fast intramolecular hydride exchange and an intermolecular exchange between the heterobimetallic complex and its homometallic parts in solution. The Crimmin group has also published an example of this type: soluble in toluene and hexane **63-Al** exists in equilibrium with the alane and $[Cp_2ZrH(\mu\text{-H})]_2$ (Figure 1.14).[119]

Many of the Zr^{IV}/Al heterobimetallic hydride complexes are synthetically accessible by salt-metathesis reactions of the parent zirconocene dihalide with aluminium hydride reagents.[120] Similar reactions with titanium(IV) precursors commonly lead to isolation of products with Ti in the +3 oxidation state.[121-128] This is displayed most nakedly in the recent report of **64** by Beweries.[129] Six-, five- and four- coordinate aluminium centres have been reported in $\{Ti_2Al_2H_8\}$, $\{Ti_2AlH_5\}$, and $\{TiAlH_2\}$ cores respectively (**65**–**72**).[118,120-134] There is only limited

precedent for similar reduction chemistry occurring with Zr.[132,133] The observed coordination modes of Al_xH_y units in these and related group 4 complexes are common to heterobimetallic complexes and are found in related Ta, Nb, Mn and Ru complexes (*vide infra*).

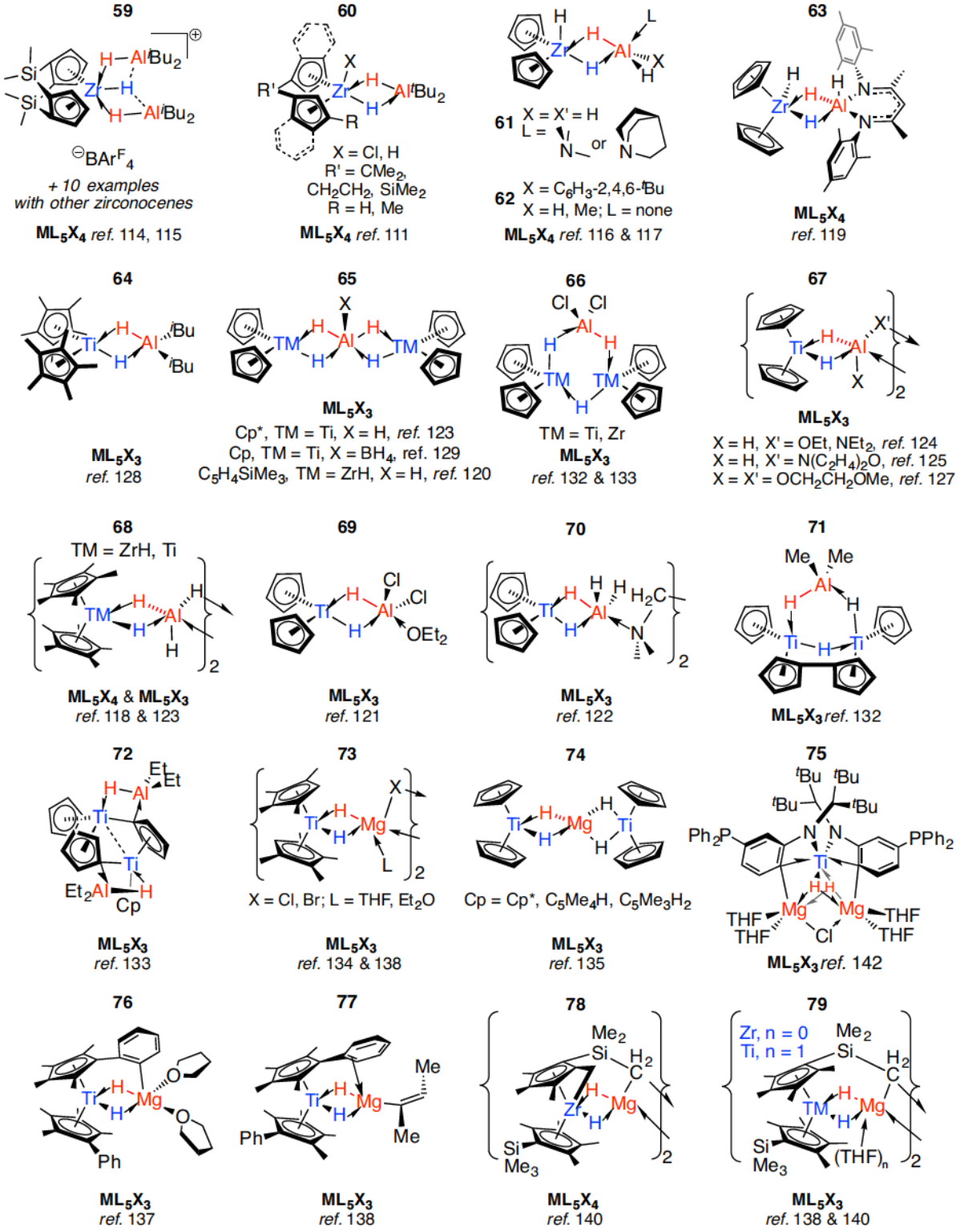


Figure 1.14. Group 4 complexes with multiple hydride bridges.

Substitution of the terminal, X-type hydrides on aluminium for halide,[121,132] alkyl,[128,132,133] alkoxide[124,127] or amide[124,125] has little influence on structure. Magnesium-based

heterobimetallics of group 4 metallocenes (**73**–**77**) can be prepared by reaction of the parent metallocene dichloride with either Grignard reagents or Mg^0 powder in etheric solvents.[134-142] For preparations in which a main group hydride is not used as a reagent the hydride ligands result from either: i) C–H atom abstraction from the solvent (THF), ii) β-hydride elimination from a main group alkyl, or iii) C–H bond activation of the cyclopentadienyl ligand (or its substituents). Ligand activation is common in these complexes and intramolecular deprotonation to form dianionic Cp ligands, including "tuck-in" complexes has been observed to lead to both diamagnetic TM^{IV} and paramagnetic Ti^{III} complexes (**72** & **78**–**79**).[125,132,133,143,144]

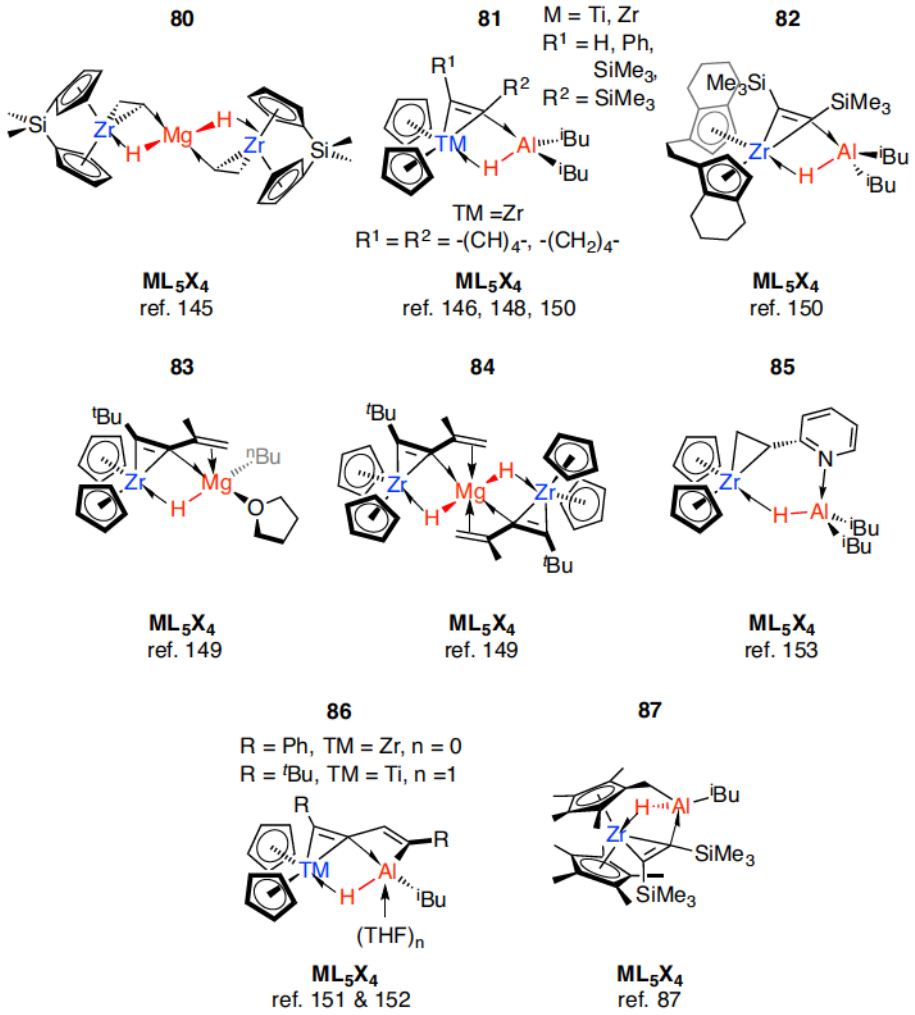


Figure 1.15. Coordination of M–H to Zr and Ti metallocyclopropene and metallocyclopropane complexes

The first confirmed zirconium-ethylene complex **80** was reported by Parkin and co-workers (Figure 1.15).[145] By dint of the bridging carbon, **80** is structurally related to a class of heterobimetallic complexes containing a planar, four-coordinate carbon in the same position. The TM–H–M connection in these zirconium(IV) and titanium(IV) species is supported by a bridging metallacyclopropane or metallacyclopropene (**80**–**87,** Figure 1.15).[87,146-153] A ketene analogue is also known which incorporates an oxycyclopropane ring (not represented in Figure

1.15).[154] The structures of **83**–**87** are distorted to accommodate additional intramolecular binding interactions. Calculations have shown that electron donation from the bridging Zr–C bond to the Lewis acidic main group centre plays a key role in the stabilisation of these species (**81**) and explains the unusual geometry at the bridging carbon.[147]

1.6.3 Late Transition Metal Adducts

Multiply-bridged main group complexes (M = Mg, Zn, Al and Ga) of late transition metals have been known for more than 50 years. Much of the early work is limited by the accuracy of the spectroscopic methods of the period.[20] Nevertheless, it has been clear for some time that the electronegativity difference between late TM and main group metals creates a significant ionic contribution to the bonding.[20] Complexes **88**–**96** are mostly products of salt metathesis between lithium aluminohydrides and TM chlorides.[155-169,171]

Common themes emerge in the coordination geometries of these complexes (Figure 1.16).[170] Unlike the group 4 analogues described above, the $(\mu\text{-H})_3$ bridge is a reoccurring feature. Geometries at aluminium are typically trigonal pyramidal (5-coordinate)[159] or *distorted*-octahedral (6-coordinate). The high coordination number and the geometry of ligands around the TM centres provides coordinative saturation, and in most cases makes the existence of a metal–metal bond very unlikely. For **88,** this finding is in direct contrast to the data reported for the related Rh/Al species **19-Al** and **18** (Figure 1.5).[171]

In solution many of these complexes are fluxional and provide time-averaged ^{1}H NMR chemical shifts for bridging and terminal hydrides. In relation to this phenomenon, the complexes **97** and **98** re-illustrate the ionic component of the bonding. The main group fragment of **97** and **98** is $\{AlMe_2\}^+$, which may exchange between different positions on the face of the $\{P_3ReH_4\}^-$ and $\{P_2ReH_6\}^-$ polyhedra.[172] For comparison, $[ReH_9]^{2-}$ is well-known as the dipotassium salt.[173]

The low-spin ground state structure of **99** has been thoroughly investigated by computational methods.[174] The frontier molecular orbitals of **99** do not support bonding between Fe and Al, and the authors present the complex as being dominated by a strong donation of electron density from a $\{Fe–H\}^-$ fragment to $\{AlX_2\}^+$ (X = O-C_6H_3-2,6-^{t}Bu). This conclusion is a good general insight into the electronic structure of the late-TM$(H)_n$Al bonding, the dimeric examples of which are summarised in **94**–**96**.

An alternative synthetic approach to multiply-bridged main group complexes of the late transition metals is through the addition of H_2 across an unsupported Ru–Zn bond. The $Ru(H)_2Zn$ moiety in **100-H$_2$** discovered by Whittlesey and co-workers demonstrated good thermodynamic stability and survives extrusion of dihydrogen by heating *in vacuo* to form **100**.[175] The hydride ligand *trans* to H_2 in **100-H$_2$** is protic and significantly closer to Ru, while

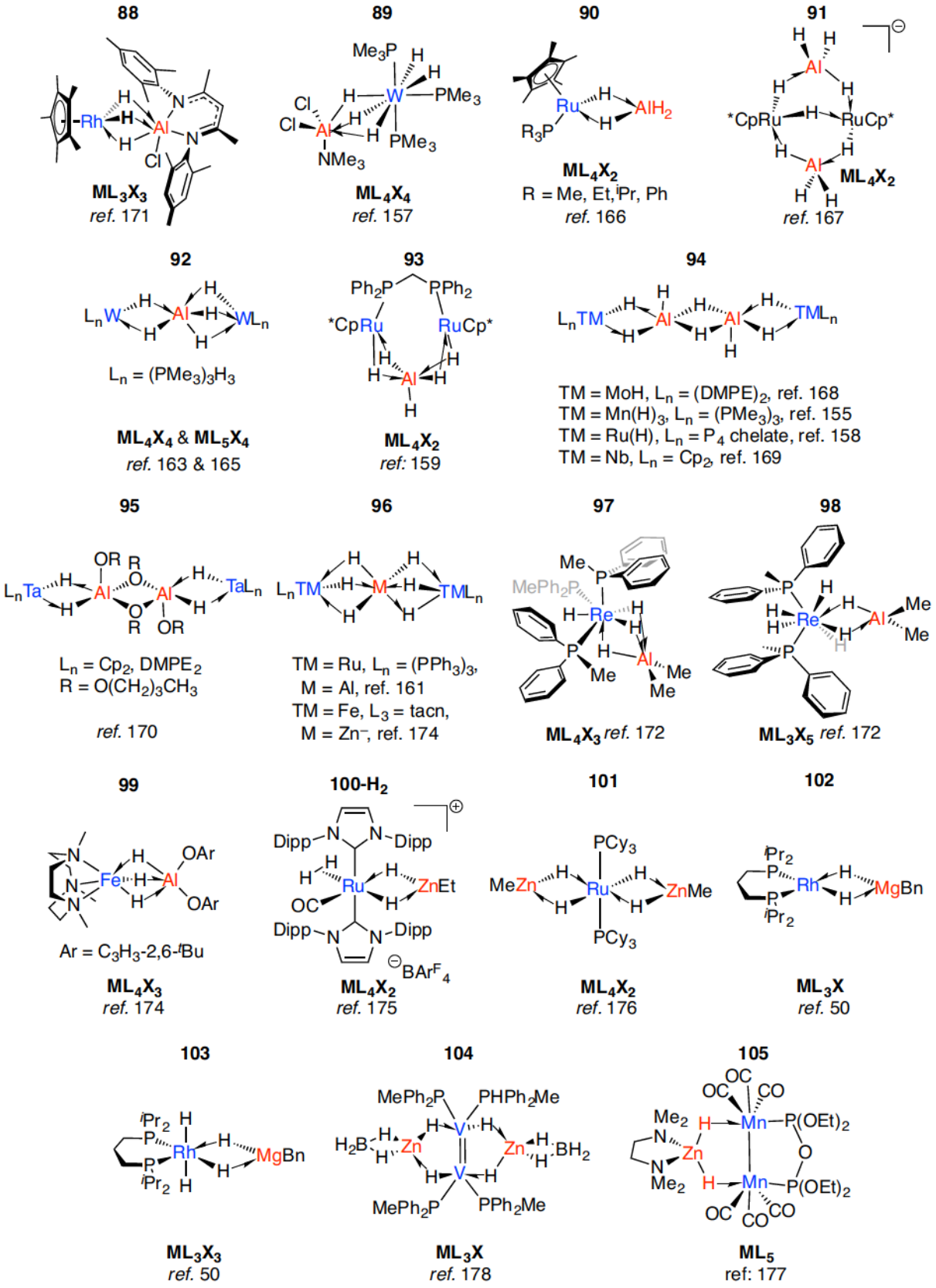


Figure 1.16. Late TM Heterobimetallics containing multiple bridging hydrides.

the hydride *trans* to CO is hydridic and equidistant between the metals. NBO calculations show no sign of Ru–Zn interaction in either complex. However, a QTAIM calculation on **100** shows a Ru–Zn bond path and only one Zn–H bond path. It can be tentatively concluded that the μ-H atoms in **100-H_2** and **100** are intermediate and "flexible" between terminal and bridging character. Fischer and co-workers have reported the related complex **101**, which results from addition of 4.5 equivalents of $ZnMe_2$ to a Ru/Al heterometallic complex prepared *in situ* by mixing $[Ru(PCy_3)_2(\eta^2\text{-}H_2)_2(H)_2]$ and $[Cp^*Al]_4$.[176] Two decades before, Rh/Mg complexes **102** and **103** were prepared by Fryzuk, however their thermal instability precluded characterisation by anything other than ^1H and ^{31}P NMR spectroscopy (Figure 1.16). A number of dinuclear (with respect to TM) complexes supported by chelating ligands or involving TM–TM bonding including **104**–**105** are also known.[177,178]

1.7 Discussion

Presented above is an exhaustive account of the heterobimetallic hydride complexes reported over the last half a century, along with their preparation and structural features. During the Crimmin group's research in this area and through analysis of the material above, recurring issues in the understanding of this family of complexes have appeared. For the benefit of potential future studies, these issues are discussed below.

1.7.1 Structure and Bonding

1.7.1.1 Sigma-Complexes and Oxidative Addition

The current understanding of the TM←H–M linkage (M = Mg, Zn, Al, Ga) in σ-complexes is that it is comprised primarily of a donor interaction from main group metal hydride to a vacant orbital of suitable symmetry on the transition metal fragment. There is limited data to support significant back-donation from the metal to the M–H σ*-orbital. For example, calculations on complexes **1**–**3** elucidate a donor-acceptor interaction with the 4s-orbital of the Cu d^{10} fragment acting as the acceptor: second-order perturbation calculations reveal only a small contribution from back-donation (Figure 1.17).[27]

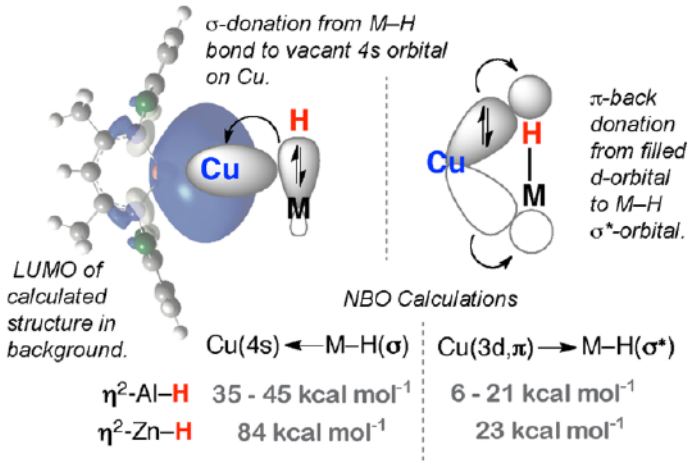


Figure 1.17. Bonding description of **1**–**3**.

The model is supported by comparison of the carbonyl stretching frequencies of complexes of the form $[(\eta^5\text{-}C_5H_4Me)Mn(CO)_2L]$ where L is an E–H or M–H bond. Listed in Table 1.1 these data show that σ-alane, σ-gallane and σ-zincane complexes are similar to those formed from four coordinate boranes such as $H_3B{\bullet}NMe_3$. The data are consistent with limited back bonding into the M–H bond and contrast those of three-coordinate σ-boranes and σ-silanes where increased back-donation to the E–H bond results in higher frequency carbonyl stretching frequencies.[37] The domination of the σ-donation component of the bonding, and the

importance of the ionic component to bonding, is readily understood by considering the difference in the Pauling electronegativity of the elements involved for coordination of E–H ($\Delta\chi_p$: B = 0.18, Si = 0.32) and M–H bonds ($\Delta\chi_p$: Mg = 0.92, Zn = 0.57, Al = 0.61, Ga = 0.41).

Table 1.1. Comparison of CO stretching frequencies in [(η^5-C_5H_4Me)Mn(CO)$_2$L]. *BDI* = (2,6-^{i}Pr$_2$C$_6$H$_3$CNMe)$_2$CH. Adapted from reference 37.

L	ν_1 (cm^{-1})	ν_2 (cm^{-1})
H_2	1982	1922
HBCat	1995	1937
$HSiPh_3$	1983	1926
$HGePh_3$	1965	1910
$HSnPh_3$	1934	1925
$H_3B{\bullet}NMe_3$	1918	1839
H–Al(H)*BDI*	1947	1879
H–Ga(H)*BDI*	1951	1886
H–Zn*BDI*	1937	1852

Considering the structures of the isolated complexes in sections 1.2 and 1.3, it becomes clear that the well understood continuum between σ-complexes and oxidative addition products detailed for addition of E–H bonds to transition metals also applies to M–H bonds.

The triangular TM–H–M unit is subject to structural changes as the electron density changes at the TM (Figure 1.18). The formal shortness ratio (*fsr*)[179] normalises the metal···metal distance and has been used to evaluate the intermetallic interaction in complexes containing two metals in close proximity.[37] For data collected to date, this metric appears to conveniently describe the extremes of the reaction coordinate: σ-complexes (*fsr* approx. > 1) and products of oxidative addition / hydride transfer (*fsr* approx. ≤ 1).

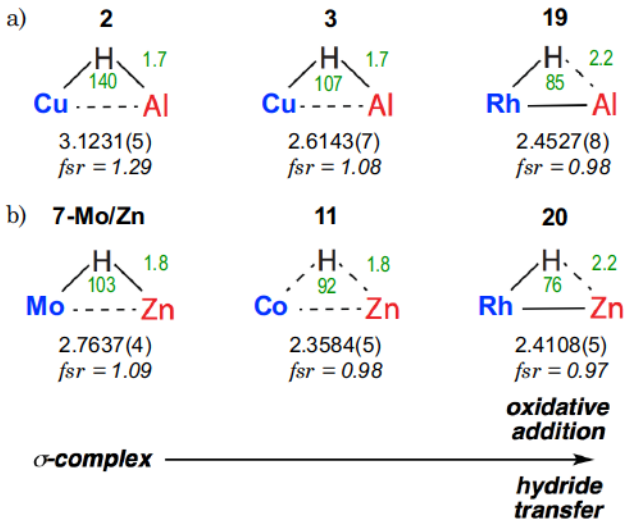
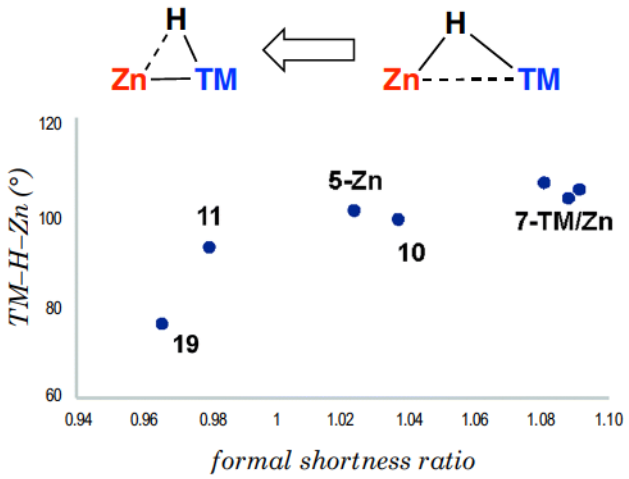


Figure 1.18. Comparison of key distances [Å] and angles [°] from X-ray (TM···M) structures of coordinated (a) Al–H and (b) Zn–H bonds. Trends confirmed by DFT studies.

Very recently the Crimmin group has described the reaction coordinate for the addition of zinc–hydrides to transition metal centres. Through isolation of a series of different transition metal complexes and DFT studies, a bonding continuum was outlined. It is characterised by the transfer of electron density from the breaking of the (largely ionic) Zn–H bond to forming the (increasingly covalent) TM–H and TM–Zn bonds (Graph 1.1). Only at very short TM···Zn separations does the Zn–H bond begin to lengthen significantly. The Zn–H bond varies between approximately 1.7–1.8 Å for σ-zincane complexes but increases dramatically to 2.2 Å for the product of oxidative addition. Similarly, for σ-alane complexes the Al–H separation of 1.6–1.8 Å increases to > 2.0 Å for products defined as oxidative addition. The breaking point of this bond appears to occur quite late along the reaction coordinate.



Graph 1.1. Reaction coordinate for the approach of a Zn–H bond to a transition metal, adapted from reference 37.

Comparison of a series of E–H and M–H complexes of a single transition metal fragment, {Cp*Rh(H)($SiEt_3$)} has allowed us to conclude that the ionic component to bonding remains important for the products of oxidative addition and is such that for M = Zn and Mg these complexes can accurately be described as a result of hydride transfer. The two extreme valence bond descriptions of **17** and the related H–$SiEt_3$ and H–Bpin complexes are represented in Figure 1.19. DFT calculations show that the covalent contribution to the TM–M bond (Wiberg Bond Index) decreases along the series Si ~ B < Al < Mg ~ Zn while the charge on rhodium becomes significant for the Zn and Mg members of the series (NPA charge on Rh: Bpin = –0.03, Al(H)*BDI* = –0.11, Mg*BDI* = –0.99). In combination the data suggest that the ionic contribution becomes more significant for the more electropositive elements.

There are clear parallels between the zwitterionic valence bond description **E** and the neutral donor-acceptor complexes, TM→M–H. These species are connected parts of a continuum of bonding descriptions as are σ-complexes of the form TM←H–M and TM–H→M adducts. It appears that as the *fsr* provides some insight when comparing coordination

complexes of the M–H bond to TM, it may also be of some use in considering coordination of the TM–H fragment to M. The bond distances and angles around the Nb–H–Zn moiety of **34** and **35** are compared in Figure 1.20. The *fsr* ratio decreases and TM–H–M angle becomes increasingly acute when comparing a complex with a genuine TM–M bond (**34**) against that in which the primary interaction between the two metals occurs through a 3-centre 2-electron TM–H–M bond.

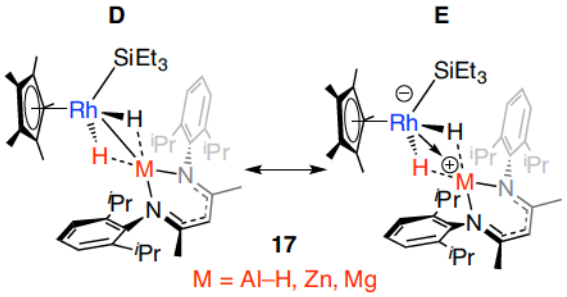


Figure 1.19. Extreme bonding description of **17** and related complexes. Adapted from reference 43.

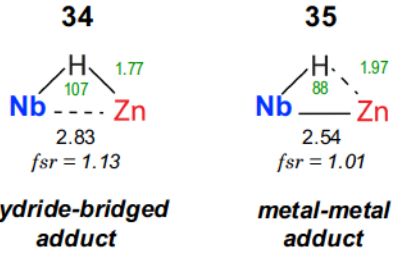


Figure 1.20. Comparison of the bond lengths [Å] and angles [°] in **34** and **35**. Figure adapted from reference 76.

While, in general, the higher electronegativity of the main group element in silanes (and to an extent boranes) means that TM–H→ER_n bonding descriptions are less common, there is growing appreciation that these descriptions may be relevant in σ-silane and σ-borane chemistry. For example, an $\{Ir–H\}^{-}\rightarrow SiR_3^{+}$ interaction has recently been invoked to explain the electronic structure of an intermediate isolated during catalytic studies in the dehydrocoupling of silanes and alcohols.[180] Related borane-capped transition metal hydrides, especially those generated by reversible addition across TM→B bonds are gaining increasing attention in catalytic hydrogenation processes.[181]

1.7.1.2 Multiply bridged hydride complexes

As the number of bridging hydride ligands increases so does the complexity of the structure and of the bonding descriptions. Wilkinson has commented:

"The similarity of…transition metal aluminohydrides to alanes suggest that, whereas it is correct to consider transition metal borohydrides as consisting of L_nM^{+} and BH_4^{-} moieties,

similar models for aluminium analogues are not as accurate. It may be wiser to consider the complexes as being derived from donor-acceptor interactions."[20]

Although generally true for rare earth and group 4 complexes described in section 1.6.2, many late transition metal adducts are described as ate-complexes formed of $\{TM–H_n\}^-$ and M^+ fragments (Figure 1.21).

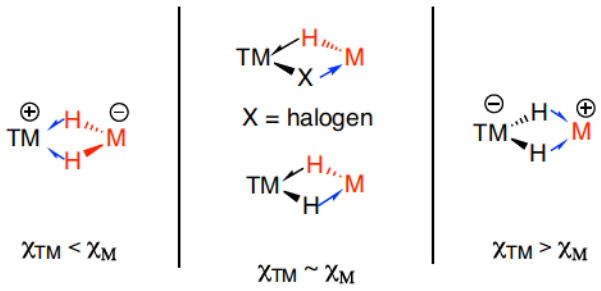


Figure 1.21. Limiting bonding descriptions in multiply bridged heterobimetallic complexes.

A number of species have been isolated that can be considered coordinated complexes of the trapped parent hydrides, these include $\{MgH_4\}^{2-}$, $\{AlH_4\}^-$, $\{AlH_5\}^{2-}$, $\{AlH_6\}^{3-}$, $\{ZnH_6\}^{4-}$, and $\{Al_2H_8\}^{2-}$ structural cores, which can be compared to similar complexes containing $\{SiH_4\}$ and $\{SiH_6\}^{2-}$ trapped between two transition metals.[182,183] These species elucidate the general coordination modes found in multiply hydride bridged species (Figure 1.22). More recently, the Crimmin group has found that the aggregation state of the complexes may be reduced by incorporating kinetically stabilising ligands on M.[27,37,43,119,171]

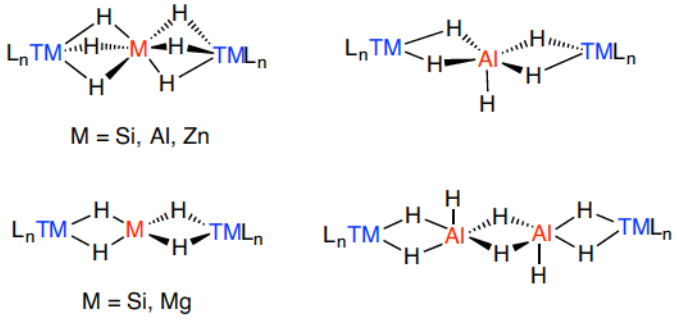


Figure 1.22. Coordination geometries of trapped $\{MH_x\}^{n-}$ units and comparison to silane chemistry.

1.7.2 Reactivity

The 3-centre 2-elecron TM–H–M moiety is surprisingly stable. The novel ground state structures found in heterobimetallic TM–H–M complexes are often assumed to herald unusual reactivity. This correlation is far from proven. Indeed, when it comes to reactivity, the understanding of the ground state structure is not enough. For example, a common feature of

the data for the multiply-bridged hydrides is exchange between hydride positions in the solution phase.[175]

By far the most well understood reaction of TM–H–M groups are those which involve elimination of dihydrogen. Experimentally, while this reactivity has been observed for both Al and Ga complexes, examples of the latter dominate. Through the isolation of intermediates and kinetic analysis, a number of mechanisms for H_2 elimination have been identified and are presented in Figure 1.23. Both α-migration and 1,2-elimination of H_2 across a TM–M bond have been used to rationalise the formation of Ga^I ligands in the coordination sphere of transition metals.

The microscopic reverse of the 1,2-elimination of dihydrogen from a TM(H)–M(H) unit is H_2 addition across a dative TM←M bond. A handful of examples of this type of reactivity are known, albeit from adducts in which the roles of the metals in the Lewis acid-base adduct are reversed. For example, the addition of dihydrogen across Pt→Al and Ru→Zn bonds to form heterobimetallic complexes is known.[82,175] It remains likely that similar reactivity will be discovered for TM←M adducts. This may well be foreshadowed by the existing observations of both inter- and intramolecular addition of carbon–hydrogen bonds across *in situ* generated TM←M (**16**) and TM–M (**20, 31**, **44**) complexes.

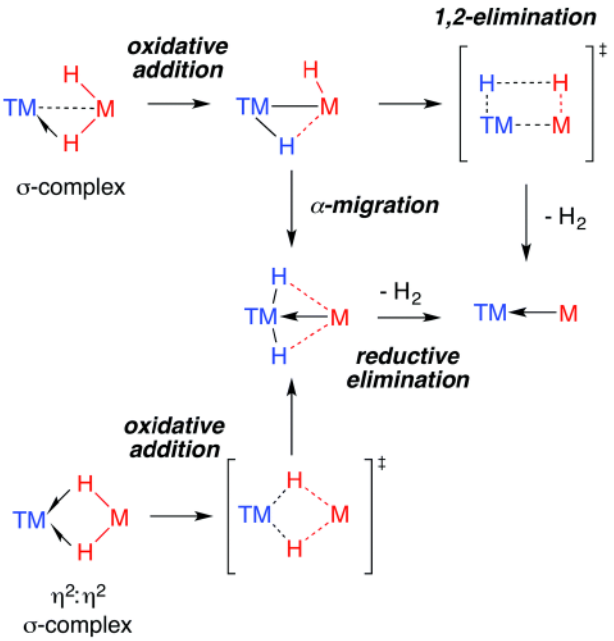


Figure 1.23. Proposed mechanisms for H_2 elimination from heterobimetallic hydrides.

DFT studies on TM–H–Zn complexes have shown that as the hydride is transferred from zinc it becomes less hydridic and more acidic.[37] While the data would suggest that a rich acid/base chemistry may be possible with heterobimetallic hydride complexes, the reactivity of these species remains understudied. The same can be said for insertion of unsaturated substrates (e.g. alkenes, alkynes, CO, CO_2, etc.) into 3-centre 2-electron TM–H–M bonds: it

remains unclear how this chemistry will compare to the well-studied reactions of transition metal hydrides.

1.7.3 Potential in Catalysis

Transition metal hydride complexes are known intermediates in the hydrogenation of unsaturated hydrocarbons, CO (Fischer-Tropsch), and CO_2 along with numerous other small molecules.[184-186] They also play a key role in hydrogenase enzymes and related catalysts for H^+ reduction to H_2 and have been invoked as (off-cycle) intermediates during a number of important polymerisation reactions including Ziegler-Natta catalysis.[85,109]

To date however, defined catalytic reactions believed to involve heterobimetallic hydride complexes are limited. Systems that are catalytic in both the transition and main group metal are the most attractive. Lu and co-workers have reported the heterobimetallic complexes **106** as catalysts for alkene hydrogenation and isomerisation and demonstrated that the nature of the main group metal, M, effects the activity (Figure 1.24).[187] Dihydrogen activation by addition across a Ni→M bond has been proposed as a key step in hydrogenation catalysis. Additionally, Iwasawa & Takaya have very recently engineered Pt–M complexes (M = Al, Ga, In), inspired by Lu's complex, but with pincer-type ligands and the aim of improving substrate access to the transition metal.[188] When M = Al, their system catalyses hydrosilylation of CO_2 with the best *TOF* reported to date (19300 h^{-1}), and excellent conversion of the silane substrate. The mechanism is yet to be described, but the pre-catalytic mixture creates very suitable conditions for CO_2 insertion into Pt/Al hydride intermediates.

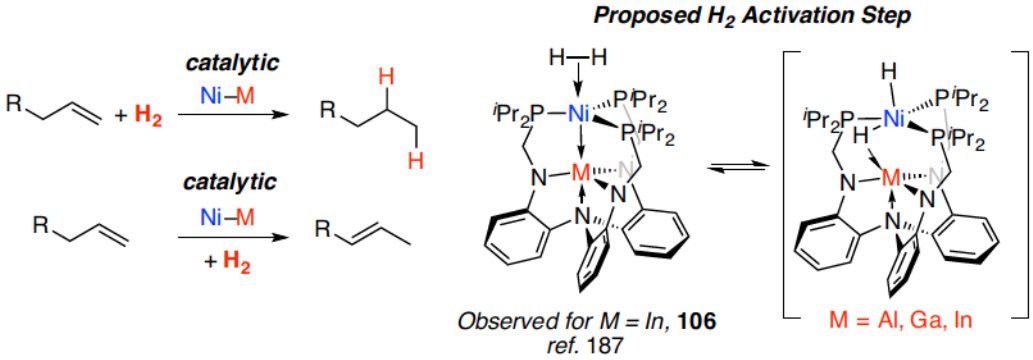


Figure 1.24. Catalytic alkene hydrogenation and isomerisation by heterobimetallic complexes

The importance of transition metal hydrides to numerous aspects of catalysis is not up for debate. Whether or not heterobimetallic complexes will be able to offer advantages over existing monometallic systems remains an open question for the community. It is clear that substantial developments in the stoichiometric and catalytic reactivity of heterobimetallic hydrides need to be made. Nevertheless, the co-location of two metals by direct metal–metal

bonds and/or bridging ligands offers two opportunities in catalysis: new fundamental reactivity, and fine tuning of selection events in known reactions.

The task for the current generation of chemists is to transcribe the known methods for preparation, and the structural understanding of, heterobimetallic hydride complexes into new reactivity. While progress in this area seems to have been made in stops and starts, given the renewed interest in heterobimetallic and main group complexes for catalysis, the challenge appears timely.[186,189-190]

1.8 APPENDIX

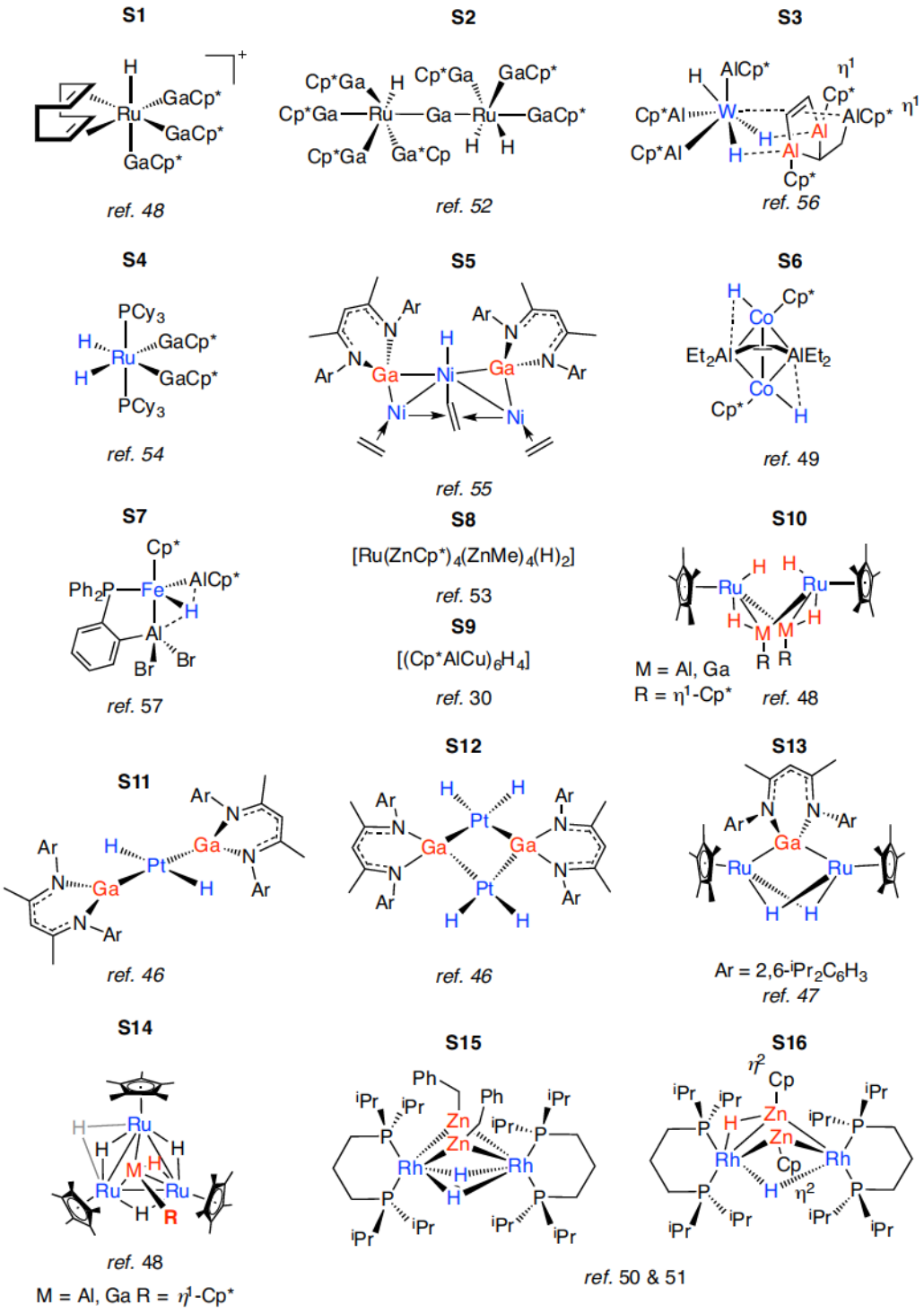


Figure 1.25. Structure of heterobimetallic hydrides (many containing non-bridging hydrides) not included in main text.

1.9 REFERENCES

1 R. H. Crabtree, *Angew. Chem., Int. Ed.*, 1993, **32**, 789–805.
2 M. Brookhart, M. L. H. Green and G. Parkin, *Proc. Natl. Acad. Sci. U. S. A.*, 2007, **104**, 6908–6914.
3 G. J. Kubas, *Proc. Natl. Acad. Sci. U. S. A*, 2007, **104**, 6901–6907.
4 G. J. Kubas, *J. Organomet. Chem*, 2001, **635**, 37–68.
5 G. J. Kubas, *Acc. Chem. Res.*, 1988, **21**, 120–128.
6 S. Sabo-Etienne and B. Chaudret, *Coord. Chem. Rev.*, 1998, **178-180**, 381–407.
7 G. Alcaraz, M. Grellier and S. Sabo-Etienne, *Acc. Chem. Res.*, 2009, **42**, 1640–1649.
8 J. Y. Corey, *Chem. Rev.*, 2016, **116**, 11291–11435
9 S. Lachaize and S. Sabo-Etienne, *Eur. J. Inorg. Chem.*, 2006, 2115–2127.
10 G. I. Nikonov, *J. Organomet. Chem*, 2001, **635**, 24–36.
11 J. C. Green, M. L. H. Green and G. Parkin, *Chem. Commun.*, 2012, **48**, 11481–11503.
12 J. Y. Corey, *Chem. Rev.*, 2011, **111**, 863–1071.
13 S. B. Duckett and R. N. Perutz, *Organometallics*, 1992, **11**, 90–98.
14 S. Sakaki, N. Mizoe and M. Sugimoto, *Organometallics*, 1998, **17**, 2510–2523.
15 G. J. Kubas, *Catal. Lett*, 2005, **104**, 79–101.
16 G. J. Kubas, *Chem. Rev.*, 2007, **107**, 4152–4205.
17 C. E. Webster, Y. Fan, M. B. Hall, D. Kunz and J. F. Hartwig, *J. Am. Chem. Soc.*, 2003, **125**, 858–859.
18 J. F. Hartwig, K. S. Cook, M. Hapke, C. D. Incarvito, Y. Fan, C. E. Webster and M. B. Hall, *J. Am. Chem. Soc.*, 2005, **127**, 2538–2552.
19 I. A. I. Mkhalid, J. H. Barnard, T. B. Marder, J. M. Murphy and J. F. Hartwig, *Chem. Rev.*, 2010, **110**, 890–931.
20 A. R. Barron and G. Wilkinson, *Polyhedron*, 1986, **5**, 1897–1915.
21 G. L. Soloveichik and B. M. Bulychev, *Russ. Chem. Rev.*, 1983, **51**, 43–60.
22 G. Parkin, in *Metal-Metal Bonding*, ed. G. Parkin, Springer Berlin Heidelberg, 2010, vol. 136, pp. 113–145.
23 R. A. Fischer and J. Weiß, *Angew. Chem., Int. Ed.*, 1999, **38**, 2830–2850.
24 C. Gemel, T. Steinke, M. Cokoja, A. Kempter and R. A. Fischer, *Eur. J. Inorg. Chem.*, 2004, 4161–4176.
25 T. Bollermann, C. Gemel and R. A. Fischer, *Coord. Chem. Rev.*, 2012, **256**, 537–555.
26 S. Gonzalez-Gallardo, G. Prabusankar, T. Cadenbach, C. Gemel, M. von Hopffgarten, G. Frenking and R. A. Fischer, in *Metal-Metal Bonding*, ed. G. Parkin, Springer Berlin Heidelberg, 2010, vol. 136, pp. 147–188.
27 A. E. Nako, Q. W. Tan, A. J. P. White and M. R. Crimmin, *Organometallics*, 2014, **33**, 2685–2688.
28 S. Schlecht and J. F. Hartwig, *J. Am. Chem. Soc.*, 2000, **122**, 9435–9443.
29 T. Kakizawa, Y. Kawano and M. Shimoi, *Organometallics*, 2001, **20**, 3211–3213.
30 C. Ganesamoorthy, J. Weßing, C. Kroll, R. W. Seidel, C. Gemel and R. A. Fischer, *Angew. Chem., Int. Ed.*, 2014, **53**, 7943–7947.
31 I. M. Riddlestone, S. Edmonds, P. A. Kaufman, J. Urbano, J. I. Bates, M. J. Kelly, A. L. Thompson, R. Taylor and S. Aldridge, *J. Am. Chem. Soc.*, 2012, **134**, 2551–2554.
32 I. M. Riddlestone, J. Urbano, N. Phillips, M. J. Kelly, D. Vidovic, J. I. Bates, R. Taylor and S. Aldridge, *Dalton Trans.*, 2013, **42**, 249–258.
33 J. A. B. Abdalla, I. M. Riddlestone, R. Tirfoin, N. Phillips, J. I. Bates and S. Aldridge, *Chem. Commun.*, 2013, **49**, 5547–3.
34 J. A. B. Abdalla, I. M. Riddlestone, J. Turner, P. A. Kaufman, R. Tirfoin, N. Phillips and S. Aldridge, *Chem. Eur. J.*, 2014, **20**, 17624–17634.
35 I. M. Riddlestone, J. A. B. Abdalla and S. Aldridge, in *Advances in Organometallic Chemistry*, 2015, vol. 63, pp. 1–38.
36 J. Turner, J. A. B. Abdalla, J. I. Bates, R. Tirfoin, M. J. Kelly, N. Phillips and S. Aldridge, *Chem. Sci.*, 2013, **4**, 4245–4250.
37 O. Ekkert, A. J. P. White and M. R. Crimmin, *Angew. Chem., Int. Ed.*, 2016, **55**, 16031–16034.
38 K. Ueno, T. Yamaguchi, K. Uchiyama and H. Ogino, *Organometallics*, 2002, **21**, 2347–2349.
39 T. Muraoka and K. Ueno, *Coord. Chem. Rev.*, 2010, **254**, 1348–1355.
40 K.-R. Porschke, W. Kleimann, Y.-H. Tsay, C. Kruger and G. Wilke, *Chem. Ber.*, 1990, **123**, 1267–1273.
41 T. Steinke, C. Gemel, M. Cokoja, M. Winter and R. A. Fischer, *Angew. Chem., Int. Ed.*, 2004, **43**, 2299–2302.

42 T. Steinke, M. Cokoja, C. Gemel, A. Kempter, A. Krapp, G. Frenking, U. Zenneck and R. A. Fischer, *Angew. Chem., Int. Ed.*, 2005, **44**, 2943–2946.
43 O. Ekkert, A. J. P. White, H. Toms and M. R. Crimmin, *Chem. Sci.*, 2015, **6**, 5617–5622.
45 L. J. Hounjet, D. Adhikari, M. Pink, P. J. Carroll and D. J. Mindiola, *Z. Anorg. Allg. Chem.*, 2015, **641**, 45–48.
46 L. Fohlmeister, S. Liu, C. Schulten, B. Moubaraki, A. Stasch, J. D. Cashion, L. Gagliardi and C. Jones, *Angew. Chem., Int. Ed.*, 2012, **51**, 8294–8298.
46 A. Kempter, C. Gemel and R. A. Fischer, *Chem. Eur. J.*, 2007, **13**, 2990–3000.
47 A. Doddi, G. Prabusankar, C. Gemel, M. Winter and R. A. Fischer, *Eur. J. Inorg. Chem.*, 2013, 3609–3615.
48 T. Cadenbach, T. Bollermann, C. Gemel and R. A. Fischer, *Dalton Trans.*, 2009, 322–329.
49 J. J. Schneider, C. Kruger, M. Nolte, I. Abraham, T. S. Ertel and H. Bertagnoli, *Angew. Chem., Int. Ed.*, 1994, **33**, 2435–2437.
50 M. D. Fryzuk, D. H. McConville and S. J. Rettig, *Organometallics*, 1990, **9**, 1359–1360.
51 M. D. Fryzuk, D. H. McConville and S. J. Rettig, *Organometallics*, 1993, **12**, 2152–2161.
52 T. Cadenbach, C. Gemel, R. Schmid, M. Halbherr, K. Yusenko, M. Cokoja and R. A. Fischer, *Angew. Chem., Int. Ed.*, 2009, **48**, 3872–3876.
53 T. Cadenbach, T. Bollermann, C. Gemel, M. Tombul, I. Fernandez, M. V. Hopffgarten, G. Frenking and R. A. Fischer, *J. Am. Chem. Soc.*, 2009, **131**, 16063–16077.
54 T. Cadenbach, C. Gemel, T. Bollermann, I. Fernandez, G. Frenking and R. A. Fischer, *Chem. Eur. J.*, 2008, **14**, 10789–10796.
55 A. Kempter, C. Gemel, T. Cadenbach and R. A. Fischer, *Organometallics*, 2007, **26**, 4257–4264.
56 M. Molon, C. Gemel and R. A. Fischer, *J. Organomet. Chem*, 2014, **751**, 573–578.
57 B. Buchin, C. Gemel, A. Kempter, T. Cadenbach and R. A. Fischer, *Inorg. Chim. Acta*, 2006, **359**, 4833–4839.
58 G. Tan, T. Szilvási, S. Inoue, B. Blom and M. Driess, *J. Am. Chem. Soc.*, 2014, **136**, 9732–9742.
59 R. A. Fischer, T. Priermeier and W. Scherer, *J. Organomet. Chem*, 1993, **459**, 65–71.
60 R. A. Fischer, M. M. Schulte, J. Weiß, L. Zsolnai, A. Jacobi, G. Huttner, G. Frenking, C. Boehme and S. F. Vyboishchikov, *J. Am. Chem. Soc.*, 1998, **120**, 1237–1248.
61 R. A. Fischer and T. Priermeier, *Organometallics*, 1994, **13**, 4306–4314.
62 J. T. Golden, T. H. Peterson, P. L. Holland, R. G. Bergman and R. A. Andersen, *J. Am. Chem. Soc.*, 1998, **120**, 223–224.
63 H. Brunner, P. C. Wailes and H. D. Kaesz, *Inorg. Nucl. Chem. Lett.*, 1965, **1**, 125–129.
64 A. Storr and B. S. Thomas, *Can. J. Chem.*, 1971, **49**, 2504–2507.
65 J. W. Bruno, J. C. Huffman and K. G. Caulton, *J. Am. Chem. Soc.*, 1984, **106**, 444–445.
66 M. Amati and F. Lelj, *Can. J. Chem.*, 2009, **87**, 1406–1414.
67 P. C. Wailes, H. Weigold and A. P. Bell, *J. Organomet. Chem*, 1972, **43**, C29–C31.
68 M. L. H. Green, R. E. MacKenzie and J. S. Poland, *J. Chem. Soc., Dalton Trans.*, 1976, 1993–1994.
69 M. Stender, H. Oesen, S. Blaurock and E. Hey Hawkins, *Z. Anorg. Allg. Chem.*, 2001, 980–984.
70 R. A. Forder and K. Prout, *Acta Cryst.*, 1974, **B30**, 2312–2317.
71 S. J. Rettig, A. Storr, B. S. Thomas and J. Trotter, *Acta Cryst.*, 1974, **B30**, 666–672.
72 D. E. Crotty, T. J. Anderson, M. D. Glick and J. P. Oliver, *Inorg. Chem.*, 1977, **16**, 2346–2350.
73 R. L. Geerts, J. C. Huffman and K. G. Caulton, *Inorg. Chem.*, 1986, **25**, 590–591.
74 M. A. Porai-Koshits, A. S. Antsyshkina, A. A. Pasynskii, G. G. Sadikov, Y. V. Skripkin and V. N. Ostrikova, *Inorg. Chim. Acta*, 1979, **34**, L285–L287.
75 F. N. Tebbe, *J. Am. Chem. Soc.*, 1973, **95**, 5412–5414.
76 P. H. M. Budzelaar, A. A. H. Van Der Zeijden, J. Boersma, G. J. M. Van Der Kerk, A. L. Spek and A. J. M. Duisenberg, *Organometallics*, 1984, **3**, 159–163.
77 P. H. M. Budzelaar, K. H. Den Haan, J. Boersma, G. J. M. Van Der Kerk and A. L. Spek, *Organometallics*, 1984, **3**, 156–159.
78 M. Ohashi, K. Matsubara, T. Iizuka and H. Suzuki, *Angew. Chem., Int. Ed.*, 2003, **49**, 937–940.
79 M. Ohashi, K. Matsubara and H. Suzuki, *Organometallics*, 2007, **26**, 2330–2339.
80 K. Prout and R. A. Forder, *Acta Cryst.*, 1975, **B31**, 852–856.
81 M. L. H. Green, G. A. Moser, I. Packer, F. Petit, R. A. Forder and K. Prout, *J. Chem. Soc., Chem. Commun.*, 1974, 839–840.
82 M. Devillard, R. Declercq, E. Nicolas, A. W. Ehlers, J. Backs, N. Saffon-Merceron, G. Bouhadir, J. C. Slootweg, W. Uhl and D. Bourissou, *J. Am. Chem. Soc.*, 2016, **138**, 4917–4926.
83 R. A. Fischer, D. Weiß, M. Winter, I. Müller, H. D. Kaesz, N. Fröhlich and G. Frenking, *J. Organomet. Chem*, 2004, **689**, 4611–4623.
84 B. E. Cowie, F. A. Tsao and D. J. H. Emslie, *Angew. Chem., Int. Ed.*, 2014, **54**, 2165–2169.
85 L. V. Parfenova, P. V. Kovyazin, I. E. Nifant'ev, L. M. Khalilov and U. M. Dzhemilev,

Organometallics, 2015, **34**, 3559–3570.
86 V. V. Burlakov, P. Arndt, W. Baumann, A. Spannenberg and U. Rosenthal, *Organometallics*, 2006, **25**, 519–522.
87 J. Kopf, H. J. Vollmer and W. Kaminsky, *Cryst. Struct. Commun.*, 1980, **9**, 985.
88 A. I. Sizov, T. M. Zvukova, A. A. Gorkovskii, Z. A. Starikova and B. M. Bulychev, *Russ. Chem. Bull.*, 2004, **53**, 2175–2178.
89 T. M. Arkhireeva, V. K. Bel'skii, B. M. Bulychev and G. L. Soloveichik, *Russ. Chem. Bull.*, 1986, **35**, 2585–2587.
90 D. Schädle, C. Schädle, D. Schneider, C. Maichle-Mössmer and R. Anwander, *Organometallics*, 2015, **34**, 4994–5008.
91 C. Schädle, C. Maichle-Mössmer, K. W. Törnroos and R. Anwander, *Organometallics*, 2015, **34**, 2667–2675.
92 C. Schädle, D. Schädle, K. Eichele and R. Anwander, *Angew. Chem., Int. Ed.*, 2013, **52**, 13238–13242.
93 M. G. Klimpel, P. Sirsch, W. Scherer and R. Anwander, *Angew. Chem., Int. Ed.*, 2003, **42**, 574–577.
94 S. Y. Knjazhanski, B. M. Bulychev, V. K. Belsky and G. L. Soloveichik, *J. Organomet. Chem*, 1987, **327**, 173–179.
95 C. Schädle, A. Fischbach, E. Herdtweck, K. W. Törnroos and R. Anwander, *Chem. Eur. J.*, 2013, **19**, 16334–16341.
96 C. Schädle and R. Anwander, *Eur. J. Inorg. Chem.*, 2013, 3302–3306.
97 E. B. Lobkovskii, G. L. Soloveichik, A. B. Erofeev, B. M. Bulychev and V. K. Bel'skii, *J. Organomet. Chem*, 1982, **235**, 151–159.
98 E. Lobkovsky, G. L. Soloveychik, B. M. Bulychev, A. B. Erofeev, A. I. Gusev and N. I. Kirillova, *J. Organomet. Chem*, 1983, **254**, 167–172.
99 V. K. Bel'skii, B. M. Bulychev, A. B. Erofeev and G. L. Soloveichik, *J. Organomet. Chem*, 1984, **268**, 107–111.
100 V. K. Belsky, A. B. Erofeev, B. M. Bulychev and G. L. Soloveichik, *J. Organomet. Chem*, 1984, **265**, 123–133.
101 S. Y. Knjazhanski, B. M. Bulychev, O. K. Kireeva, V. K. Belsky and G. L. Soloveichik, *J. Organomet. Chem*, 1991, **414**, 11–22.
102 V. K. Belsky, Y. K. Gun'ko, B. M. Bulychev and G. L. Soloveichik, *J. Organomet. Chem*, 1991, **419**, 299–310.
103 Y. K. Gun'ko, B. M. Bulychev, A. I. Sizov, V. K. Belsky and G. L. Soloveichik, *J. Organomet. Chem*, 1990, **390**, 153–158.
104 A. B. Erofeev, B. M. Bulychev, V. K. Bel'skii and G. L. Soloveichik, *J. Organomet. Chem*, 1987, **335**, 189–199.
105 S. Y. Knjazhanski, E. B. Lobkovsky, B. M. Bulychev, V. K. Belsky and G. L. Soloveichik, *J. Organomet. Chem*, 1991, **419**, 311–324.
106 M. F. Lappert, A. Singh, J. L. Atwood and W. E. Hunter, *J. Chem. Soc., Chem. Commun.*, 1983, 206–207.
107 K. D. Conroy, W. E. Piers and M. Parvez, *Organometallics*, 2009, **28**, 6228–6233.
108 Y. K. Gun'ko, B. M. Bulychev, V. K. Belsky and G. L. Soloveichik, *J. Organomet. Chem*, 1992, **440**, 47–52.
109 H. G. Alt and A. Köppl, *Chem. Rev.*, 2000, **100**, 1205–1222.
110 L. I. Shoer, K. I. Gell and J. Schwartz, *J. Organomet. Chem*, 1977, **136**, C19–C22.
111 S. M. Baldwin, J. E. Bercaw and H. H. Brintzinger, *J. Am. Chem. Soc.*, 2008, **130**, 17423–17433.
112 U. M. Dzhemilev and A. G. Ibragimov, *Russ. Chem. Rev.*, 2012, **81**, 524–548.
113 K. P. Bryliakov, E. P. Talsi, A. Z. Voskoboynikov, S. J. Lancaster and M. Bochmann, *Organometallics*, 2008, **27**, 6333–6342.
114 S. M. Baldwin, J. E. Bercaw, L. M. Henling, M. W. Day and H. H. Brintzinger, *J. Am. Chem. Soc.*, 2011, **133**, 1805–1813.
115 S. M. Baldwin, J. E. Bercaw and H. H. Brintzinger, *J. Am. Chem. Soc.*, 2010, **132**, 13969–13971.
116 K. Khan, C. L. Raston, J. E. McGrady, B. W. Skelton and A. H. White, *Organometallics*, 1997, **16**, 3253–3254.
117 R. J. Wehmschulte and P. P. Power, *Polyhedron*, 1999, **18**, 1885–1888.
118 N. Etkin, A. J. Hoskin and D. W. Stephan, *J. Am. Chem. Soc.*, 1997, **119**, 11420–11424.
119 S. Yow, S. J. Gates, A. J. P. White and M. R. Crimmin, *Angew. Chem., Int. Ed.*, 2012, **51**, 12559–12563.
120 N. Etkin and D. W. Stephan, *Organometallics*, 1998, **17**, 763–765.
121 E. B. Lobkovskii, G. L. Soloveichik, B. M. Bulychev, R. G. Gerr and Y. T. Struchkov, *J. Organomet. Chem*, 1984, **270**, 45–51.

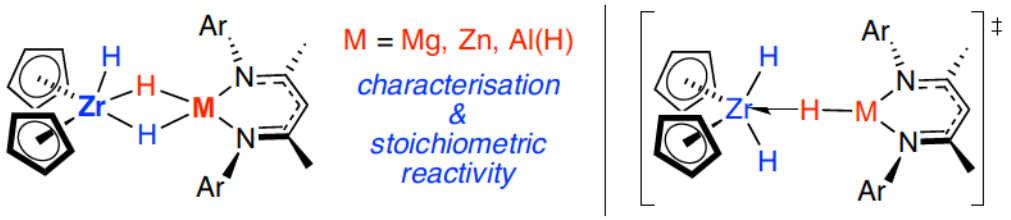
122 E. B. Lobkovskii, G. L. Soloveichik, A. J. Sisov, B. M. Bulychev, A. I. Gusev and N. I. Kirillova, *J. Organomet. Chem*, 1984, **265**, 167–173.
123 V. K. Bel'sky, A. I. Sizov, B. M. Bulychev and G. L. Soloveichik, *J. Organomet. Chem*, 1985, **280**, 67–80.
124 T. Y. Sokolova, A. I. Sizov, B. M. Bulychev, E. A. Rozova, V. K. Belsky and G. L. Soloveichik, *J. Organomet. Chem*, 1990, **288**, 11–19.
125 A. I. Sizov, T. M. Zvukova, V. K. Belsky and B. M. Bulychev, *Russ. Chem. Bull.*, 1998, **47**, 1186–1192.
126 A. I. Sizov, T. M. Zvukova, B. M. Bulychev and V. K. Belsky, *J. Organomet. Chem*, 2000, **603**, 167–173.
127 R. Sun, J. Liu, S. Yang, M. Chen, N. Sun, H. Chen, X. Xie, X. You, S. Li and Y. Liu, *Chem. Commun.*, 2015, **51**, 6426–6429.
128 J. Thomas, M. Klahn, A. Spannenberg and T. Beweries, *Dalton Trans.*, 2013, **42**, 14668–14672.
129 A. I. Sizov, I. V. Molodnitskaya, B. M. Bulychev, V. K. Bel'skii and G. L. Soloveichik, *J. Organomet. Chem*, 1988, **344**, 185–193.
130 A. I. Sizov, T. M. Zvukova, V. K. Belsky and B. M. Bulychev, *J. Organomet. Chem*, 2001, **619**, 36–42.
131 A. I. Sizov, T. M. Zvukova, V. K. Belsky and B. M. Bulychev, *Russ. Chem. Bull.*, 2001, **50**, 2200–2202.
132 L. J. Guggenberger and F. N. Tebbe, *J. Am. Chem. Soc.*, 1973, **95**, 7870–7872.
133 F. N. Tebbe and L. J. Guggenberger, *J. Chem. Soc., Chem. Commun.*, 1973, 227–228.
134 S. I. Troyanov, V. Varga and K. Mach, *J. Organomet. Chem*, 1993, **461**, 85–90.
135 R. Gyepes, K. Mach, I. Cisarova, J. Loub, J. Hiller and P. Sindelar, *J. Organomet. Chem*, 1995, **497**, 33–41.
136 M. Horáček, J. Hiller, U. Thewalt, M. Polášek and K. Mach, *Organometallics*, 1997, **16**, 4185–4191.
137 V. Kupfer, U. Thewalt, M. Horáček, L. Petrusova and K. Mach, *Inorg. Chem. Commun.*, 1999, **2**, 540–544.
138 K. Mach, R. Gyepes, M. Horáček, L. Petrusová and J. Kubišta, *Collect. Czech. Chem. Commun.* **2003**, 68, 1877-1896
139 M. Horáček, I. Cisarova, J. Cejka, J. Karban, L. Petrusova and K. Mach, *J. Organomet. Chem*, 1999, **577**, 103–112.
140 M. Horáček, P. Štěpnička, J. Kubišta, K. Fejfarová, R. Gyepes and K. Mach, *Organometallics*, 2003, **22**, 861–869.
141 J. G. Kenworthy, J. Myatt and M. C. R. Symons, *J. Chem. Soc., A*, 1971, 1020–1025.
142 Q. F. Mokuolu, P. A. Duckmanton, A. J. Blake, C. Wilson and J. B. Love, *Organometallics*, 2003, **22**, 4387–4389.
143 E. B. Lobkovskii, G. L. Soloveichik, A. I. Sizov and B. M. Bulychev, *J. Organomet. Chem*, 1985, **280**, 53–66.
144 E. B. Lobkovskii, A. I. Sizov, B. M. Bulychev and I. V. Sokolova, *J. Organomet. Chem*, 1987, **319**, 69–75.
145 H. Lee, T. Hascall, P. J. Desrosiers and G. Parkin, *J. Am. Chem. Soc.*, 1998, **120**, 5830–5831.
146 G. Erker, M. Albrecht, C. Kruger, S. Werner, P. Binger and F. Langhauser, *Organometallics*, 1992, **11**, 3517–3525.
147 R. Gleiter, I. Hyla-Kryspin, S. Niu and G. Erker, *Angew. Chem., Int. Ed.*, 1993, **32**, 754–756.
148 M. Albrecht, G. Erker and C. Kruger, *Synlett*, 1993, 441–448.
149 G. Bender, T. Wiegand, H. Eckert, R. Fröhlich, C. G. Daniliuc, C. Mück-Lichtenfeld, S. Ndambuki, T. Ziegler, G. Kehr and G. Erker, *Angew. Chem., Int. Ed.*, 2012, **51**, 8846–8849.
150 P. Arndt, A. Spannenberg, W. Baumann, S. Becke and U. Rosenthal, *Eur. J. Inorg. Chem.*, 2001, 2885–2890.
151 V. V. Burlakov, P. Arndt, W. Baumann, A. Spannenberg and U. Rosenthal, *Organometallics*, 2004, **23**, 4160–4165.
152 V. V. Burlakov, K. Kaleta, T. Beweries, P. Arndt, W. Baumann, A. Spannenberg, V. B. Shur and U. Rosenthal, *Organometallics*, 2011, **30**, 1157–1161.
153 P. Arndt, A. Spannenberg, W. Baumann, V. V. Burlakov, U. Rosenthal, S. Becke and T. Weiss, *Organometallics*, 2004, **23**, 4792–4795.
154 R. M. Waymouth, B. D. Santarsiero, R. J. Coots, M. J. Bronikowski and R. H. Grubbs, *J. Am. Chem. Soc.*, 1986, **108**, 1427–1441.
155 G. S. Girolami, G. Wilkinson, M. Thornton-Pett and M. B. Hursthouse, *J. Am. Chem. Soc.*, 1983, **105**, 6752–6753.
156 G. S. Girolami, C. G. Howard, G. Wilkinson, H. M. Dawes, M. Thornton-Pett, M. Motevalli and M. B. Hursthouse, *J. Chem. Soc., Dalton Trans.*, 1985, 921–929.

157 A. R. Barron, G. Wilkinson, M. Motevalli and M. B. Hursthouse, *J. Chem. Soc., Dalton Trans.*, 1987, 837–846.
158 R. Gilbert-Wilson, L. D. Field and M. Bhadbhade, *Inorg. Chem.*, 2014, **53**, 12469–12479.
159 G. S. Girolami, *Organometallics*, 1997, **16**, 2987–2994.
160 M. Plois, T. Wiegand and R. Wolf, *Organometallics*, 2012, **31**, 8469–8477.
161 M. Plois, R. Wolf, W. Hujo and S. Grimme, *Eur. J. Inorg. Chem.*, 2013, 3039–3048.
162 T. N. Gieshoff, M. Villa, A. Welther, M. Plois, U. Chakraborty, R. Wolf and A. Jacobi von Wangelin, *Green Chem.*, 2015, **17**, 1408–1413.
163 A. R. Barron, M. B. Hursthouse, M. Motevalli and G. Wilkinson, *J. Chem. Soc., Chem. Commun.*, 1985, 664–665.
164 A. R. Barron and G. Wilkinson, *J. Chem. Soc., Dalton Trans.*, 1986, 287–3.
165 A. R. Barron, D. Lyons, G. Wilkinson, M. Motevalli, A. J. Howes and M. B. Hursthouse, *J. Chem. Soc., Dalton Trans.*, 1986, 279–285.
166 D. H. Lee, H. Suzuki and Y. Moro-oka, *J. Organomet. Chem*, 1987, **330**, C20–C22.
167 M. D. Fryzuk, G. K. B. Clentsmith and S. J. Rettig, *Inorg. Chim. Acta*, 1997, **259**, 51–59.
168 V. Saboonchian, G. Wilkinson, B. Hussain-Bates and M. B. Hursthouse, *Polyhedron*, 1991, **10**, 595–603.
169 G. I. Nikonov, L. G. Kuzmina and J. A. K. Howard, *J. Chem. Soc., Dalton Trans.*, 2002, 3037–3046.
170 T. J. McNeese, S. S. Wreford and B. M. Foxman, *J. Chem. Soc., Chem. Commun.*, 1978, 500–502.
171 O. Ekkert, S. D. A. Strudley, A. Rozenfeld, A. J. P. White and M. R. Crimmin, *Organometallics*, 2014, **33**, 7027–7030.
172 W. A. Skupinski, J. C. Huffman, J. W. Bruno and K. G. Caulton, *J. Am. Chem. Soc.*, 1984, **106**, 8128–8136.
173 K. Knox and A. P. Ginsberg, *Inorg. Chem.*, 1964, **3**, 555–558.
174 M. Oishi, T. Endo, M. Oshima and H. Suzuki, *Inorg. Chem.*, 2014, **53**, 5100–5108.
175 I. M. Riddlestone, N. A. Rajabi, J. P. Lowe, M. F. Mahon, S. A. Macgregor and M. K. Whittlesey, *J. Am. Chem. Soc.*, 2016, **138**, 11081–11084.
176 M. Molon, C. Gemel and R. A. Fischer, *Eur. J. Inorg. Chem.*, 2013, 3616–3622.
177 V. Riera, M. A. Ruiz, A. Tiripicchio and M. Tiripicchio-Camellini, *Organometallics*, 1993, **12**, 2962–2972.
178 R. L. Bansemer, J. C. Huffman and K. G. Caulton, *J. Am. Chem. Soc.*, 1983, **105**, 6163–6164.
179 The *fsr* is defined as the d(TM−M)/[r_M(TM)+r_M(M)] where r_M is the single-bond radius of the atom defined by L. Pauling, *J. Am. Chem. Soc.*, 1947, **69**, 542–553.
180 M. Hamdaoui, M. Ney, V. Sarda, L. Karmazin, C. Bailly, N. Sieffert, S. Dohm, A. Hansen, S. Grimme and J.-P. Djukic, *Organometallics*, 2016, **35**, 2207–2223.
181 W. H. Harman and J. C. Peters, *J. Am. Chem. Soc.*, 2012, **134**, 5080–5082.
182 I. Atheaux, B. Donnadieu, V. Rodriguez, S. Sabo-Etienne, B. Chaudret, K. Hussein and J.-C. Barthelat, *J. Am. Chem. Soc.*, 2000, **122**, 5664–5665.
183 M. C. Lipke and T. D. Tilley, *Angew. Chem., Int. Ed.*, 2012, **51**, 11115–11121.
184 R. N. Perutz and B. Procacci, *Chem. Rev.*, 2016, **116,** 8506–8544
185 E. S. Wiedner, M. B. Chambers, C. L. Pitman, R. M. Bullock, A. J. M. Miller and A. M. Appel, *Chem. Rev.*, 2016, **116**, 8655–8692.
186 A. Maity and T. S. Teets, *Chem. Rev.*, 2016, **16**, 8873–8911
187 R. C. Cammarota and C. C. Lu, *J. Am. Chem. Soc.*, 2015, **137**, 12486–12489.
188 J. Takaya and N. Iwasawa, *J. Am. Chem. Soc.*, 2017, **139**, 6074–6077.
189 N. P. Mankad, *Chem. Eur. J.*, 2016, **22**, 5822–5829.
190 R. J. Eisenhart, L. J. Clouston and C. C. Lu, *Acc. Chem. Res.*, 2015, **48**, 2885–2894

"To see what is in front of one's nose needs a constant struggle."

George Orwell, *In Front of Your Nose*

CHAPTER 2 – Characterisation of (Hydrido)Zirconocene Complexes of Magnesium, Zinc and Aluminium



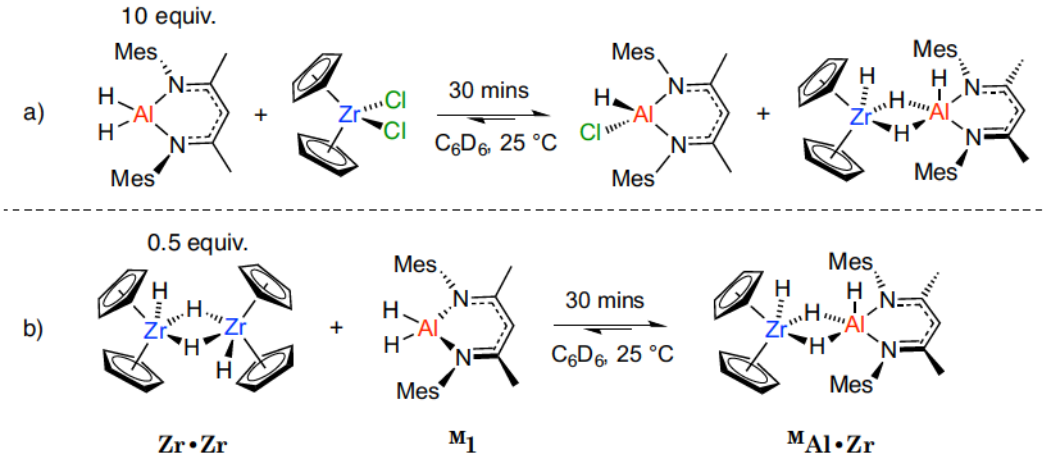
The zirconocene/β-diketiminate complex of Al can be synthesised from its parent Al and Zr hydrides, as reported previously by the Crimmin group. The synthesis of the Mg and Zn homologues is herein developed. Following scale-up and isolation, solid- and solution-state structures are confirmed and correlated by single-crystal X-ray diffraction, DFT studies, CHN analysis, and multinuclear and variable-temperature NMR spectroscopy. Unlike the Al analogue, the Mg and Zn complexes show very little evidence of dissociation under 363 K. The M^{II}/Zr heterobimetallic complexes are therefore found to be much more stable in experimental and computational tests. Calculations find the most stable homologue, the Mg/Zr system, to have a large ate complex component to its bonding character. An exchange process between a terminal and bridging hydride is quantified by variable-temperature ^{1}H NMR spectroscopy, and the mechanism is proposed using DFT calculations. Finally, heterobimetallic species are found to have varied reactivities with regards to C_{Ar}–F bond cleavage and an oxazirconacycle fragment.

Parts of this chapter have been published:

M. J. Butler, A. J. P. White and M. R. Crimmin, *Angew. Chem. Int. Ed.*, 2016, **55**, 6951–6953.

2.1 INTRODUCTION

Previous investigations into equilibration of a [Cp_2ZrCl_2] pre-catalyst (Scheme 2.1a) with alane ^{M}**1** in a 1:10 mixture yielded ^{M}**Al•Zr** (seen in Chapter 1 and numbered previously as **1.63**).[1] In order to isolate and confirm the heterobimetallic complex, a more workable preparative scale synthesis was achieved by using the parent hydrides of the two metal fragments, **Zr•Zr** and ^{M}**1** (Scheme 2.1b). Growth of single crystals of ^{M}**Al•Zr** suitable for an X-ray diffraction study failed. The aryl groups on the aluminium compound were changed. The 2,6-xylyl analogue, ^{X}**Al•Zr** gave the crystal structure shown in Figure 2.1.



Scheme 2.1. a) Synthesis of ^{M}**Al•Zr** by ligand exchange; b) synthesis of ^{M}**Al•Zr** by parent hydride combination. Figure adapted from a previous publication by the Crimmin group.[1]

Upon dissolving pure crystals of ^{X}**Al•Zr,** ^{1}H NMR signals for **Zr•Zr** and ^{X}**1** are present; the equilibrium between the homo- and heterobimetallic hydrides was evidenced by crossover experiments of ^{X}**Al•Zr** with ^{M}**1**. The considerably broadened bridging hydride ^{1}H NMR signals appear in the characteristic region upfield of δ = 0 ppm. Variable-temperature (VT) and NOESY NMR experiments show that, in part, the line broadening is due to site-exchange. Above 263 K, all of the hydride atoms in ^{M}**Al•Zr** are in fast exchange. The ^{1}H NMR data and solution-state behaviour are summarised in Figure 2.2.

The terminal hydrides possess positive chemical shift values (relative to tetramethylsilane), which is typical of d^0 metals. They are involved in a coalescence event with both H_μ signals (T_c = 283 K). The exchange of the hydrides is a consequence of the significant propensity of ^{M}**Al•Zr** to dissociate.[1] The dissociation constant was not quantified in the study, but at room temperature the equilibrium lies towards ^{M}**Al•Zr**. In toluene-d_8 at 293 K the ratio of ^{M}**1**:^{M}**Al•Zr** is roughly 1:5.

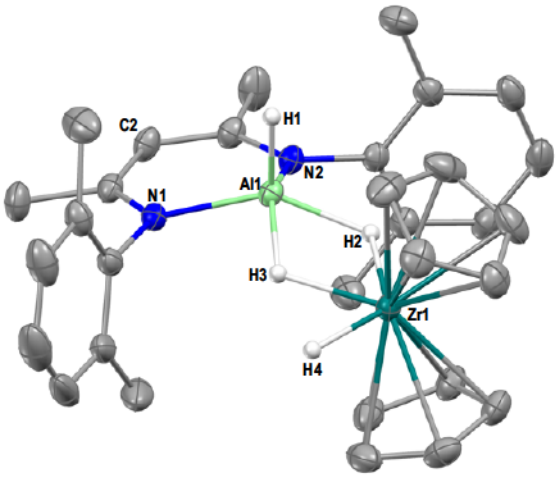


Figure 2.1. Crystal structure of ^{X}**Al•Zr** (50% probability ellipsoids). Figure adapted from ref. 1. Selected bond lengths [Å] and bond angles [°]: Al1---Zr1 3.006(4), Al1–N3 1.9464(10), Al1–N1 1.9493(10), Zr–C 2.4964(14)–2.5219(13); N1-Al-N3 93.14(4)

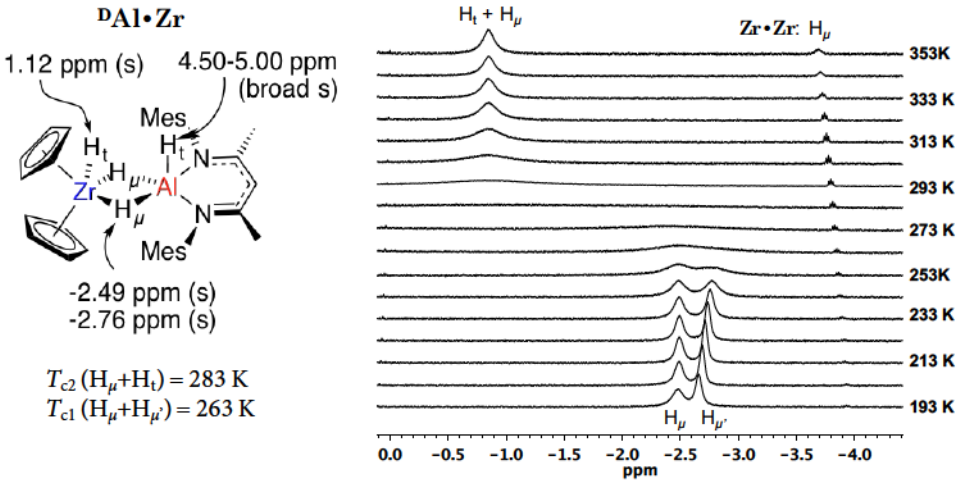


Figure 2.2. Hydride-related ^{1}H NMR data for ^{M}**Al•Zr** in toluene-d_8 (400 MHz). Left: the chemical shifts of the hydride atoms at 233 K. Right: the hydride region of the variable-temperature NMR experiment.

2.1.1 Aims

Compounds ^{X}**Al•Zr** and ^{M}**Al•Zr** were catalytically competent for C–F bond cleavage. For a similar inert bond cleavage catalysis, ^{M}**Al•Zr** has also been applied as a catalyst: the formal insertion of Al into an etheric C–O bond is mediated by ^{M}**Al•Zr**,[2] as well as $[Cp_2ZrCl_2]$.[3] Therefore, the group was interested in expanding the series of heterobimetallic complexes to include other main group metals. This undertaking might eventually lead to discovery of catalytic technologies that are environmentally and economically agreeable. Mg, Al, Zn and Zr are several orders of magnitude more abundant than common catalyst materials such as the noble metals.[4] Thus there is a clear benefit in cost. Hill *et al.* give the example of: rhodium

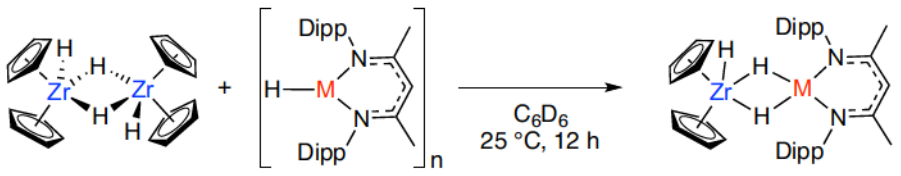
US$1300/troy oz, platinum US$1600/troy oz, iridium US$1070/troy oz *versus* magnesium US$0.13/troy oz.[5]

Moreover, from a fundamental standpoint, there is limited precedent for complexes containing Zr–H–Mg groups, and no previous examples where the Mg atom is stabilised by either a sterically demanding or κ^2 spectator ligand (see Chapter 1). Molecules containing a Zr–H–M (M = Ca, Zn, Ga) moiety are unknown. We envisaged that comparison of ^{M}**Al•Zr** amongst a series of M•**Zr** (M = Al, Mg, Zn) analogues would lead to an advance in understanding of the modulated reactivity of heterobimetallic complexes linked by three-centre-two-electron metal-hydride bonds.

2.2 Synthesis & Ground State Characterisation

2.2.1 Preparation

The reactions of one equiv. of [^{Dipp}*BDI*Mg(μ-H)]$_2$ (^{D}**2$_2$**)[6] or two equiv. of [^{Dipp}*BDI*ZnH] (^{D}**3**)[7] with a slurry of [Cp$_2$ZrH(μ-H)]$_2$ (**Zr•Zr**) in C_6D_6 were monitored by ^{1}H NMR spectroscopy (^{Dipp}*BDI* = {[2,6-^{i}Pr$_2$C$_6$H$_3$]CNMe}$_2$CH). Within 12 h at 25 °C the heterobimetallic complexes ^{D}**M•Zr** (M = Mg, Zn) were formed (Scheme 2.2), as evidenced by inspection of the hydride region of the ^{1}H NMR spectrum. No by-products can be detected when this synthesis is followed by NMR spectroscopy. Both terminal and bridging hydride signals of [Cp$_2$ZrH(μ-H)]$_2$ were lost, and two negative chemical shift signals of equal intensity suggested two bridging hydrides in a new complex. Scale-up in toluene gives isolated yields of 55% (^{D}**Mg•Zr**) and 38% (^{D}**Zn•Zr**).



Scheme 2.2. Preparation of ^{D}**Mg•Zr** or ^{D}**Zn•Zr** from the parent hydrides.

2.2.2 Structural Characterisation

2.2.2.1 Single-Crystal X-ray Diffraction

Crystal structures were obtained from the (colourless) single crystals of ^{Dipp}*BDI*MH•**Zr** grown from *n*-hexane at –30 °C. Neither of the crystals could be used to supply the hydrides' location. The (μ-H)$_2$ linkage is represented by an intermetallic vector in the structures (Figure 2.3). Both of the crystals gave a unit cell containing two molecules with very slightly different heterobimetallic geometries, which are isostructural (see section 2.6.3). Arbitrary choice of one structure will be quoted here. The Zr---Zn distance of 2.8866(9) Å is in excess of the sole example of a Cp$_2$Zr–ZnR bond, found to be 2.7721(7) Å.[8] The longer distance for Mg---Zr, 3.095(3) Å, seems to reflect the increase in covalent radii of Zn and Mg (1.22 and 1.41 Å respectively).[9] Related hydride-bridged Mg/Zr complexes (covered in Figure 1.15)[10-12] have smaller *fsr* values than ^{D}**Zn•Zr** and ^{D}**Mg•Zr** (1.07 and 1.10 respectively). These data do not, in our opinion, change the expectation for bridging hydrides.

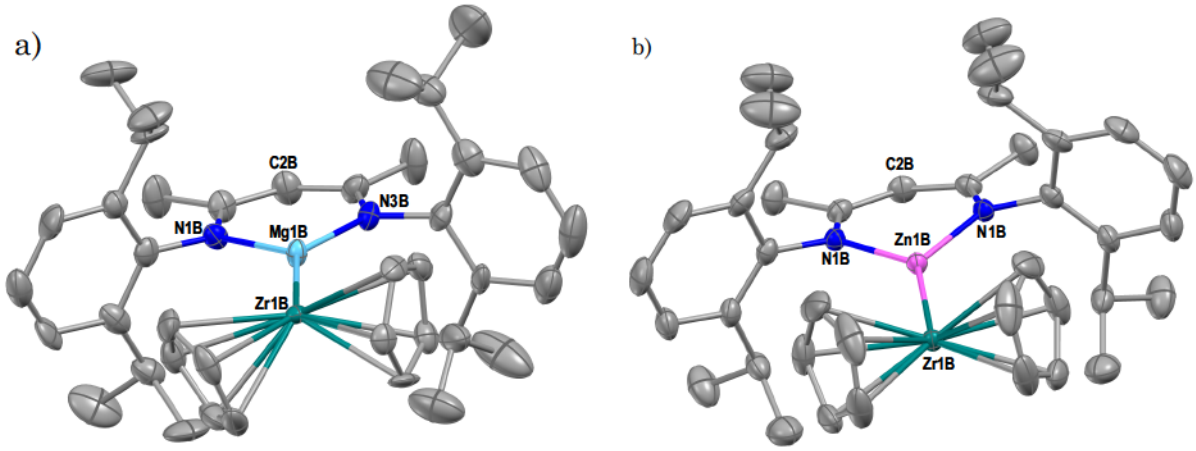


Figure 2.3. Crystal structures of a) ^{D}**Mg•Zr** and b) ^{D}**Zn•Zr** – 50% probability ellipsoids.

Table 2.1. Selected geometrical parameters for ^{D}**Mg•Zr** and ^{D}**Zn•Zr**. In ^{X}**Al•Zr,** the N(3)-Al(1)-Zr(1) and N(1)-Al(1)-Zr(1) angles: 121.26(3)° and 124.64(3)° respectively – other ^{X}**Al•Zr** data is in Figure 2.1.

Bond Distances [Å]			
Zr(1B)-Mg(1B)	3.095(3)	**Zr(1B)-Zn(1B)**	2.8866(9)
Mg(1B)-N(3B)	2.032(8)	**Zn(1B)-N(1B)**	1.984(3)
Mg(1B)-N(1B)	2.042(8)		
Zr–C	2.475(10)–2.516(13)	**Zr–C**	2.478(5)–2.516(13)
Bond Angles [°]			
N(3B)-Mg(1B)-N(1B)	91.8(3)	**N(1B)-Zn(1B)-N(1'B)**	95.01(19)
N(3B)-Mg(1B)-Zr(1B)	137.5(2)	**N(1B)-Zn(1B)-Zr(1B)**	132.42(10)
N(1B)-Mg(1B)-Zr(1B)	130.7(3)	-	-

Hydride Positions

Both X-ray diffraction experiments reveal roughly flat over-all shapes (ignoring the perpendicular di-*iso*-propylaryl (Dipp) groups). The intermetallic areas are less sterically crowded on one face. This opening is most likely to be the location of the terminal hydride atom (Figure 2.4a). The molecular orbital arguments are consistent. Complexes of the form $[Cp_2MH_3]$ require that that the three hydride ligands fan out from the metal centre in a plane that bisects the $Cp_{centroid}$–Žr–$Cp_{centroid}$ reflex angle (Figure 2.4b).[13] It was therefore predicted that the position of the M(μ-H)$_2$Zr(H$_t$) plane is orthogonal to the κ^2-*BDI*–M ring (the black-shaded plane in Figure 2.4a).

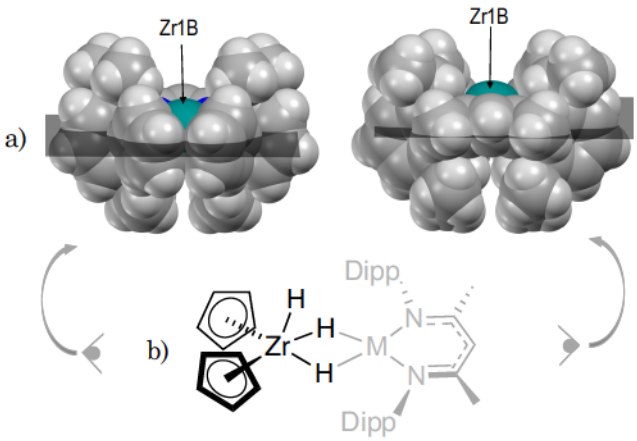


Figure 2.4. a) Space-filling (1 van der Waals radius) crystal structure, revealing the suspected terminal hydride interstice above the N-N-Zn-Zr plane in ^{D}**Zn•Zr** (from both ends of the molecule). b) The predicted [Cp_2MH_3] hydride positions from MO theory.[13]

The apparent position of the hydride ligands in ^{D}**Mg•Zr** and ^{D}**Zn•Zr** contrasts ^{x}**Al•Zr**. In the latter, the five-coordinate Al imparts its own strong demands on the coordination geometries (Figure 2.1), and {CpZrCp} is perpendicular to the position in ^{D}**Mg•Zr** and ^{D}**Zn•Zr**. The stubbornness of the Al centre's square-based pyramidal coordination environment can be quantified using the tau index for five-coordinate complexes (τ_5).[14] ^{x}**Al•Zr** has a τ_5 value of 0.01, which on a scale of 0–1, shows a minuscule distortion towards trigonal bipyramidal geometry. This renders the $(\mu\text{-H})_2$ atoms parallel to the κ^2-*BDI*–M ring, and therefore the zirconocene falls into an essentially orthogonal position.

Steric Concerns

The orientation of the M^{II} complexes and the lesser number of hydrides around M is better for minimising steric clash; steric concerns can have crucial effects on the stability of compounds such as these. For example, in ^{x}**Al•Zr** the {CpZrCp} leans away from Al–H_t; thus, H atoms on the Cp ligand opposite to Al–H_t come into close contact (0.3 Å below the sum of van der Waals radii)[15] with a methyl proton on the xylyl rings. A larger amount of short contacts can be envisaged in the structure of the Dipp analogue. ^{D}**Al•Zr** was not detected by equivalent synthesis (see section 2.3.1). We might predict that the latter is disfavoured due purely to steric clash.

Two different distortions of the essential ^{Dipp}*BDI*MH•**Zr** structure are seen. Both seem to create further space for the terminal hydride in their own way. In ^{D}**Zn•Zr** the space seems to arise from β-diketiminato-Zn metallacycle adopting a shallow boat structure. The 'stern' and 'prow' are the slightly raised C_β and Zn atoms. The Dipp groups and the Cp ligands drop with the hull, leaving the open region above the coplanar N,N-Zn---Zr. These ligand groups also remain eclipsed. This symmetry is abandoned in ^{D}**Mg•Zr**, the twisting of a Cp ligand

downwards and away from the κ^2-*BDI*---M plane (by 18.3°) creates space for H_t. The different conformations in ^{D}**Mg•Zr** and ^{D}**Zn•Zr** may be caused by the M---Zr distances. A shorter M---Zr distance in ^{D}**Zn•Zr** would force greater evasive action by the larger groups around the M---Zr region, and this is perhaps part of the reason for the boat structure of the *BDI* chelate.

Non-Covalent Interactions

There are some outstandingly short contacts between atoms in ^{D}**Zn•Zr** and ^{D}**Mg•Zr**. Rather than areas of steric clash, the proximity of some C_{Cp}–H bonds to Dipp aryl rings in ^{Dipp}*BDI*MH•**Zr** may actually be ascribed weakly stabilising (roughly 5 kcal mol^{-1})[16] CH/π interactions. Figure 2.25 (see Experimental) illustrates these short C_{Cp}H---$Ar_{centroid}$ distances in ^{D}**Zn•Zr** and ^{D}**Mg•Zr**, which are shorter than those in the related examples. The π-system acts as a soft Lewis base to the very slightly acidic C_{Cp}–$H^{\delta+}$ bond, with directionality. The edges of the cyclopentadienyl anion have been seen to act this way in *inter*molecular solid state interactions.[16,17] These minimal forces are more usually associated with ground states in macromolecular chemistry, but organometallic and coordination chemists are giving them increasing appreciation,[16,18-20] along with dispersion forces, as structure-[21] and reaction-defining[22] features.

The CH/π interactions differ in the Mg and Zn analogues' (see Figure 2.25). ^{D}**Mg•Zr** only has one such short contact, whereas ^{D}**Zn•Zr** displays contacts on both 'wings'. This difference is not attributable to one single structural factor. However, the geometrical contraction brought about by the shorter M---Zr vector in ^{D}**Zn•Zr** may allow the double-sided C–H---$Ar_{centroid}$ approach. Furthermore, the differences in crystal packing in ^{D}**Zn•Zr** and ^{D}**Mg•Zr** may be part of the reason for the conformational differences between the two. Additionally, C_{iPr}–H---N interactions (Figure 2.25) are possible (see Experimental, section 2.6.3.2).

2.2.2.2 Structure by Density Functional Theory

DFT studies on the M^{II} heterobimetallic complexes demonstrate that the three hydrides do indeed co-exist in a plane orthogonal to that created by the β-diketiminate ligand. This was made clear by an initial set of calculations – m062x functional and hybrid basis set 6,31G (C/H/N) and Lanl2DZ (Al/Zn/Mg/Zr) – on the three heterobimetallic complexes ^{D}**Mg•Zr**, ^{D}**Zn•Zr** and ^{M}**Al•Zr**. With the hydride positions placed in a varied range of inputs, the same arrangement always resulted. Using the GAIO method on the optimised structures of ^{D}**Mg•Zr** and ^{D}**Zn•Zr**, the assignment of H_μ and $H_{\mu'}$ signals in the NMR data was made. The most upfield hydride signal is that of $H_{\mu'}$, the bridging atom distal to the H_t. All H---H (hydride) distances are over 1.6 Å, meaning the possibility of meaningful H–H bonds can be excluded. This conclusion was borne out in the results of T_1 NMR experiments and of an NBO analysis.

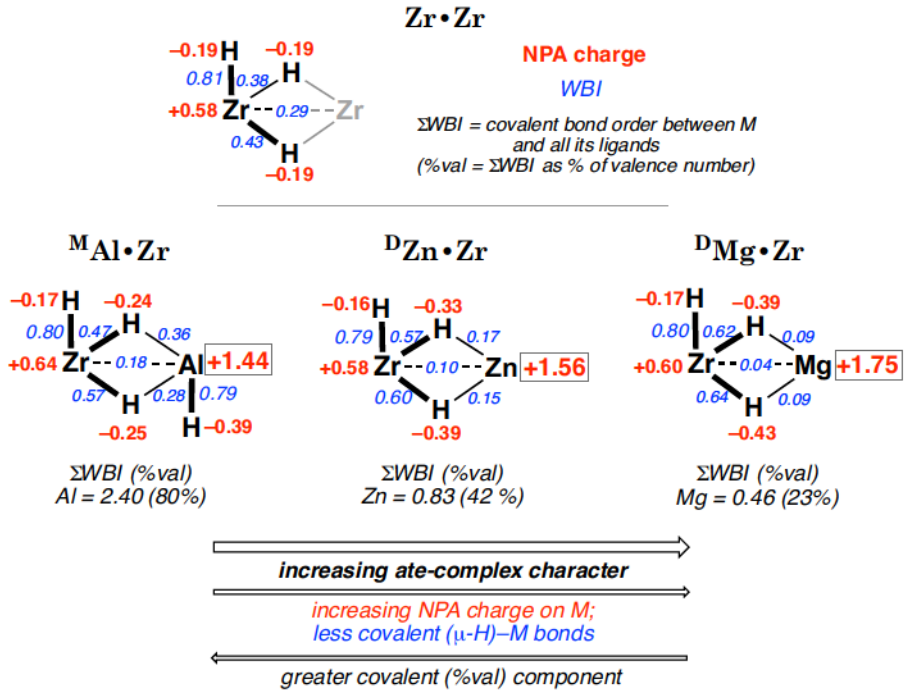


Figure 2.5. NPA charges and Wiberg bond indices (WBI) for the metal-hydride cores of the key bimetallic complexes (ωB97xD functional and hybrid 6,311G/SDD basis set). The WBI-related parameters take all ligands into consideration, not only the cores.

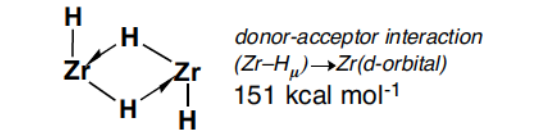
The NBO analysis (carried out using a level of theory established elsewhere in the study) and Wiberg bond index calculations,[23] allows comparison of bridging modes in bimetallic systems, as well as their overall degree of ionic character.[24-26] It was found that a zirconate description of the complexes becomes increasingly significant in the order: **^{M}Al•Zr** < **^{D}Zn•Zr** < **^{D}Mg•Zr**. This is evidenced by the increasing charge on M and the weaker bond indices for the (μ-H)–M bonds (Figure 2.5). The 3c,2e bridges are much more covalent on the Zr side.

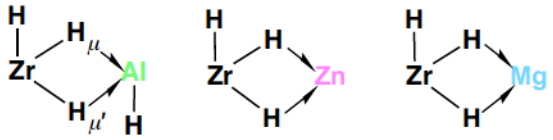
Wiberg bond indices are often similar to the bond orders proposed by valence bond theory.[27] They describe solely covalent interactions.[23] The bond orders summed around M (i.e. Σ*WBI*) form a decreasing percentage of the theoretical valence number on M (*i.e.* %val), implying that an increasing portion of the bonding is ionic. For example, the valence number of Mg should be 2, and not only is its NPA charge very close to this value, but also its Wiberg bond indices total only 0.46 – therefore, just 23% of the bonding around M is covalent.

The data agrees with the discussion in section 1.7.1.2: in multiply-bridged hydride complexes, unequivocally electropositive metals will unbalance neutral donor-acceptor bridging systems. The acceptor frontier molecular orbital of **Zr** lies inside the H-Žr-H angle, and second-order perturbation theory calculations show how the dimer, **Zr•Zr**, is held together by strong dative covalent (Zr–H$_{\mu}$)→{Zr} donation into this orbital (Figure 2.6). This seems to align with the slight disparity in WBI values between the Zr–H$_{\mu}$ and Zr–H$_{\mu'}$ bonds in **Zr•Zr**, Figure 2.5. The bond is slightly weaker for the donor-acceptor side of the bridge. The same

disparity appears in **^{M}Al•Zr** and **^{D}Zn•Zr**, where the metals are less electropositive. This suggests that a resonance structure involving the *neutral* parent hydride fragments may be more relevant in these cases. Any metal-metal bonding in Figure 2.5 was ascribed to the computational interpretation of the η^2 (M–H)→M interaction (see Experimental section – there is no evidence for metal-metal orbitals elsewhere in the NBO results).

In the heterobimetallic complexes, second-order perturbation analysis finds a greater emphasis of the anionic $\{Cp_2ZrH_3\}^-$ fragment over $\{Cp_2ZrH_2\}$. The magnitude of the donor-acceptor interactions from $\{Cp_2ZrH_3\}^-$ to M drops in the order Al > Zn > Mg. We know that **^{M}Al•Zr** is by far the weakest bound heterobimetallic complex (see equilibrium in Figure 2.2), therefore, the contrasting trend in binding interaction energies in Figure 2.6 is probably demonstrating the weaker covalent interactions in the Zn and Mg analogues. Findings discussed below (section 2.3.2.2) seem to add further evidence to the strength of the ionic bonding in **^{D}Mg•Zr**.





acceptor orbital

(kcal mol^{-1})		Al 3p	Al sp^2	Zn 4s	Mg 3s
donator	**Zr–H$_\mu$**	45	94	77	29
	Zr–H$_{\mu'}$	-	180	70	28

increasing ate-complex character

decreasing magnitude of donor-acceptor interaction(s)

Figure 2.6. The energies of hydride-metal donor-acceptor interactions, calculated using second-order perturbation theory in DFT calculations.

2.2.2.3 Structure by NMR Characterisation

The bridging and terminal hydrides were resolved by ^{1}H and COSY NMR experiments. For example, in **^{D}Mg•Zr** the bridging hydrides H_μ and $H_{\mu'}$ are chemically and magnetically inequivalent; at 298 K in toluene-d_8 they resonate at δ = –2.00 and –2.87 ppm respectively. Both bridging hydrides couple to the terminal hydride (H_t) found at δ = 1.55 ppm. Long T_1 relaxation times (0.5–1.2 s) for the series of complexes make the existence of H---H interactions improbable (Table 2.2).[28] A summary of the NMR data is collected in Table 2.3.

Table 2.2. T_1 relaxation times in toluene-d_8 (298 K).

Hydride	^{D}**Zn•Zr**	^{D}**Mg•Zr**
H_t	950 ms	700 ms
H_μ	570 ms	530 ms
$H_{\mu'}$	1.1 s	1.2 s

Rotation of the N–C_{ipso} bond is ostensibly hampered at lower temperatures. Decoalescence of the Dipp signals occurs between 293–303 K in ^{D}**Zn•Zr;** the analogous decoalescence in ^{D}**Mg•Zr** requires a much lower temperature (below 223 K), but in this case the ^{i}Pr methanetriyl signal is not clearly decoalesced. The more compact solid-state structure of ^{D}**Zn•Zr** may be related to the higher activation energy of this restricted rotation. Absence of the phenomenon in the mesityl signals of ^{M}**Al•Zr** adds to previous conclusions. Namely, the {Cp_2ZrH_2} fragment is held relatively farther away from {^{Mes}*BDI*AlH_2} (see: *fsr* values, and short contacts in Figure 2.25). Additionally, the reversible binding of ^{M}**1** and {Cp_2ZrH_2} could facilitate N–C_{ipso} bond rotation at all observed temperatures.

The ligand groups that sterically impinge upon the hydrides in the crystal structure – Dipp and Cp – present an nuclear Overhauser effect in NOESY experiments when the hydride signals were irradiated (see section 2.3.2.1, Figure 2.12 & Figure 2.13). The peaks affected are consistent with the crystallographic structure being retained in solution.

Table 2.3. A summary of the ^{1}H NMR data for the heterobimetallic complexes (298 K, toluene-d_8).

	^{D}**Zn•Zr**	^{D}**Mg•Zr**	^{M}**Al•Zr** (‡)
H_t	1.80 ppm	1.55 ppm	1.12 ppm
mult.	dd	dd	s
$^{2}J_{H\text{-}H}$	8.3, 6.3 Hz	13.0, 6.6 Hz	-
H_μ	–1.22 ppm	–2.00 ppm	–2.49 ppm
mult.	d	dd	s, br
$^{2}J_{H\text{-}H}$	8.3 Hz	13.0, 6.6 Hz	-
$H_{\mu'}$	–2.20 ppm	–2.87 ppm	–2.76 ppm
mult.	d	dd	s, br
$^{2}J_{H\text{-}H}$	6.3 Hz	6.6, 6.6 Hz	-
$T_{c(Dipp)}$	283 K	213 K	-
$T_{c(Ht/H\mu)}$	373 K	393 K	283 K

‡ δ values quoted are for the 233K spectrum.
Terminal hydride on Al δ = 4.85 ppm.

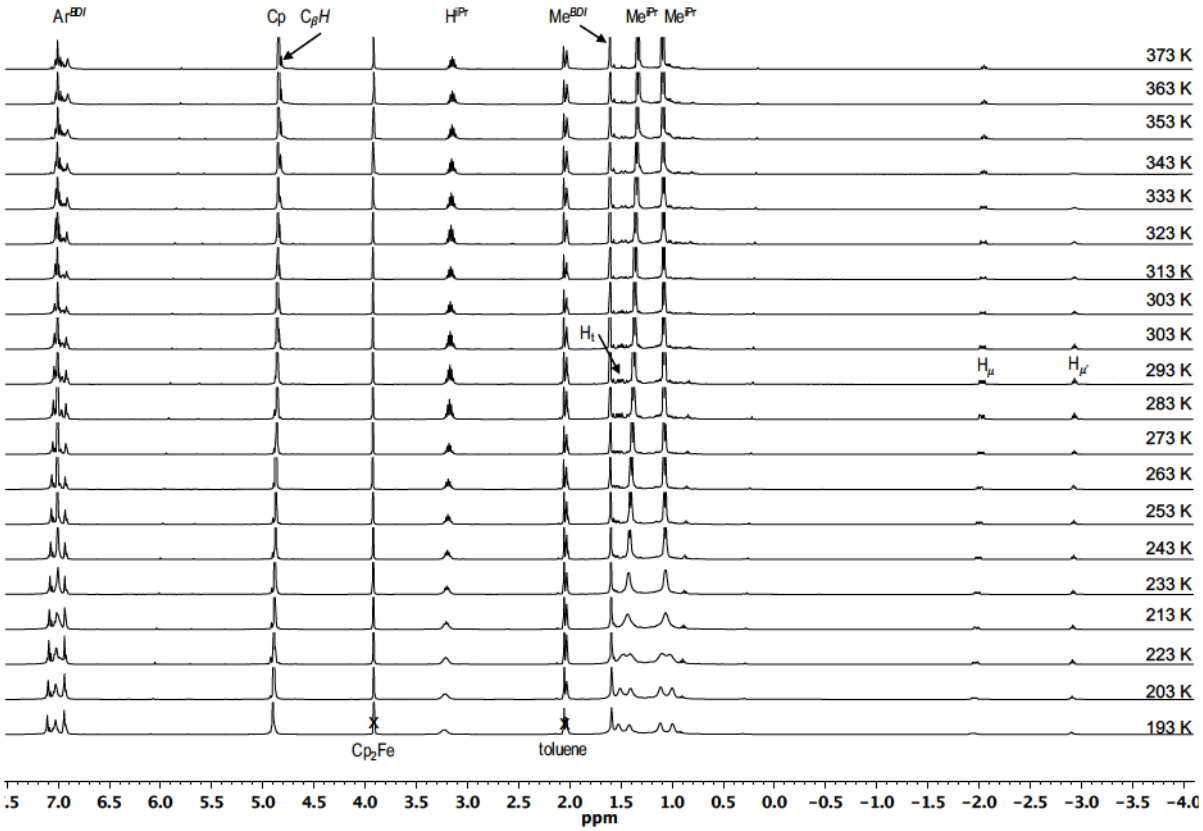


Figure 2.7. VT ^{1}H NMR spectra of ^{D}**Mg•Zr** between 193–373 K (toluene-d_8).

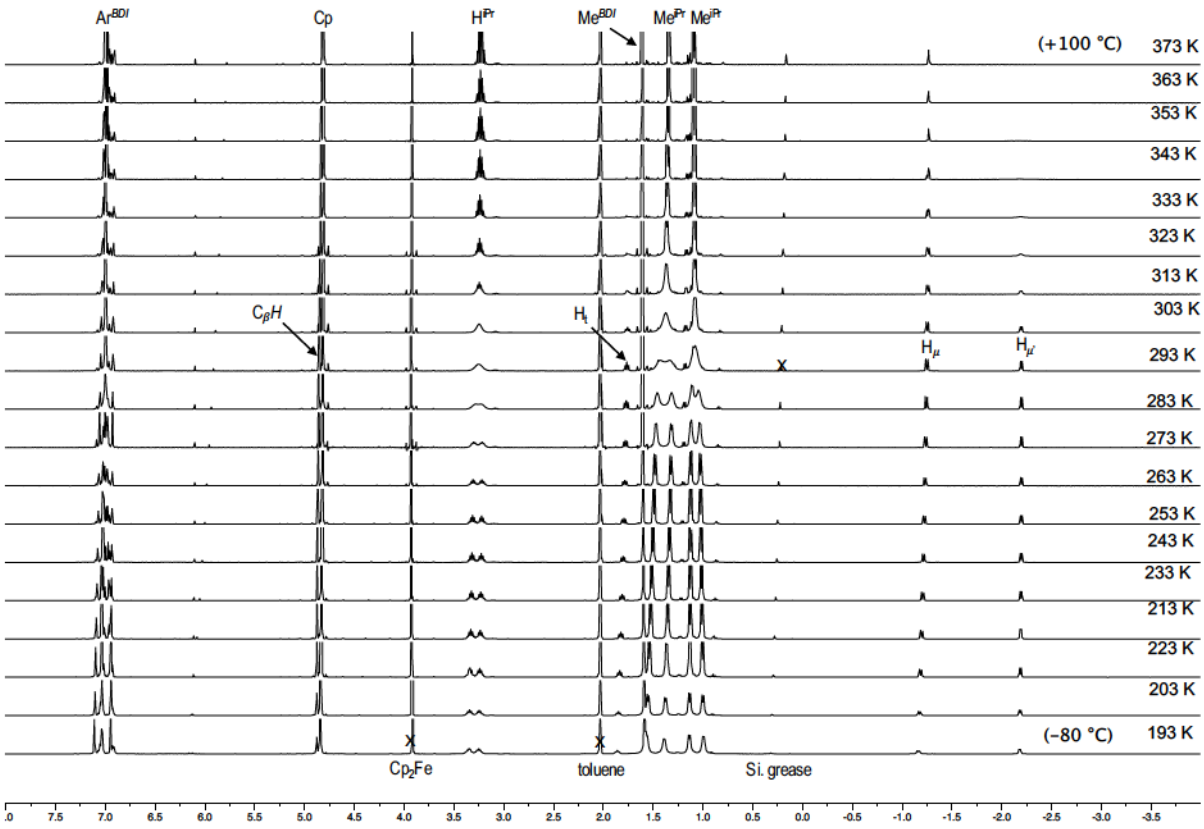


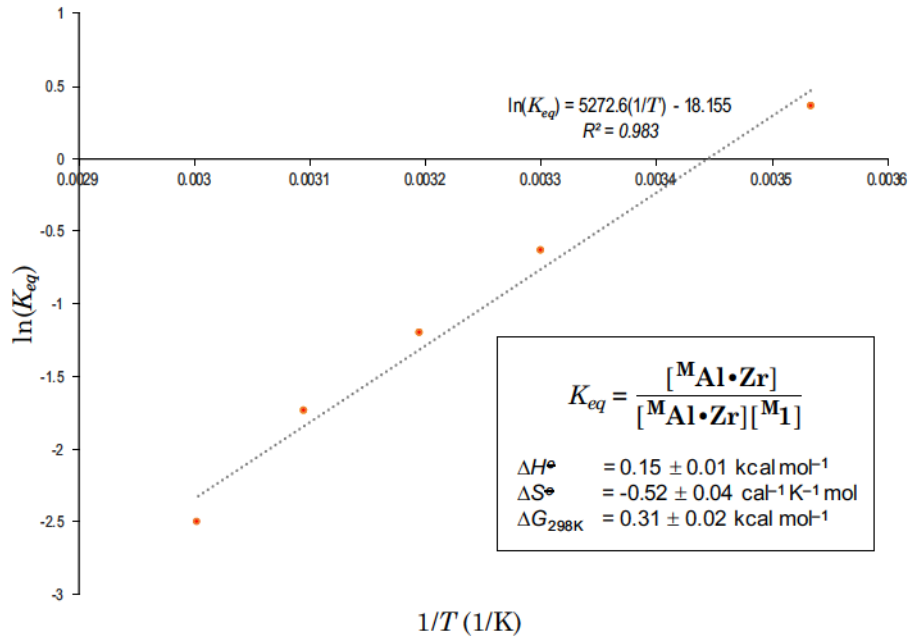
Figure 2.8. VT ^{1}H NMR spectra of ^{D}**Zn•Zr** between 193–373 K (toluene-d_8).

2.3 Characterisation of Structural Integrity

2.3.1 Relative Stabilities

2.3.1.1 Experimental Studies

There is no indication of the dissociation of ^{D}**Mg•Zr** or ^{D}**Zn•Zr** in benzene-d_6 or toluene-d_8 solutions between 193 and 373 K. The equilibrium between ^{M}**Al•Zr** and the monometallic reactants has been re-examined and quantified by the van't Hoff analysis (283–333 K, Graph 2.1). A value from the ^{1}H NMR spectrum at 293 K was not included because of poor shimming. According to these results, formation of the ^{M}**Al•Zr** heterobimetallic complex from its parent hydrides is effectively a thermoneutral process. When mixed with ^{M}**Al•Zr** (or ^{X}**Al•Zr**), the magnesium or zinc hydride complexes were expected to displace the weakly bound alane fragment. Combining ^{M}**Al•Zr** with 0.5 equiv. ^{D}**2**$_2$, *or* 1 equiv. ^{D}**3**, proved this to be the case.

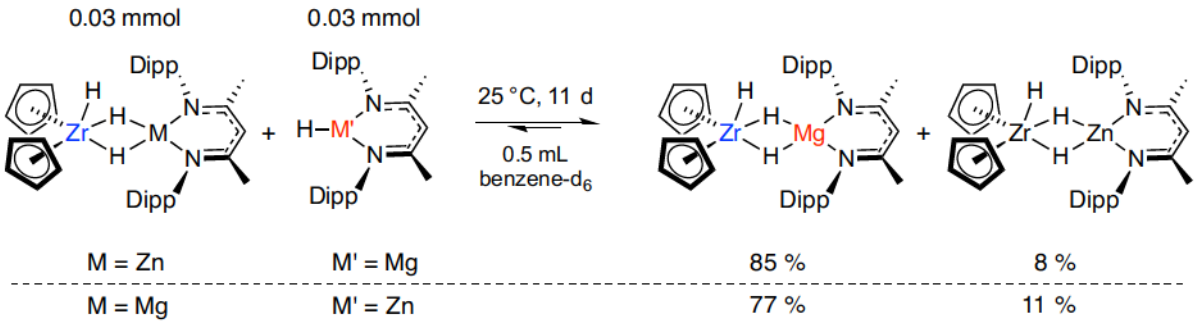


Graph 2.1. A van't Hoff plot for the dissociation of ^{M}**Al•Zr** (57.0 mM) in toluene-d_8 between 283 and 333 K at 10 K intervals. Inset: the derivation of K_{eq} and subsequently obtained thermodynamic values.

Put tentatively, {^{Dipp}*BDI*MgH} seems to be the strongest binder of {$Cp_2ZrH(\mu$-H)}. However, this distinction between the M^{II} hydride partners is not clear cut. Scheme 2.3 shows how a crossover experiment was approached from both Mg and Zn parent hydride starting materials. Both give similar (yet slightly imperfect) results. The reactions led to the formation of ^{D}**Mg•Zr** as the major product. But a complete conversion is not seen from either starting position. In fact, the ^{D}**Mg•Zr** yields in Scheme 2.3 after 11 d are 10% below the yields after 1 d. Further

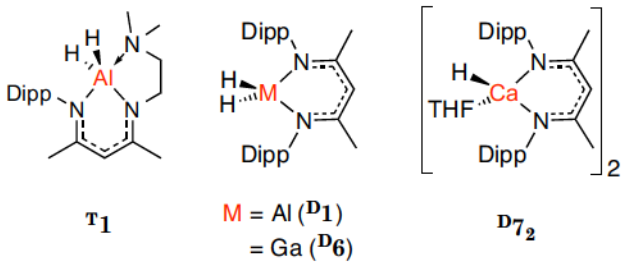
heating of the samples at 80 °C did not move the product distribution. In searching for movement of the position of equilibrium, variable-temperature NMR experiments showed only the known line shape changes and exchange processes (section 2.3.2.1) and no clear change in yield towards either product.

There is a large disparity in the yields (10–15%) depending on which peaks are used for the integrals; the lower estimates are quoted. As a consequence of this imprecision, the differences in equilibrium position between the parallel runs may not be significant. Hysteretic change in the hydride resonance shapes (see section 2.4.3.1) may be a further cause of the error in the measurements. The barely avoidable impurity of $^{D}\mathbf{2_2}$ also compromises the fidelity of the experiment. What can be concluded is that, when in competition with $^{D}\mathbf{3}$, the parent Mg hydride is the most favoured in binding **Zr**.



Scheme 2.3. Results of crossover experiments between ^{D}**Zn•Zr** and $^{D}\mathbf{2_2}$, and ^{D}**Mg•Zr** and $^{D}\mathbf{3}$. Yields represent results (lowest estimates) after 11 d.

Attempted Syntheses of Analogues



$^{T}\mathbf{1}$ $^{D}\mathbf{7_2}$

Figure 2.9. Main group compounds that failed in the synthesis of heterobimetallic hydride complexes, ^{R}*BDI*M•**Zr**.

In addition to the crossover experiments, we found that $[Cp_2ZrH(\mu\text{-}H)]_2$ and [^{Dipp}*BDI*AlH_2] do not form a stable isolable heterobimetallic at 25 °C. The influence of increasing steric demand on the position of the equilibrium is thus demonstrated. Thus, [^{Dipp}*BDI*AlH_2] will almost certainly not eject $^{M}\mathbf{1}$ from ^{M}**Al•Zr**. The formation of ^{D}**Al•Zr** by the Crimmin group has previously been misattributed,[29] and it is now ruled out through this route. A five-coordinate Al^{III} dihydride ($^{T}\mathbf{1}$)

was, not surprisingly, also unsuccessful in forming a donor-acceptor complex with {$Cp_2ZrH(\mu$-H)} (Figure 2.9).

The heavier main group metals Ca and Ga could not be prepared by the method outlined in section 2.2.1. No formation of **^{D}Ga•Zr** was witnessed in a test reaction using β-diketiminate-supported gallium hydride (**^{D}6**). Treatment of β-diketiminate-supported calcium hydride (**^{D}7$_2$**) with **Zr•Zr** gave ligand redistribution around the Ca centre at room temperature to form [Ca{(DippNCMe)$_2$CH}$_2$], and the putative **^{D}Ca•Zr** heterobimetallic could not be isolated. On the basis of some precedent for organohydroborate zirconocene complexes,[30] an attempt was made to add B and Si to the series of {Zr(H$_t$)(μ-H)$_2$M} complexes. Although reactive with **Zr•Zr**, none of pinacolborane, phenylsilane and dimethylphenylsilane yielded workable results when mixed with it. The black and intractable mixtures acquired may contain Zr^{II} species formed after initial formation of the hydride-bridged species.[31]

The sterically undressed analogues, **^{M}Zn•Zr** and **^{M}Mg•Zr,** have been briefly investigated. We were unable to obtain the Mes-substituted zinc hydride (**^{M}3**) via the synthetic route of **^{D}3**. Jones and co-workers have unsuccessfully attempted synthesis of [^{Mes}*BDI*Mg(μ-H)$_2$]$_2$ (**^{M}2**);[32] we were also unsuccessful by this route, which fails to give the necessary [^{Mes}*BDI*Mg–^{n}Bu]$_2$ intermediate.

However, in the case of **^{M}Zn•Zr**, we were able to provide proof of synthesis by using the isolable [^{Mes}*BDI*ZnEt]. Its reaction with **Zr•Zr** at room temperature gives a number of signals in the bridging hydride region of the ^{1}H NMR spectrum after less than an hour at room temperature (Figure 2.10). The signals at δ = –1.43 and –2.31 ppm look like correspondents of the signals in **^{D}Zn•Zr,** shifted upfield. The reaction mixture remained dark green throughout, and a signal at δ = –3.12 ppm grew in after heating the same sample for 4 h at 80 °C. Based on the hydride peaks (against the [^{Mes}*BDI*ZnEt] starting material), a 55% yield of **^{M}Zn•Zr** was seen by NMR. Other products are likely to be mixed hydrido alkyl complexes.

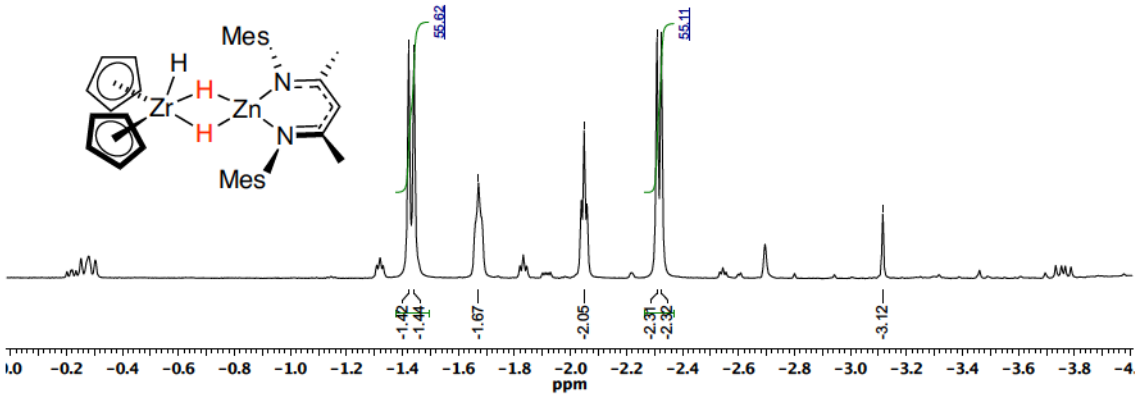
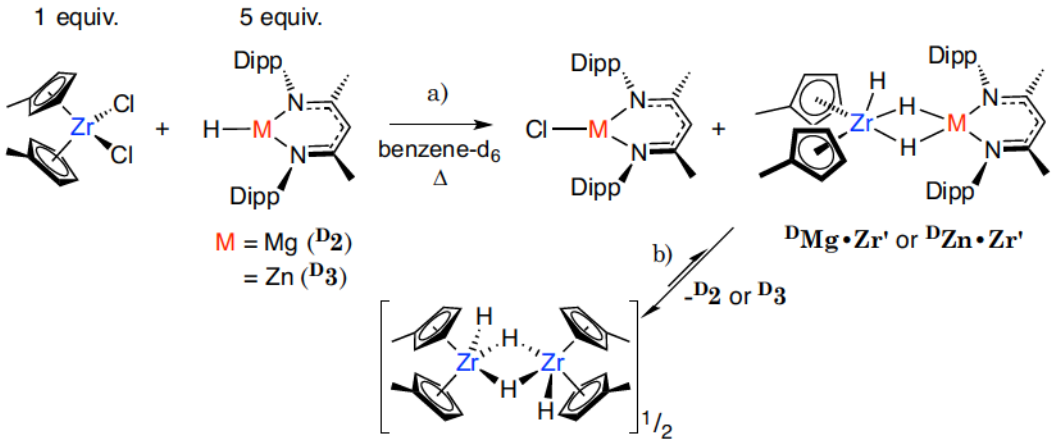


Figure 2.10. The ^{1}H NMR spectrum (0 — –4 ppm, 298 K, benzene-d$_6$) of the reaction of [^{Mes}*BDI*ZnEt] after 4 h at 80 °C. The supposed bridging hydride signals of **^{M}Zn•Zr** are integrated against an internal standard to give the yield.

Greater sterics on the cyclopentadienyl ligands were tested fleetingly by the experiments in Scheme 2.4a, *i.e.* ligand exchange reactions based on Scheme 2.1a. The smallest possible addition to the sterics was made, by use of (1,1'-dimethyl)zirconocene dichloride. The results are encouraging, although the insolubility of the starting material and products makes for difficult reading of the ^{1}H NMR spectra. Signals corresponding to (1,1'-dimethyl)zirconocene dihydride (**Zr'•Zr'**) are clear after < 1 h with ^{D}**2$_2$** at room temperature. The symptomatic hydride triplets, at δ = +4.17 and –2.74 ppm ($^{2}J_{H\text{-}H}$ = 7.3 Hz), are of the appropriate integration values. Either side of the upfield peak, a very broad pair of peaks sit, looking like bridging hydride signals for ^{D}**Mg•Zr'** (δ = –1.67 and –2.95 ppm). A β-diketiminato species, presumably [^{Dipp}*BDI*MgCl] (δ = 4.78 (C_βH) ppm) is the by-product. The result shows a relatively unfavourable association constant (Scheme 2.4b) for the putative Mg/Zr heterobimetallic complex, after the ligand-exchange step (Scheme 2.4a). The presence of **Zr'•Zr'** suggests that the route is likely to lead to an equilibrium amongst products, favouring the parent hydrides. The equilibrium should be more akin to that of ^{M}**Al•Zr** (Scheme 2.1b), with reversible binding of the heterobimetallic complex and a larger positive ΔG_{298K} value. Analogous ligand exchange preparations of ^{D}**Mg•Zr** and ^{D}**Zn•Zr** do not suffer from this problem *i.e.* no zirconocene dihydride species is seen in the ^{1}H NMR spectrum.



Scheme 2.4. a) The desired ligand exchange route to (1,1'-dimethyl)zirconocene-containing heterobimetallic complexes. b) A rationale for the observation of **Zr'•Zr'**.

By the same route, attempted ^{D}**Zn•Zr'** production was less informative. Addition of 3 equiv. (or more) of ^{D}**3** to **Zr'•Zr'** led to very little change in the ^{1}H NMR spectrum and no signals in the hydride region. (The Me_{Cp} resonance divided into several species, suggesting reactivity, but ^{D}**3** showed only changes in relative peak intensity.) Conversely, a 1:1 combination of ^{D}**3** to **Zr'•Zr'** did react, showing a trace amount of a pair of bridging hydrides seen clearly at δ = –0.79 (d, $^{2}J_{HH}$ 9.1 = Hz, H_μ) and –1.85 (d, $^{2}J_{HH}$ = 6.5 Hz, $H_{\mu'}$) ppm in the ^{1}H NMR spectrum, with

no sign of the hydride signals for **Zr'•Zr'**. Synthesis of **^{D}Zn•Zr'** from parent hydrides is therefore not ruled out.

2.3.1.2 Theoretical Studies

Simple calculation of the relative stability of parent hydrides and M/Zr products can be used to investigate the Gibbs free energies of formation. For reasons relating to Chapter 3, calculations were run with the ωB97x functional. The formation of **^{M}Al•Zr** was found to be unfavourable (ΔG_{298K} = +5.3 kcal mol^{-1}) under these computational conditions – a result at odds with the experimental data. Hence, dispersion was included in the functional (*i.e.* ωB97xD was used), and a favourable ΔG_{298K} value was realised. The necessity of dispersion forces in the computational experiments states the significance of the interactions of the bulky ligands around the metal hydride core. Importance of non-classical interactions was touched upon in the analysis of crystallographic data (section 2.2.2.1).

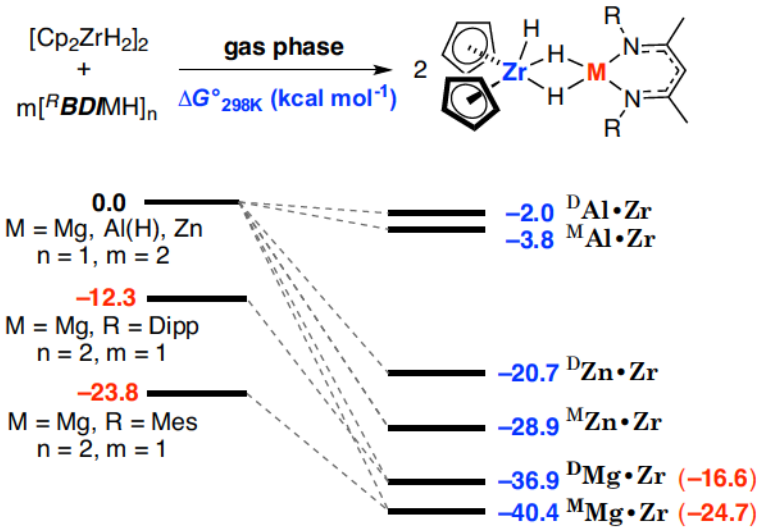


Figure 2.11. Computational results for the relative stabilities of **^{R}M•Zr** as formed from **Zr•Zr** and the parent main group hydride complexes (using the ωB97xD functional and SDD/6-311G basis sets). Values in brackets are ΔG_{298K} values derived from the dimeric Mg hydride starting materials.

Figure 2.11 gives a comparison of the heterobimetallic complexes' stabilities across all three main group metals and the Dipp or Mes ligands. Undoubtedly – and in line with the experimental data – the Al/Zr complexes are much less favoured than the M^{II} analogues. In all cases, the Mes ligand analogue is more stable than the Dipp correspondent. This is most apparent with the M^{II} complexes, particularly with Zn. The removal of some $C_{Cp}H$---Me_{iPr} clash (as shown in Figure 2.25) would explain this effect. When considering the probable dimeric nature of the parent magnesium hydride (**^{D}2$_2$**),[33] the ΔG_{298K} values for the formation of the Mg/Zr complexes become less favourable; Mg is four-coordinate in both starting material and

product, and the magnitudes of favourability are roughly halved because part of the driving force for formation is removed. The relative stability of Mg and Zn congeners does not agree with experimental evidence when the dimeric Mg parent hydride is used. This is likely a failure of the computational level of theory, for example the absence of solvent correction.

2.3.2 Hydride Exchange Phenomena

2.3.2.1 NMR Studies

Variable temperature and NOESY NMR experiments show a chemical exchange process between H_t and $H_{\mu'}$ in **^{D}Mg•Zr** and **^{D}Zn•Zr**. This phenomenon indicates at least partial loosening of the heterobimetallic complex in toluene-d_8 solution. Purity seems to have an effect on the ease of the site exchange (*vide infra*, section 2.4.3.1). Reported here is the upper limit at which the chemical exchange between H_t and $H_{\mu'}$ is observed – with the implicit assumption that trace impurities are aiding the hydride site-exchange in the lower temperature case. Figure 2.12 shows the results for **^{D}Zn•Zr**, where three spectra were obtainable at either temperature, one for each hydride including H_t. Figure 2.13 shows the results for **^{D}Mg•Zr**, where the H_t resonance was hidden, allowing only two spectra to be measured, one for the irradiation of $H_{\mu'}$ and one of H_{μ}.

The data are consistent with the chemical exchange of $H_t/H_{\mu'}$. When the irradiated peak shows signal enhancement to another peak of the same phase, chemical exchange is operating between the two. A nuclear Overhauser effect (nOe) amongst resonances belonging to protons around the intermetallic region is also displayed. Inverse phase signal enhancement is indicative of nOe between the peaks.

At high temperatures, the ^{1}H NOESY experiments appear to highlight a participation of peaks other than $H_t/H_{\mu'}$ in the chemical exchange. This is due to proximity and broadness of the irradiated peaks, and is treated as an artefact of the experimental process. It is particularly important that this is discounted in the case of **^{D}Mg•Zr**, where H_{μ} seems to be part of the site-exchange with $H_{\mu'}$ (Figure 2.13). When the broad $H_{\mu'}$ peak is irradiated, signal enhancement for H_{μ} (δ = –2.05 ppm) is observed. However, upon irradiation of the latter, the complementary signal enhancement of $H_{\mu'}$ does not occur. Involvement of H_{μ} is not seen in the equivalent **^{D}Zn•Zr** tests; the broadness of $H_{\mu'}$ does not impinge upon the H_{μ} signal.

Table 2.4. The coalescence temperatures for the chemical exchange process between H_t and $H_{\mu'}$.

	^{D}Zn•Zr	**^{D}Mg•Zr**	**^{M}Al•Zr**
$T_{c(Ht/H\mu')}$	373 K	393 K	283 K

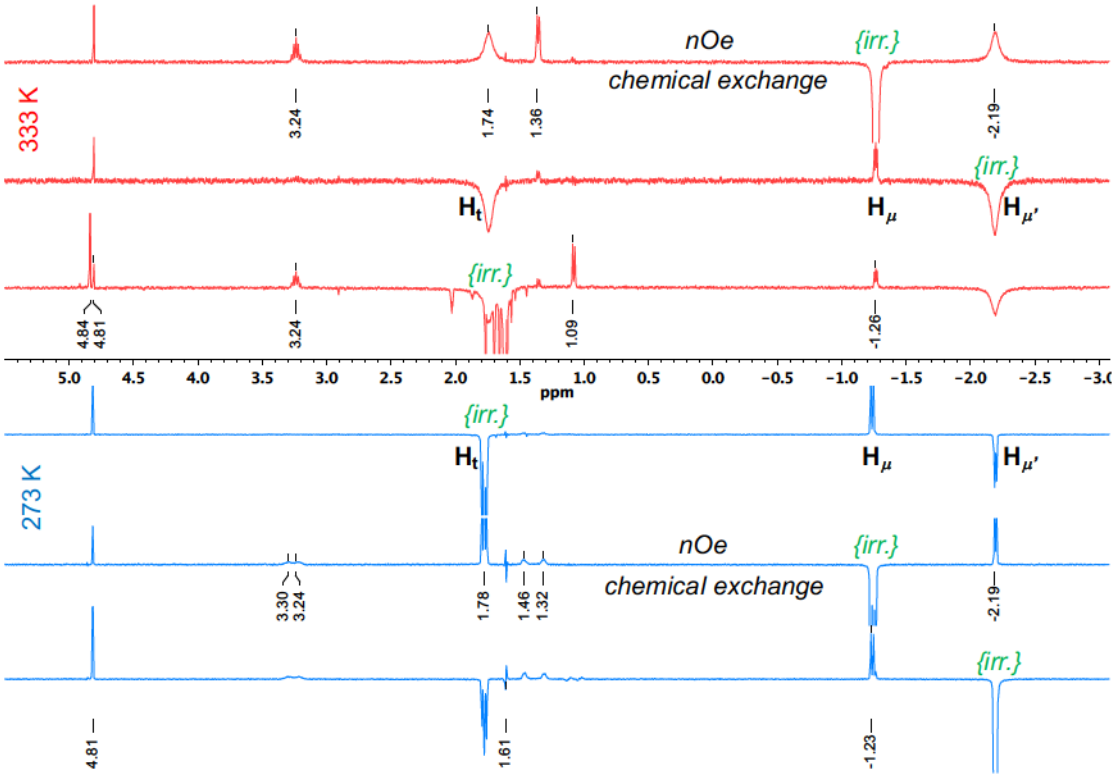


Figure 2.12. A stack plot of the NOESY ^{1}H NMR experiments for ^{D}**Zn•Zr** in toluene-d$_8$. Chemical exchange signalled by peak enhancement in the negative phase. The peaks subject to irradiation are marked with {irr.}.

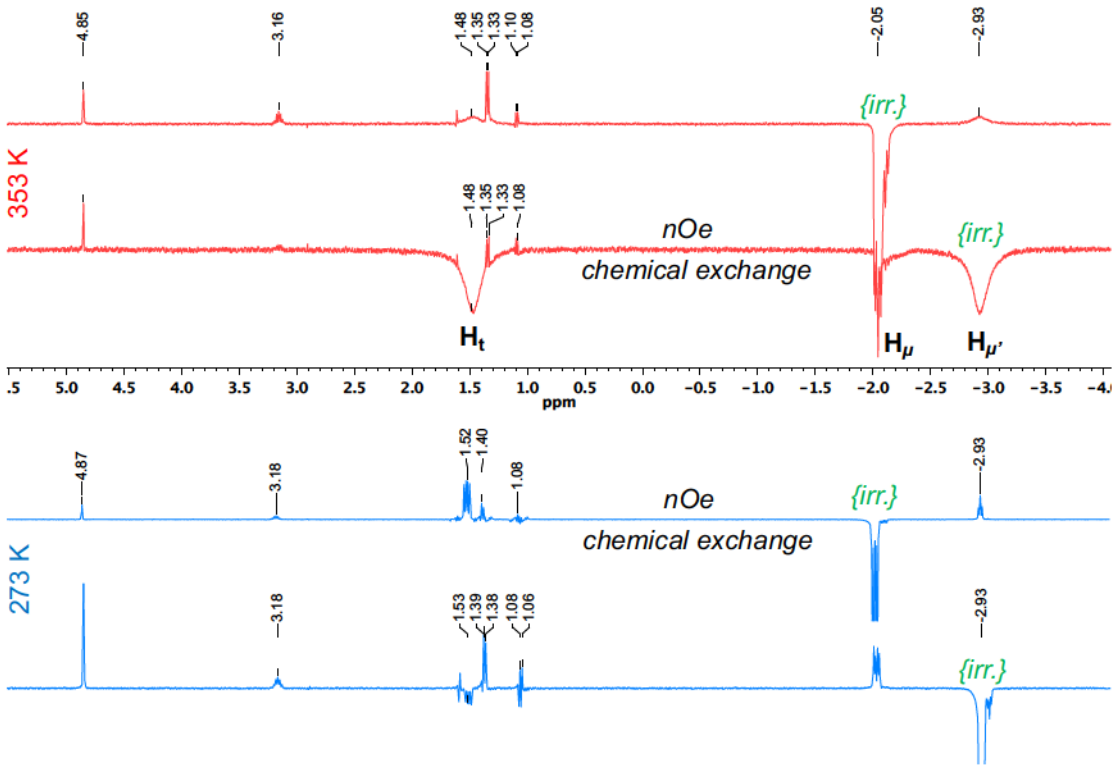


Figure 2.13. A stack plot of the NOESY ^{1}H NMR experiments for ^{D}**Mg•Zr** in toluene-d$_8$. Chemical exchange signalled by peak enhancement in the negative phase. The peaks subject to irradiation are marked with {irr.}.

The T_c values shown in Table 2.4 are taken from the variable-temperature NMR stack plots discussed above. They can be interpreted as a measure of the activation temperature for chemical exchange. As the temperature is increased, there is a concomitant collapse of the H_μ doublet of doublets to form a triplet. Therefore, the relative tightness of binding of $\{Cp_2ZrH_2\}$ to the main group hydride fragment can be considered; $\{^{D}\mathbf{2}\}$ is the most tightly bound – $^{M}\mathbf{1}$ clearly the loosest. Contrary to data for ^{M}**Al•Zr**, the fast exchange regime is not revealed in ^{D}**Zn•Zr** and ^{D}**Mg•Zr**. The conclusion matches the crossover experiments and computational results, where $^{D}\mathbf{3}$ was also shown to be nearly as tightly bound as $^{D}\mathbf{2}$.

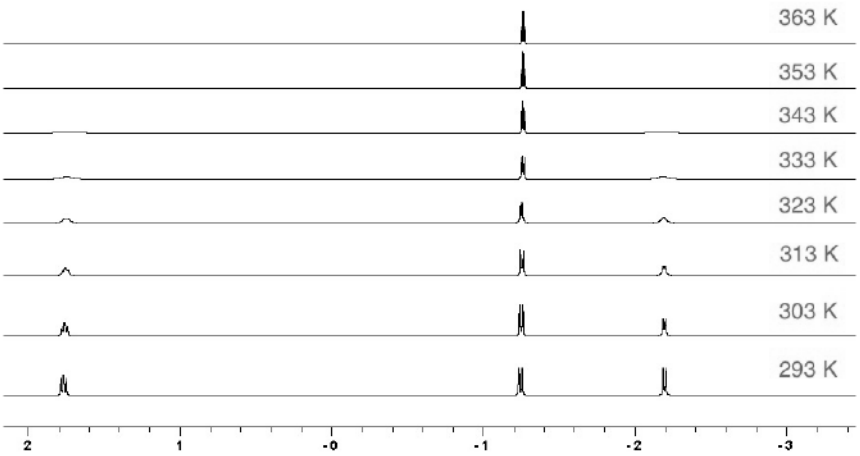
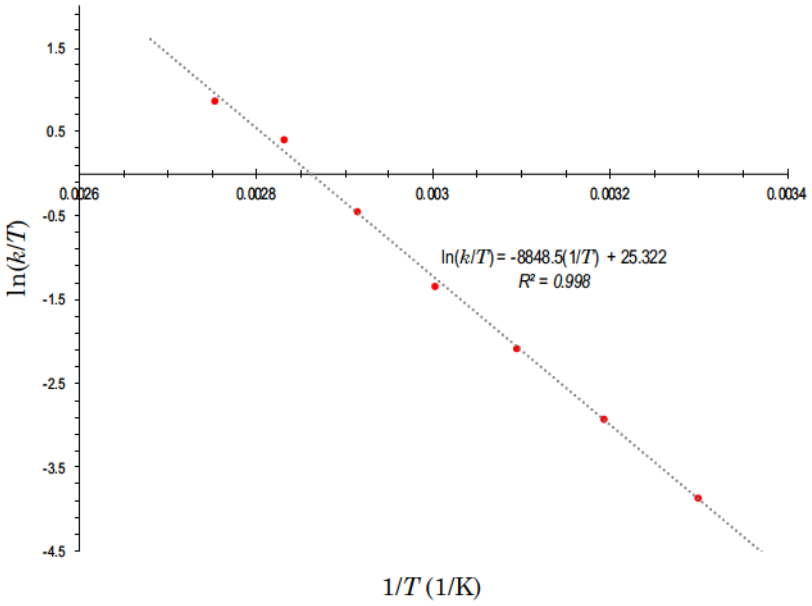


Figure 2.14. Modelled hydride resonances of ^{D}**Zn•Zr** from 293 to 363K.

VT NMR data was treated by computational line shape analysis to further scrutinise the chemical exchange processes. The modelled data are presented in Figure 2.14 and the Eyring analysis in Graph 2.2. Fits for *k* were optimised to the experimental data, giving the following activation parameters for the exchange of H_t with H_μ: $\Delta H^{\ddagger} = 17.6 \pm 0.3$ kcal mol^{-1}, $\Delta S^{\ddagger} = +3.1 \pm 1.1$ cal K^{-1} mol^{-1}, $\Delta G^{\ddagger}_{298K} = 16.6 \pm 0.0$ kcal mol^{-1}. Due to the inability to observe clear peaks for H_t across the coalescence temperatures by 1D NMR experiments, data for ^{D}**Mg•Zr** have not been modelled. A similar set of activation parameters are expected. Certainly, a cautious prediction could be made considering the aforementioned data showing ^{D}**Mg•Zr** to be more tightly bound. The Gibbs free energy of activation should be greater. Moreover, crude estimations of $\Delta G^{\ddagger}_{298K}$ can be made using the T_c value (see Experimental). A value of 17 kcal mol^{-1} is obtained from an equation that also fittingly predicts $\Delta G^{\ddagger}_{298K}$ = 16 kcal mol^{-1} for the exchange in ^{D}**Zn•Zr**. The relevant estimate for ^{M}**Al•Zr** is $\Delta G^{\ddagger}_{298K}$ = 12 kcal mol^{-1}.

A positive entropy of activation is indicative of a dissociative rate-determining step for the hydride exchange mechanism. A possible mechanism is proposed in Figure 2.15. It involves the partial dissociation of the complex to the single hydride bridge structure (^{D}**M-η^1-Zr**), before a reconnection of the double bridge through the erstwhile terminal hydride. The initial step

(breaking of the *outer* hydride bridge) constitutes a loss in order, which agrees with the positive $\Delta S^{\ddagger}$ value. An alternative mechanism of $H_t/H_{\mu'}$ exchange has been posited previously: Shore and co-workers proposed a rotation around a single hydride bridge in a $[Cp_2ZrH_t(\mu\text{-}H)_2BR_2]$ system.[34] The exchange was examined by NMR line shape analysis in the $[Cp_2ZrH_t(\mu\text{-}H)_2B(C_5H_{10})]$ system to give activation parameters of $\Delta H^{\ddagger}$ = 19.3 kcal mol^{-1}, $\Delta S^{\ddagger}$ = +15 cal K^{-1} mol^{-1}, and $\Delta G^{\ddagger}_{298K}$ = 14.9 kcal mol^{-1} (standard errors not provided).[34] This Gibbs free energy of activation is intermediate between **^{M}Al•Zr** and **^{D}Mg•Zr**/**^{D}Zn•Zr** (so too is the estimated value based on the T_c: +13.5 kcal mol^{-1}). The entropy of activation is much larger than in the Mg/Zr system, perhaps indicating the greater disorder in the rotational action. The ligand sterics may block the rotation around the Zr---H_μ–M axis. In the β-diketiminate complexes.



Graph 2.2. Eyring analysis of hydride exchange in **^{D}Zn•Zr,** as per modelled ^{1}H NMR lineshapes.

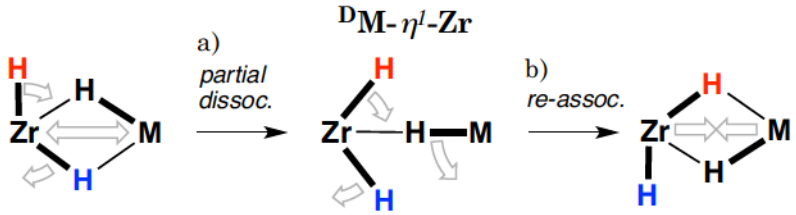


Figure 2.15. Proposed mechanism for the chemical exchange between H_t and H_μ in **^{D}M•Zr** (M = Zn, Mg), showing the rearrangement pattern in the hydride core.

In the related B/Zr analogue studies, Shore *et al.* also observed an exchange between the two *bridging* hydrides.[30,31,34] A mechanism was posited in which the inner hydride (H_μ) bridge was broken (instead of the outer, as in Figure 2.15a). For the rate-determining step, when the

exchange kinetics were analysed, a negative entropy of activation was found (–0.9 cal K^{-1} mol^{-1}).[34] Hence, a reversible α-elimination of a Zr–C_{Cp}–H bond was used to explain the entropic order. We do not believe such a process is at play in ^{D}**Zn•Zr** and ^{D}**Mg•Zr**.

2.3.2.2 Theoretical Studies on the Exchange Mechanism

Hydride Exchange via a Cog Mechanism

Before engaging in DFT studies pertaining to the hydride exchange mechanism, the proposed mechanism (Figure 2.15) was contemplated. This mechanism can be likened to turning of a cog system, whereby the three metal-hydride bonds take the role of the cogwheels' teeth. The metals are the cogwheels themselves. In Figure 2.15, ^{D}**M-η^1-Zr** represents the structure halfway through this cog turning process (where the angle M-H-Zr = 180°). Importantly, this structure may be an intermediate – an end-on η^1 coordination of M–H to **Zr** – or it may be a transition state between the two equivalent M^{II}/Zr structures.

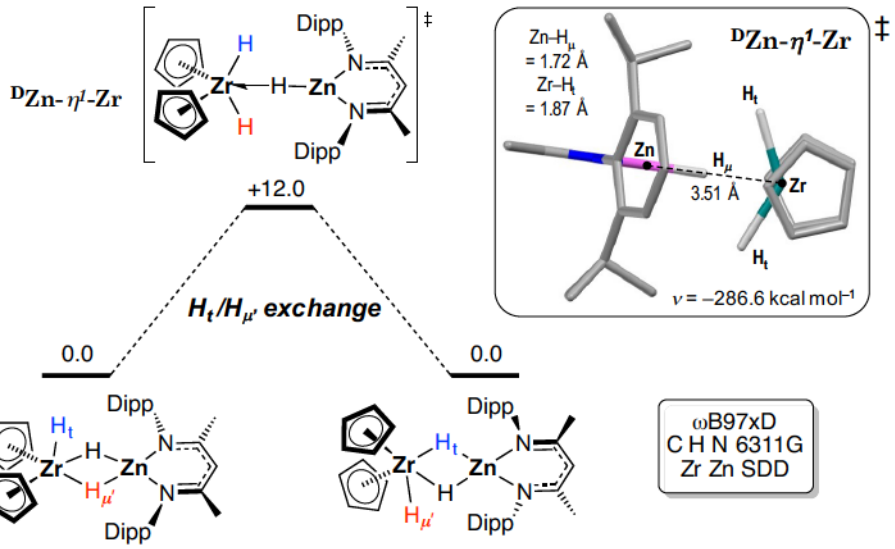


Figure 2.16. The calculated transition state (kcal mol^{-1}, at 298 K) for single-step $H_t/H_{\mu'}$ exchange in ^{D}**Zn•Zr** *via* the "cog mechanism".

The simplest approach to optimising the ^{D}**M-η^1-Zr** complexes was taken, namely freezing the M-H_μ-Zr angle at 180°. In the case of ^{D}**Zn-η^1-Zr**, the structure returned proved to be a transition state, *i.e.* [^{D}**Zn-η^1-Zr**]‡. The crucial vibration in this transition structure is the rocking of the hydride bonds as illustrated and predicted in Figure 2.15a. The relevant Gibbs free energy barrier to hydride exchange is 12.0 kcal mol^{-1}; this value is not prohibitively large and is in the right region compared to the experimental data (*cf.* 16.6 ± 0.03 kcal mol^{-1} from Graph 2.2). By DFT, [^{D}**Mg-η^1-Zr**]‡ has a 14.6 kcal mol^{-1} Gibbs free energy barrier. This is near to, yet higher, than that of [^{D}**Zn-η^1-Zr**]‡ – in line with the experimental evidence. The structural changes of the Mg/Zr transition state (Figure 2.17a) may explain the higher $\Delta G^{\ddagger}_{298K}$ value.

The same approach to [^{D}**Mg-η^1-Zr**]‡ construction did not immediately yield a transition state. Optimisation of [^{D}**Mg-η^1-Zr**]‡ eventually leads to a structure in which the M-H_μ-Zr angle is bent to 148.7° (Figure 2.17a – bending within the plane of (N,N)-Mg-Zr). No other ligand group (on either metal fragment) is significantly moved, and thus H_μ is still equidistant from both H_t atoms. Interestingly, it breaks the plane of the metals and the hydrides. This plane is maintained in [^{D}**Zn-η^1-Zr**]‡, ^{D}**Zn•Zr** and ^{D}**Mg•Zr** and is constant with the zirconocene FMO arguments.[13] The structure nevertheless represents the midpoint of the "cogs" turning. However, the distortion to the Zr-$(H)_3$ plane may play a part in making the hydride exchange less favourable. Intrinsic reaction coordinate (IRC) calculations show that the ground and transition states are linked by the expected pathways – *i.e.* the movements in Figure 2.15. The exceptional placement of H_μ in [^{D}**Mg-η^1-Zr**]‡ means that the path of the H_μ is slightly different. As the Mg–H_μ bond is moved during the mechanism, it swings out of the Mg-(H_μ,$H_{\mu'}$)-Zr plane in an arc. This quirk means the Mg---Zr distance in the transition state need not lengthen as much as Zn---Zr (Figure 2.17b), whilst the H_μ keeps the same distance from Zr in both. In both transition states, the M–H_μ bond is lengthened.

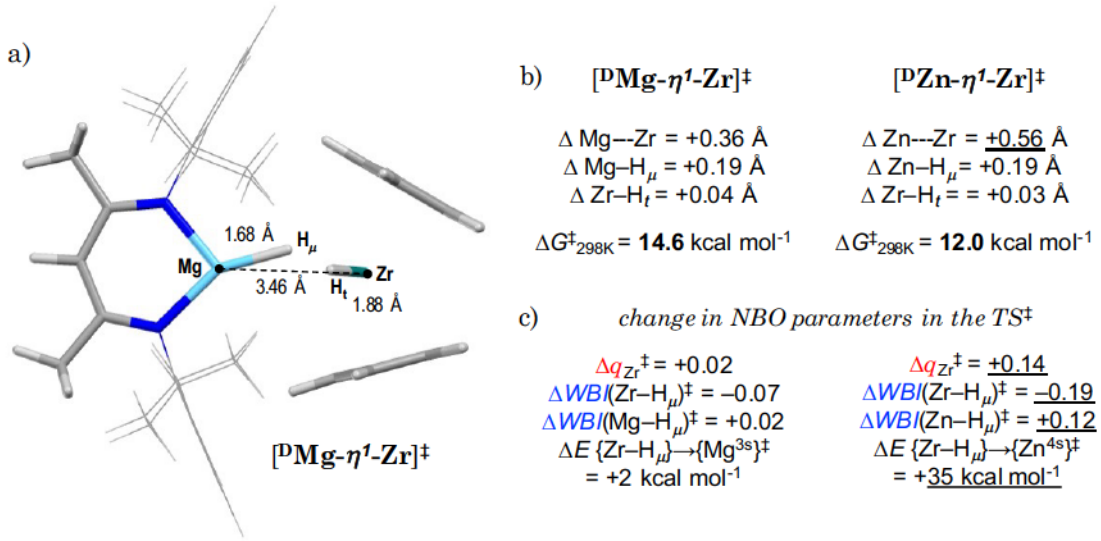


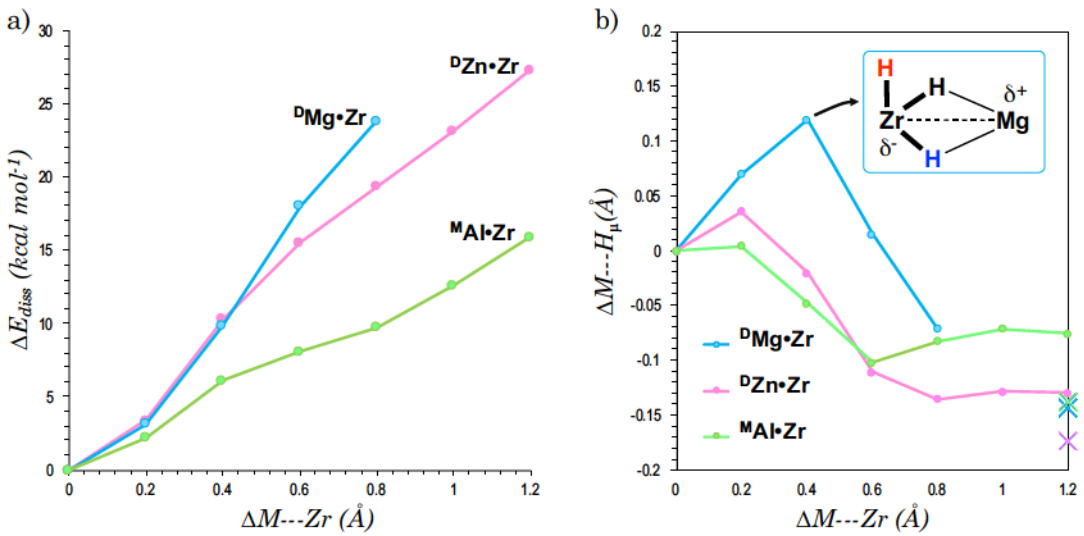
Figure 2.17. a) Structure of [^{D}**Mg-η^1-Zr**]‡; b) the increase in key structural parameters of the metal-hydride cores of [^{D}**M-η^1-Zr**]‡ relative to their ground states; and c) the change in selected NBO parameters (including, donor-acceptor interaction energies).

The small difference between Mg and Zn exchange mechanisms is likely due to the significance of the ionic bonding and the $\{Cp_2ZrH_3\}^-$ fragment in the Mg/Zr system (section 2.2.2.2). The coulombic attraction in ^{D}**Mg•Zr** appears to be strong enough to tug Mg and Zr closer together regardless of the preference for a 180° M-H_μ-Zr angle suggested by molecular orbital arguments. The data in Figure 2.17c are consistent in showing that the more covalently bonded Zn/Zr heterobimetallic complex is more obliging to partial dissociation, based on the

greater change seen in the parameters. During the mechanism, there is very little change in the relative NPA charge difference between Mg and Zr ($\Delta\{q_{Zr} - q_{Mg}\}^{‡}$ = +0.02). This is not so for ^{D}**Zn•Zr** → [^{D}**Zn-η^1-Zr**]‡: a clear increase in Zn/Zr charge separation ($\Delta\{q_{Zr} - q_{Zn}\}^{‡}$ = +0.14) stems from development of positive charge on Zr in [^{D}**Zn-η^1-Zr**]‡. This presents a picture of a stubbornly ionic Mg/Zr heterobimetallic complex, already very charge-separated ($q_{Zr} - q_{Mg}$ = –1.17 *vs.* $q_{Zr} - q_{Zn}$ = –0.83), and quite inflexible to intramolecular structural change. Nevertheless, the kinetic parameters are still not very far removed from those of the Zn/Zr system. Both agree with the M/Zr experimental estimates.

Partial Dissociation and Other Mechanistic Possibilities

With the mechanism of Shore *et al.* in mind (*vide supra*) – in which **Zr** may rotate around an η^1 bridged *intermediate* – the incremental dissociation of the M^{II}/Zr complexes to ^{D}**M-η^1-Zr** was mimicked using a relaxed dissociation scan. The M---Zr distance was increased incrementally by 0.2 Å, and the structure of the complex optimised at each distance. Taking the electronic energies along the points of the scan gives the potential energy surfaces in Graph 2.3a. For further comparison, the dissociation scan was also calculated for ^{M}**Al•Zr**. Graph 2.3b helps to detail the structural changes upon M/Zr dissociation. It shows how the M–H_μ bond distance varies during the scan, compared to the ground state heterobimetallic structure.



Graph 2.3. a) Change in energy and b) change in M---H_μ bond distance in the relaxed dissociation scan in the M/Zr heterobimetallic hydride complexes (ωB97xD functional and SDD/6-311G basis sets). On (b), the M–H bond distance in the isolated main group fragment is marked with ×. Inset: the exceptional asymmetric metal-hydride core geometry.

The results tell us two things: i) a rotational hydride exchange mechanism is very probably higher in energy than the cog mechanism; ii) the action of dissociation is again different

between the Mg and Zn analogues. With regards to i), the rotational movement of **Zr** around the η^1 bridge was itself approximated to require 10–20 kcal mol^{-1} in Gibbs free energy, but this is additional to the >10 kcal mol^{-1} needed to separate the M/Zr complexes to the η^1 condition (Graph 2.3, *n.b.* energy in ΔE here). The comparison of energies involves mixing of electronic and free energies, but the cog mechanism does appear more likely to occur, with *at most* around half of the energy barrier.

The Mg–H_μ plot on Graph 2.3b shows the difference in dissociation patterns. Unlike the symmetrical stretching seen in ^{D}**Zn•Zr**, *both* H_μ *and* $H_{\mu'}$ were drawn away by the Zr centre during the first 0.4 Å of M---Zr stretching (Graph 2.3b, inset). It takes more than 0.6 Å of metal dissociation before the collapse of the Mg–H_μ distance below that of the respective bond in ^{D}**Mg•Zr**. This reiterates the recalcitrance of the ate complex character and the pervasiveness of $[Cp_2ZrH_3]^-$ near the ground state of ^{D}**Mg•Zr**. Once the metal centres are 0.6 Å apart, the Mg-H_μ-Zr angle relaxes quickly towards 180°, which it has all but reached by 0.8 Å Mg/Zr dissociation.

In contrast to [^{D}**M-η^1-Zr**]‡, the Al analogue (^{M}**Al-η^1-Zr**) actually optimised to a local minimum. It is calculated to be +7.7 kcal mol^{-1} above ^{M}**Al•Zr**. From Figure 2.2 and Figure 2.11 we know that the doubly bridged ^{M}**Al•Zr** is only slightly favoured with respect to its parent hydrides. The G_{diss} for ^{M}**Al•Zr** is calculated to be 14.6 kcal mol^{-1}. Therefore, the significance of any hydride exchange mechanism involving ^{M}**Al-η^1-Zr** is perhaps questionable, owing to the probable competition with an entirely dissociative intermolecular mechanism. On the other hand, the calculated G_{diss} values for ^{D}**Mg•Zr** and ^{D}**Zn•Zr** are +31.2 and +23.1 kcal mol^{-1} respectively. This means that the M^{II}/Zr complexes have the stability from which to perform intramolecular exchange processes (such as in Figure 2.16) without being troubled by complete dissociation.

2.4 Stoichiometric Reactivity

Once characterised, the Mg and Zn heterobimetallic complexes were subjected to some exploratory reactivity tests. These tests are specifically related to two previous publications made by the group,[1,3] and more generally to the Crimmin group's search for catalytic inert bond activation using metals that are environmentally palatable.[35]

2.4.1 C–F bond Cleavage of Pentafluorobenzene

The group's previous work with main group metal hydrides and C–F bonds of fluoroarenes has been focused on catalytic hydrodefluorination.[1,36] Chemoselective metalation of these inert bonds has been the domain of low-valent main group metal reactants.[35,37] For this reason, it was satisfying to find almost quantitative zincation of pentafluorobenzene (C_6F_5H) when **^{D}Zn•Zr** is treated with large and small excesses (10 or 1.3 equiv.). Figure 2.18 shows the crystal structure of the Zn–Ar^{F} product [^{Dipp}*BDI*Zn(*p*-C_6F_4H)]. Hydrodefluorination is revealed in the minor by-product: *para*-$C_6F_4H_2$ is formed in a 1:2 ratio against [^{Dipp}*BDI*Zn(*p*-C_6F_4H)]. The Zr centre takes the equivalents of fluoride to form [Cp_2ZrF_2] (1:1.3 against [^{Dipp}*BDI*Zn(*p*-C_6F_4H)]).

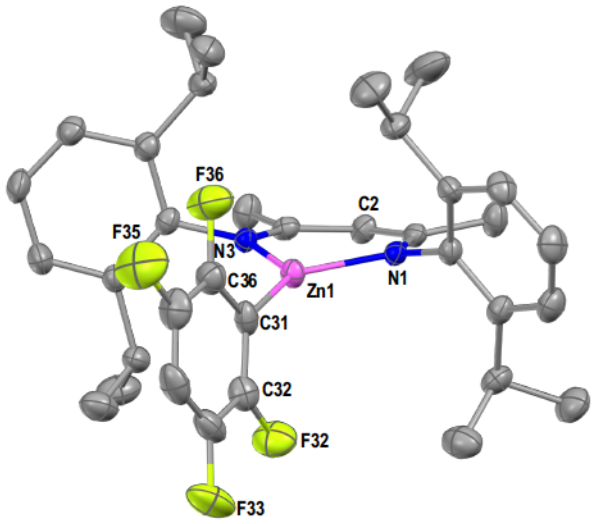
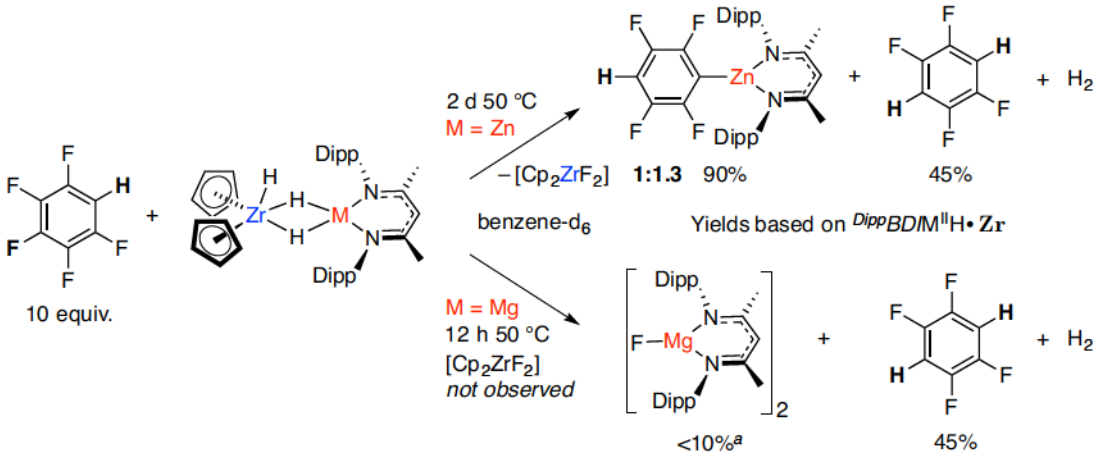


Figure 2.18. The crystal structure of [^{Dipp}*BDI*Zn(*p*-C_6F_4H)] (50% probability ellipsoids). Selected bond lengths [Å] and bond angles [°]. Zr(1)–O(1) 2.2163(17), Zr(2)–O(1) 2.1915(18), Zr(1)–C(7) 2.362(3), O(1)–Zr(1)–C(7) 70.79(8).

With the related systems, **^{M}Al•Zr** and **Zr•Zr**, M–Ar^{F} products have been observed in reactions with C_6F_5H. Jones and co-workers found that **Zr•Zr** gives a zirconation product, [Cp_2Zr(*p*-C_6F_4H)F];[38] and in a Al/Zr system, [^{Mes}*BDI*Al(*p*-C_6F_4H)F] is the major product when 1 equiv. **^{M}1** and C_6F_5H are reacted in the presence of 5 mol% [Cp_2ZrCl_2].[3] In the exploratory

reaction with the Zn/Zr system (Scheme 2.5), no catalytic turnover resulted when further ^{D}**3** is added. The Zn–H bonds are not able to activate the strong Zr–F bonds of [Cp_2ZrF_2]. This contrasts the case with Al–H, where Al–F is strong enough to force reformation of Zr–H bonds.[39] There is no evidence of [^{Dipp}*BDI*Zn–F] formation at all during the reaction in Scheme 2.5.



Scheme 2.5. Exploratory C–F bond cleavage of pentafluorobenzene by ^{Dipp}*BDI*M^{II}H•**Zr**.

Glaringly, in the case of ^{D}**Mg•Zr**, the main group metal is successful at activation of [Cp_2ZrF_2], and none of the latter is observed (Scheme 2.5). However, it appears that the fluorophilicity of Mg is too severe, completely preventing any metalation of the fluoroarene. A significant amount of free ligand (1,3-diketimine) was identified in the reaction mixture by ^{1}H NMR, which suggests that degradation of Mg complexes is leading to insoluble $Mg_xZr_yF_z$ material. This is supported by a spread of small peaks towards –200 ppm in the ^{19}F NMR. The hydrodefluorination process is still successful, showing no difference to the Zn/Zr reaction in terms of yield. Recently, separate (unpublished) work within the group has found that ^{D}**2$_2$** alone performs magnesiation of C_6F_5H to give [^{Dipp}*BDI*Mg(*p*-C_6F_4H)].[40] The analogous control with ^{D}**3** gives C–H functionalisation of C_6F_5H to form [^{Dipp}*BDI*Zn(C_6F_5)].[41]

Some discussion of mechanism is needed in order to attempt to explain the presence of dihydrogen in the reactions. It is probable that several mechanisms are operating in competition. This is thought to be the case for **Zr•Zr** reactivity,[38,42] and of course a main group fragment should create even more mechanistic possibilities. The competition amongst mechanisms will be affected by the identity of M, and so a different mechanism is likely for Zn/Zr compared to Mg/Zr.

For the Zr/Zr complex, the S_NAr mechanism is favoured by Jones *et al.*, whereby the hydrides of {Cp_2ZrH_2} are thought to be nucleophilic. As found in Figure 2.5, the hydrides of the heterobimetallic complexes are more negatively charged than the homobimetallic counterpart. The monomer, **Zr**, holds a q_H = –0.30 charge on its hydride atoms, which is just

shy of the values for ^{D}**Zn•Zr**. The outer bridging hydride is the most hydridic in ^{D}**Mg•Zr** and ^{D}**Zn•Zr** (e.g. q_H = –0.43 for ^{D}**Mg•Zr**). This atom is feasible as a nucleophile because the calculated HOMOs of both ^{D}**Mg•Zr** and ^{D}**Zn•Zr** are based on Zr–$H_{\mu'}$ bonding orbitals (see Experimental, Figure 2.27). A S_NAr transition state such as that in Figure 2.19a may therefore be proposed. A pathway through this transition state could lead to production of *p*-$C_6F_4H_2$. The fluoride leaving group could be abstracted by a transient cationic heterobimetallic complex. After these S_NAr steps, the metal species is likely to dissociate into single metal fragments. During the reaction, ^{D}**3** is observed immediately. It steadily gives way to [^{Dipp}*BDI*Zn(*p*-C_6F_4H)] over the following 24 h. Therefore, [Cp_2ZrHF] might be expected, from which **Zr** and [Cp_2ZrF_2] are accessible.

The Zn hydride complex may form dihydrogen in a σ-bond metathesis reaction with the hydrodefluorination product (*p*-$C_6F_4H_2$). A H_2 resonance was seen in the ^{1}H NMR spectra of the reaction of ^{D}**3** with various fluoroarene substrates.[41] ^{D}**Zn•Zr** is inert when treated with $C_6F_4H_2$ under the same conditions as in Scheme 2.5.

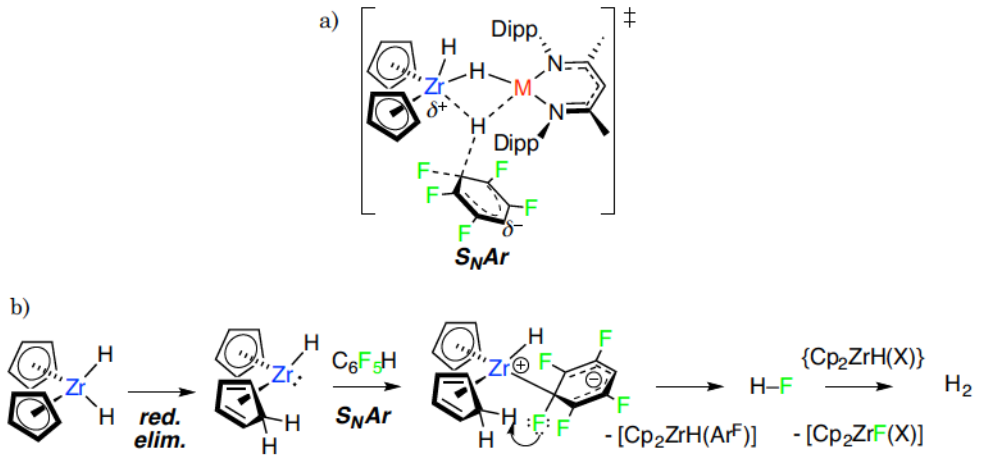


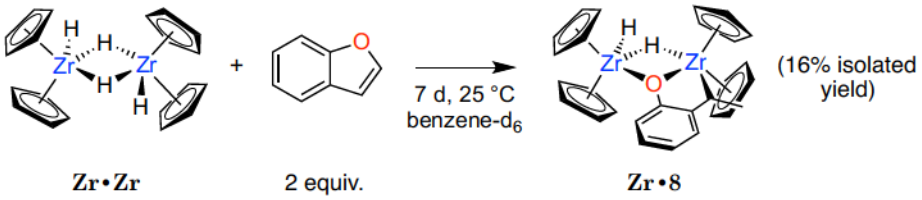
Figure 2.19. a) Possible transition state for C–F activation on a hydrodefluorination pathway and b) a proposed pathway for dihydrogen production.[43]

However, the mechanistic rationale above does not explain the Mg/Zr reactivity: no Mg–Ar^F species are seen, and with {^{D}**2**} only Ar^F–F bond activation occurs.[40] An alternative mechanism proposed by Jones and co-workers could yet explain the origin of dihydrogen in the ^{D}**Mg•Zr** reaction mixture. The pathway in Figure 2.19b shows how a Zr^{II} species can originate in **Zr** by reductive elimination of CpH. Jones *et al.* have suggested this reversible process for [$Cp^*_2ZrH_2$],[43] but the mechanism should occur with Cp ligands too: in unpublished deuterium-labelling experiments relating to **Zr•8** (see below) exchange between hydrides and Cp group protons has been observed.[2] After attack of Zr^{II} on the fluoroarene, HF is produced that will quickly protonate and remove available metal hydride to form H_2. This pathway in Figure 2.19b is more likely in the case of the Mg/Zr system because, after the transition state

in Figure 2.19a, the very fluorophilic Mg should win out in the battle for the fluoride ligand, leaving {Cp_2ZrH_2}. This also explains the absence of [Cp_2ZrF_2], which *does* build up when M^{II} is the less fluorophilic Zn.

2.4.2 Crossover with an Oxazirconacycle Fragment

In the stoichiometric reaction of benzofuran with **Zr•Zr**, **Zr•8** is isolated from a mixture of C–O bond cleavage products (Scheme 2.6). This product has been reported within the group. The reaction has emerged as part of the aforementioned mechanistic studies into the catalytic C_{vinyl}–O cleavage of benzofuran.[3,44] The crystal structure of **Zr•8** is displayed in Figure 2.20. The behaviour of **Zr•8** towards Mg, Zn and Al hydride fragments is interesting – in particular, the potential for crossover between the two types of bimetallic complex.



Scheme 2.6. Synthesis of **Zr•8** by C–O cleavage of benzofuran.

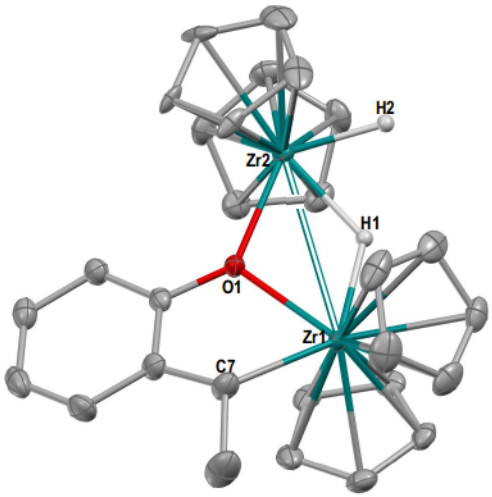
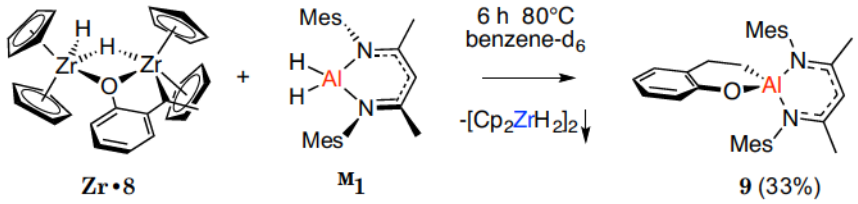


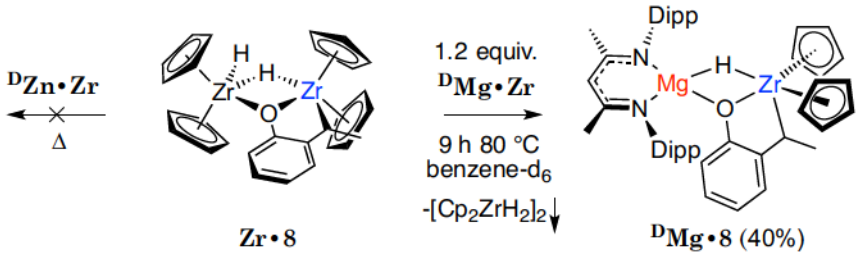
Figure 2.20. The crystal structure of **Zr•8**. Selected bond lengths [Å] and bond angles [°]. Zr(1)–O(1) 2.2163(17), Zr(2)–O(1) 2.1915(18), Zr(1)–C(7) 2.362(3), O(1)–Zr(1)–C(7) 70.79(8).

A transmetallation is effected when ^{M}**1** and **Zr•8** are reacted with forcing conditions, giving the oxa-alumacycle **9** (Scheme 2.7). This reaction was followed by ^{1}H NMR spectroscopy, and **9** confirmed against literature data.[3] The aluminium hydrides of ^{M}**1** are formally transferred to the alkyl-ligated Zr of **8** to give **Zr•Zr** as by-product. The Al product **9** is a major product in the catalytic process developed by the group – a formal insertion of Al into the C_{vinyl}–O bond of benzofuran.

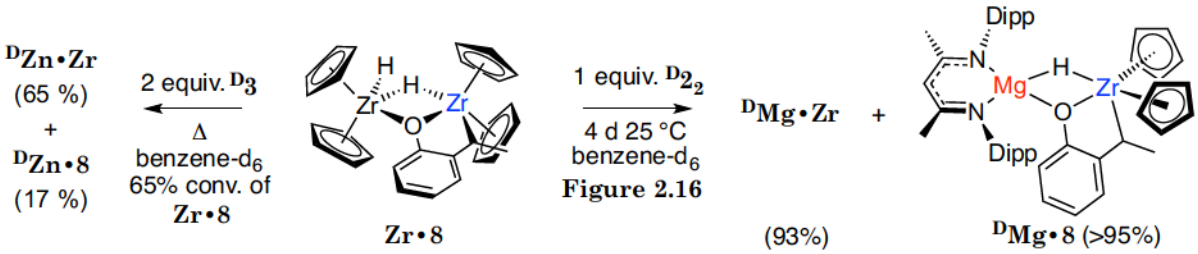


Scheme 2.7. Production of **9** via ligand exchange.

Considering the divalency of Mg and Zn, a transmetallation of the type in Scheme 2.7 is not allowed. In this chapter, the strong preference for Zr/M^{II} heterobimetallic complexes over the monometallic parent hydrides has been demonstrated. This led to the hope that {Cp_2ZrH_2} might be displaced by the fragments ^{D}**2** or ^{D}**3** to give ^{Dipp}*BDI*MH•**8**, with the added benefit that the insolubility of {Cp_2ZrH_2} would separate the products. The results of crossover reactions in benzene-d_6 are shown in Scheme 2.8 and Scheme 2.9. The tests have shown that although the transfer of **8** is definitely feasible, isolation and characterisation of the resulting complexes is made difficult by the experimental practicalities.



Scheme 2.8. Reactivity of ^{D}**Mg•Zr** with the oxazirconacycle **Zr•8**.



Scheme 2.9. Production of putative ^{D}**Mg•8** (and ^{D}**Zn•8**) from **Zr•8**.

On reaction with ^{D}**Mg•Zr**, a singlet resonance at δ = 0.23 ppm emerged after heating. It was assumed to arise from a single bridging hydride in ^{D}**Mg•8**. After extensive heating, the crossover could not be advanced further than a 50–60% consumption of **Zr•8** and ^{D}**Mg•Zr.** A 40% yield of ^{D}**Mg•8** was returned. Rather than the planned clean production of ^{D}**Mg•8**, several unknown multiplets were seen in the bridging hydride region of the ^{1}H NMR spectrum after 5 h at 80 °C. Further heating only grew these peaks. Extensive heating to an analogous ^{D}**Zn•Zr**

reaction mixture gives no clear reaction at all (Scheme 2.8). The thermolysis necessary to see displacement of {Cp_2ZrH_2} from **Zr•8** limits the viability of the reaction as a synthetic route to isolable M^{II}/Zr alkoxide structures.

Use of the parent hydrides is much more successful in generating the alkoxide-bridged heterobimetallic complexes (Scheme 2.9). These reactions were completed cleanly (see Figure 2.21) with the aim of uncovering a confident assignment of the putative **^{D}Mg•8** by ^{1}H NMR spectroscopy. Figure 2.22 shows an assignment of peaks to **^{D}Mg•8**. Interestingly, an eligible species is also produced in the *zinc* form of the reaction. The singlet resonance (presumed to be of the bridging hydride) is found at δ = –0.40 ppm, albeit with incomplete conversion, even after extended heating at 80 °C. The signals for the zinc analogue, **^{D}Zn•8** are similar to **^{D}Mg•8** in pattern. Unfortunately, the structure is less clearly assignable because of the broadness of signals in the other product (**^{D}Zn•Zr**), and the incomplete reaction leads to a crowded spectrum.

The reason for any conversion at all in this zinc/oxazirconacycle reaction is probably the action of the concomitantly formed **^{D}Zn•Zr** as a thermodynamic sink. The oxazirconacycle moiety (**8**) is thus freed for binding with another equivalent of **^{D}3**. The same explanation could be given for the quantitative yield and facile conditions in the case of **^{D}Mg•8**.

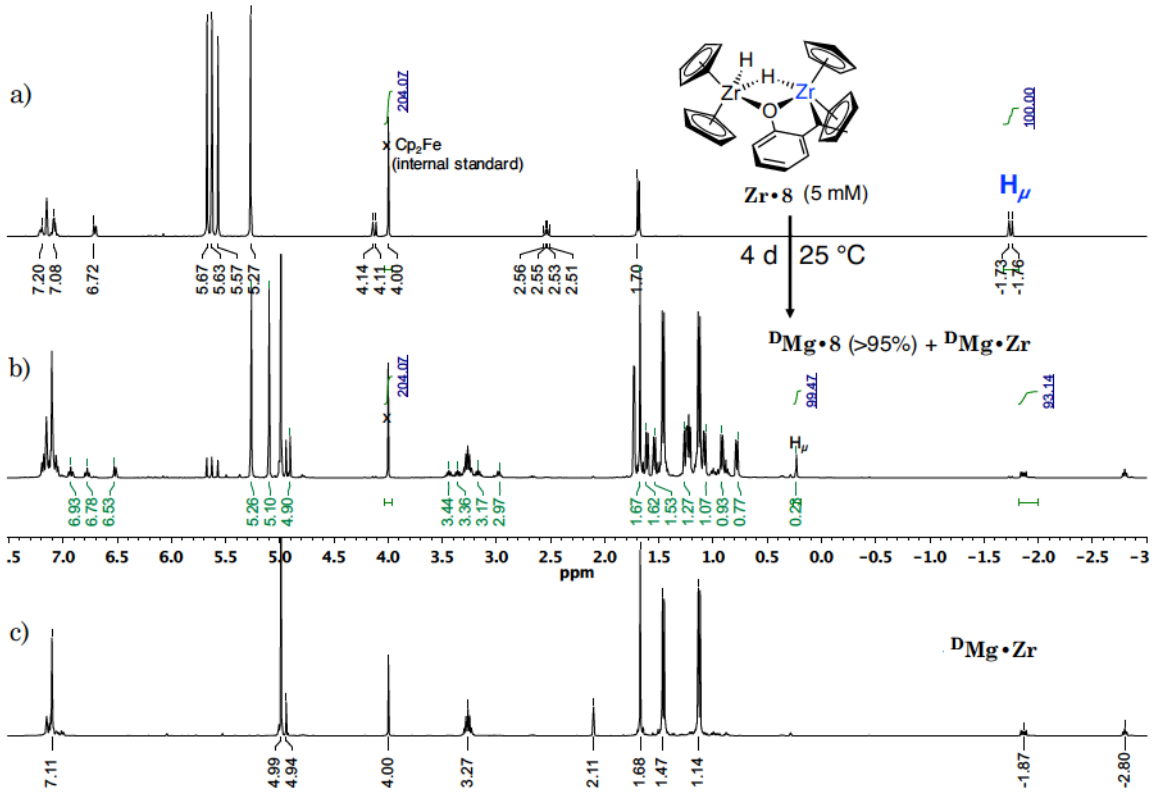


Figure 2.21. The ^{1}H NMR data for the reaction components of Scheme 2.9 in the **^{D}Mg•8** from: a) ^{1}H spectrum of **Zr•8**; b) reaction mixture after 4 d containing **^{D}Mg•8**; c) **^{D}Mg•Zr** for comparison.

The products ^{D}**Mg•8** and ^{D}**Zn•8** are not easily isolable from the reaction mixtures in which they are produced, and hence, preparative scale reactions have not been attempted. Notwithstanding, the outcomes of these experiments with **8** compliment conclusions made previously in this chapter. The binding of a zirconocene fragment is ostensibly more favourable with {^{Dipp}*BDI*MgH} than with [^{Dipp}*BDI*ZnH]. In this case, the superior oxophilicity of Mg over Zn may add to the difference between the binding strengths.

As touched upon above, **Zr•8** and **9** are formed from the C–O bond cleavage of benzofuran by zirconocene dihydride (with and without the presence of ^{M}**1** respectively). Thus, the heterobimetallic hydride complexes should be probed for their inert bond activation capabilities with the same substrate. However, no reaction was seen between ^{D}**Mg•Zr** and benzofuran when a 1:1 mixture was heated for 24 h at 80°C in benzene-d_6.

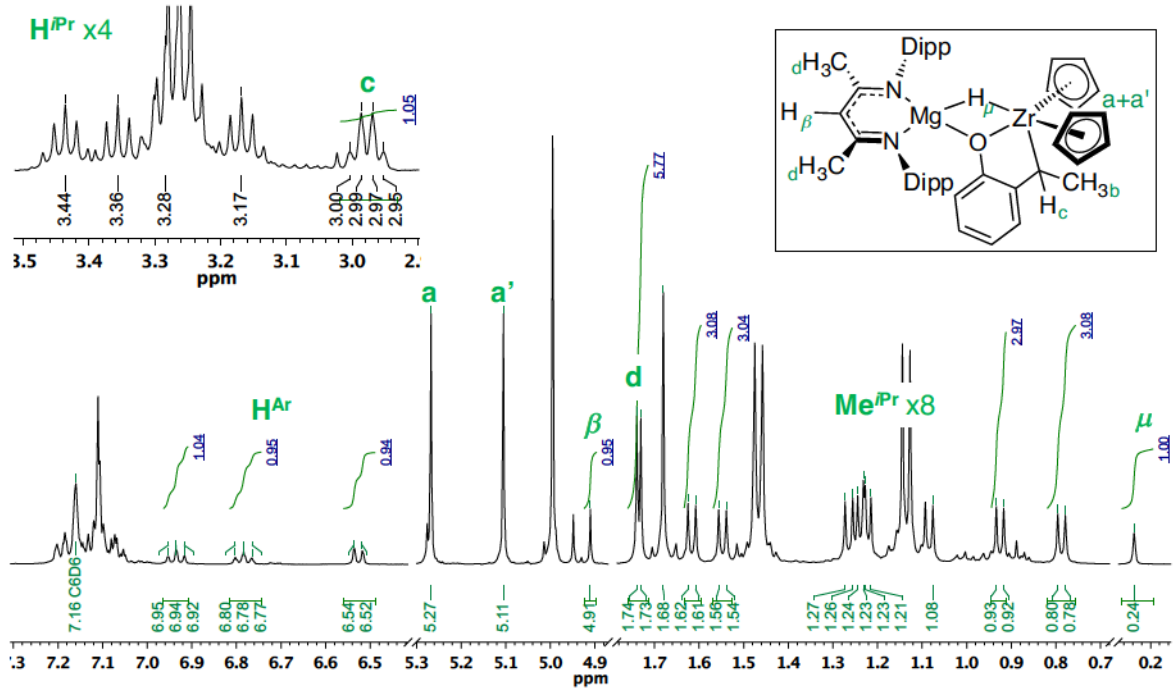


Figure 2.22. Assignment of ^{1}H NMR resonances ^{D}**Mg•8** from a reaction mixture containing ^{D}**Mg•Zn** and residual **Zr•8**.

2.4.3 Purity

Before going into extended investigations on the reactivity and catalytic properties of the heterobimetallic complexes (Chapters 3 and 4), their purity needs to be examined. The yields and the purity of the heterobimetallic complexes are no doubt limited by the impurities in the starting materials. This is especially a concern with ^{D}**2**$_2$ and **Zr•Zr**. Washing of ^{D}**2** has been unable to remove the ~5–10% of an unknown β-diketiminato impurity. For procedures reported herein, **Zr•Zr** retains the red-purple colour of its mother liquor when washed in THF – according to literature the product should be colourless.

Observations and experiments pertaining to impurities are discussed below in three parts: (i) ^{1}H NMR peak shapes of the upfield hydrides (ii) colour and colour-changes, and (iii) by some basic quantitative analysis.

2.4.3.1 ^{1}H NMR

There are two strange phenomena in the bridging hydride ^{1}H NMR signals of ^{D}**Mg•Zr** which reveal unknown dimensions of the purity.

Shoulder Peaks

Both bridging hydride signals show a smaller resonance of the same shape on the upfield shoulder (Figure 2.23). The phenomenon is sometimes seen for the Zn analogue (Figure 2.23a), but to a less detectable extent than in ^{D}**Mg•Zr** (Figure 2.23b). The 'deputy peak' follows the behaviour of its bigger relative at all temperatures. There is no sign that one peak is consumed before the other during reactivity. No 'deputy peak' is seen in the ^{D}**Mg•Zr** or ^{D}**Zn•Zr** products if they are prepared from the ligand exchange procedure *i.e.* [Cp_2ZrCl_2] with excess main group hydride. No specific experiments have been carried out to see if this is a concentration-dependent effect, but it does not appear to be. One explanation could be minor presence of an isotopomer, as a result of H/D exchange.

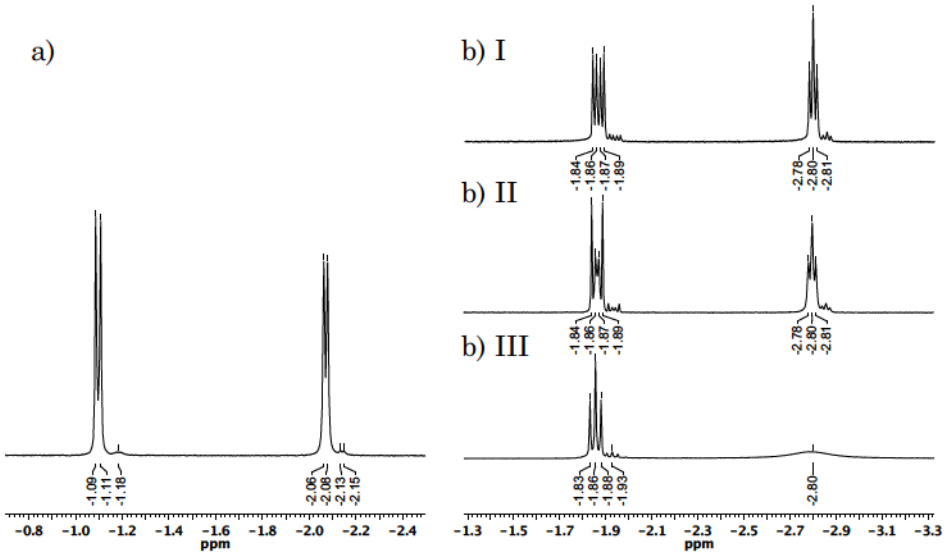


Figure 2.23. a) The upfield facsimiles on the shoulder of the main bridging hydride resonances in ^{D}**Zn•Zr**. b) The ^{1}H NMR signals for three separate samples of ^{D}**Mg•Zr**. All samples are between 47–55 mM in benzene-d_6 at 298 K.

Line Shape Changes

Variable temperature NMR experiments on ^{D}**Mg•Zr** and ^{D}**Zn•Zr** show a process of chemical exchange involving the hydride ^{1}H NMR signals (see Table 2.3, Figure 2.7 and Figure 2.8). *For* ^{D}**Mg•Zr** *only*, the ease of the exchange processes appears to be dependent on the trace

impurity profile and/or preparative circumstances. Different batches of ^{D}**Mg•Zr** showed the same chemical exchange process but operating at lower temperature (Figure 2.23b). It should be noted that this is seen *only in the hydride signals*. Type **III** peaks are seen when the preparation of ^{D}**Mg•Zr** is followed by ^{1}H NMR, so it was proposed that trace remains of the parent hydrides facilitate the site exchange of the hydrides.

To test this hypothesis, doping experiments were carried out, whereby small amounts of parent hydrides were added to 'pure' samples of **I** or **III** types. The results (see 2.6 Experimental, Table 2.5) do not suggest involvement of the parent hydride samples in exchange processes; no changes in the peak shapes were seen with addition of these individual additives. However, puzzlingly, the crossover experiment (Scheme 2.3, M' = Mg) where equimolar {^{D}**2**} displaces ^{D}**3** from ^{D}**Zn•Zr**, showed development of **I** into peak type **III** (*via* **II**). With no dopants present, heating samples of **I** and **III** gave further results that are contradictory and hard to reconcile. After extended heating (50 or 80 °C), the room temperature NMR signals of type **I** move towards type **III**. However, the opposite transition is seen when **III** was generated *in situ* from the parent hydrides and heated at 50 °C for a week. Isolated samples with signals of **III** did not do this.

One possible explanation for the transitions between the slow/intermediate exchange regimes is the presence other impurities – impurities that build up/break down when the sample is extensively heated. The impurities should assist in the chemical exchange between hydride atoms, either by disrupting the bridge between the transition-main group metal fragments, or by supply of extrinsic hydride atoms in an intermolecular fashion.[45] The slow exchange-type sample (**I**) was used in the VT NMR experiments used in section 2.3.2 (Figure 2.7 and Figure 2.13) for characterisation of the hydride exchange mechanism. Therefore, the data shown is the upper limit of the T_c and activation parameters, which may be lowered by impurities in **III**. The same impurities in the ^{D}**Mg•Zr** system may also be culpable for the better substitution of **Zr** by **8** in Scheme 2.9, when compared with the Zn/Zr system.

2.4.3.2 Colour

In the preparative scale syntheses of ^{D}**Mg•Zr** and ^{D}**Zn•Zr** development of colour is displayed in the reaction solutions. Although the recrystallised ^{D}**Mg•Zr** and ^{D}**Zn•Zr** are colourless, oftentimes the reaction mixture's colour has been persistent on the recrystallised material. The ^{D}**Mg•Zr** synthesis turns gradually red-brown as the toluene slurry gradually takes up **Zr•Zr** into the solution and the mixture becomes homogeneous. The red-brown colour is familiar to Zr/Mg chemistry. An alternative preparation of **Zr•Zr** defined by Wailes *et al.* uses $Mg_{(s)}$ and zirconocene dichloride;[46]. A strong red hue was seen in the supernatant solution suggesting minor formation of Zr^{III} species such as **1.79** (see section 1.6.2). Moreover, the latter was discovered as a minor, inseparable Zr^{III} relative of a major Zr^{IV}/Mg heterobimetallic complex

(**1.78**).[11] Therefore, it cannot be discounted that the yields of ^{D}**Mg•Zr** and ^{D}**Zn•Zr** are limited by formation of relatively soluble paramagnetic species. The historic work by Wailes *et al.*[46,47] also suggests that such by-products may be oligomers between Zr and main group metal complexes.

2.4.3.3 Quantitative Analysis

Elemental analysis has been carried out on the bulk isolated samples of ^{D}**Mg•Zr** and ^{D}**Zn•Zr** for which the isolated yields are reported. The values returned are within the suitable range but do not find excellent agreement. (For ^{D}**Mg•Zr** (C, 70.29%; H, 8.17%: N, 4.20%) experiment found: C, 70.11%, H, 8.00%; N, 4.36%. For ^{D}**Zn•Zr** (C, 66.21%; H, 7.69%; N, 3.96%) experiment found: C, 66.09%, H, 7.49%; N, 3.98%.) This quantitative analysis of purity has its limitations with air-sensitive compounds.[48]

2.5 CONCLUSIONS

This chapter has thoroughly investigated the coordination chemistry of two new heterobimetallic complexes, **^{D}Mg•Zr** and **^{D}Zn•Zr**. The complexes are prepared from simple stoichiometric addition of the parent hydride fragments, $\{Cp_2ZrH_2\}$ and $\{^{Dipp}BDI MH\}$, to create a metal hydride core within a β-diketiminate/metallocene ligand system. Unlike the Al analogue and precedent (**^{X}Al•Zr**) the hydride atoms could not be located in single crystal X-ray diffraction experiments. Frontier molecular orbital arguments, study of the wider anatomy of the complex, and *in silico* calculations placed the hydrides perpendicular to the β-diketiminate plane.

The **^{Ar}M•Zr** complexes (M = AlH, Mg, Zn) are increasingly stable in the order **^{M}Al•Zr** < **^{D}Zn•Zr** < **^{D}Mg•Zr**, a series confirmed computationally and through M fragment displacement experiments. This is partly due to the sensitivity of the complexes to the sterics of the Ar group: the smaller Zn atom and extra valence on Al require closer approach of the two ligand systems. This is demonstrated by the failure to synthesise **^{D}Al•Zr**, and by the hampered rotational processes of the Dipp group observed in ^{1}H NMR studies of **^{D}Zn•Zr**. The same series describes the increasing ionicity to the bonding in the compounds, and increasing hydricity of their bridging H atoms.

Variable-temperature and NOESY ^{1}H NMR experiments show a different rate of terminal-to-distal hydride exchange in ^{Dipp}BDIMH**•Zr**: the exchange is faster with **^{D}Zn•Zr** (at 373 K). The exchange process was probed with Eyring analysis (for **^{D}Zn•Zr**) and DFT calculations, and a "cog" mechanism was found. In a single step, the central (M) hydride appears to flick the outer (Zr) hydrides between bridging and terminal roles. The more stable **^{D}Mg•Zr** has an increased free energy of activation, and it takes less energy to dissociate the metals in **^{D}Zn•Zr**. More DFT analysis suggests the significant ate complex description in the Mg/Zr complex is the root of these differences.

Both heterobimetallic species can hydrodefluorinate C_6F_5H. However, the fluorophilicity of Mg, competing with that of Zr, appears to lead to a degradation of organometallic by-products. In the case of **^{D}Zn•Zr**, the Zr centre takes the fluoride and a very large yield of *para*-zincated fluoroarene is afforded. An **S_NAr** mechanism of hydrodefluorination is proposed to involve the hydride based HOMO of the M^{II}/Zr systems. An oxazirconacycle fragment (**8**) appears to marry with the Mg hydride fragment most clearly. This is perhaps also due to the superior oxophilicity of the group two metal.

2.5.1 Future Work

As the following chapter will illustrate, these complexes hold potential for exceptional reactivity. Finally, Chapter 4 details some catalytic capabilities of the complexes. Therefore, extension of the series of compounds with respect to the ligand could see tuning of the reactivity and catalytic properties. For example, DFT studies predict greater stability of the Mes analogues ^{M}**M•Zr**. Jones and co-workers have found developments in a lot of their own work on Mg and Zn bimetallic complexes through diversification of the β-diketiminate ligand.[32,49-51] This will depend on the use and design of (circuitous) methods to generate the parent hydride complexes. Further calculations can also be undertaken in order to judge whether the Cp' (**$^{Ar'}$M•Zr'**) analogues are worth following up experimentally.

Mainly for the investigation of the hydride exchange process(es), deuteride analogues of the compounds were briefly considered during the experimental studies that form this chapter. Only $[Cp_2ZrD_2]_2$ was accessible, and use of a (90% pure) batch for synthesis of the ^{D}M•**Zr**-d_2 (M = Mg, Zn) complexes led to full scrambling of the deuterides amongst the hydridic positions. Further information on intra- *and inter*molecular exchange processes should come about if the parent deuterides are synthetically accessible with good purity. An Eyring analysis on the kinetics of the main group fragment crossover reaction in Scheme 2.3 should also be able to support this.

It shall also be interesting to abstract a hydride from the ^{Ar}**M•Zr** complexes. If they can survive in an associated state, a free coordination site (presumably on Zr^{+}) will create potential for polymerisation or hydrometallation catalysis.[52-54] Work on the elimination of H_2 to form low-valent M/Zr species is on-going, and is covered in the subsequent chapters.

2.5.1.1 Inert Bond Cleavage (C–F / C–O)

As described in the Introduction, all of the work on ^{Ar}**M•Zr** has stemmed from a single mechanistic experiment relating to precatalyst activation in C–F and C–O activation chemistry. The study will continue to pursue the C–O activation (of benzofuran) with the M^{II} compounds. Although ^{D}**Mg•Zr** failed to react with benzofuran, evidence in Chapter 3 suggests that ^{D}**Zn•Zr** may be more successful as it is a little looser bound. The *in situ* formation of the heterobimetallic compounds (Scheme 2.1a) in the presence of benzofuran will be an interesting comparison to the Al work. Other studies have suggested that formation of reduced species is key to the activation of benzofuran;[44,55] therefore, strategies such as photolytic conditions and hydrogen traps should be conducive.

Work is already successfully underway within the group to extend the substrate scope of the fluoroarene zincation by ^{D}**Zn•Zr**.[41] One interesting observation which was omitted from section 2.4.1 is formation of a bridging hydride-containing intermediate. (The ^{1}H NMR of the

reaction, showing the intermediate, is to be found in the Experimental section, Figure 2.24.) This unknown intermediate is eminently isolable, and may inform the assignment of the mechanism. Kinetic analysis should also be achievable. The reactivities of the main group (hydride) fragments are modulated by their attachment to **Zr**; this will fit into the groups' raft of studies on ^{Ar}*BDI*MH compounds, their mixing with various transition metal fragments, and the reactivity with C–F bonds.

2.6 EXPERIMENTAL

2.6.1 General

All manipulations were carried out using standard Schlenk-line and glovebox techniques under an inert atmosphere of argon or dinitogen. A MBraun Labmaster glovebox was employed, operating at <0.1 ppm O_2 and <0.1 ppm H_2O. Solvents were dried over activated alumina from an SPS (solvent purification system) based upon the Grubbs design and degassed before use. Glassware was dried for 12 h at 120 °C prior to use. Benzene-d_6 and toluene-d_8 were stored over molecular sieves and distilled prior to use. NMR-scale reactions were conducted in J. Young's tap tubes and prepared in a glovebox. All heating mentioned was done using silicone oil baths. ^{1}H, ^{13}C, and ^{19}F NMR spectra were obtained on BRUKER 400 MHz or 500 MHz machines unless otherwise stated. ^{19}F resonances are quoted against the standard $CFCl_3$. All ^{1}H peak intensities are derived against an internal standard peak (^{1}H $\underline{Cp_2}Fe$, δ = 4.00 ppm) with values quoted in ppm. Data was processed using the MestReNova software. Elemental analyses were carried out by Stephen Boyer at London Metropolitan Univeristy.

2.6.1.1 Data Treatment & Equations

Error values were calculated in all situations by use of the regression analysis calculation in Microsoft Excel software. VT NMR data was fitted using line shape analysis (Figure 2.14) with the DNMR program integrated into Topspin v3.1. The hydride resonances of ^{D}**Zn•Zr** were fitted over the 303–353 K range with an initial line broadening factor of 2 Hz.

The Holm-Gutowsky equation was used for estimation of the Gibbs free energy of activation for hydride exchange in the heterobimetallic systems (section 2.3.2.1):

$$\Delta G^{\ddagger}_{298K} = RT_c(23.76 \times \ln\frac{T_c}{k}), \text{ where } k = \frac{\pi\Delta\nu}{\sqrt{2}}$$

and k = the rate of exchange between the hydride peaks (Hz),

T_c = coalescence temperature (K),

R = gas constant (cal K^{-1} mol^{-1}),

and $\Delta\nu$ = maximum separation of hydride peaks (Hz).

2.6.1.2 Materials

The syntheses of the pro-ligand *BDI*H and the series of β-diketiminate-stabilised magnesium,[32] aluminium,[56] zinc,[7] gallium[57] and calcium[58] complexes was achieved using literature procedures. Ferrocene was sublimed before use. Hydrocarbons were dried over

activated 3 Å molecular sieves and freeze-pump-thaw degassed before use. All other chemicals were purchased from Sigma Aldrich and used without purification unless stated.

Zirconocene Dihydride

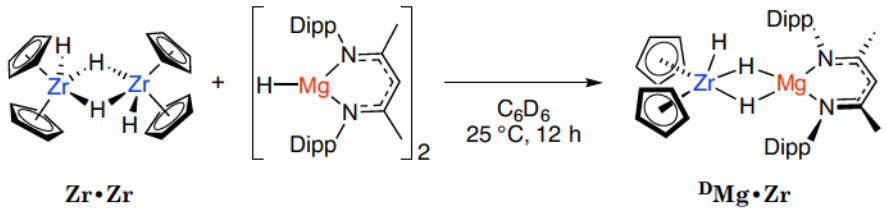
Zirconocene dihydride (**Zr•Zr**) was prepared by the procedure of Wailes and Weigold.[46] For use in the reduction of [{Cp_2ZrCl}$_2$O], $LiAlH_4$ was purified by extraction from THF; 10 grams of grey $LiAlH_4$ (Sigma Aldrich) was slurried in approximately 50 mL of THF. This was followed by filtration and removal of the solvent under reduced pressure. The mixture was heated to 45 °C to remove the last traces of solvent and the colourless solid isolated proved soluble in THF and Et_2O.

With our own preparations of **Zr•Zr**, varying shades of red-pink developed in the reduction step, the shade seemingly dependent on the batch of THF-extracted $LiAlH_4$; $LiAlH_4$ purified by extraction from Et_2O was unsuccessful in the synthesis of **Zr•Zr**. Washed in THF, **Zr•Zr** retains the red-purple colour of its mother liquor. After storage of our **Zr•Zr** for long periods in a N_2 glovebox (several months), the colour was lost. The literature describes the isolated microcrystalline compound as colourless, but related (hydrido)zirconocenes as pink, or turning pink after exposure to light.[46]

The purity of **Zr•Zr** was judged by an NMR tube-scale titration with reaction-grade acetone.[59,60] This method is best for detecting the amount of zirconocene chloride hydride (Schwartz' reagent) in the zirconocene dihydride material. The quantitative information comes in the ratio of the produced mono- and di-*iso*-propoxides, which is read as [$Cp_2Zr(H)Cl$]:[Cp_2ZrH_2]$_2$. The integration of the methyl peaks ([$Cp_2Zr(O^iPr)_2$] δ = 0.99 ppm, 6 H, d, $^3J_{H\text{-}H}$ = 6 Hz; [$Cp_2Zr(O^iPr)Cl$] δ = 1.10 ppm, 12 H, d, $^3J_{H\text{-}H}$ = 6 Hz) showed 1:10 ratio of [$Cp_2Zr(H)Cl$]:[Cp_2ZrH_2]$_2$. A concern in the titration results is the presence of many other trace peaks. The spectrum is dominated by [$Cp_2Zr(O^iPr)_2$] signals, but the unknown trace species deny a quantitative estimate of the overall purity by the acetone method. The efficacy of the technique is limited by the error in pipetting a small amount of acetone, and the detrimental effects that large amounts of **Zr•Zr** can have on NMR signal shimming. **Zr•Zr** shows acceptable elemental analysis results: expected C 53.68%, H 5.43%; found C 53.76%, H, 5.41%.

2.6.2 Synthesis and Characterisation of the Bimetallic Hydride Complexes

2.6.2.1 Preparative-scale Synthesis

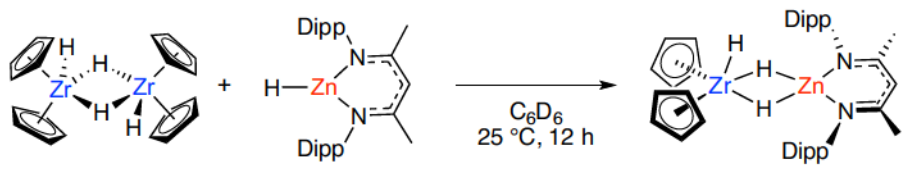


Zr•Zr **^{D}Mg•Zr**

Scheme 2.10. Synthesis of [(Dipp*NCMe*)$_2$CH$_2$]Mg(μ-H)$_2$HZrCp$_2$, *Mg•Zr* (Dipp = 2,6-di-*iso*-propylphenyl)

Synthesis of ^{D}Mg•Zr

In a glovebox, the magnesium(II) hydride (298 mg, 0.336 mmol, 1 equiv.) was added to a 20 mL scintillation vial and dissolved in 15 mL dry toluene. The zirconocene dihydride (150 mg, 0.336 mmol, 1 equiv.) was weighed and added to the flask as a solid. The reaction mixture was stirred for 48 h. The solvent was removed under reduced pressure to give a glassy oil of yellowish hue. Dissolving the crude material in ca. 20 mL of *n*-hexane gave a red-brown solution, which was filtered and concentrated to ca. 5 mL. Storage of this solution a –35 °C resulted in crystallisation of the product **^{D}Mg•Zr** (254 mg, 0.369 mmol, 55%). ^{1}H NMR (400 MHz, 298 K, benzene-d$_6$) δ = 7.12-7.00 (m, 6H, H$_{Aryl}$), 4.99 (s, 10H, Cp$_2$), 4.94 (s, 1H, C$_\beta$), 3.27 (hept, $^{3}J_{H\text{-}H}$ = 6.6 Hz, 4H, C*H*Me$_2$), 1.46 (d, $^{3}J_{H\text{-}H}$ = 6.6 Hz, 6H, CH*Me*$_2$), 1.13 (d, $^{2}J_{H\text{-}H}$ = 6.6 Hz, 6H, CH*Me*$_2$), -1.87 (dd, 1H, $^{2}J_{H\text{-}H}$ = 13.0, 6.6 Hz,), -2.80 (dd, 1H, $^{2}J_{H\text{-}H}$ = 6.6, 6.6 Hz,). ^{13}C NMR (101 MHz, 298 K, benzene-d$_6$) δ = 169.33 (N–C$_\alpha$), 144.66 (C$_{ipso}$), 142.49 (C$_o$), 126.36 (C$_p$), 124.46 (C$_m$), 97.41 (Cp$_2$), 94.90 (C$_\beta$), 28.54 (C$_{i\text{Pr}}$), 24.43 (CH*Me*$_2$), 24.34 (CH*Me*), 23.85 (*Me*); FTIR ν (cm^{-1}): 2959 s, 2868 s, 1551 s, 1523 s, 1436 s, 1403 s, 1317 s, 1261s, 1179 s, 1100 s, 1017 s, 936 s, 855 s, 795 s. Elemental analysis calc. for C$_{39}$H$_{54}$MgN$_2$Zr: C, 70.29%; H, 8.17%; N, 4.20%; found C, 70.11%, H, 8.00%; N, 4.36%

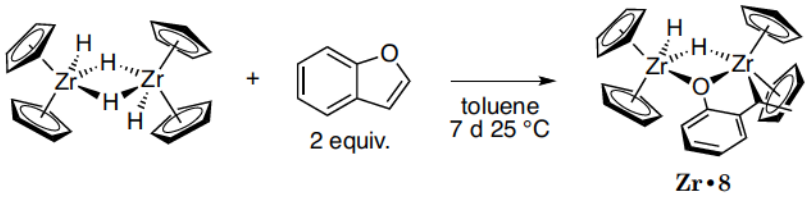


Zr•Zr 2 equiv. **^{D}Zn•Zr**

Scheme 2.11. Synthesis of [(DippNCMe)$_2$CH$_2$]Zn(μ-H)$_2$HZrCp$_2$, **^{D}Zn•Zr** (Dipp = 2,6-di-*iso*-propylphenyl)

Synthesis of <u>^{D}Zn•Zr</u>

In a glovebox, the zinc(II) hydride (325 mg, 0.671 mmol, 2 equiv.) was added to a dry schlenk flask and dissolved in dry toluene to make a 0.056 M solution. The zirconocene dihydride (150 mg, 0.336 mmol, 1 equiv.) weighed and added to the flask as a solid. The reaction mixture was stirred overnight. The reaction mixture acquired a violet-blue colour. The solution was filtered and concentrated to a crude off-white solid. The product was extracted into *n*-hexane, the volume reduced to saturation of concentration, and the desired product was recrystallised from this solution over two days at -35 °C. Large, colourless, cubic crystals of **^{D}Zn•Zr** were obtained (179 mg, 0.253, *38%)*. ^{1}H NMR (400 MHz, 298 K, benzene-d_6) δ 7.12 – 7.09 (m, 6H, H_{Aryl}), 4.95 (s, 1H, H_β), 4.94 (s, 10H, Cp_2), 3.36 (br, 4H, C*H*Me_2), 1.95 – 1.91 (dd, $^{2}J_{H\text{-}H}$ 8.3, 6.3 Hz, 1H, H_t), 1.47 (br, 6H, CH*Me*$_2$), 1.14 (br, 6H, CH*Me*$_2$), -1.08 (d, $^{2}J_{H\text{-}H}$ = 8.3 Hz, 1H, H_μ), -2.06 (d, $^{2}J_{H\text{-}H}$ = 6.3 Hz, 1H, $H_{\mu'}$). ^{13}C NMR (101 MHz, 298 K, benzene-d_6) δ 167.46 (C_α), 146.09 (C_{ipso}), 142.51 (C_o), 126.41 (C_p), 124.52 (C_m), 97.97 (Cp_2), 94.64 (C_β), 28.39 ($C_{i\text{Pr}}$), 24.47 (CH*Me*$_2$), 24.29 (CHMe$_2$), 24.05 (*Me*); FTIR ν (cm^{-1}): 2959 s, 2866 s, 1622 s, 1549 s, 1519 s, 1460 s, 1436 s, 1402 s, 1363 s, 1314 s, 1259 s, 1174 s, 1103 s, 1063 s, 1015 s, 934 s, 792 s. Elemental analysis calc. for $C_{39}H_{54}ZnN_2Zr$: C, 66.21%; H, 7.69%; N, 3.96%; found C, 66.09%, H, 7.49%; N, 3.98%



Zr•8

Scheme 2.12. Synthesis of **Zr•8**

Synthesis of <u>Zr•8</u>

In a glovebox, benzofuran (0.16 g, 1.3 mmol, 2 equiv.) and $[Cp_2ZrH(\mu\text{-}H)]_2$ (0.30 g, 0.67 mmol) were weighed and transferred to a J Young's tap ampoule. Toluene (5 mL) was added, the ampoule was sealed, removed from the glovebox and the reaction mixture stirred for 7 days at 25 °C. The mixture was filtered, and the volume reduced to ca 3 mL. Storage of this solution at -20 °C gave colorless crystals of **Zr•8** (0.064 g , 0.11 mmol, 16 %). ^{1}H NMR (C_6D_6, 400 MHz, 298 K) δ –1.74 (d, 1H, *J* = 12.0 Hz, Zr–H_μ), 1.69 (d, 3H, *J* = 6.8 Hz, *Me*), 2.53 (q, 1H, *J* = 6.8 Hz, C*H*Me), 4.13 (d, 1H, *J* = 12.0 Hz, Zr–H_t), 5.27 (s, 5H, Cp*H*), 5.57 (s, 5H, Cp*H*), 5.62 (s, 5H, Cp*H*), 5.67 (s, 5H, Cp*H*), 6.70–6.72 (m, 1H), 7.05–7.10 (m, 2H), 7.19–7.21. ^{13}C NMR (C_6D_6, 100 MHz, 298 K) δ 19.7, 47.1, 103.6, 105.4, 106.9, 108.3, 114.5, 121.2, 122.9, 123.0, 148.7, 166.4; FTIR ν (cm^{-1}): 2829 s, 1470 s (H_t), 1438 s, 1400 s, 1280 s (H_μ), 1012 s, 802 s, 754 s, Preparation of the deuteride analogues was attempted, but hydrogen atoms are

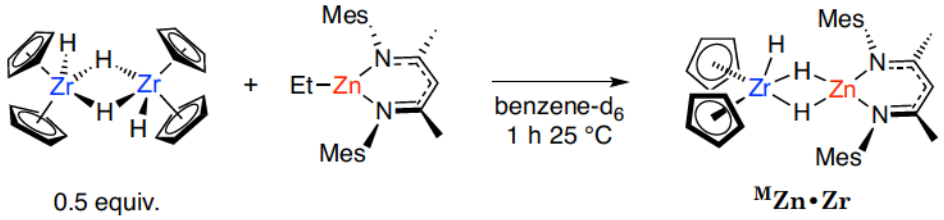
scrambled into the positions to give mixed systems. Due to the sensitivity of the complex repeated attempts to acquire satisfactory CHN analysis failed.

2.6.2.2 NMR-scale Experiments

Unless stated otherwise, NMR-scale experiments with yield calculations were carried out by the following general procedure:

In a glovebox, the starting material (yield-determining reactant) was weighed into a 4 mL scintillation vial. The solid was dissolved in 0.5 mL of benzene-d_6, and ferrocene (ca. 2–3 mg) was added to the solution directly by spatula. This mixture was transferred into a J Young's NMR tube, and a ^{1}H NMR spectrum collected for the yield calculation purposes. The tube was reopened back inside the glovebox, and emptied into another 4 mL scintillation vial containing the required amount of second reactant. The reaction mixture was agitated to homogeneity and pipetted back into the same NMR tube.

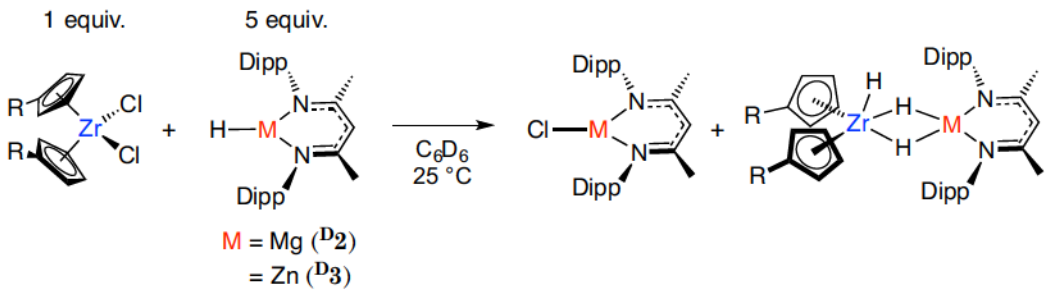
Ethyl Exchange Synthesis of ^{M}*Zn•Zr*



Scheme 2.13. *In situ* synthesis of putative **^{M}Zn•Zr**.

^{Mes}*BDI*ZnEt (20 mg, 0.39 mmol, 1 equiv.) was weighed in a 4 mL scintillation vial and then dissolved in benzene-d_6 (0.5 mL). Zirconocene hydride (9 mg, 0.020 mmol, 0.5 equiv.) was weighed by removal from the bulk stock on to spatula tip. The load on the spatula was then dropped into the J Young's NMR tube. The resealed tube was shaken and the reaction mixture turned from yellow to dark green. The reaction progress was followed by ^{1}H NMR at room temperature. The final mixture was black-green and contained solids.

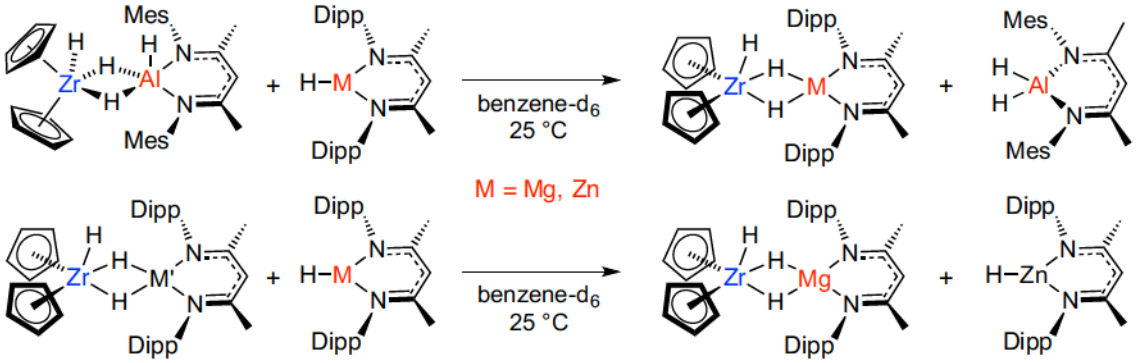
Chloride Exchange Synthesis of ^{Dipp}*BDI*M^{II}H•*Zr*



Scheme 2.14. Ligand exchange synthesis of M^{II}•**Zr** (R = H, Me).

The ligand exchange synthesis of the heterobimetallic hydride complexes (**^{D}Mg•Zr**, **^{D}Zn•Zr**, **^{D}Mg•Zr'** and **^{D}Zn•Zr'**) was adapted from the previous work within the group because of poor solubility of the M^{II} hydrides compared to the alane.[1] In a glovebox, zirconocene dichloride or (1,1'-dimethyl)zirconocene dichloride (0.034 mmol, 1 equiv.) and the main group hydride (0.17 mmol, 5 equiv.) were weighed separately in 4 mL scintillation vials. Benzene-d_6 (0.6 mL) was added to the main group hydride vial and the mixture agitated until all material could be transferred to the zirconocene dihydride vial. The mixture was then transferred as entirely as possible to a J Young's tap NMR tube, via Pasteur pipette.

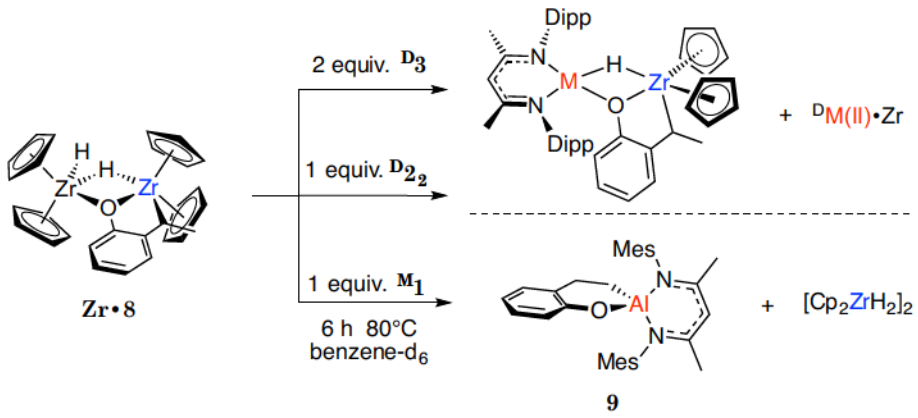
Crossover of the Main Group Hydride Fragment



Scheme 2.15. Substitution of the main group hydride fragment in the heterobimetallic complexes.

In a glovebox, **^{M}Al•Zr** (11 mg, 0.019 mmol, 1 equiv) was used for the displacement experiments with the relevant ^{Dipp}*BDI*M^{II}H complexes: **^{D}2$_2$** (8 mg, 0.009 mmol, 0.5 equiv) and **^{D}3** (9 mg, 0.019 mmol, 1 equiv). Larger amounts were used to reduce the effects of error in the more balanced Mg/Zn experiments (0.5 mL benzene-d_6 solutions). Moreover, the starting mixture and yields were based on the parent hydrides to judge their purity before the reaction: **^{D}2$_2$** 13 mg (0.015 mmol, 0.5 equiv.) and **^{D}3** 14 mg (0.030 mmol, 1 equiv.). **^{D}Mg•Zr** or **^{D}Zn•Zr** were then added: 21 mg, 0.030 mmol, 1 equiv.).

Crossover of the Oxazirconacycle Fragment from Zr•8



Scheme 2.16. Reactions of **Zr•8** with main group parent hydrides.

The same experimental set up was employed for all three Mg, Zn and Al analogues of the experiment (Scheme 2.7 and Scheme 2.9). The yield was calculated based on the starting material **Zr•8** (11 mg, 0.019 mmol, 1 equiv.). The amount of relevant main group hydride complex used was: ^{M}**1** (7 mg, 0.019 mmol), ^{D}**3** (18 mg, 0.038 mmol), and ^{D}**2$_2$** (17 mg, 0.038 mmol). The product **9** was identified in the ^{1}H NMR by the peaks reported in the previously published work of the group.[3] The yield was calculated based on the starting material **Zr•8**. For the reaction in Scheme 2.8, the yield was again based on the same starting solution of **Zr•8**, but ^{D}**Mg•Zr** (14 mg, 0.021 mmol, 1.1 equiv.) was then added in the same way.

Reactions with Fluorinated Benzenes

Benzene-d$_6$ solutions (0.45 mL) of ^{D}**Mg•Zr** (10 mg, 0.015 mmol, 1 equiv). or ^{D}**Zn•Zr** (11 mg, 0.015 mmol, 1 equiv.) were made up in the standard procedure. The large excess of fluorinated benzenes were added by mechanical micropipette: C_6F_5H (17 μL, 0.150 mmol, 10 equiv.), *para*-$C_6F_4H_2$ (17 μL, 0.150 mmol, 10 equiv.). Crystals of [^{Dipp}*BDI*Zn(*p*-C_6F_4H)] were grown by concentration of the reaction mixture, extraction with *ca.* 3 mL hexane, and storage at –35 °C. The crop was only enough for the X-ray diffraction experiment.

For [Cp_2ZrF_2], ^{1}H NMR (benzene-d$_6$): δ = 5.95 (s, 10H, Cp) ppm. ^{19}F NMR checked against a literature report[38] (377 MHz, benzene-d$_6$): δ = +31.0 (s, 2F, ZrF_2) ppm. For [^{Dipp}*BDI*MgF]$_2$ ^{19}F NMR checked against a literature report[61] (377 MHz, benzene-d$_6$): δ = –187.8 (s, MgF) ppm. For **[^{Dipp}*BDI*Zn(*p*-C_6F_4H)]** ^{1}H NMR (benzene-d$_6$): δ = 6.06–5.97 (m, 1H, C_6F_4H), 5.06 (s, 1H, $C_\beta H$), 3.26 (sept., 4H, $^3J_{H\text{-}H}$ = 6.8 Hz, C*H*Me$_2$), 1.67 (s, 6H, N=CMe), 1.26 (d, 12H, $^3J_{H\text{-}H}$ = 6.8 Hz, CH*Me*$_2$), 1.11 (d, 12H, $^3J_{H\text{-}H}$ = 6.8 Hz, CH*Me*$_2$) ppm. ^{19}F NMR (benzene-d$_6$): δ = –116.49— –116.82 (m, 2H, F-2,6), –139.27— –139.63 (m, 2H, F-3,5) ppm. For $C_6F_4H_2$, ^{1}H NMR

(benzene-d_6): δ = 6.12 (qn, 2H, $^3J_{H\text{-}F}$ = 8.7 Hz, $C_{Ar}H$) ppm. ^{19}F NMR (benzene-d_6): δ = –139.49 (t, 4H, $^3J_{H\text{-}F}$ = 8.7, $C_{Ar}F$) ppm.

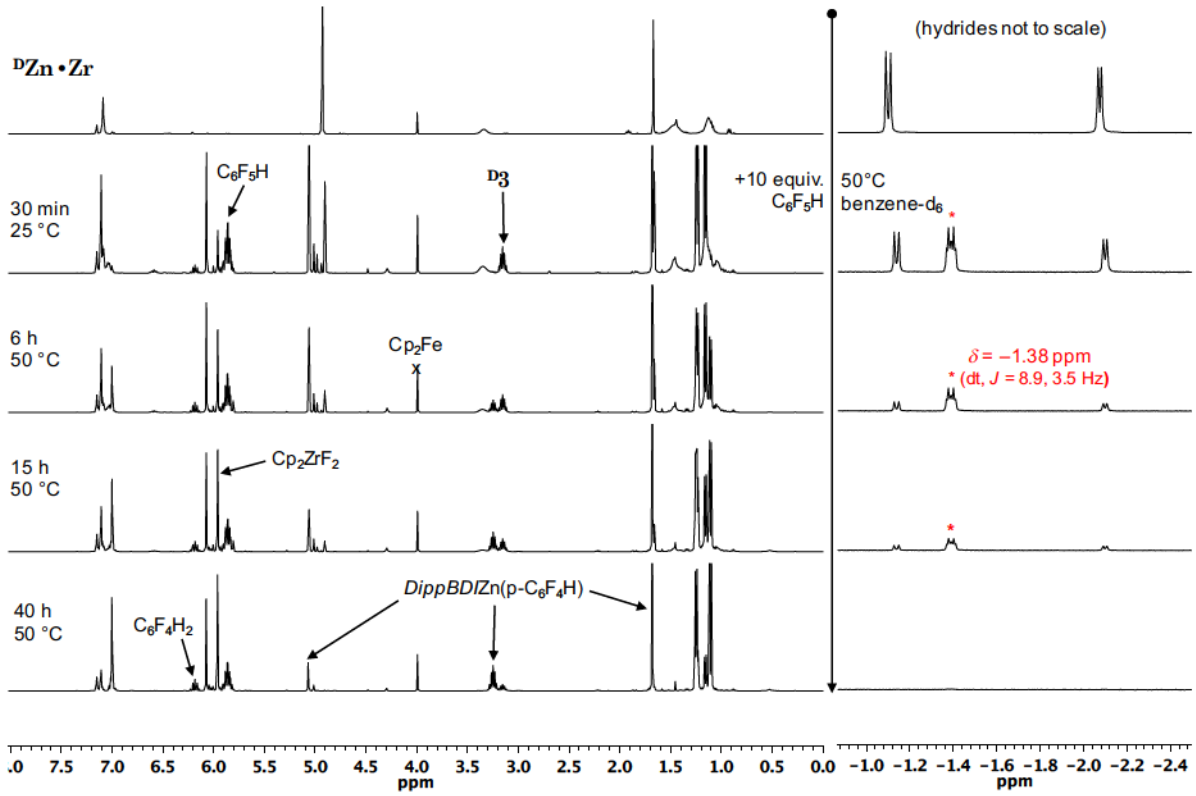
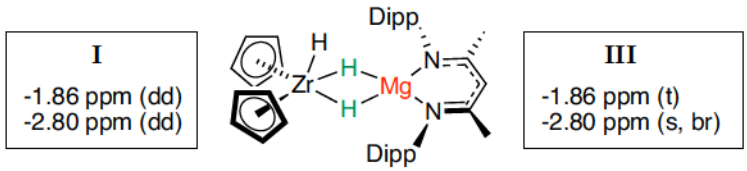


Figure 2.24. A stack plot highlighting an unknown intermediate (δ = –1.38 ppm) in the reaction of ^{D}**Zn•Zr** with 10 equiv. C_6F_5H in benzene-d_6.

Doping of Heterobimetallic Complex Solutions

Addition of *ca.* 1–2 mg of the dopant was made *via* spatula directly to the NMR tube containing the 0.055 mM starting solution (benzene-d_6). The results are summarised in Table 2.5.

Table 2.5. The array of control experiments (room temperature, 1 d) for inducement of ^{1}H NMR peak shape change. ‡Sequential addition of $^{D}\mathbf{2_2}$ and $[Cp_2ZrH_2]_2$ was used as equivalent to addition of **III**



main sample (15 mg)	additive (1 mg)		
	$^{D}\mathbf{2_2}$	$[Cp_2ZrH_2]_2$	**III**(‡)
I	**I**	**I**	**I**
III	**III**	**III**	**III**
$^{D}\mathbf{2_2}$	-	**III**	-
$[Cp_2ZrH_2]_2$	**III**	-	-

2.6.3 X-ray Crystallography

2.6.3.1 Data and Parameters

X-ray Crystal Structure of ^{D}Mg•Zr

$C_{39}H_{54}MgN_2Zr{\cdot}C_7H_8$, M = 758.50, triclinic, P-1 (no. 2), a = 11.03001(18), b = 18.1450(3), c = 22.1419(8) Å, α = 106.340(3), β = 90.840(3), γ = 90.0603(13)°, V = 4251.96(18) Å^3, Z = 4 (two independent molecules), ρ_{calcd} = 1.185 g cm^{-3}, μ(Mo$_{K\alpha}$) = 0.305 mm^{-1}, T = 173 K, yellow blocks, Agilent Xcalibur 3 E diffractometer; 19516 independent measured reflections, F^2 refinement, R_1(obs) = 0.1080, wR_2(all) = 0.3178, 13970 independent observed absorption-corrected reflections [$|F_o| > 4\sigma(|F_o|)$, $2\theta_{max}$ = 58°], 937 parameters. CCDC 1454102.

X-ray Crystal Structure of ^{D}Zn•Zr

$C_{39}H_{54}N_2ZnZr$, M = 707.43, monoclinic, $P2_1/m$ (no. 11), a = 9.0201(4), b = 20.8878(7), c = 19.4369(6) Å, β = 91.350(3)°, V = 3661.1(2) Å^3, Z = 4 (two independent C_S-symmetric molecules), ρ_{calcd} = 1.283 g cm^{-3}, μ(Mo$_{K\alpha}$) = 0.967 mm^{-1}, T = 173 K, colourless tablets, Agilent Xcalibur 3 E diffractometer; 7496 independent measured reflections (R_{int} = 0.0286), F^2 refinement, R_1(obs) = 0.0537, wR_2(all) = 0.1319, 6245 independent observed absorption-corrected reflections [$|F_o| > 4\sigma(|F_o|)$, $2\theta_{max}$ = 57°], 408 parameters. CCDC 1454103.

***X-ray Crystal Structure of* ^{Dipp}BDIZn(o-C_6F_5H)**

$C_{35}H_{42}F_4N_2Zn$, M = 632.07, triclinic, P-1, a = 10.7866(6), b = 11.9826(6), c = 13.6357(6) Å, α = 81.335(4), β = 83.153(4), γ = 70.434(5)°, V = 1637.24(15) Å^3, Z = 2, ρ_{calcd} = 1.282 g cm^{-3}, μ(Mo$_{K\alpha}$) = 0.798 mm^{-1}, T = 173 K, colourless blocks, Agilent Xcalibur 3 E diffractometer; 6447 independent measured reflections (R_{int} = 0.0192), F^2 refinement, R_1(obs) = 0.0411, wR_2(all) = 0.0823, 5306 independent observed absorption-corrected reflections [$|F_o| > 4\sigma(|F_o|)$, $2\theta_{max}$ = 57°], 389 parameters.

***X-ray Crystal Structure of* Zr•8**

$C_{28}H_{30}OZr_2$, M = 643.07, monoclinic, P $2_1/c$, a = 11.9711(3) Å, α = 90°, b = 8.13376(20) Å, β = 92.893(3)°, c = 28.8641(8) Å, γ = 90°, V = 2806.92(13) Å^3, Z = 4, ρ_{calcd} = 1.522 g cm^{-3}, μ(Mo$_{K\alpha}$) = 0.768 mm^{-1}, T = 173 K, pale yellow tablular needles, Agilent Xcalibur 3 E diffractometer; 5629 independent measured reflections (R_{int} = 0.0239), F^2 refinement, R_1(obs) = 0.0355, wR_2(all) = 0.0599, 4890 independent observed absorption-corrected reflections [$|F_o| > 4\sigma(|F_o|)$, $2\theta_{max}$ = 57°], 347 parameters.

2.6.3.2 Additional Comments on the Crystal Structures of the Heterobimetallic Complexes

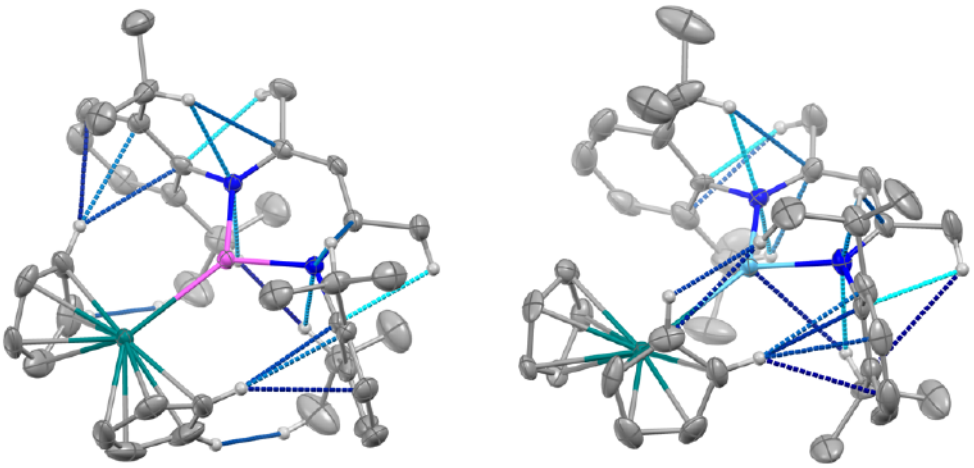


Figure 2.25. Selected intramolecular short contacts (smaller than sum of van der Waals radii) in **^{D}Zn•Zr** (left), **^{D}Mg•Zr** (right). Contacts are colour coded on a long-to-short/cyan-to-dark blue spectrum.

The one-sided **^{D}Mg•Zr** contains a shorter C–H---Ar$_{centroid}$ bond than in **^{D}Zn•Zr** (2.515 compared to 2.614 Å). The conformational freedom of having a remote Cp ligand could allow CH---Ar$_{centroid}$ in **^{D}Mg•Zr** to reach better optimum length. The freed up Cp makes longer intermolecular short contacts with Cp and ^{i}Pr in the crystal lattice. The latter is possibly $C_{Ar}H$---π_{Ar} attraction ($C_{iPr}H$---π_{Cp} = 2.724 Å).

Intramolcular hydrogen bond-type interactions have been asserted previously in Dipp-substituted ketiminate and β-diketiminate ligands, whereby the methanetriyl proton and N atom are involved in a C–H---N short contact.[62-64] The N atom acts as a soft base towards the softly acidic proton. These interactions are apparent in the ^{Dipp}*BDI*M^{II}H•Zr species. The protons sit near the N atoms (*cf*. sum of van der Waals radii[15] = 2.75 Å), and their stooping distorts the tetrahedral geometry of the methanetriyl C$_{i\text{Pr}}$ atom. Only two close contacts of this kind show in **^{X}Al•Zr**, and they are ~0.1–0.2 Å longer than in the four-coordinate main group metal complexes: **^{D}Zn•Zr**, **^{D}Mg•Zr** and ^{Dipp}*BDI*Al(η^1-Cp)R (R = Et, Me).[64]

Perhaps another non-covalent interaction in **^{X}Al•Zr** is that of the terminal aluminium hydride and the methanetriyl protons: Al–H$^{\delta-}$--- $^{\delta+}$H–C$_{i\text{Pr}}$ (2.30, 2.33 Å). An Al–H$^{\delta-}$---$^{\delta+}$H–X "dihydrogen bond" has not been recorded crystallographically,[65] but an Al–H$^{\delta-}$---$^{\delta+}$H–C interaction has been seen in a computed intermediate.[66] The near linear arrangement of H$^{\delta-}$---$^{\delta+}$H–C$_{i\text{Pr}}$ (156.1°) fits the requirement for directionality in these special hydrogen bonds.[65]

2.6.4 DFT Studies

Calculations were conducted in Gaussian09. All minima were confirmed by frequency calculations and solid-state data were used as an input for the atom coordinates. NBO calculations were run using NBO v5.9 within g09. A series of functionals (B3LYP, M-062x, ωB97x, ωB97xD) and basis-sets (6,311G / 6,31G / LanL2DZ / SDD) were investigated. In all cases the geometries were compared against the solid-state data. An ωB97xD functional and hybrid basis set 6,311G (C/H/N) and SDD (Al/Zn/Mg/Zr) were employed. Transition states were confirmed by intrinsic reaction coordinate calculations and a single negative frequency vibration appearing in the results of frequency calculations.

2.6.4.1 Calculated Structures

Some reference structures were been subjected to an NBO analysis, in order to make a comparison between the binding modes in them and the structures in Figure 2.5, and how the method quantifies donor-acceptor bonding.

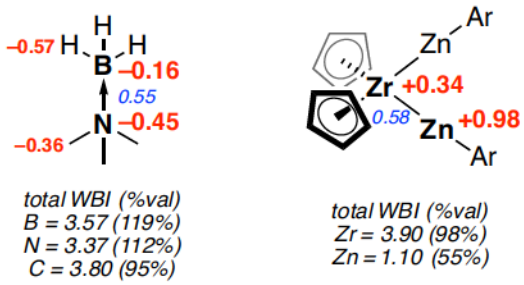


Figure 2.26. NPA charges and Wiberg bond indices (WBI) for the heteroatom-heteroatom bonds in borane trimethylamine and a structure reported by Robinson *et al.*[8] (ωB97xD functional and hybrid 6,311G/SDD basis set).

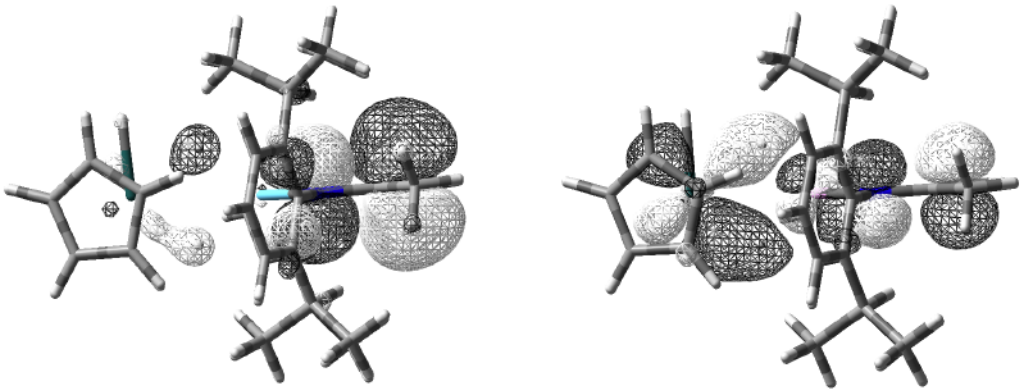


Figure 2.27. Calculated HOMO of ^{D}**Mg•Zr** (left) and ^{D}**Zn•Zr** (right).

2.7 REFERENCES

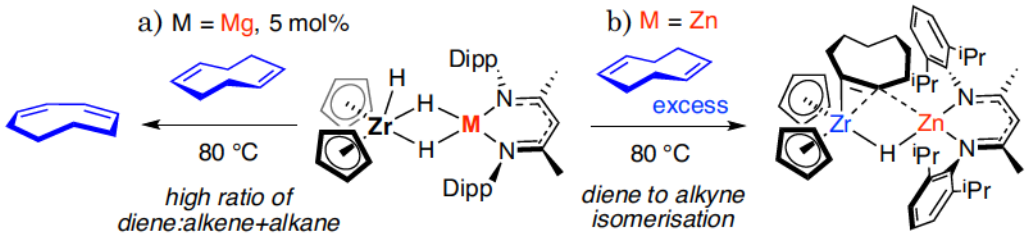
1 S. Yow, S. J. Gates, A. J. P. White and M. R. Crimmin, *Angew. Chem., Int. Ed.*, 2012, **51**, 12559–12563.
2 M. J. Butler and M. R. Crimmin, *unpublished results*, 2014.
3 S. Yow, A. J. P. White, A. E. Nako, L. Neveu and M. R. Crimmin, *Organometallics*, 2013, **32**, 5260–5262.
4 A. A. Yaroshevsky, *Geochem. Int.*, 2006, **44**, 48–55.
5 M. S. Hill, D. J. Liptrot and C. Weetman, *Chem. Soc. Rev.*, 2016, **45**, 972–988.
6 S. P. Green, C. J. Jones and A. Stasch, *Angew. Chem., Int. Ed.*, 2008, **47**, 9079–9083.
7 J. Spielmann, D. Piesik, B. Wittkamp, G. Jansen and S. Harder, *Chem. Commun.*, 2009, 3455–3456.
8 Y. Wang, B. Quillian, C. S. Wannere, P. Wei, P. V. R. Schleyer and G. H. Robinson, *Organometallics*, 2007, **26**, 3054–3056.
9 B. Cordero, V. Gómez, A. E. Platero-Prats, M. Revés, J. Echeverría, E. Cremades, F. Barragán and S. Alvarez, *Dalton Trans.*, 2008, 2832–2838.
10 H. Lee, T. Hascall, P. J. Desrosiers and G. Parkin, *J. Am. Chem. Soc.*, 1998, **120**, 5830–5831.
11 M. Horacek, P. Štěpnička, J. Kubišta, K. Fejfarová, R. Gyepes and K. Mach, *Organometallics*, 2003, **22**, 861–869.
12 G. Bender, T. Wiegand, H. Eckert, R. Fröhlich, C. G. Daniliuc, C. Mück-Lichtenfeld, S. Ndambuki, T. Ziegler, G. Kehr and G. Erker, *Angew. Chem., Int. Ed.*, 2012, **51**, 8846–8849.
13 C. J. Ballhausen and J. P. Dahl, *Acta Chem. Scand. B*, 1961, **15**, 1333–1336.
14 A. W. Addison, T. N. Rao, J. Reedijk, J. van Rijn and G. C. Verschoor, 1984, 1349–1356.
15 A. Bondi, *J. Phys. Chem.*, 1964, **68**, 441–451.
16 S. Harder, *Chem. Eur. J.*, 1999, **5**, 1852–1861.
17 S. Szumacher, I. D. Madura, J. Zachara and A. R. Kunicki, *J. Organomet. Chem.*, 2005, **690**, 1125–1132.
18 O. Takahashi, Y. Kohno and M. Nishio, *Chem. Rev.*, 2010, **110**, 6049–6076.
19 M. Nishio, Y. Umezawa, K. Honda, S. Tsuboyama and H. Suezawa, *CrystEngComm*, 2009, **11**, 1757–32.
20 D. Quiñonero, P. M. Deyà, M. P. Carranza, A. M. Rodríguez, F. A. Jalón and B. R. Manzano, *Dalton Trans.*, 2010, **39**, 794–806.
21 J.-D. Guo, D. J. Liptrot, S. Nagase and P. P. Power, *Chem. Sci.*, 2015, **6**, 6235–6244.
22 M. Yamakawa and I. Yamada, *Angew. Chem., Int. Ed.*, 2001, **40**, 2818–2821.
23 K. B. Wiberg, *Tetrahedron*, 1968, **24**, 1083–1096.
24 P. Cui, T. P. Spaniol, L. Maron and J. Okuda, *Chem. Commun.*, 2014, **50**, 424–426.
25 Y. Zeng, H. Feng, Y. Xie, R. B. King and H. F. Schaefer III, *Eur. J. Inorg. Chem.*, 2013, 2070–2077.
26 K. Nijesh, S. De and P. Parameswaran, *Dalton Trans.*, 2016, **45**, 7836–7846.
27 L. K. Harper, A. L. Shoaf and C. A. Bayse, *ChemPhysChem*, 2015, **16**, 3886–3892.
28 D. G. Hamilton and R. H. Crabtree, *J. Am. Chem. Soc.*, 1988, **110**, 4126–4133.
29 I. M. Riddlestone, J. A. B. Abdalla and S. Aldridge, *Adv. Organomet. Chem.*, 2015, **63**, 1–38.
30 X. Chen, S. Liu, C. E. Plečnik, F.-C. Liu, G. Fraenkel and S. G. Shore, *Organometallics*, 2003, **22**, 275–283.
31 F.-C. Liu, J. Liu, E. A. Meyers and S. G. Shore, *Inorg. Chem.*, 1998, **37**, 3293–3300.
32 S. J. Bonyhady, C. J. Jones, S. Nembenna, A. Stasch, A. J. Edwards and G. J. McIntyre, *Chem. Eur. J.*, 2010, **16**, 938–955.
33 S. J. Bonyhady, D. Collis, G. Frenking, N. Holzmann, C. J. Jones and A. Stasch, *Nat. Chem.*, 2010, **2**, 865–869.

34 F.-C. Liu, G. Fraenkel, A. Chow and S. G. Shore, *Magn. Reson. Chem.*, 1998, **36**, 145–150.
35 W. Chen, C. Bakewell and M. R. Crimmin, *Synthesis*, 2017, **49**, 810–821.
36 A. J. P. White, M. R. Crimmin, O. Ekkert, S. D. A. Strudley and A. Rozenfeld, *Organometallics*, 2014, **33**, 7027–2030.
37 C. Bakewell, A. J. P. White and M. R. Crimmin, *J. Am. Chem. Soc.*, 2016, **138**, 12763–12766.
38 B. L. Edelbach, A. K. F. Rahman, A. K. Fazlur Rahman, R. J. Lachicotte and W. D. Jones, *Organometallics*, 1999, **18**, 3170–3177.
39 U. Jäger-Fiedler, U. Jaeger-Fiedler, P. Arndt, U. Rosenthal, M. Klahn, A. Spannenberg, W. Baumann and V. V. Burlakov, *J. Mol. Catal. A: Chem.*, 2007, **261**, 184–189.
40 M. R. Crimmin and O. Ekkert, *unpublished results*, 2017.
41 M. R. Crimmin and M. G. Padilla, *unpublished results*, 2017.
42 W. D. Jones, *Dalton Trans.*, 2003, 3991–3995.
43 B. M. Kraft and W. D. Jones, *J. Organomet. Chem.*, 2002, **658**, 132–140.
44 M. R. Crimmin, M. J. Butler and A. J. P. White, *Chem. Commun.*, 2015, **51**, 15994–15996.
45 F.-C. Liu, J. Liu, E. A. Meyers and S. G. Shore, *Inorg. Chem.*, 1999, **38**, 2169–2173.
46 P. C. Wailes and H. Weigold, *J. Organomet. Chem.*, 1970, **24**, 405–411.
47 B. Kautzner, P. C. Wailes and H. Weigold, *J. Chem. Soc., Chem. Commun.*, 1969, 1105–1105.
48 F. P. Gabbaï, P. J. Chirik, D. E. Fogg, K. Meyer, D. J. Mindiola, L. L. Schafer and S.-L. You, *Organometallics*, 2016, **35**, 3255–3256.
49 C. E. Kefalidis, C. J. Jones and L. Maron, *Dalton Trans.*, 2016, **45**, 14789–14800.
50 A. J. Boutland, I. Pernik, A. Stasch and C. J. Jones, *Chem. Eur. J.*, 2015, **21**, 15749–15758.
51 L. Maron, A. Stasch, R. Lalrempuia, C. E. Kefalidis, S. J. Bonyhady, S. J. Bonyhady, B. Schwarze and C. J. Jones, *J. Am. Chem. Soc.*, 2015, **137**, 8944–8947.
52 R. González-Hernández, J. Chai, C. Jianfang, R. Charles, O. Pérez-Camacho, S. Kniajanski and S. Collins, *Organometallics*, 2006, **25**, 5366–5373.
53 S. M. Baldwin, J. E. Bercaw and H.-H. Brintzinger, *J. Am. Chem. Soc.*, 2010, **132**, 13969–13971.
54 C. Schädle and R. Anwander, *Eur. J. Inorg. Chem.*, 2013, 3302–3306.
55 T. Chu, G. I. Nikonov, Y. Boyko and I. Korobkov, *Organometallics*, 2015, **34**, 5363–5365.
56 A. E. Nako, S. J. Gates, A. J. P. White and M. R. Crimmin, *Dalton Trans.*, 2013, **42**, 15199–15206.
57 S. Singh, H.-J. Ahn, A. Stasch, V. Jancik, H. W. Roesky, A. Pal, M. Biadene, R. Herbst-irmer, M. Noltemeyer and H.-G. Schmidt, *Inorg. Chem.*, 2006, **45**, 1853–1860.
58 S. Harder and J. Brettar, *Angew. Chem., Int. Ed.*, 2006, **45**, 3474–3478.
59 D. B. Carr and J. Schwartz, *J. Am. Chem. Soc.*, 1979, **101**, 3521–3531.
60 J. Schwartz, K. I. Gell, B. Posin and G. M. Williams, *J. Am. Chem. Soc.*, 1982, **104**, 1846–1855.
61 H. Hao, M. Noltemeyer, H. W. Roesky, Y. Ding, C. Cui, M. Schormann, H.-G. Schmidt and B. Žemva, *J. Fluorine Chem.*, 2002, **115**, 143–147.
62 M. Stender, R. J. Wright, B. E. Eichler, J. Prust, M. M. Olmstead, H. W. Roesky and P. P. Power, *J. Chem. Soc., Dalton Trans.*, 2001, 3465–3469.
63 I. D. Madura, J. Zachara, K. Leszczyńska and A. R. Kunicki, *J. Mol. Struct.*, 2010, **968**, 93–98.
64 K. Leszczyńska, I. D. Madura, A. R. Kunicki, J. Zachara and M. Łoś, *J. Organomet. Chem.*, 2007, **692**, 3907–3913.
65 N. V. Belkova, L. M. Epstein, O. A. Filippov and E. S. Shubina, *Chem. Rev.*, 2016, **116**, 8545–8587.
66 G. Tan, T. Szilvási, S. Inoue, B. Blom and M. Driess, *J. Am. Chem. Soc.*, 2014, **136**, 9732–9742.

"Seeking what is true is not seeking what is desirable."

Albert Camus, *The Myth of Sisyphus*

CHAPTER 3 – Isomerisation of Cyclooctadiene to Cyclooctyne with a Zinc/Zirconium Heterobimetallic Complex



Reaction of the zinc/zirconium heterobimetallic complex **^{D}Zn•Zr** *with cycloocta-1,5-diene (1,5-COD) results in slow isomerisation to cycloocta-1,3-diene (1,3-COD), along with the formation of a new complex that includes a cyclooctyne ligand bridging two metal centres. While analogous Mg/Zr and Al/Zr heterobimetallic complexes are competent for the catalytic isomerisation of 1,5-COD to 1,3-COD, only in the case of the zinc species is the trapped cyclooctyne observed.*

The favourable binding of cyclooctyne to bridge Zr and Zn provides a thermodynamic driving force for the otherwise contrathermodynamic isomerisation. It is shown that this driving force is not unique to the Zn case, and therefore that the mechanism of the reaction is the origin of the Zn/Zr complex's unique capacity for the reaction. Kinetic analysis of the mechanism shows a dissociative rate-limiting step with a 0^{th}-order dependence on diene concentration and 1^{st}-order dependence on **^{D}Zn•Zr**. *Experimental controls suggest this step to be the dissociation of $\{Cp_2ZrH_2\}$ and Zn hydride fragments. The step is seemingly unattainable with* **^{D}Mg•Zr** *– an observation which is ascribed to the greater integrity of its μ-hydrido linkage. Initial DFT mechanistic studies serve to elucidate a π-allyl mechanism of $\{Cp_2Zr^{II}\}$ chain walking along the diene moiety, including rare sp^2-β-hydride elimination. It is proposed that an alkyne Zr complex formed during this process is trapped by the spectator zinc hydride fragment.*

Parts of this chapter have been published:

M. J. Butler, A. J. P. White and M. R. Crimmin, *Angew. Chem., Int. Ed.*, 2016, **55**, 6951–6953.

3.1 INTRODUCTION

3.1.1 Alkynes and Dienes in Isomerisation

3.1.1.1 Background

Despite decades of research into alkene isomerisation,[1] the conversion of dienes into alkynes has, to the best of our knowledge, limited experimental support.[2,3] A related reaction, alkene-to-alkyne dehydrogenation, has only limited precedent.[4,5] The paucity of examples can be explained by considering the thermodynamics of isomerisation. From gas-phase calorimetry measurements, the $\Delta H_f°$ values for 1,3-butadiene and 2-butyne are 26.7 ± 0.2 and 34.7 ± 0.2 kcal mol^{-1} respectively.[6] Diene-to-alkyne isomerisation becomes increasingly unfavourable within small or medium carbocycles; alkyne and allene species would be expected to incorporate significant ring strain.[7,8] Calculations of the relative stabilities for C_8H_{12} rings are shown in Figure 3.1. The theoretical values are consistent with experimental thermochemical data from Taskinen and Nummelin.[9] For example, 1,5- and 1,3-COD are separated by 5 kcal mol^{-1} according to both experiment and calculation.

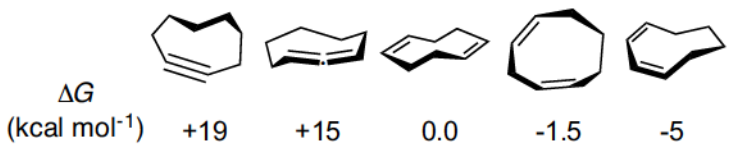


Figure 3.1. Relative Gibbs free energies (298.15 K) of isomers of C_8H_{12} (B3LYP functional and 6-311G basis set).

Consistent with these data, the microscopic reverse reaction, alkyne-to-diene isomerisation, can be catalysed by rhodium/BINAP,[10,11] ruthenium hydride,[12,13] or gold(I) complexes.[14] An organomagnesium complex has recently been employed as a catalyst for the isomerisation of terminal alkynes to allenes and internal alkynes.[15] Cyclooctyne complexes of Pt[16] and Mn[17] are prone to rearrangement into 1,3- and 1,2-diene (allene) complexes respectively. Relevant to our own studies, group 4 complexes (in combination with magnesium reducing agents) have some pedigree in alkene isomerisation. Rosenthal and co-workers have used group 4 metallocene alkyne complexes[18] to catalyse the isomerisation of linear and cyclic dienes.[19] Studies by Qian *et al.* have effected 1,3- to 1,5-COD isomerisation both with $[Cp_2TiCl_2]/Mg_{(s)}$ and with $[Cp_2TiCl_2]$/Grignard pre-catalyst mixtures.[20] Mechanistic assignments in this area must be cautious. As has been discussed in Chapter 1, both Grignard and $Mg_{(s)}$ reductions of $[Cp_2MCl_2]$ may yield unexpected M^{III} hydrides as well as $\{Cp_2M^{II}\}$. The absence or presence of a hydride ligand in the active species may distinguish between two prevalent mechanisms.

3.1.1.2 Mechanisms of Alkyne/Diene Isomerisation

Alkyne/diene isomerisation is perhaps unappreciated in the wider field of a specific case of alkene isomerisation, being without explicit consideration in review articles. For mono-alkene isomerisation there are two prevalent mechanisms for the movement of a C=C bond along a carbon chain.[21] Both mechanisms involve rotation of M–C bonds in intermediates, which acts as the selection event in the generation of the isomers. For metal centres in possession of a hydride ligand ([M]–H), reversible insertion-elimination of the C=C bond is most common.

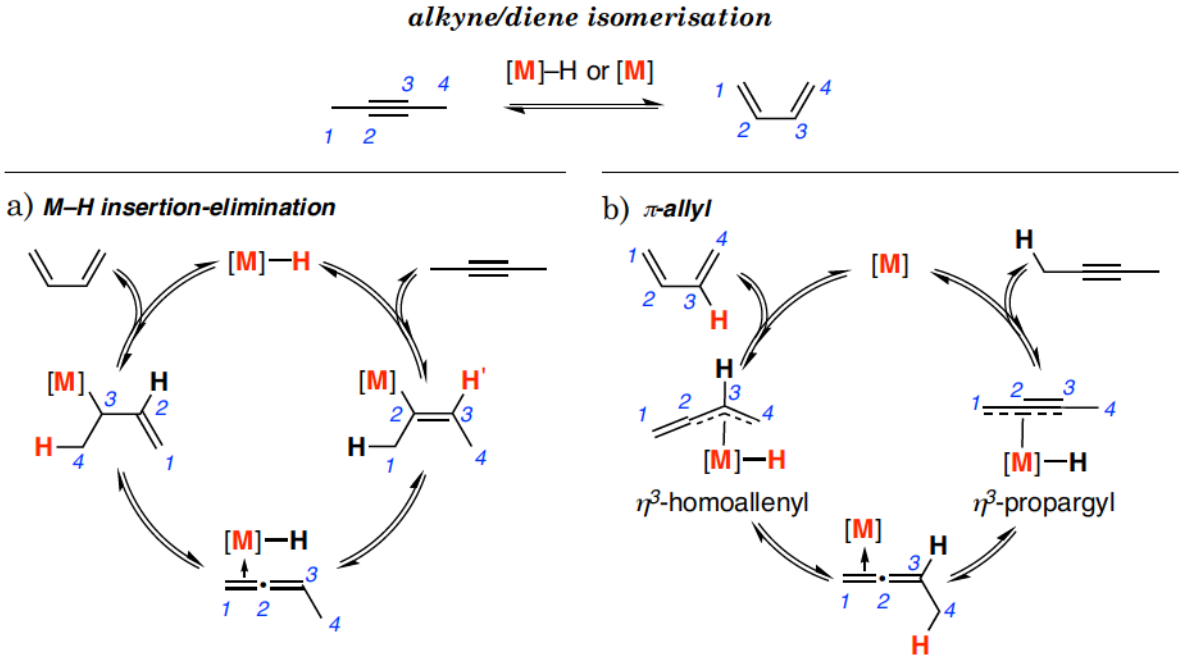


Figure 3.2. The two general mechanisms of alkene isomerisation in the context of alkyne/diene isomerisation by a metal centre, [M].

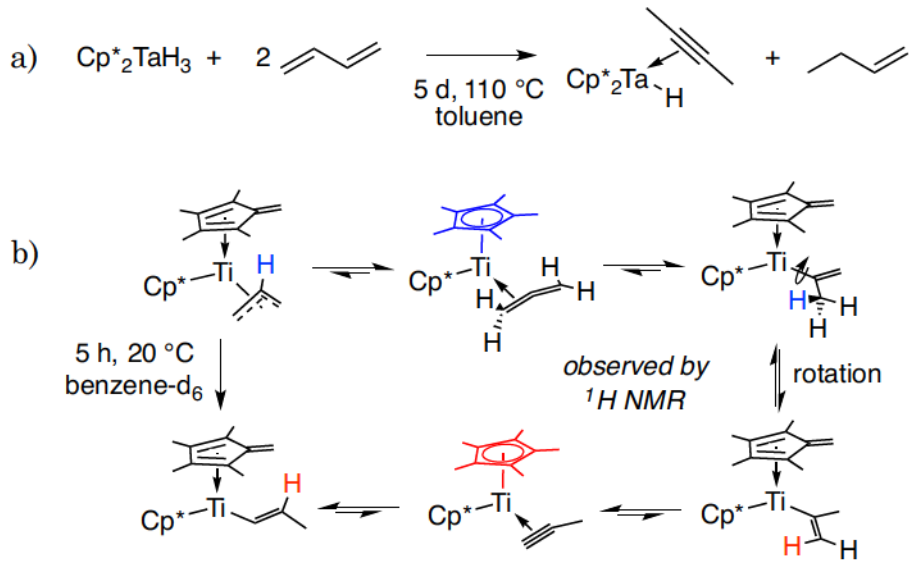
The general mechanism is easily adapted for alkyne/diene isomerisation (Figure 3.2a, M–H insertion-elimination mechanism): it has long been proposed for ruthenium hydride examples of alkyne-to-diene isomerisation.[12] The carbon-carbon multiple bond is hydrometallated, and subsequently β-hydride elimination may occur from two alternative positions to give the diene isomers. The hydrogen atoms are intermolecularly exchanged to facilitate the shuttling of the unsaturation (as shown in Figure 3.2a by the red H atoms). Catalytic turnover is possible upon the reformation of the metal hydride complex.

For alkene isomerisation by metal catalysts *without* a hydride ligand, the π-allyl mechanism is the main mechanistic alternative. After alkene complexation to [M], an allyl C–H bond is oxidatively added across the metal centre, and the metal centre gains a π-allyl and a hydride ligand. Reductive elimination of these ligands may give different alkene isomers, depending

on which C-position of the π-allyl moiety receives the H atom. Overall, this is an intramolecular migration of the hydrocarbon's protons. It is a similarly well-known mechanism,[21] and it has been proposed for some of the aforementioned examples of cyclodiene isomerisation.

In Figure 3.2b, the π-allyl mechanism has been represented within alkyne/diene isomerisation. Accordingly, the allyl intermediate must become the more exotic propargyl and homoallenyl species. It is at these intermediates that η^3-η^1 slippage allows for an M–C bond around which rotation can occur. Thus occurs the selection event in the alkyne/diene isomerisation. The resting hapticity of propargyl intermediates is metal- and ligand-dependent:[22] an η^3-propargyl intermediate is viable,[23-25] but a favouring of η^1-propargyl ligand is also possible.[26,27] NMR studies have suggested a zirconocene preference for an η^3-propargyl complex (rather than an η^1-allenic form) in one instance.[28] A metal π-homoallenyl complex (Figure 3.2b) is exceptionally rare, but has been reported as an *exo*-alkylidene-η^3-allyl ligand of Re by Casey and co-workers.[29] Again, an η^1-isomer is theoretically possible, and perhaps more likely because of the constraints of C=C coordination imposed by the orthogonality of the allenic π-bonds. It has been shown that the allene adduct may be too stable to allow the full reaction or catalytic turnover.[30] A related non-redox version of the allyl mechanism has been proposed for the gold(I) alkyne-to-diene catalysis mentioned above; it involves anchimeric assistance by a pendant amine, deprotonating the coordinated alkyne at the propargyl position.[14]

The single example of *diene-to-alkyne* isomerisation is stoichiometrically effected by [Cp*$_2$TaH$_3$] and produces an alkyne ligand bound to {Cp*$_2$TaH}.[2] The reaction involves two equivalents of buta-1,3-diene, one of which is hydrogenated by the metal complex to give but-1-ene, and the other converted to the Ta^{III} hydride species (Scheme 3.1a). Presumably, the alkyne adduct is preferred over alkene or allene analogues for its stronger stabilisation of the Ta centre. Through the authors' preparation of the hydrido intermediates, they deduced the insertion-elimination mechanism – the anti-clockwise reaction in Figure 3.2a. However, no alkyl intermediates were isolated and no isotope labelling experiments were made, so the mechanistic assignment is incomplete. Brinkmann *et al.* published a {Cp*$_2$Ti} study seven years afterwards: isomerisation of an η^3-allyl to an η^1-1-propenyl ligand (Scheme 3.1b) was revealed to proceed *via* an allene and then a propyne complex.[31] The mechanism in Figure 3.2b was implied by these species and the two other intermediates characterised *in situ*. Titanium is in the +3 oxidation state throughout. The metal redox is replaced by involvement of the redox-active fulvene/cyclopentadiene ligand.



Scheme 3.1. a) The diene-to-alkyne isomerisation reported by Gibson, Parkin and Bercaw. b) Brinkmann *et al.*'s isomerisation of an η^3-allyl ligand.

3.1.1.3 Aims

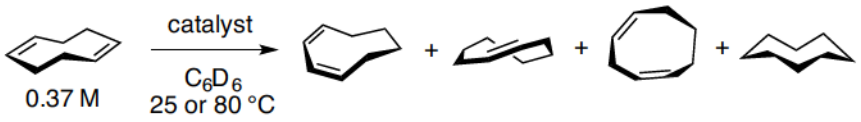
Herein, we show that the isomerisation of cyclooctadienes to cyclooctyne is possible within the coordination sphere of ^{D}**Zn•Zr**. Catalytic diene isomerisation is achieved with ^{D}**Mg•Zr**, ^{M}**Al•Zr**, and **Zr•Zr**. Primarily, the interest lies in the reason for the 'heterobimetallic effect': the exclusivity of the transformation to ^{D}**Zn•Zr** and not its Mg and Al counterparts. With this in mind the ground state structure of the octyne product has been analysed in juxtaposition with the starting materials. Subsequently, control, kinetic and theoretical experiments have allowed discussion of the reaction mechanism with regards to Figure 3.2 and Scheme 3.1.

3.2 RESULTS

3.2.1 Cyclooctadiene Isomerisation Reactions

The related bimetallic complexes ^{D}**Mg•Zr**, ^{M}**Al•Zr**, and **Zr•Zr** consistently give mixtures of 1,3-COD, cyclooctene, and cyclooctane from 1,5-COD. A summary of the results for the catalysis is shown in Table 3.1. The Mg congener simply catalyses the expected isomerisation of the diene over 3 d at 80°C. Whilst a large amount of ^{D}**Mg•Zr** survives the process and is detectable in the product mixture, this was not the case for ^{M}**Al•Zr** or simply **Zr•Zr**. Both complexes catalyse the isomerisation, but neither complex survives the first minutes of reaction time. Trace amounts of 1,4-COD and cyclooctane were observed in all cases.

Table 3.1. Results of catalyst comparison experiments with catalysts ^{D}**Mg•Zr**, ^{M}**Al•Zr**, and **Zr•Zr**.



0.37 M

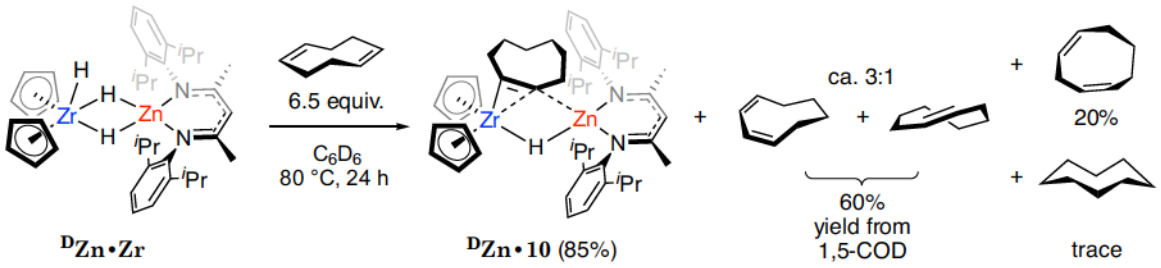
catalyst	*loading (mol%)*	*temp. (°C)*	*time (h)*	*combined yield (%)*	*1,3-COD :COE*[a]	*catalyst remains (%)*
^{D}**Mg•Zr**	5	80	9	70	20:1	60
^{M}**Al•Zr**	5	25	1	>95[b]	11:1[b]	0
Zr•Zr	1	25	48	35	10:1	0
	1	25	122	80	27:1	0

[a] The ratio is an estimate based on the relative peak heights of each product in the 2.15–2.03 ppm window. [b] Over 1 h at 25 °C, the yield diminished (240 h, 75 %) and a trace of octane was observed.

There is a very high overall yield of the catalysis using ^{M}**Al•Zr**, and the conditions are facile. However, it seems that the consumption of the pre-catalyst leads to larger amounts of cyclooctadiene hydrogenation. **Zr•Zr** does not suffer from this problem when 0.5 mol% of the complex is deployed. The Mg compound manages a good overall yield with low levels of hydrogenated product. At lower loadings, catalysis with ^{D}**Mg•Zr** shuts down. Repeated and portionwise addition of the substrate to a ^{D}**Mg•Zr** catalytic run (at 50 °C) found an upper estimate of *TON* to be 70. For comparison, the *TON* for **Zr•Zr** at 1 mol% loading and 25 °C is in excess of 100. Isomerisation using the Mg catalyst is not inhibited by presence of excess trimethylphosphine.

The reaction of ^{D}**Zn•Zr** with 1,5-COD in benzene-d_6 at 80 °C resulted in more than 50% conversion of the hydrocarbon within 24 h and formation of 1,3-COD, 1,4-COD and

cyclooctene (a sum total of 80% yield based on 1,5-COD), the heterobimetallic complex **^{D}Zn•10** (85% based on **^{D}Zn•Zr**), and trace cyclooctane (Scheme 3.2).



^{D}Zn•Zr ^{D}Zn•10 (85%)

Scheme 3.2. Isomerisation of 1,5-cyclooctadiene with **^{D}Zn•Zr**.

Over the course of the reaction, the hydride resonances of **^{D}Zn•Zr** observed at δ = –1.09 (d, $^{2}J_{H\text{-}H}$=8.3 Hz), –2.07 (d, $^{2}J_{H\text{-}H}$ = 6.3 Hz) and 1.80 (dd, $^{2}J_{H\text{-}H}$ = 8.3, 6.3 Hz) ppm slowly decreased in intensity and were replaced by a new resonance at δ = –1.22 (s) ppm. The protons adjacent to the unsaturated carbon–carbon bond in **^{D}Zn•10** are observed as a series of overlapping multiplets at δ = 3.13–3.18 ppm, while the ^{13}C NMR resonances of the alkyne appear at δ = 111.9 and 184.3 ppm for C_{μ} and C_{α} respectively. These shifts are in general agreement with precedents (which were discussed in Chapter 1).[32-35] For further comparison, the monometallic cyclohexyne adduct, [$Cp_2Zr(\eta^2$-$C_6H_8)$•PMe_3], has ^{13}C NMR resonances at δ = 150.0 and 181.6 ppm for the C≡C atoms.[36] An analogous phosphine adduct was not identified by ^{1}H or ^{31}P NMR spectroscopy when the reaction in Scheme 3.2 was run with only 1.5 equiv. of cyclooctadiene and in the presence of 5 equiv. trimethylphosphine. **^{D}Zn•Zr** was observed throughout. A pure sample of complex **^{D}Zn•10** catalyses the isomerisation of 1,5-COD to 1,3-COD at 5 mol % loading and 80 °C. The reaction is albeit extremely slow, taking a period of 4 weeks, and no **^{D}Zn•Zr** is observed.

Table 3.2. Results of 1,5-COD isomerisation with **^{D}Zn•10** as catalyst.

catalyst	*loading (mol%)*	*temp. (°C)*	*time (h)*	*combined yield (%)*	*1,3-COD :COE*[a]	*^{R}BDI•Zr remains (%)*
^{D}Zn•10	5	80	730	85	20:1	65

[a] The ratio is an estimate based on the relative peak heights of each product in the 2.15–2.03 ppm window.

3.2.2 Structural Analysis of the Cyclooctyne Adduct

Consideration of the Dewar-Chatt-Duncanson model for the binding of alkenes or alkynes to group 4 metals with a d^2 electron configuration leads to two extreme bonding pictures: a Zr^{II} adduct or a Zr^{IV} three-membered metallacycle. Group 4 metallocene precedents are

commonly deemed to be the latter; ethylene complexes of Ti and Zr metallocenes exhibit considerable dπ–π^* back-donation and have been formulated as metallacyclopropane complexes.[37,38] The C–C multiple bond in Buchwald *et al.*'s cyclohexyne adduct [$Cp_2Zr(\eta^2$-$C_6H_8)$•PMe_3] was judged to be indicative of a metallacyclopropene moiety.[36]

Two extreme, and simplified, bonding pictures can be built for **^{D}Zn•10** (Figure 3.3): a cyclooctyne Zr^{II} complex (**A**) and Zr^{IV} dimetallabicyclic complexes (**B** and **C**). After an extensive experimental survey of Zr/Al-bridging alkynes analogous to **^{D}Zn•10**, Erker and co-workers posited the dominance of **B** (and related descriptions) for the motif.[33]

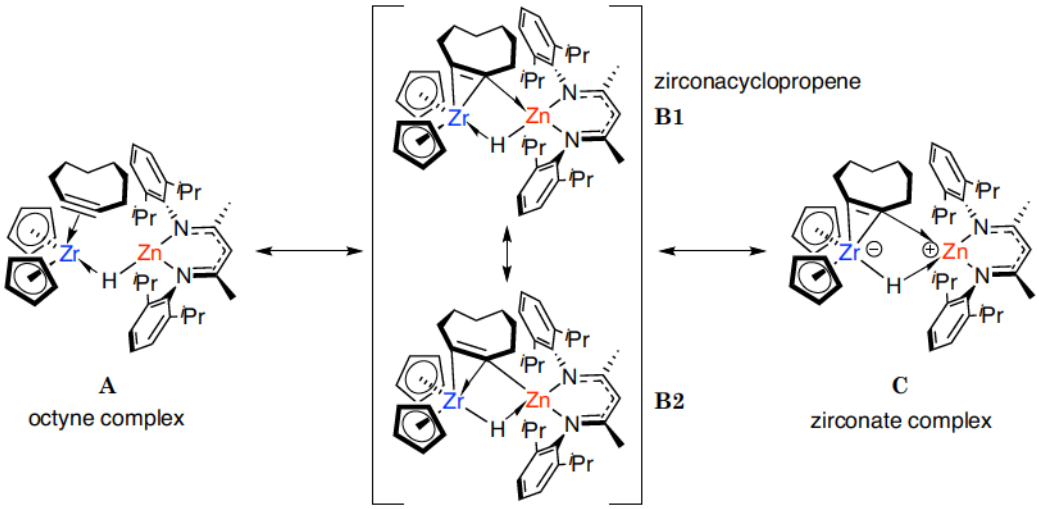


Figure 3.3. Some extreme bonding descriptions of **^{D}Zn•10**.

In the same year Gleiter *et al.* compiled an *ab initio* molecular orbital study of the general Al/Zr core system.[39] It found a five-membered dimetallacyclic covalent structure. It was apparent that the C_μ was stabilised by σ-donation to Zr and the good donor properties of Al and C_α. With no back-donation from Zr to C_μ, the conclusions fit a **B2** character. Analysis of our own structural data takes these findings into consideration.

3.2.2.1 Experimental Data

Following a preparative-scale experiment, **^{D}Zn•10** was isolated as single crystals from an *n*-hexane solution at –35 °C. Two independent molecules were observed in the unit cell. These molecules differ very slightly with respect to the conformation of the cyclooctyne ring; one conformer has ten perfectly eclipsed C–H bonds (Figure 3.4, right). Nevertheless, key bond distances and angles about the bimetallic core do not vary significantly and a single data set has been included (Figure 3.4 – image on the left shows geometry of the bridging ligands).

The zirconium and zinc metal centres are bridged by not only the alkyne ligand but also a single hydride. The Zr---Zn distance of 2.7943(3) Å is approximately 0.1 Å shorter than that observed in the parent complex **^{D}Zn•Zr**. The Zn–C bond length of 2.198(2) Å is slightly longer

than the 1.9–2.1 Å range established for non-bridging Zn–C σ-bonds, but shorter than the range of 2.2–2.3 Å reported for strongly π-coordinated alkene complexes of Zn^{II}.[40]

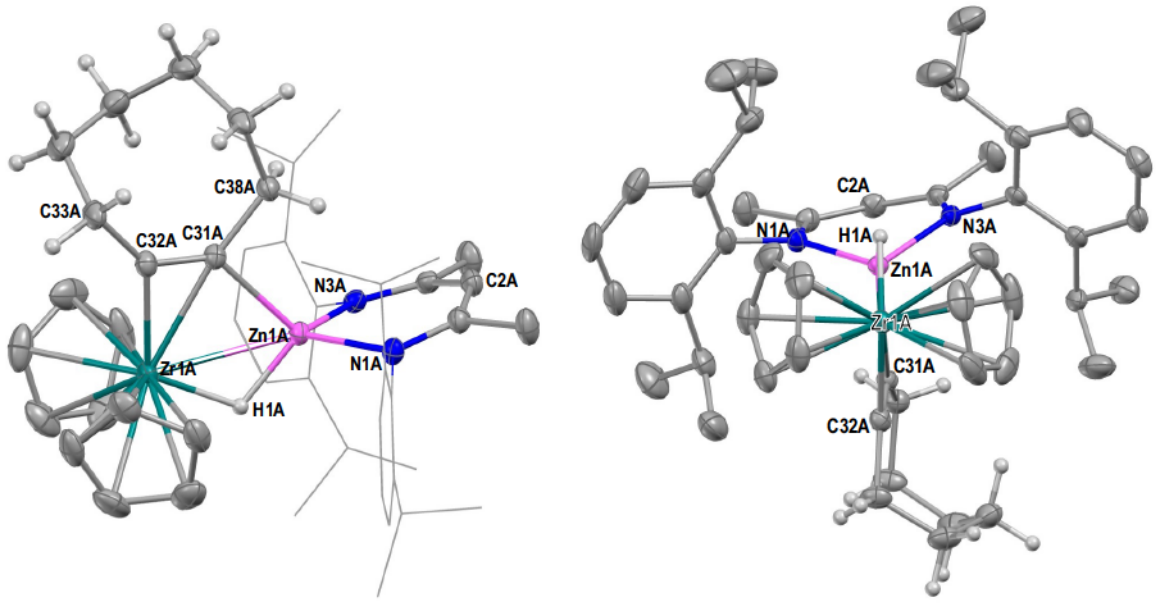


Figure 3.4. Two views of the crystal structure (50% probability ellipsoids) of molecule A in the unit cell of ^{D}**Zn•10**. Hydrogen atoms are omitted save those on the cyclooctyne fragment and the hydride ligand. Selected bond lengths [Å] and bond angles [°]: Zr(1A)–C_{Cp} 2.503(3)–2.565(3); Zn(1A)-N(3A) 2.0097(18); Zn(1A)-N(1A) 2.0101(18); N(3A)-Zn(1A)-N(1A) 96.52(7)

The synthesis of the related complexes was pioneered by Buchwald, Erker, and others as part of studies into planar tetracoordinate carbon species of the form $R_2CM^1M^2$ (M^1 = Zr, M^2 = Zr, Al, Ga, B). Indeed, in ^{D}**Zn•10** the sum of the angles around the bridging C(31A) is 360.05(55)°. Table 3.3 compares the structural data relating to the coordinated alkyne unit in ^{D}**Zn•10** Zr–H-containing precedents. The Zr–C_α and Zr–C_μ bond lengths are consistent with the asymmetric slip of the alkyne towards the zinc (as per **B** and **C**). The main group fragment in virtually all literature examples is {H–Al(^{i}Bu)$_2$}; the greater steric bulk in {^{D}**3**} appears to have a lengthening effect on the M–C_μ bond. Certainly, the steric loading on the Zn main group fragment is outstanding, but the distance between the two metals (normalised as *fsr*) is the shortest reported for a structure of its kind.

Known cyclooctyne complexes of M^I (M = Cu, Ag, Au) possess C–C bond lengths in the range 1.192(10)–1.243(11) Å,[41-43] while a Re cyclooctyne complex supported by a pincer ligand contains a C–C bond length of 1.320(10) Å,[44] similar to 1.308(3) Å observed in ^{D}**Zn•10**. The C_μ–C_α length is at the low end of the data range in Table 3.3. Only the phosphine-supported Zr-cyclohexyne complex (entry **i**) and the other M^{II} example (entry **ix**) are comparable. The C_μ–C_α bond length and obtuse C–Č–C bond angles in ^{D}**Zn•10** look appropriate next to the previously reported structures in Table 3.3, supporting the formulation

as an on-metal alkyne. Buchwald and co-workers have also reported the synthesis of [$Cp_2Zr(\eta^2$-cyclooctyne)(PMe_3)], but unfortunately this complex has not been structurally characterised.[45]

Table 3.3. Alkyne-related bond lengths [Å] and angles [°] of hydrido Zr/M complexes (M = Al, Mg, Zn, P) with related to ^{D}**Zn•10**. Estimated standard deviations given (in parentheses) when available from the primary literature. [a] PMe_3 *i.e.* no hydride. [b] ebthi = *rac*-[1,2-ethylene-1,1'-bis(η^5-tetrahydroindenyl)]

	Cp	*M*	*alkyne*	C≡C	Zr–C_μ	Zr–C_α	*fsr*
^{D}**Zn•10**	Cp_2	Zn	cyclooctyne	1.308(3)	2.444(2)	2.176(1)	1.03
i[36]	Cp_2	P[a]	cyclohexyne	1.295(25)	2.165(13)	2 244(12)	1.05
ii[46]	Cp_2	P[a]	benzyne	1.364(8)	2.267(5)	2.228(5)	1.05
iii[47]	Cp_2	Al	cyclohexyne	1.311	2.429(9)	2.163(9)	1.07
iv[32]	Cp_2	Al	benzyne	1.37(1)	2.436(9)	2.166(9)	1.07
v[47]	Cp_2	Al	4,4'-diphenylacetylene	1.326	2.398(4)	2.185(4)	1.07
vi[48]	Cp^*_2	Al	$Me_3SiC{\equiv}CH$	1.331(7)	2.489(5)	2.132(5)	1.11
vii[48]	Cp^*_2	Al	$Me_3SiC{\equiv}C–CH{=}C(M)Ph$	1.330(6)	2.354(4)	2.237(4)	1.09
viii[34]	ebthi[b]	Al	$Me_3SiC{\equiv}CSiMe_3$	1.33(2)	2.384(15)	2.221(13)	1.06
ix[35]	Cp_2	Mg	2,5,5-trimethyl-1-hexen-3-yne	1.307(5)	2.323(4)	2.198(4)	1.08

	C–$\check{C}_\mu$–C	C–$\check{C}_\alpha$–C	M–C_μ
^{D}**Zn•10**	129.0(2)	133.9(2)	2.198(2)
i	126.0(12)	125.2(12)	3.10
ii	120.2(5)	122.1(5)	3.04
iii	126.1	120.3	2.09(1)
iv	117.0	122.4	2.09(1)
v	126.0	133.2	2.162(5)
vi	111.5	127.4	2.082(5)
vii	131.4	126.0	2.107(5)
viii	117.2	140.4	2.15(2)
ix	135.0(4)	132.0(4)	2.356(4)

3.2.2.2 Density Functional Theory Calculations

In order to gain a deeper understanding of alkyne binding in ^{D}**Zn•10** and to probe the nature of the Zr---Zn interaction a series of DFT calculations were conducted. Benchmarking calculations established the ωB97x functional and hybrid basis-set 6,311G (C/H/N) and SDD (Zn/Zr) as the best combination for matching the solid-state data – specifically the intermetallic distance and Zn–atom distances (section 3.5.3). QTAIM (Bader) analysis was made on the optimised structure.

Both NBO and QTAIM analyses are consistent with the formulation of ^{D}**Zn•10** as a metallacyclopropene complex. However, the two computational approaches assign different

importance to the Zr−C_μ–Zn interaction (Figure 3.5); this is a necessary consequence of the different theoretical basis of each analytical method. In the NBO results, the NPA charge on Zn and small Wiberg bond orders for Zn–C_μ and Zn–H are suggestive of primarily ionic interactions between Zn and surrounding atoms. This picture of a type **C** compound is reinforced by the second-order perturbation theory data: two conspicuously large donor-acceptor interactions from the Zr–H (112 kcal mol^{-1}) and Zr–C_μ (106 kcal mol^{-1}) bonds to the vacant 4s orbital on a formal [Zn*BDI*]$^+$ fragment indicate ate-complex structure. Still, in combination with the C_α–C_μ bond index of 1.87, these data are certainly suggestive of significant back-donation to the alkyne ligand by Zr.

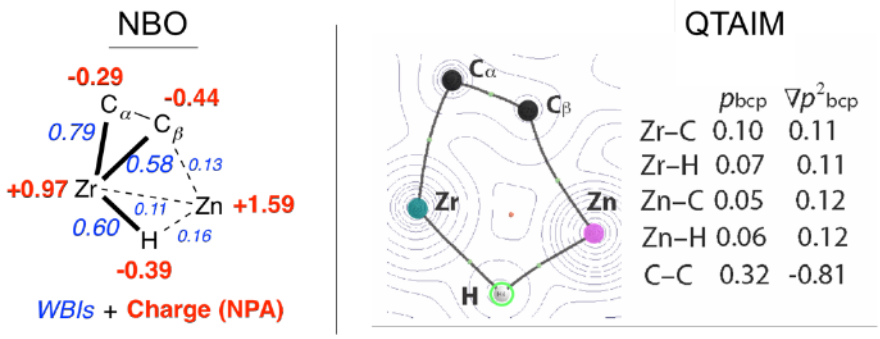


Figure 3.5. NPA charges and Wiberg Bond indices acquired for **^{D}Zn•10** by NBO calculations, and the electron-density contour plot with an overlaid calculated structure from QTAIM analysis presented in the {ZrHZn} plane; the dots show bond-critical or ring-critical points.

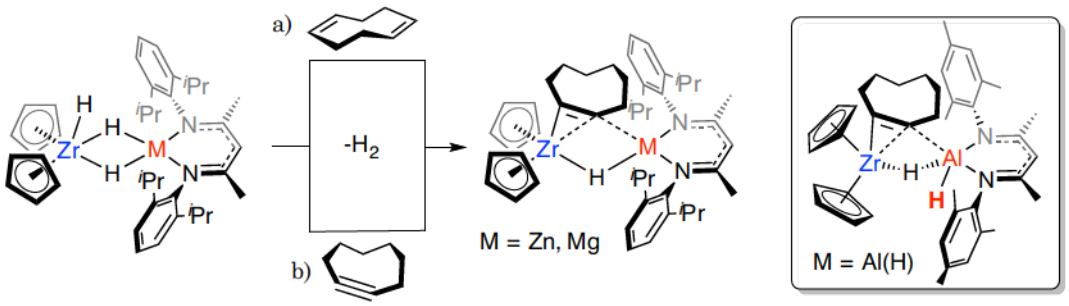
QTAIM analysis provides a valence bond description more akin to that of **B2**; calculations reveal that the core of **^{D}Zn•10** may be considered as an unusual five-membered ring incorporating two carbon atoms, a hydride, zinc and zirconium. In combination, the data suggest considerable π-bonding to the alkyne ligand and support description of **^{D}Zn•10** as a slipped metallacyclopropene. The conclusion and description does not fundamentally contradict any of the previous theoretical studies on 'planar carbon' in the Al/Zr complexes, namely the works of Gleiter and Erker *et al.*[39] and Buchwald *et al.*.[33]

3.2.3 Stability of the Metallacyclopropene

3.2.3.1 Theoretical Studies on Stability

Scheme 3.2 shows that a considerable amount of diene hydrogenation takes place during the isomerisation processes; cyclooctene is formed during the formation of **^{D}Zn•10** from 1,5-COD. Therefore, we must consider whether this transfer hydrogenation of 1,5-COD to form cyclooctene is a vital step in the formation of the slipped metallacyclopropene. DFT calculations show that transfer hydrogenation is not thermodynamically necessary for

formation of ^{D}**Zn•10**. Hence the ligand exchange reaction, ^{D}**Zn•Zr** + cyclooctyne → ^{D}**Zn•10** + H_2, is calculated to be exergonic with $\Delta G°_{rxn}$ = –22 kcal mol^{-1} (Figure 3.6).



ΔG = (kcal mol^{-1})	^{M}Al•Zr	^{D}Zn•Zr	^{D}Mg•Zr
a) *isomerisation*	20.0	-1.1	-2.2
b) *ligand exchange*	-8.0	-21.9	-23.0

Figure 3.6. Calculated values for formation of ^{D}**Zn•10** from 1,5-COD (isomerisation) and from ligand exchange of two hydrides for cyclooctyne (ωB97x functional and SDD basis set for the metals, 6,311G+(d,p) for the C/H/N atoms).

The corresponding values for the two other main group metals were also calculated, along with the Gibbs free energies of isomerisation from 1,5-COD. This involved optimisation of ^{D}**Mg•10** and ^{M}**Al•10** (see section 3.5.3). Predictably, the latter appears particularly strained, with the {Zr-cyclooctyne-H_μ} plane approaching a 45° tilt against the {*BDI*Al} plane (see Experimental section). Nevertheless, the ligand exchange formation of ^{R}*BDI*MH•**10** is favourable in all instances (M = Al(H), Mg and Zn). This result tells of a stability in the slipped metallacyclopropene moiety that is able to offset considerable destabilisation elsewhere in the molecule. Perhaps most interestingly, the products of both isomerisation and ligand exchange are 1–2 kcal mol^{-1} more stable for Mg than for Zn.

Figure 3.6 also shows the $\Delta G°_{rxn}$ values for the complete diene-to-alkyne isomerisation. These illustrate the same pattern of favourability but at a cost. The difference between the simple ligand exchange and isomerisation reactions is *ca.* 21 kcal mol^{-1} for the Mg and Zn reactions, which is only marginally larger than the energy difference between the isomers cyclooctyne and 1,5-COD (Figure 3.1). From this result, two simplified conclusions may follow: either a) the product involves very little distortion of the organic ring from its free state; or b) a large amount of distortion (and steric clash) is discounted by a strong energy of binding of the alkyne to the heterobimetallic complex. Fragment analysis of ^{D}**Zn•10** (and the other analogues) allows quantification of the important factors that affect the stability of the complex, and it shows the latter statement to be correct – strong binding of the alkyne is key.

Fragment Analyses

By breaking the molecule into organometallic and cyclooctyne fragments, the distortion and binding energies were quantified (Figure 3.7). The distortion energies of the cycloalkyne ($\Delta E_{0,distn_COC}$ = +39 kcal mol^{-1}) and bimetallic complex ($\Delta E_{0,distn_MZr}$ = +16 kcal mol^{-1}) fragments along with the energy of alkyne binding ($\Delta E_{0,bind}$ = –119 kcal mol^{-1}) reveals that the deformation energies are aptly compensated for by the large binding energy for ^{D}**Zn•10**. Metal coordination of the octyne therefore appears to have the key role in the otherwise contrathermodynamic production of alkyne from diene.

The $\Delta E_{0,distn_COC}$ value for ^{M}**Al•10** is 6 kcal mol^{-1} larger than for the ^{D}**Zn•10** and ^{D}**Mg•10**, which begins to explain the disfavoured isomerisation reaction with ^{M}**Al•10**. The only difference between the energy cycles of ^{D}**Mg•10** and ^{D}**Zn•10** is the stronger energy of binding for the former ($\Delta E_{0,bind}$ = –127 kcal mol^{-1}). Furthermore, the same value for ^{M}**Al•10** ($\Delta E_{0,bind}$ = 121 kcal mol^{-1}) is actually slightly greater than that of ^{D}**Zn•10.** The energies of formation would seem to reiterate that there is nothing inherently special about the ground state energetics of ^{D}**Zn•10** that leads to its unique formation.

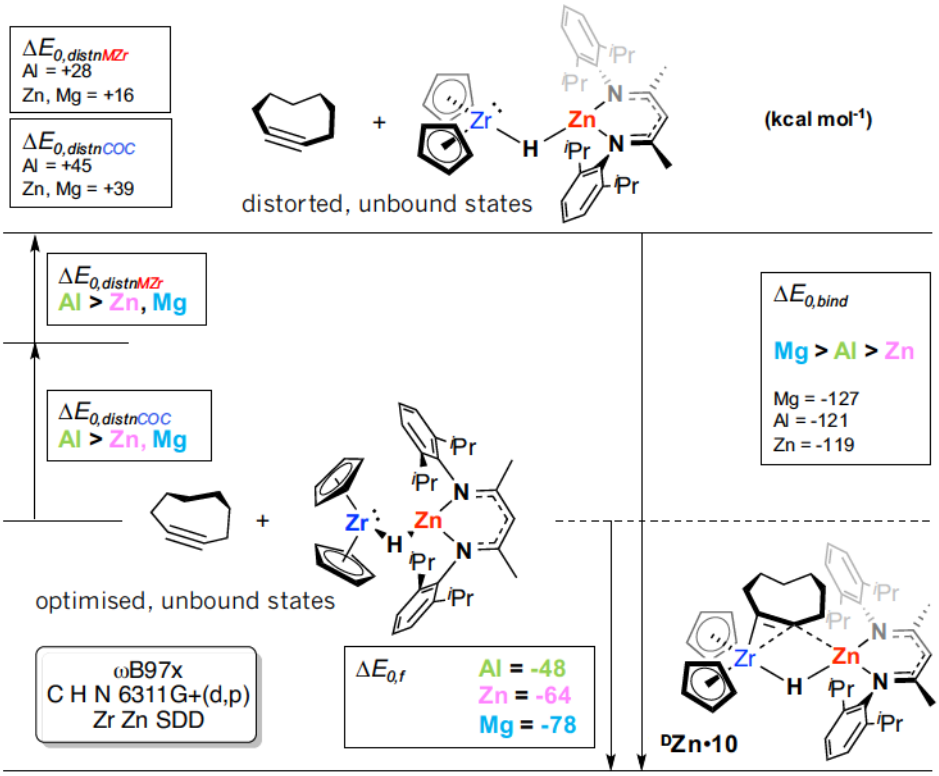


Figure 3.7. Octyne fragment analysis of ^{D}**Zn•10** and (inset) the comparison of electronic energies with the results of the analogous Mg and Al heterobimetallic complexes.

In a complementary analysis, breaking of the complexes into ^{Dipp}*BDI*MH and **10** molecules allows comparison of the distortion and binding energies of the free zirconacycle with each

main group hydride fragment (Figure 3.8). The magnitudes of distortion are in the familiar Al > Zn > Mg sequence. The {^{Dipp}*BDI*M^{II}H} fragments are relatively unperturbed compared to the $\Delta E_{0,distn_Al}$ value for {^{Mes}*BDI*AlH$_2$} (+53 kcal mol^{-1}), which is more than double the size. Despite a lot of the distortion becoming relaxed on the binding of **10** to {^{Mes}*BDI*AlH$_2$}, the additional energy cost (of distortion) is clearly an origin of its unfavourable formation (Figure 3.6).

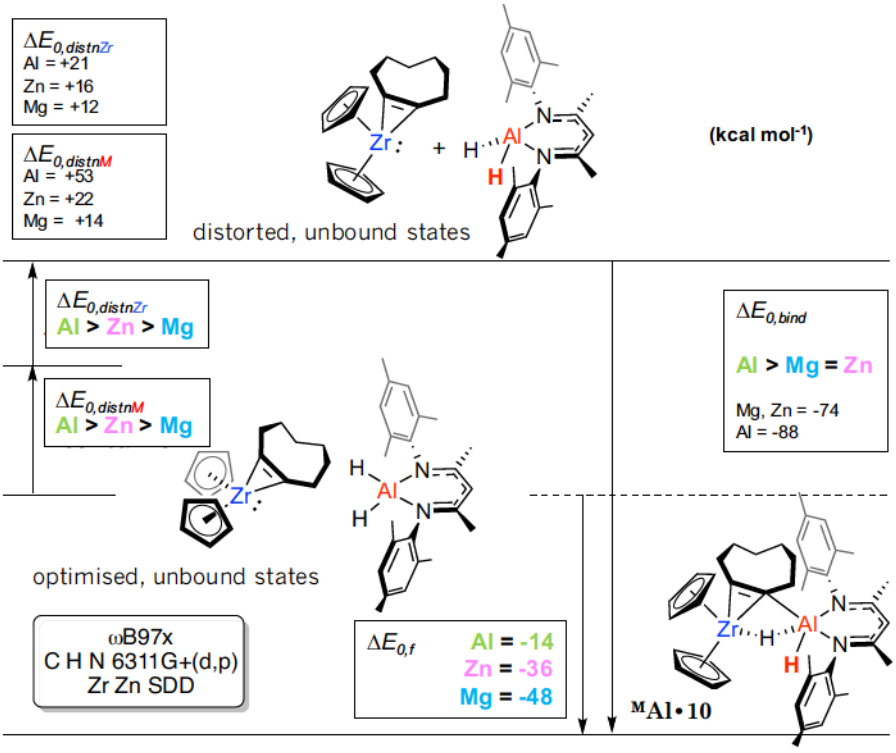
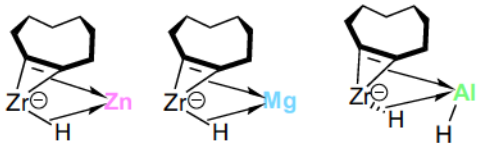


Figure 3.8. Zirconacycle fragment analysis of ^{M}**Al•10** and (inset) the comparison of electronic energies with the results of the analogous Mg and Zn heterobimetallic complexes.



acceptor unit & orbital

(kcal mol^{-1})		Zn 4s	Mg 3s	Al 3p	Al sp^2
donator	Zr–H	112	39	95	199
	Zr–C$_\mu$	106	38	-	61

Figure 3.9. Selected second-order perturbation theory data for inter-metal fragment electron donation.

Ate complexes (bonding description **C**, Figure 3.3) may be considered as part of the structural comparison and fragment analysis. A direct approach is the comparison of the second-order perturbation theory data (Figure 3.9) previously discussed in section 3.2.2.2.

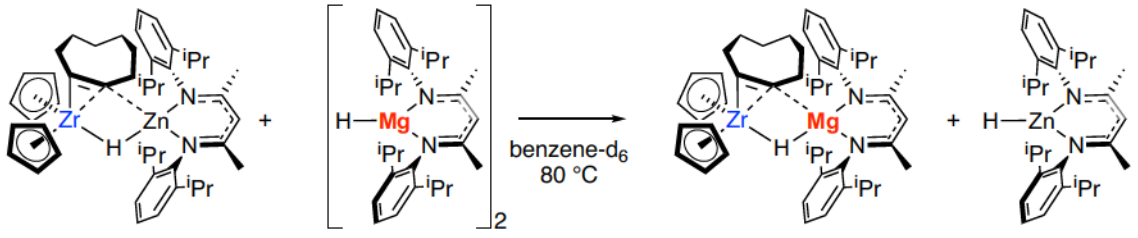
Here there is a big difference between all three congeners. The Mg atom has the weakest interaction with the zirconate fragment. The data correlate with the order of Pauling electronegativity for each main group metal. They do not correlate with the order of relative stabilities of each slipped metallacyclopropene. The strength of these interactions is therefore not stability-defining.

In the interest of computational affordability, the presented calculations were run without a dispersion correction. This means that the energies of binding are perhaps underestimated (as seen in section 2.3.1.2). Although this puts a limitation on the accuracy of the computational methods, conclusions made within the self-consistent series of heterobimetallic complexes ought to be reliable.

3.2.3.2 Experimental Stability and Reactivity

Initial attempts to displace the cyclooctyne fragment from a pure sample of ^{D}**Zn•10** with excess trimethylphosphine at 80 °C led to no change in the reaction mixture. Variable-temperature ^{1}H NMR data (toluene-d_8) reveal that ^{D}**Zn•10** retains its integrity in solution, undergoing little or no change across the 193 to 353 K temperature range.

Despite this apparent lack of structural flexibility and capacity for ligand dissociation, it is possible to exchange the {^{Dipp}*BDI*MH} fragment. Half an equivalent of ^{D}**2$_2$** was heated in benzene-d_6 at 80 °C for 2 d in the presence of ^{D}**Zn•10** (Scheme 3.3). A hydride resonance in ^{1}H NMR spectrum at δ = –1.85 ppm (along with some other visible peaks) was assumed to be a sign of the formation of ^{D}**Mg•10** (*cf.* δ = –1.23 ppm for ^{D}**Zn•10**). Only small amounts of ^{D}**2** and traces of ^{D}**Zn•Zr**, 1,3-COD and cyclooctene were discernible. The ^{1}H NMR spectrum revealed 88% consumption of ^{D}**Zn•10** yet the reaction yielded just 15% of ^{D}**Mg•10**.



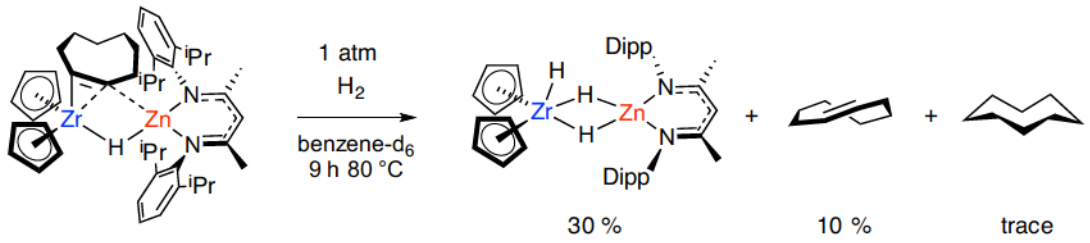
1 equiv.	0.5 equiv.	2 d	^{D}**Mg•10** (15%)	^{D}**3** (11%)
	+ 0.5 equiv.	+ 2 w	^{D}**Mg•10** (25%)	^{D}**3** (trace)

Scheme 3.3. Experimental displacement of the zinc hydride fragment in ^{D}**Zn•10** by a magnesium counterpart.

An uneven mass balance may be explained by the obvious development of grey solids in the tube, and colour change from yellow to dark green – both signs of significant degradation in zirconocene systems. Addition of a further equivalent of ^{D}**2** and heating for a further 2 weeks sees survival of ^{D}**Mg•10** and only trace ^{D}**Zn•10**. The trace 1,3-COD is consumed, leaving only

cyclooctane. Despite the poor yield, it is apparent that ^{D}**Mg•10** is formed in this reaction and that this heterobimetallic complex is not only synthetically accessible but may be more thermodynamically stable than the Zn analogue. The experiment confirms the conclusions from the DFT calculations, in particular, the fragment analysis of Figure 3.8, where a ^{Dipp}*BDI*MH molecule can trap **10**.

When ^{D}**Zn•10** is heated in a sealed tube under 1 atm of dihydrogen (Scheme 3.4) a similar amount of degradation (including blackening of the mixture) was witnessed. A control experiment showed no such degradation of ^{D}**Zn•Zr** under H_2 atmosphere. The slipped metallacyclopropene is hydrogenolysed to the Zn/Zr trihydride and cyclooctene, albeit with modest yield. This low-yielding and relatively forced reversion of ^{D}**Zn•10** to ^{D}**Zn•Zr** confirms that ^{D}**Zn•10** is relatively stable. There was no production of any C_8H_{14} molecules – no free cyclooctyne or, "reverse-isomerised" dienes. To check if such C_8H_{14} rings may have been intermediates in the Scheme 3.4 reaction, a reaction of ^{D}**Zn•Zr** and 1,5-COD was conducted under H_2 atmosphere: there was no noticeable increase in cyclooctene production. Thus, in combination with literature precedent,[49] the reaction in Scheme 3.4 is a hydrogenolysis of the Zr–C bonds of the metallacyclopropene unit.



Scheme 3.4. Hydrogenolysis of ^{D}**Zn•10**: a 20% yield of [^{Dipp}*BDI*ZnPh] was also returned (see following section and Figure 3.17 for discussion).

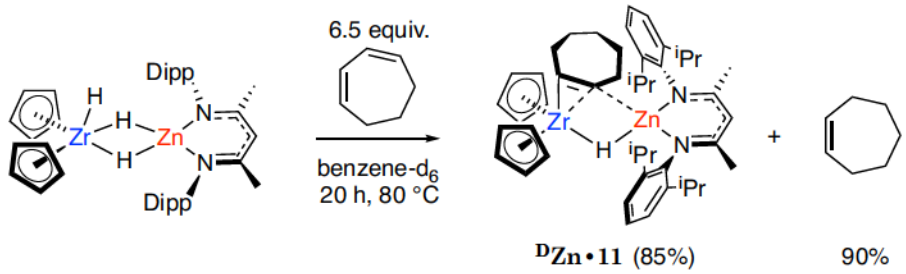
The computational results also indicated that the on-metal isomerisation does not require thermodynamic pay-off by production of 1,3-COD. A control experiment confirms this. Reaction of ^{D}**Zn•Zr** with excess of 1,3-COD (rather than 1,5-COD) gives ^{D}**Zn•10** in 90% yield by NMR spectroscopy. There was no noticeable difference in reaction time compared to the reaction in Scheme 3.2 and no 1,4-COD is formed. If exergonic isomerisation of diene were required for simultaneous ^{D}**Zn•10** production, then a depleted yield of ^{D}**Zn•10** may be expected when the diene substrate is already the most stable isomer. Conversely, the calculations suggested that hydrogenation of an equivalent of cyclooctadiene was not *thermodynamically* required. The ratio of ^{D}**Zn•10**:cyclooctene in the experimental data (1:1.2) intimates that this hydrogenation may be a requirement of the mechanistic pathway.

3.2.4 Mechanistic Studies

The comparative ground state structural calculations offer no obvious clues as to why **^{D}Zn•Zr** is unique in performing the on-metal isomerisation. Therefore, a selection event along the mechanistic route should be the source of the differences between the reactivities of the heterobimetallic trihydride complexes. Below is presented a determination of the reaction kinetics and a series of mechanistic experiments and controls. Also included is a brief initial assessment of substrate scope. Although the success and failure of various substrates only partly depends on mechanism, is it presented here because the work mentioned above (Table 3.3) has shown that slipped zirconacyclopropenes from various alkynes is feasible, and certain failures give interesting by-products.

3.2.4.1 Substrate Scope

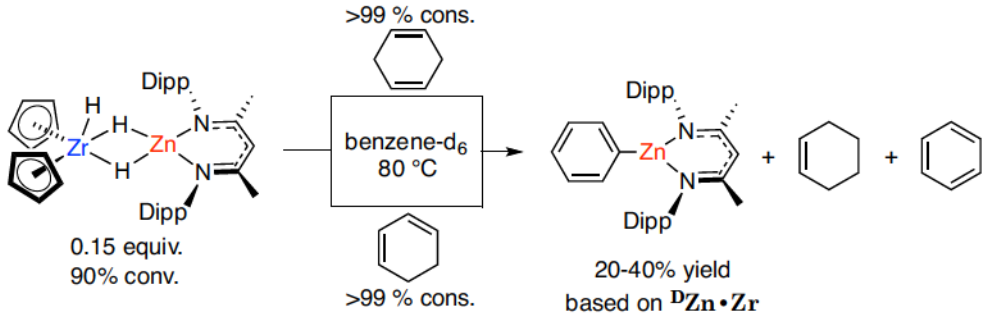
The mechanism tolerates a slightly smaller diene ring size. Isomerisation is barely affected by cutting the hydrocarbon from 8 to 7 carbons (Scheme 3.5); **^{D}Zn•11** is formed with an 85% yield in the ^{1}H NMR spectrum based on **^{D}Zn•Zr**. Also based on **^{D}Zn•Zr**, 90% cycloheptene is formed. The product was isolated and fully characterised by ^{1}H and ^{13}C NMR spectroscopy (see 3.5 Experimental). Calculations (the same as performed for the C_8H_{14} isomers) give a difference in free energy of 27 kcal mol^{-1} between free cycloheptyne and cyclohepta-1,3-diene.



Scheme 3.5. Successful slipped metallacyclopropene-forming reactions.

With cyclohexadiene substrates no cyclohexyne products were observed. When reacted with **^{D}Zn•Zr**, reactions of both cyclohexa-1,3- and -1,4-diene gave peaks for cyclohexene in the ^{1}H NMR spectra (Scheme 3.6). Disproportionation of the diene is to be expected.[19] The complimentary disproportionation product, benzene, was expected because the yield of cyclohexadiene accounted for no more than 20% of the starting material. However, the singular major organometallic product in the ^{1}H NMR spectra was [^{Dipp}*BDI*ZnPh], with its *BDI* methylylidene resonance seen clearly at δ = 5.04 ppm; the other signals of the ^{Dipp}*BDI* ligand also agree with the literature values (see Experimental, Figure 3.22).[50] However, the phenyl ligand peaks overlap with the benzene produced in the reaction, making the quantity of the organic compound inestimable. For the same reasons, it is not possible to say if the phenyl

moiety is deuterated (from solvolysis of the starting material). The only sign of an accompanying zirconocene-related species was the reaction mixture developing an opaque black colour.



Scheme 3.6. Oxidation and C–H activation of cyclohexadienes with **^{D}Zn•Zr**.

The strong blackening of the solution is typically accompanied by an intractable ^{1}H NMR spectrum, but this was not the case here. Also unusual was the increasing of the cyclohexene yield after time points when there was no ostensible presence of diene reactant. NMR-silent products may be responsible for this and an incomplete mass balance. During the reaction, H/D exchange into the hydride positions of **^{D}Zn•Zr** was observed, as evidenced by the formation of a series of isotopomers by ^{1}H NMR. This change in hydride peak shapes is evidence for solvolysis; the [^{Dipp}*BDI*ZnPh] complex may not acquire its phenyl ligand from the cyclohexadienes but from the benzene-d_6 solvent (to give [^{Dipp}*BDI*Zn(Ph-d_5)]).

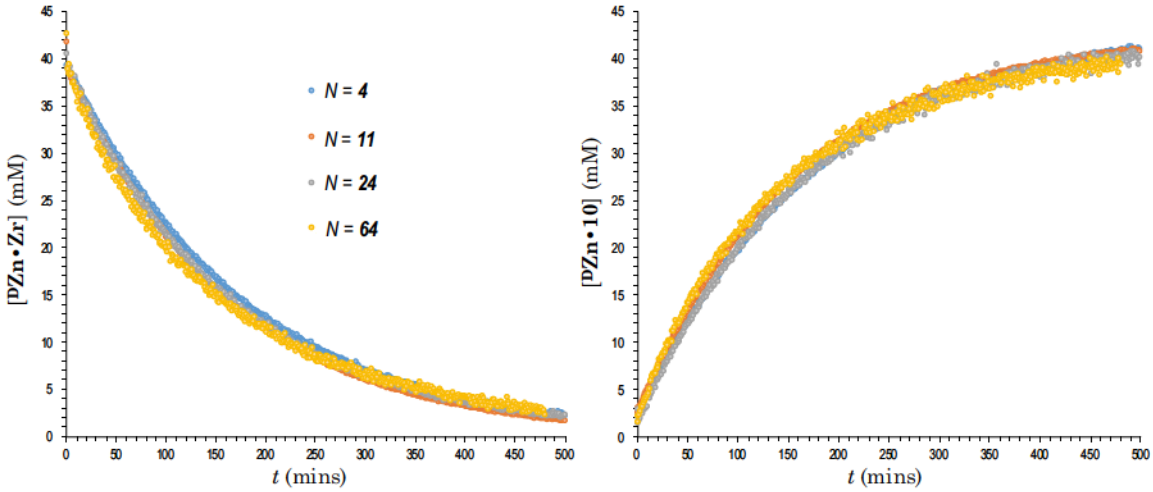
The commercially available *E,E,Z*-cyclododeca-1,5,9-triene and octa-1,7-diene were attempted for alkyne formation on **^{D}Zn•Zr**, but the products are not yet understood.

3.2.4.2 Reaction Kinetics

Cycloocta-1,3-diene is the substrate that gives the slightly tidier and more direct formation of **^{D}Zn•10**. It was therefore used for kinetic analysis by ^{1}H NMR spectroscopy of an in-probe reaction. A plot of the concentration of **^{D}Zn•Zr** as a function of time shows a first-order decay under pseudo-first-order conditions (11-fold excess of 1,3-COD and 80 °C heating – Graph 3.1, red markers). The production of **^{D}Zn•10** effectively mirrors the decay. Removing the pseudo-first-order conditions and dropping to just 4 equiv. of the diene (Graph 3.1, blue marks) leads to an almost identical reaction profile. Larger excesses of 1,3-COD (24- and 64-fold) gives the same result – a $t_{½}^{(1)}$ of around 6600 s.

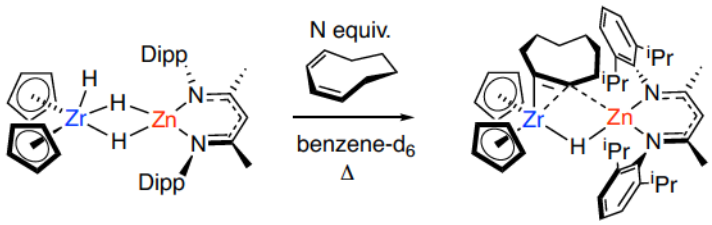
The observed rate constants (k_{obs}) are essentially unaffected varying the excess of 1,3-COD. The coefficient of determination taken from Graph 3.3a is poor, but by visual inspection it is clear that the rate is unaffected by 1,3-COD. The reaction is therefore first order overall. The activation parameters for the isomerisation are $\Delta H^{‡}$ = +33.6 ± 0.7 kcal mol^{-1}, $\Delta S^{‡}$ = +23.2 ± 1.9 cal mol^{-1} K^{-1}, and $\Delta G^{‡}_{298K}$ = +26.7 ± 1.2 kcal mol^{-1} as determined from an

Eyring plot (Graph 3.3b) and rate constants obtained between 353 and 368 K (Graph 3.2 and Table 3.4). The rate-determining step involves a significant amount of bond-breaking and an increase in disorder compared with the ground state.



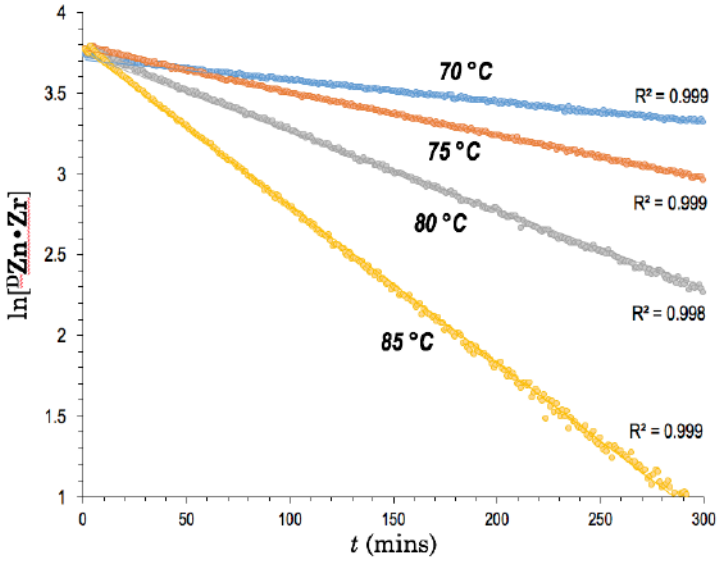
Graph 3.1. Decays of ^{D}**Zn•Zr** and production curves of ^{D}**Zn•10** in the 1,3-COD isomerisation reactions, where the excess of the latter (*N*, in equiv.) is varied.

Table 3.4. Summary of kinetic analysis for isomerisation of 1,3-COD by ^{D}**Zn•Zr**.

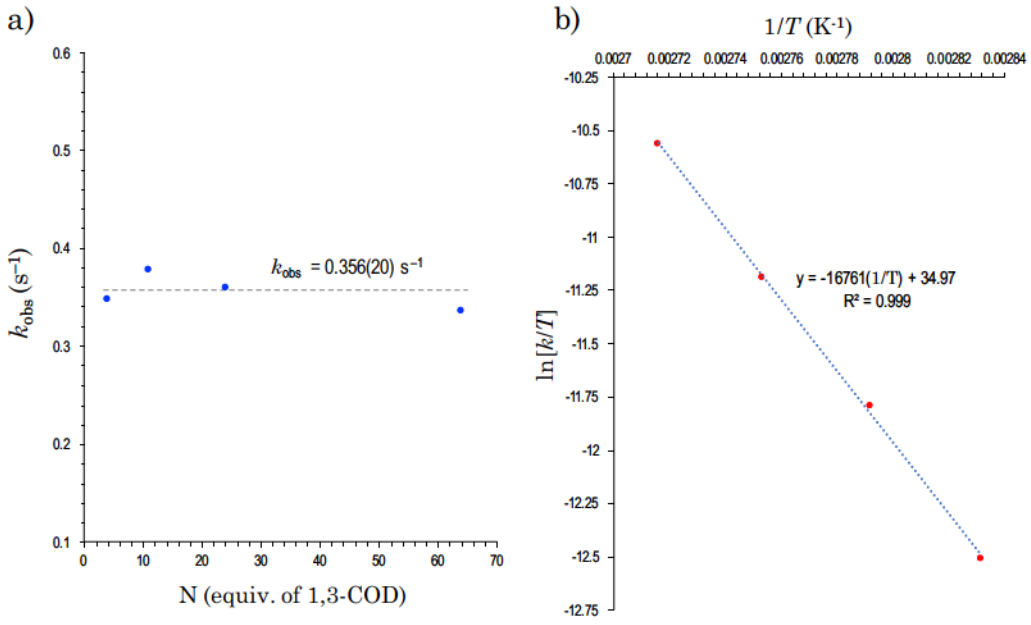


	Entry	N	temp. (°C)	k_{obs} (s^{-1})	1,3-COD :COE[a]
1,3-COD	**i**	4	80	0.348	4.5:1
	ii	11	80	0.378	11:1
	iii	24	80	0.360	22:1
	iv	64	80	0.342	50:1
Eyring	**v**	11	70	0.078	13:1
	vi	11	75	0.162	13:1
	vii	11	80	0.300	10:1
	viii	11	85	0.582	11:1

[a]The ratio (after third half life) is an estimate based on the integration of the slightly obscured multiplets at δ = 5.83–5.77 ppm and 5.64–5.57 ppm respectively.



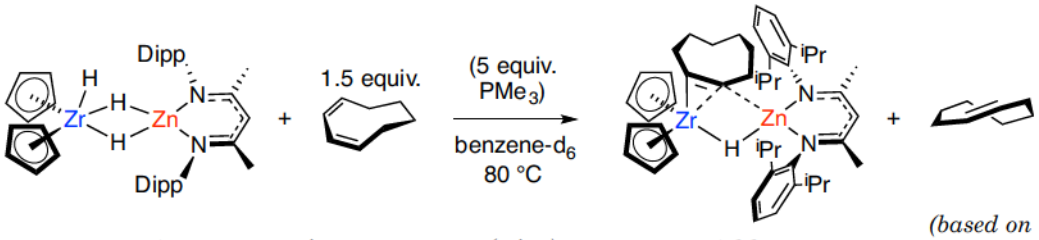
Graph 3.2. The semi-log plot of the Eyring analysis of reaction rate between 70–85°C.



Graph 3.3. a) Determination of order in 1,3-COD between 4–64 equivalents. b) An Eyring plot between 353 and 368 K at 5 K intervals.

The half-life of the organometallic compound is not changed by use of only 1.5 equiv. of the diene. The results of this reaction as an infrequent point kinetics experiment are shown in Scheme 3.7. Additionally, the presence of potential reaction inhibitor, PMe_3, has no visible effect on the isomerisation. The maximum observed yield of **^{D}Zn•10** was 30%, which then stalls and depletes with further heating. During this time, the amount of cyclooctene also passes through a maximum – for comparison to Table 3.4, the ratio 1,3-COD:COE after $t_{½}^{(3)}$ is 1:2. This concomitant collapse in yield is possibly due to two side reactions. Both **^{D}Zn•Zr** and **^{D}Zn•10** are likely to react with cyclooctene, especially when there is a lack of competition

from the diene. It follows that neither of the reactions would seem to generate ^{D}**Zn•10.** Mechanistic control experiments have explored this – Section 3.2.4.3.

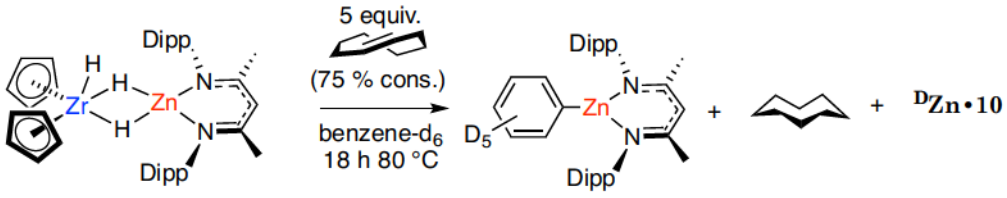


consumption	*equiv. cons.*	*t (mins)*	*yield*	*(based on ^{D}Zn•Zr)*
60%	1.1 equiv.	120	25 %	20 %
75%	1.2 equiv.	240	30 %	25 %
85%	1.4 equiv.	390	30 %	30 %
95%	1.5 equiv.	750	20 %	20 %

Scheme 3.7. A sparse point kinetics experiment (and results) for reaction of ^{D}**Zn•10** with a 1.5 equiv. excess of 1,3-COD.

3.2.4.3 Mechanistic Probes and Control Experiments

When reacted in isolation, ^{D}**Zn•Zr** and 6.5 equiv. cyclooctene are unable to give formation of ^{D}**Zn•10** (Scheme 3.8). This result is suggestive of a chain-walking mechanism for ^{D}**Zn•10** formation. It is not consistent with formation of ^{D}**Zn•10** by hydrogenation of 1,3-COD followed by dehydrogenation and subsequent binding of the resulting cyclooctene by a Zr/Zn complex. During this reaction, the heterobimetallic complex decomposes completely, and it is largely converted to [^{Dipp}*BDI*ZnPh] (60% yield). This is a similar result to that of the cyclohexadiene substrates, and again the heated reaction mixture is black with no zirconocene product detectable by ^{1}H NMR. Here, the formation of [^{Dipp}*BDI*ZnPh] definitely indicates C–H activation of the solvent. Furthermore, a control experiment established that C–H activation does not result from the reaction of ^{D}**Zn•10** with cyclooctene: there is no reaction between the two after extensive heating at 80 °C. Cyclooctene is quickly hydrogenated by **Zr•Zr** under the same conditions, with no discernable organometallic products in the ^{1}H NMR spectrum.



90% conv.

60% yield based on ^{D}Zn•Zr

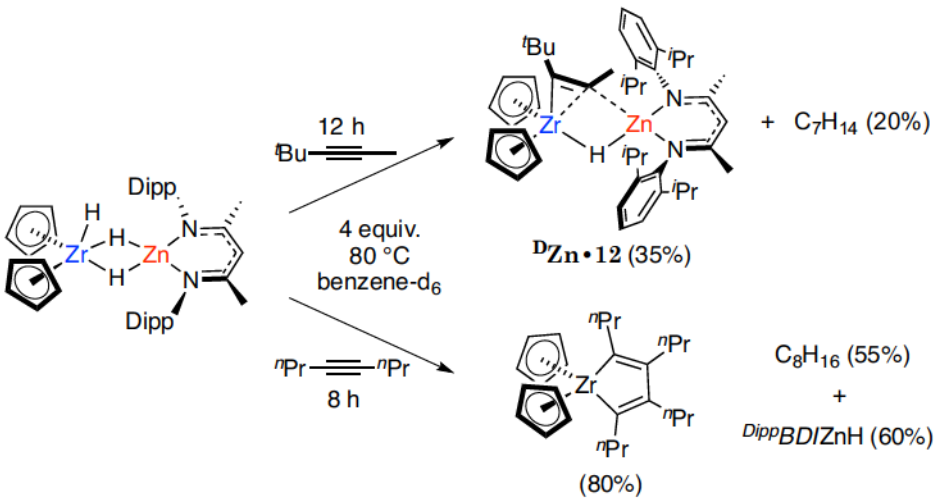
trace

Scheme 3.8. Control reaction of ^{D}**Zn•Zr** with cyclooctene.

An amount of hydrogenation of the diene (and alkene) is observed in all of the aforementioned reactions with ^{R}*BDI*MH•**Zr** complexes. No free dihydrogen has been observed in any of the isomerisation reactions. Hence we may posit that transfer of two hydrides from ^{R}*BDI*MH•**Zr** to a sacrificial equivalent of the substrate is an unavoidable mechanistic step. Thermodynamic calculations give a $\Delta G°_{rxn}$ of –15 kcal mol^{-1} for the reaction of ^{D}**Zn•Zr** + 2(cycloocta-1,3-diene) → ^{D}**Zn•10** + cyclooctene. Hydrometallation and transfer hydrogenation by ^{D}**Zn•Zr** is investigated below.

Hydrometallation and Transfer Hydrogenation

A previous mechanistic study has used 4,4-dimethylpent-2-yne as a trap for zirconocene hydrides due to its very fast Zr–H bond insertion rate.[51] Its reaction with ^{D}**Zn•Zr** did not allow observation of a trapped hydrometallation product, such as a complex containing {Cp_2Zr(H)–C(Me)=C(H)^{t}Bu}. In fact, the alkyne formally displaces two hydride ligands of ^{D}**Zn•Zr** and produces ^{D}**Zn•12** (Scheme 3.9 and Figure 3.10); the product of transfer hydrogenation (*i.e.* 4,4-dimethylpent-2-ene) was identified. A sole new hydride signal emerged in the experiment's ^{1}H NMR spectra at δ = –1.41 (s) ppm, accounting for the H_{μ} atom in ^{D}**Zn•12**. Colourless crystals of ^{D}**Zn•12** grew from the reaction mixture after 1 month at room-temperature and allowed characterisation. Thus, in this experiment 4,4-dimethylpent-2-yne does not act as the intended hydrometallation trap, but as a hydrogen trap, taking two hydrides from ^{D}**Zn•Zr**. A second equivalent of 4,4-dimethylpent-2-yne then traps the resulting Zn/Zr fragment(s).



Scheme 3.9. Full consumption of ^{D}**Zn•Zr** *via* its hydrogenation and insertion chemistry with linear alkynes – all yields based on ^{D}**Zn•Zr** by ^{1}H NMR.

^{D}**Zn•12** reinforces the general idea that the initiation step in the isomerisation reaction(s) is transfer hydrogenation. A {Cp_2Zr^{II}} fragment then follows, which is subsequently bound by unsaturated hydrocarbon to form a three-membered zirconacycle. In the case of ^{D}**Zn•12**, the

latter is already a zirconacyclo*propene*, and no isomerisation of the hydrocarbon takes place. The formation of **^{D}Zn•12** exhibits regioselectivity. The *tert*-butyl group appears on the Zr side of the heterobimetallic complex, presumably due to the minimisation of steric clash with the ^{i}Pr groups.

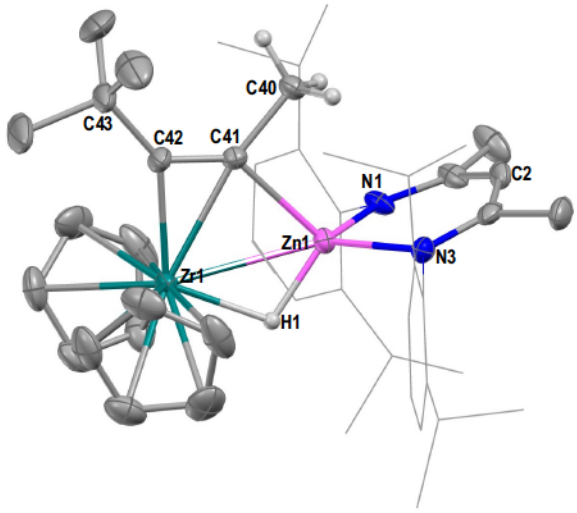


Figure 3.10. The crystal structure (50% probability ellipsoids) of **^{D}Zn•12**. Hydrogen atoms are omitted save those on the C(40) methyl group in **12** and the hydride ligand. Selected bond lengths [Å] and bond angles [°]:C(42)–C(41) 1.312(6), Zr(1)–H(1) 1.971(13), Zn(1)–H(1) 1.614(15); Zr(1)–H(1)–Zn(1) 102.24(7)

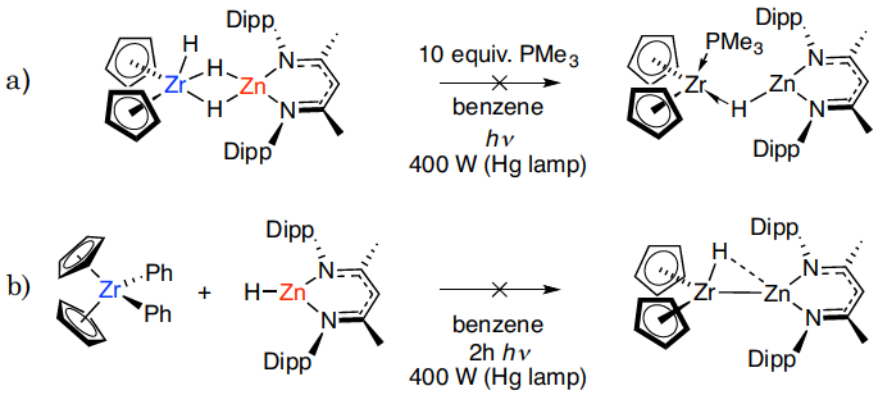
The reaction of oct-4-yne with **^{D}Zn•Zr** also gave similar evidence of hydrometallation and transfer hydrogenation: the product mixture contains alkene(s). However, in this case, the major Zr product is the zirconacyclopentadiene (Scheme 3.9).[52] This species is known from the cross coupling of alkynes around Zr^{II} centres.[53-56] It is a trapped {Cp_2Zr} fragment and a monometallic equivalent of the slipped metallacyclopropenes. Accordingly, the Zn fragment (parent hydride) **^{D}3** is ejected from the Zn/Zr starting material.

Also used previously as a Zr–H trap was methylenecyclohexene.[57] Its reaction with **^{D}Zn•Zr** is messy, but hydrogenated alkene is clearly identified by its methyl doublet at δ = 0.87 ($^{3}J_{H\text{-}H}$ = 6.4) ppm in the ^{1}H NMR spectrum.[58] However, the observable organometallic complex in the mixture is not a {Cp_2Zr^{II}}-related fragment but [^{Dipp}*BDI*ZnPh]. This product could be telling with regards to the fate of {Cp_2Zr} generated from transfer hydrogenation. Reduced organometallic species (such as {Cp_2Zr^{II}}) are almost certainly a necessary by-product of transfer hydrogenation. Whereas the reactions in Scheme 3.9 show alkyne molecules able to stabilise Zr as a metallacyclopropene, similar treatment with alkenes (methylenecyclohexane or cycloctene) does not lead to trapped {Cp_2Zr}, presumably because of weaker propensity of alkenes to bind the transition metal. As a result, the Zr centre remains highly reactive, and eventually the reaction mixture is able to effect zincation of the solvent. This raises the question: do *heterobimetallic* low-valent species exist in the reaction mixtures?

Low-valent Intermediates

Attempts have been made to isolate heterobimetallic low-valent intermediates using PMe_3. Phosphine adducts of Zr in a low-valent species such as that shown in Scheme 3.10 have proven un-isolable thus far. Nevertheless, following the photolysis of **^{D}Zn•Zr** by ^{31}P and ^{1}H NMR has shown some evidence of low-valent species. Running the experiment in benzene-d_6 gave D scrambling into the hydride positions, as determined by the familiar line shape changes. Dihydrogen appears in the ^{1}H NMR spectrum. In ^{1}H NMR spectra taken immediately after photolysis, a series of peaks akin to a ^{Dipp}*BDI*-ligated complex appear to be the major products of the reaction (see Experimental). Most notable of these is a signal in the bridging hydride region at δ = –3.04 (d, $J_{H\text{-}P}$ = 36 Hz) ppm. By the size of the coupling constant and multiplicity, this signal appears to be coupling to a ^{31}P atom. However, after a period of several days at room temperature outside of the photolysis apparatus these peaks are significantly decreased in intensity. The intensity of **^{D}Zn•Zr** peaks is partly regenerated. Because of this equilibrium effect, we have not yet been able to isolate the major product. More frustratingly, the ^{31}P NMR experiments do not display an unmistakably proton-coupled signal.

In the experiment with [Cp_2ZrPh_2], the untidy photolysis process competes with a (room-temperature) thermal reaction; [^{Dipp}*BDI*ZnPh] is slowly produced from the ligand exchange between the two species. This may or may not be derived from a desired Zr–Zn bonded product, and serves to remind us that monometallic Zr may activate Ph–H alone, and pass the phenyl ligand to Zn.



Scheme 3.10. Experimental attempts made on reduced zirconocene species related to **^{D}Zn•Zr**.

3.3 Mechanistic Discussion and DFT Studies

The results above provide an outline for the mechanism: a dissociative rate-determining step (independent of diene concentration under saturation conditions), transfer hydrogenation of one C=C bond in 1 equiv. of diene, and the potential for low-valent organometallic intermediates are all features that need to be resolved. The mechanism must also explain how two C–C π-bonds are brought between the same two C atoms to create the alkyne system. In Chapter 2, the association/dissociation of **^{D}Zn•Zr** and **^{D}Mg•Zr** was analysed by DFT and partly by VT NMR with the essential conclusion that **^{D}Zn•Zr** more easily dissociates below 80 °C.

3.3.1 Mechanistic Hypothesis from Experiment

Taken in combination with the results of the Eyring analysis, we may propose a starting point for the mechanism. Rate-determining dissociation of Zr and Zn parent hydride fragments (Figure 3.11) fits the experimental zero-order dependence of rate on 1,3-COD. Moreover, full dissociation of {Cp_2ZrH_2} and {^{Dipp}*BDI*ZnH} involves an increase in entropy, which is consistent with the experimental value ($\Delta S^{\ddagger}$ = +22.3 ± 1.7 cal mol^{-1} K^{-1}). Rate-limiting insertion of alkenes into a Zr–H bond (in [$Cp^*_2ZrH_2$]) was found to have large *negative* entropy of activation:[51] alkene insertion is therefore discounted as part of the rate-determining step. Cyclooctadiene-induced separation of the Zr/Zn complex is not included in the hypothesis because a previous Zr/Al study has calculated this type of initial step to have a large barrier height, and therefore be dependent on alkene concentration.[59]

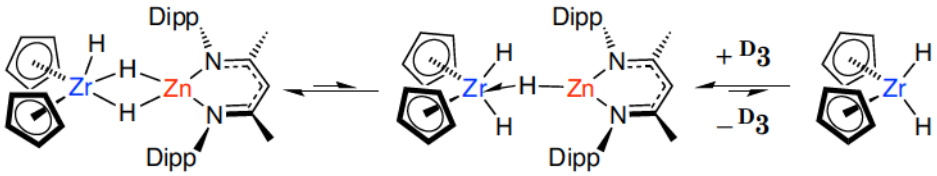
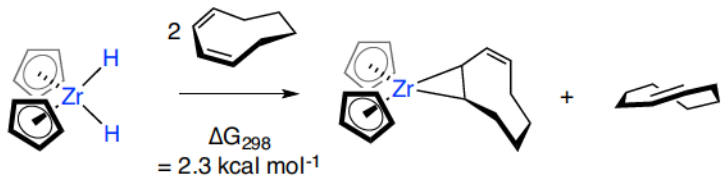


Figure 3.11. Rate-determining generation of free zirconocene dihydride from **^{D}Zn•Zr.**

The failure of **^{D}Mg•Zr** to react with the alkynes in Scheme 3.9 (and to convert to **^{D}Mg•10**) could be explained by the difference in the dissociation mechanism and/or energy of the Zr/Mg system. The very loosely bound **^{M}Al•Zr** gave catalysis of cyclooctadiene isomerisation, rather than **^{M}Al•10** formation, presumably *via* a separate monometallic mechanism. Free and monomeric zirconocene dihydride is likely to react very quickly with unsaturated cyclic hydrocarbons *via* hydrometallation.[60] It has been shown that incoming L-type ligand induces the elimination of alkane from (alkyl)zirconocene hydride complexes.[61] After insertion of a diene C=C bond into the Zr–H bond of zirconocene dihydride, a further equivalent of diene may promote the reductive elimination of cyclooctane. The result is net transfer hydrogenation

by zirconocene dihydride, and formation of a zirconacyclopropane on the resulting {Cp_2Zr^{II}} fragment (Scheme 3.11). As mentioned above, Gibson, Parkin and Bercaw saw simultaneous production of but-1-ene (Scheme 3.1) when they produced a (hydrido)tantallocene η^4-butyne complex from buta-1,3-diene and [$Cp^*_2TaH_3$]. The sterically unencumbered {Cp_2Zr^{II}} may also be able to facilitate η^4-coordination of cycloocta-1,3-diene.[62]



Scheme 3.11. Transfer hydrogenation of 1,3-COD by zirconocene dihydride.

Scrutiny of the product mixture in the syntheses of **^{D}Zn•10** shows that there is an approximate 1:1 ratio of product to cycloctene. For example, for the 85% yield of **^{D}Zn•10** from reaction of 1,5-COD with **^{D}Zn•Zr** (Scheme 3.2), there is around 1.2 equivalents of cycloctene. The same ratio is seen for the experiment using large excesses of 1,3-COD (Table 3.4). This evidence seems to support the reliance of the mechanism upon transfer hydrogenation by free zirconocene dihydride. With supposedly relatively low kinetic barriers for the coordination and hydrometallation of 1,3-COD, its concentration should not appear in the rate equation – especially if it is after the rate-determining step. From the produced zirconacyclopropane, a π-allyl mechanism of diene isomerisation is proposed (Figure 3.12), which ends with recombination of the Zn and Zr fragments (Figure 3.13). This reaction is thus described as a 'hetereobimetallic rebound mechanism' on account of the final Zr/Zn 'rebound' step. The C–H bond cleavage steps can be viewed as sp^2-β-hydride elimination. There is no reason that the chain walking could not start on 1,5-COD and also reach the alkyne (*via* 1,4- and 1,3-COD).

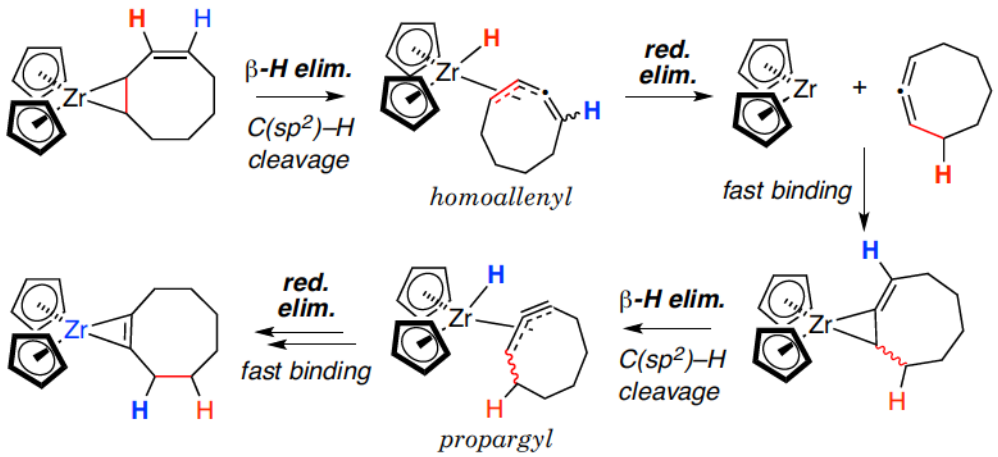


Figure 3.12. Mechanistic hypothesis for the diene-to-alkyne isomerisation of 1,3-COD on zirconcocene.

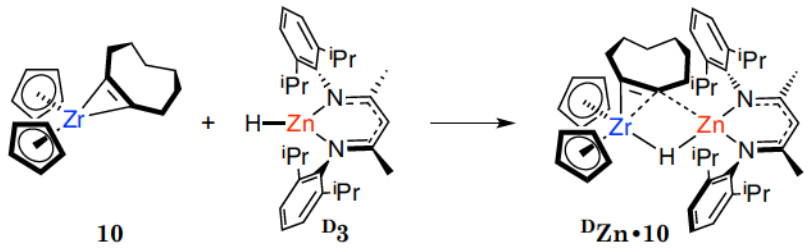


Figure 3.13. The 'rebound' step whereby zirconacyclopropene and main group hydride fragments reassociate to form the product.

The hypothetical mechanism is thus divided into four general stages: (i) dissociation of the heterobimetallic complex; (ii) transfer hydrogenation to eliminate two H atoms from the zirconocene; (iii) the diene-to-alkyne isomerisation; and (iv) the 'rebound' association of **10** with ^{D}**3**. Whilst the combination of fundamental steps in the third stage has been previously proposed for group 4 systems,[19] precedent cannot be found for the production of an alkyne by this route. With this in mind, the basic premise of the π-allyl mechanism – specifically the unusual C(sp^2)–H cleavage *en route* to rare diene-to-alkyne isomerisation – has been scrutinised by a preliminary DFT study (section 3.3.2). The analysis ignores (at this stage in the study) the fundamental steps involved in the transfer hydrogenation of the diene and formation of the 1,3-COD complex of Cp_2Zr. We may assume for now that energy barriers for the hydrometallation steps are relatively small.[59]

3.3.2 C(sp^2)–H Cleavage Theoretical Investigation

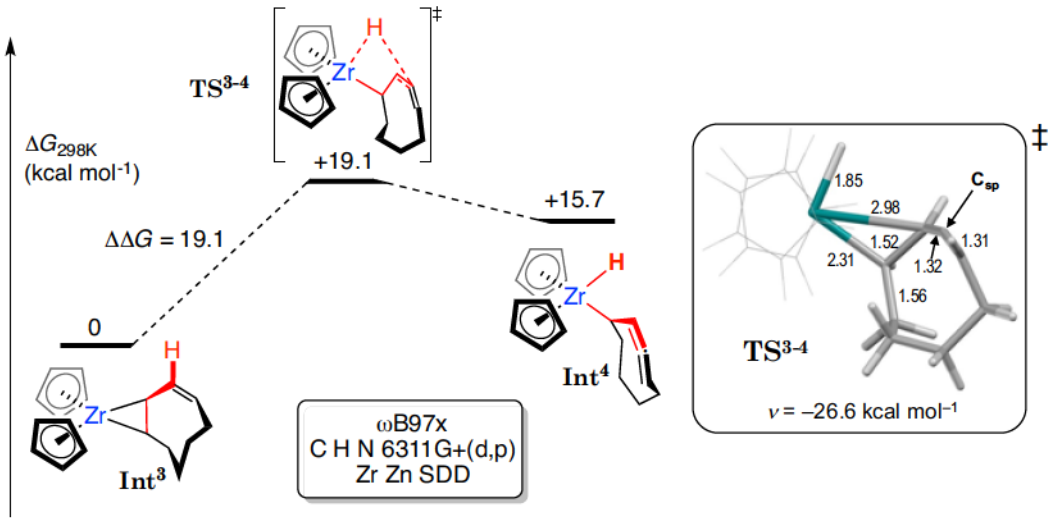


Figure 3.14. The activation of a C(sp^2)–H bond in bound cycloocta-1,3-diene by β-hydride elimination, as calculated by DFT.

The diene to alkyne isomerisation section of the reaction begins with **Int**^{3} in Figure 3.14. (It is preceded by transfer hydrogenation from **Zr**, where **Int**^{1} = Cp_2ZrH_2•(η^2-1,3-COD) and **Int**^{2} =

Cp_2Zr). The C(sp^2)–H β-hydride elimination energy barrier was found to be 19.1 kcal mol^{-1}. This is a surprisingly modest magnitude considering the strained-looking twist in the organic ring of the transition state (**TS$^{3–4}$**). **Int^4** was input as the η^3-homoallenyl hydride intermediate, yet it freely optimises to the η^1-isomer. Visual inspection of the optimisation of **Int^4** suggests that steric clash between proximal Cp and homoallenyl ligands is at least part of the reason for the η^1 configuration. Nevertheless, this structure is scarcely more stable than **TS$^{3–4}$** and accordingly, **TS$^{3–4}$** is a late transition state by appearance. For example, the Zr–H and Zr–C_α bonds in **Int^4** are the same length as in **TS$^{3–4}$**. The following reductive elimination steps (**Int^4** → **Int^2** + cycloocta-1,2-diene) are ignored here; there is likely to be a substantial thermodynamic penalty to separation of the fragments, but incoming C=C ligand is known to be rate-accelerating and would not necessarily appear in the rate equation.[56,63] A strong rebinding energy to give the η^2-cycloocta-1,2-diene complex (**Int^5**) is also predicted.

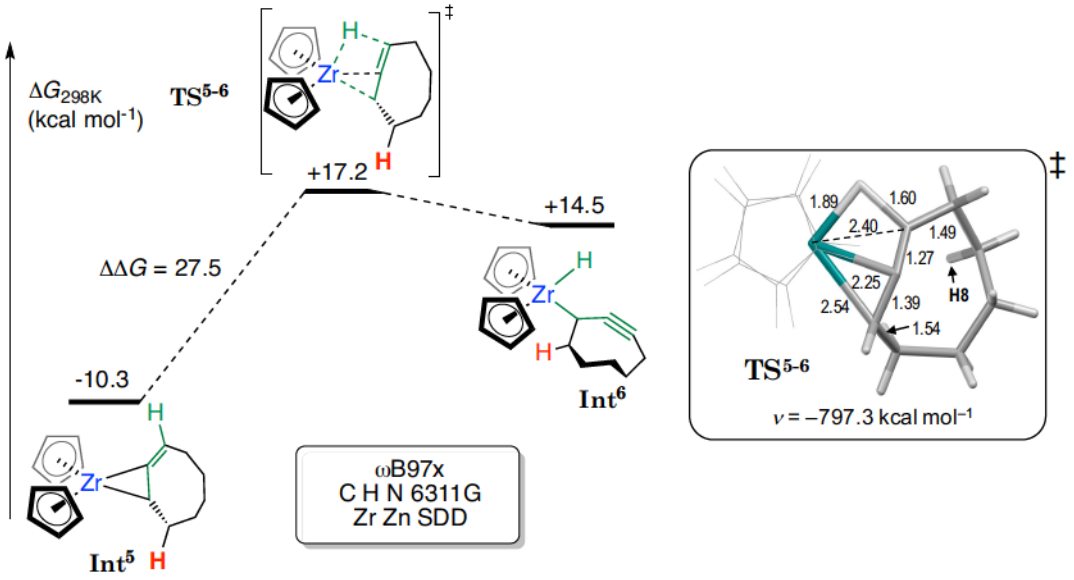


Figure 3.15. The activation of a C(sp^2)–H bond in bound cycloocta-1,2-diene by β-hydride elimination, as calculated by DFT, and the relative energy of the zirconacylopropene **10**, formed by propargyl reductive elimination.

The η^2-cycloocta-1,2-diene complex, **Int^5**, is 10.3 kcal mol^{-1} more stable than **Int^3** (Figure 3.15). The η^2-cycloocta-1,3-diene found in **Int^3** is tipped out towards a Cp group, causing some short contacts between H and C atoms (*ca.* 2.6 Å). Contrastingly, the ring system in **Int^5** keeps flat and equidistant from the Cp ligands. Moreover, ring strain from the allene moiety is relieved by the η^2-binding, explaining the relative stability. At 27.5 kcal mol^{-1}, the barrier height for **Int^5**→**TS$^{5-6}$** is 8.4 kcal mol^{-1} larger than the previous β-hydride elimination step: **Int^3**→**TS$^{3-4}$**. As the alkyne bond develops and forms a strained η^2/η^3-transition state, the C_8H_{12} ring is forced to buckle towards a Cp ligand and make destabilising short contacts again. It is predicted that

Int^{5}→**TS**$^{5\text{-}6}$ will be the highest kinetic barrier on the complete reaction potential energy surface, but it is not so high as to preclude the "π-allyl" mechanism by itself. As with **TS**$^{3\text{-}4}$→**Int**^{4}, the succeeding intermediate (**Int**^{6}) is only slightly lower in energy. However, in this case, the late transition state is visibly very different from the resulting intermediate, in which is the propargyl ligand is η^1 bound.

Intermediate **10** is 32.4 kcal mol^{-1} more stable than **Int**^{6}. It can be feasibly produced by reductive elimination, and rebinding of the cycloalkyne (steps not yet calculated or shown on Figure 3.15). Like the allene analogue, the bound alkyne is more stable than the bound diene. This continues the succession of evermore stable η^2-intermediates. From experiment, the stability of **10** is not sufficient to see it observed in the reaction of cyclooctadiene with **Zr•Zr**. In the reaction mixture, the unsaturated Zr centre in **10** is liable to kinetic instability. Therefore, crucially, the heterobimetallic rebound capture of **10** (Figure 3.13) confers complete stability on the zirconocene. The binding event **10** + ^{D}**3**, as calculated in Figure 3.8, has a free energy change of around –11.5 kcal mol^{-1}. This ought to be the thermodynamic sink that causes the procession across the unfavourable barriers of **TS**$^{3\text{–}4}$ and **TS**$^{5\text{–}6}$ and away from ^{D}**Zn•Zr** and the kinetically unstable intermediates.

3.3.3 Selectivity and By-products

3.3.3.1 By-Products

Cyclooctadienes

The proposed mechanism gives an interesting perspective on the coming together of [^{Dipp}*BDI*MH] and **10**. The product ^{D}**Zn•10** is effectively a partial insertion of the Zn–H bond into a Zr–C bond of the **10**. Were [^{Dipp}*BDI*ZnH] to attempt an "early rebound" and reinsert at earlier points in the mechanism,[64] it would likely suffer from steric clash and/or conformational contorsion.

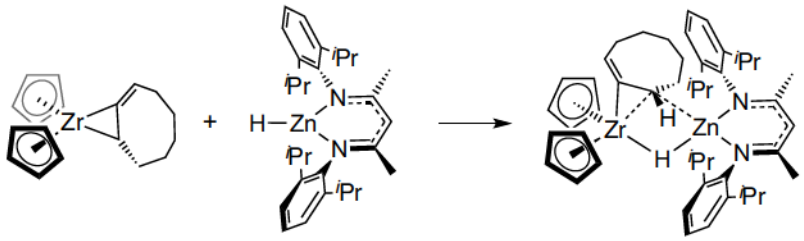


Figure 3.16. Theoretical formation of an Zr/Zn μ^2:η^2-cycloallene complex related to ^{D}**Zn•10**, after Parkin and co-workers.[37]

Nevertheless, recombination of Zn and Zr fragments at the η^2-allene complex (Figure 3.16) is a possibility considering the five-coordinate bridging vinylic carbon of **1.80** (see Chapter

1).[37] Such a bridging alkene would have less of a problem fitting into the cleft between the Dipp groups on the chelate ligand, and ring strain in the allene would be lessened. The potential for this species should be investigated in future computational work.

*Other Substrates & the Generation of [^{Dipp}BDI*ZnPh*]*

It is speculated that loss in yield of **^{D}Zn•10** is due to unwanted products formed from insertion of bonds into the Zr–C[54] or Zr–H bonds of the various intermediates. For instance, the insertion of a C=C bond into a zirconacylopropene was implied by the result in Scheme 3.9. Thus, a zirconacyclopentadiene was formed from two oct-4-yne molecules. This has previously been observed as an unwanted by-product from a reaction mixture containing oct-4-yne and {Cp_2Zr^{II}}.[53] With the cyclohexadiene substrates, disproportionation was seen. Literature precedent has suggested this can occur at the π-allyl intermediate,[19] through insertion of a second molecule of cyclohexadiene inserting into the Zr–H bond.

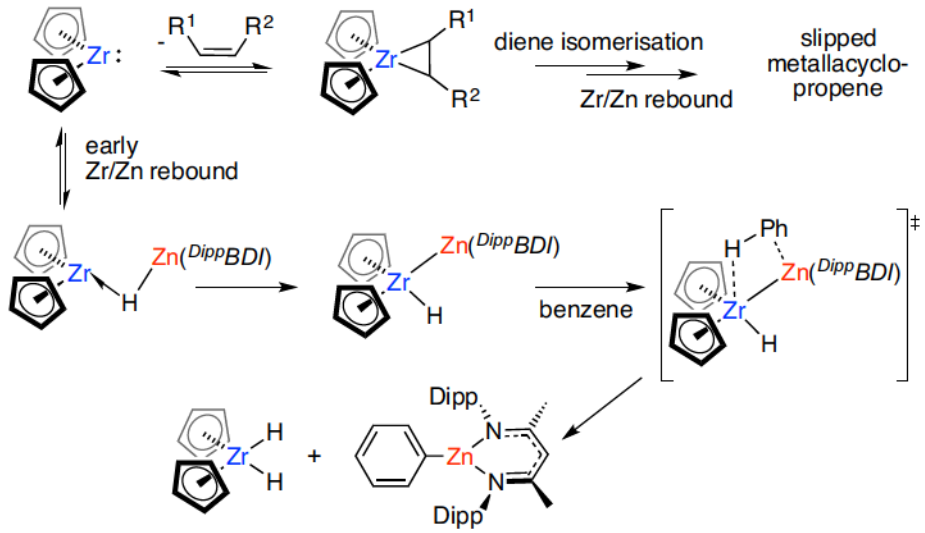


Figure 3.17. A route to [^{Dipp}*BDI*ZnPh] during reaction of **^{D}Zn•Zr** with alkene, stemming from 'early rebound' of Zr and Zn fragments.

The existence of {Cp_2Zr^{II}} in the systems means that oxidative addition of Zn–H across Zr is possible.[69] In the cases of cyclooctene and the cyclohexadienes, the amount of alkene or alkyne ligands drops drastically due to hydrometallation processes. Thus, the {Cp_2Zr^{II}} fragment is more vulnerable to attack by Zn–H. Figure 3.17 shows how formation of a direct Zr–Zn bond gives one explanation for the production of [^{Dipp}*BDI*ZnPh]. Activation of aryl C–H bonds by metallocene-bound main group metal fragments was noted in Chapter 1 (compounds **1.20**, **1.31**, **1.44**).[70-72] All previous reported examples have been intramolecular. Benzene (deutero- or proteo-) acts as a hydride source for Zr, which can continue to hydrometallate and transfer hydrogenate. It should be interesting to see if C–H activation occurs in alkane solutions. In the reactivity of Zr^{II} metallocenes, the non-innocence of the Cp

ligands (specifically the C–H bonds) also offers many routes for decomposition.[18,31,56,65-68] Direct oxidative addition of Ph–H to {Cp_2Zr^{II}} is possible: phenyl ligand exchange would then generate [^{Dipp}*BDI*ZnPh] (see discussion surrounding Scheme 3.10b).

3.3.3.2 The Heterobimetallic Effect with Zinc

The Gibbs free energy change is –11.5 kcal mol^{-1} for the association of the Zn–H ligand with **10** (not including a dispersion correction, with which the binding can be expected to be stronger). In comparison, the analogous event for [^{Dipp}*BDI*MgH] is twice as exergonic (ΔG_{298K} = –22.5 kcal mol^{-1}). If **10** and {^{Dipp}*BDI*MgH} were formed in any significant concentration when ^{D}**Mg•Zr** is reacted with cycloctadiene then ^{D}**Mg•10** should be observed. Therefore, the selectivity of the Zn/Zr system for this reaction should not be derived from the rebound step.

However, it is possible that {^{D}**2**} may be bound up in [^{Dipp}*BDI*MgH]$_2$, which is itself –22.4 kcal mol^{-1} more stable than its monomeric fragment (ΔG_{298K}, including dispersion forces, from section 2.3.1.2), and hence weakened in its Gibbs free energy of binding of **10**. Notwithstanding, Scheme 3.3 crucially showed that, under reaction conditions, [^{Dipp}*BDI*MgH]$_2$ can slowly replace [^{Dipp}*BDI*ZnH] from ^{D}**Zn•10**. Neither [^{Dipp}*BDI*MgH]$_2$ or ^{D}**Zn•10** would be very good electrophiles/nucleophiles in an associative substitution mechanism, considering their cumbersome steric loading. A dissociative equilibrium between **10** and [^{Dipp}*BDI*ZnH] is therefore assumed.

So, if the selectivity does not hinge upon the rebound event, we may predict that the dissociative equilibrium between [^{Dipp}*BDI*MH] and **Zr** differentiates between the two types of isomerisation reaction shown in Table 3.1 and Scheme 3.2. Kinetics experiments have shown that this dissociation cannot depend upon the concentration of incoming alkene substrate. Calculations in Chapter 2 have shown that the dissociation constant for [*BDI*MH]•**Zr** decreases in the order Mg > Zn >> Al(H) (where *BDI* = ^{Dipp}*BDI* for Mg and Zn, and *BDI* = ^{Mes}*BDI* for Al(H)). It appears that for ^{D}**Zn•Zr**, **Zr** is available to operate a monometallic diene-to-alkyne isomerisation mechanism, being not too tightly bound (*cf.* Mg). The Zr alkyne complex formed in this mechanism is additionally able to be trapped by the main group fragment, having not too loose an affinity (*cf.* Al(H)).

3.4 CONCLUSIONS

This study has uncovered the production and isolation of a Zn/Zr slipped metallocene (^{D}**Zn•10**) of the type pioneered by Erker and Rosenthal in the last quarter of a century. Outstandingly, this is the first Zn main group fragment example, the first example in which that fragment is sterically bulky, the first example not to use an alkyne starting material, and the first example to be formed from a heterobimetallic complex. The synthesis of ^{D}**Zn•10** is only the second example of diene-to-alkyne isomerisation. Further analogues have been developed by varying the alkyne, and substituting the zinc fragment of the complex with a magnesium one. The resulting Mg/Zr analogue is the first example of a slipped zirconocene formed by fragment substitution. It also proved that the mechanism, rather than the thermodynamics, is crucial in the unique success of ^{D}**Zn•10** formation by the diene isomerisation route.

Mechanistic experiments and calculations have pointed towards a π-allyl hydride path to ^{D}**Zn•10**, which is conducted by a monometallic zirconocene complex. It has been inferred that overly tight and overly loose binding of the Mg/Zr and Al/Zr heterobimetallic hydride complexes defers their reactivity to that of regular diene isomerisation catalysis by different mechanism(s). Whether or not the mechanistic proposal is correct does not detract from a surprising conclusion; in the catalytic isomerisation of dienes, alkyne-containing intermediates are possible off-cycle. This report is possibly an exceptional case of their stoichiometric observation due to the binding by a zinc hydride complex and the favourable mechanistic landscape prior to that event.

3.4.1 Future Work

3.4.1.1 Theoretical Studies

The immediate concern of future work should be to complete a full computational study on the proposed mechanism of the diene-to-alkyne isomerisation. Notably, this should include a) careful deduction of the rate-limiting step and b) a considered comparison of C(sp^3)–H vs. C(sp^2)–H β-hydride elimination, as the latter is particularly rare. Detailed reports have not been found. The other general issue for DFT study is the range of alternative possibilities for the active organometallic species in the on-metal isomerisation. Anti-hypotheses need to be considered, *inter alia* the survival of a Zn/Zr complex throughout, and the M–H insertion-elimination mechanism.

3.4.1.2 Diene/Alkyne Variation

Results in section 3.2.4 (^{D}**Zn•11** and ^{D}**Zn•12**) have shown that the slipped metallacyclopropene moiety is available for at least two other zirconacyclopropene fragments.

Comparison of the rate constant for these two reactions (to the cycloocta-1,3-diene reaction) should confirm or rule out the current mechanistic hypothesis. Identical rate constants would indicate that the diene/alkyne moiety plays no part in the rate-limiting step. Such a result would therefore heavily favour the dissociation of ^{D}**Zn•Zr** as the slowest step.

The putative reaction mechanism may be blocked with use of dienes containing tertiary carbons, norborna-2,5-diene and 4-vinylcyclohexane being two such candidates. Intermediates related to **Int^{5}** or the product in Figure 3.16 may become observable as a result.

3.4.1.3 Experimental Work on Zr

There are still areas in which the experimental work done thus far can be expanded and developed. The main concern of these experiments should be the interrogation of {Cp_2Zr^{II}} as a functional part of the mechanism. Primarily, this should involve refined attempts to create synthons and traps for this low-valent intermediate and its related structures (*cf.* section 3.2.4.3); treatment with cyclooctadienes and/or ^{D}**3** should follow. For example, phosphine adducts of **10** or earlier intermediates may be attainable through routes developed by Buchwald,[36,45,73] and benzyne and cyclohexyne analogues of ^{D}**Zn•10** could be possible through these approaches. The Negishi reagent method is yet to be tried,[74,75] and advances are still being made in the area of Zr^{II} synthon generation.[76] In the photolysis of [Cp_2ZrPh_2] with ^{D}**3**, phosphine coordination or even hydrometallation traps may be able to arrest Zr/Zn intermediates. An in-probe kinetics experiment with a large excess of cycloocta-1,3-diene may show signs of disruption if PMe_3 were also present in excess or with use of a coordinating solvent; Schwartz and Gell have noted the ability of phosphines to induce reductive elimination of alkane from (hydrido)zirconocene alkyl complexes.[56]

Qian *et al*. have used variable-temperature hydrolysis experiments to quench the reaction mixture at different stages of progression.[77] By analysing the hydrolysed mixture for diene or alkene products, differentiation between the two general mechanisms (Figure 3.2) is theoretically possible. Possible paramagnetic species in the formation of ^{D}**Zn•10** could be investigated at a later stage, if further results demand it.

3.4.1.4 Heterobimetallic Effects with Al/Zr and Mg/Zr Systems

The monomeric zirconocene dihydride – supposedly accessible – is evidently on the wrong side of the minuscule dissociation constant of ^{D}**Zn•Zr** (and **Zr•Zr**). This makes its study problematic, and only small indirect evidence suggests ^{D}**Zn•Zr** completely dissociates at all. In the case of ^{M}**Al•Zr** complete dissociation is assured; no ^{M}**Al•Zr** and no obvious bridging hydride signals are seen in the ^{1}H NMR spectra of the active reaction mixture for 1,5-COD isomerisation. This has been discounted as a related mechanism, but cooling, slowing and probing of the reaction may provide general conclusions. At the other extreme lies ^{D}**Mg•Zr**, showing less dissociation than ^{D}**Zn•Zr**. Alkyne intermediates could be produced in its

isomerisation of 1,5- to 1,3-COD, and this might be trapped with addition of ^{D}**3** to the active reaction mixture. Unfortunately, practicalities do not allow quality kinetic analysis of either Mg/Zr or Al/Zr cycloocta-1,5-diene isomerisation.

The evidence for {Cp_2Zr^{II}} (and the hydrogenation of ^{D}**Zn•10**) suggests that the Zn/Zr system may be employable as a hydrogenation catalyst. Gratifyingly, a test experiment has shown that the reaction of 1,5-COD and ^{D}**Zn•Zr** under H_2 atmosphere increases the intensity of the cyclooctane signal relative to the N_2 atmosphere reaction. Of course, the series of M/Zr complexes are all candidates for investigation of catalysts for hydrogenation technologies.

3.4.1.5 Wider Work

The proposed mechanism is distinct from the M–H insertion-elimination ascribed to the previous diene-to-alkyne isomerisation example. Reviewing the 25-year-old report finds no results that completely rule out the π-allyl mechanism. With a full computational study on the mechanism of ^{D}**Zn•10** formation, a parallel study of [Cp^*_2Ta(H)(MeC≡CMe)] (Scheme 3.1a) would be particularly interesting: could {Cp^*_2TaH} isomerise cyclooctadiene and other dienes?

3.5 EXPERIMENTAL

3.5.1 General

All manipulations were carried out using standard Schlenk-line and glovebox techniques under an inert atmosphere of argon or dinitogen. A MBraun Labmaster glovebox was employed, operating at <0.1 ppm O_2 and <0.1 ppm H_2O. Solvents were dried over activated alumina from an SPS (solvent purification system) based upon the Grubbs design and degassed before use. Glassware was dried for 12 h at 120 °C prior to use. Benzene-d_6 and toluene-d_8 were stored over molecular sieves and distilled prior to use. NMR-scale reactions were conducted in J. Young's tap tubes and prepared in a glovebox. All heating mentioned was done using silicone oil baths. ^{1}H, ^{13}C, and ^{31}P NMR spectra were obtained on BRUKER 400 MHz or 500 MHz machines unless otherwise stated; all peak intensities are derived against an internal standard peak (^{1}H $\underline{Cp_2}Fe$ δ = 4.00 ppm) with values quoted in ppm. Data was processed using the MestReNova software. Elemental analyses were carried out by Stephen Boyer at London Metropolitan Univeristy.

3.5.1.1 Materials

Hydrocarbons were dried over activated 3 Å molecular sieves and freeze-pump-thaw degassed before use. All other chemicals were purchased from Sigma Aldrich and used without purification unless stated.

3.5.2 Preparative-scale Synthesis

Synthesis of $\underline{^{D}Zn \bullet 10}$

In a glovebox 84 mg of **^{D}Zn•Zr** (0.119 mmol) was weighed in a 2 mL glass scintillation vial. The material was slurried in 700 μL of C_6D_6 and 2–3 mg of ferrocene added (as internal standard for quantification). The reaction mixture was transferred by Pasteur pipette into a J Young NMR tube. 1,5-Cyclooctadiene (95 μL, 0.772 mmol, 6.5 equiv.) was then added to the reaction mixture by calibrated pipette. The NMR tube was sealed and removed from the glovebox. The reaction mixture was heated in an oil bath at 80 °C for 24 h and the course of the reaction monitored by ^{1}H NMR spectroscopy (giving an 85% yield of **^{D}Zn•10** by internal standard). The NMR tube was returned to the glovebox, and the mixture was transferred to a 20 mL scintillation vial. The solution was concentrated *in vacuo*, leaving a yellow solid. The crude material was triturated with 2 mL of *n*-hexane; the resulting yellow supernatant liquid was decanted and the remaining material recrystallised from toluene at –35 °C. The colourless crystalline solid **^{D}Zn•10** was collected as three crops (24.6 mg, 0.296 mmol, 25%). ^{1}H NMR

data (C_6D_6, 298K, 500 MHz): δ –1.22 (s, 1H, Zr*H*), 1.12 (d, 6H, *J* = 6.5 Hz, CH*Me*$_2$), 1.25 (d, 12H, *J* = 6.5 Hz, CH*Me*$_2$), 1.43–1.47 (m, 2H), 1.62 (d, 6H, *J* = 6.5 Hz), 1.72 (s, 6H, (NC*Me*)$_2$), 1.70–1.76 (m, 2H), 1.92–1.98 (m, 2H), 3.15-3.18 (m, 4H), 3.21 (heptet, 2H, *J* = 6.5 Hz), 3.79 (heptet, 2H, *J* = 6.5 Hz), 4.87 (s, 1H, C*H*), 4.91 (s, 10H, Cp*H*), 7.06-7.13 (m, 4H, Ar*H*), 7.22 (d, 2H, *J* = 7.5 Hz) ppm. ^{13}C NMR data (C_6D_6, 298K, 100 MHz): δ24.3 (CH*Me*$_2$), 24.4 (CH*Me*$_2$), 24.8 ((NC*Me*)$_2$), 25.3 (CH*Me*$_2$), 25.5 (CH*Me*$_2$), 25.6 (*C*H$_2$), 27.5 (*C*H$_2$), 27.6 (*C*H$_2$), 28.3 (*C*HMe$_2$), 29.0 (*C*HMe$_2$), 29.2 (*C*H$_2$), 34.0 (*C*H$_2$), 37.0 (*C*H$_2$), 95.2 (*C*H), 102.6 (*Cp*), 111.9 (*C*≡*C*), 124.2 (*Ar*H), 124.6 (*Ar*H), 126.1 (*Ar*H), 142.6 (quart. *Ar*), 143.0 (quart. *Ar*), 147.0 (quart. *Ar*), 167.4 (*C*=N), 184.3 (*C*≡*C*) ppm. Infrared (solid, cm^{-1}) 3128 (w), 3064 (w), 2960 (m), 2918 (m), 2868 (m), 1612 (w), 1547 (m), 1519 (m), 1432 (s), 1404 (s), 1360 (m), 1311 (s), 1229 (m), 1175 (m), 1097 (m), 1059 (w), 1021 (m). Repeated attempts to acquire satisfactory CHN analysis failed due to the air and moisture sensitive nature of this complex.

Synthesis of ^{D}*Zn•11*

The procedure carried out was the same as with **^{D}Zn•11**, only with less starting material; 20 mg of **^{D}Zn•Zr** (0.056 mmol) was weighed in a 4 mL glass scintillation vial. The material was dissolved in 0.5 mL of benzene-d_6. Added were 20 μL (0.353 mmol, 6.5 equiv.) of cyclohepta-1,3-diene. The colourless crystalline solid **^{D}Zn•11** was collected (4.6 mg, 0.028 mmol, 20%). ^{1}H NMR data (C_6D_6, 298K, 400 MHz): δ –1.07 (s, 1H, ZrH), 1.09 (d, 6H, *J* = 6.5 Hz, CH*Me*$_2$), 1.22 (d, 6H, *J* = 6.5 Hz, CH*Me*$_2$), 1.24 (d, 6H, *J* = 6.5 Hz, CH*Me*$_2$), 1.63 (d, 6H, *J* = 6.5 Hz, CH*Me*$_2$), 1.61–1.69 (m, 2H), 1.71 (s, 6H, (NC*Me*)$_2$), 1.72–1.78 (m, 4H), 2.79-2.85 (m, 2H), 3.05–3.11 (m, 4H), 3.16 (heptet, 2H, *J* = 6.5 Hz), 3.79 (heptet, 2H, *J* = 6.5 Hz), 4.85 (s, 1H, CH), 4.89 (s, 10H, CpH), 7.05–7.12 (m, 4H, ArH), 7.22 (d, 2H, J = 7.5, 1.8 Hz) ppm. ^{13}C NMR data (C_6D_6, 298 K, 100 MHz): δ24.3 (CH*Me*$_2$), 24.4 (CH*Me*$_2$), 24.6 ((NC*Me*)$_2$), 25.2 (CH*Me*$_2$), 25.6 (CH*Me*$_2$), 27.8 (*C*HMe$_2$), 29.0 (*C*HMe$_2$), 30.2 (CH$_2$), 31.1 (CH$_2$), 34.5 (CH$_2$), 39.9 (CH$_2$), 95.0 ({N=C}$_2$*CH*), 102.6 (Cp), 111.9 (C≡C), 124.2 (ArH), 124.6 (ArH), 126.1 (ArH), 142.5 (quart. Ar), 143.0 (quart. Ar), 146.9 (quart. Ar), 167.3 (C=N), 189.4 (C≡C) ppm.

Synthesis of Cp$_2$ZrPh$_2$

On a vacuum line, PhMgBr (2.0 M, 7.5 mL, 15 mmol) was transferred to a Schlenk tube by syringe and the solvent removed under reduced pressure. The sample was transferred to a glovebox and Et$_2$O (30 mL) added followed by solid Cp_2ZrCl_2 (2.1 g, 7.18 mmol). A large amount of colourless precipitate formed. The mixture was stirred overnight and the solvent removed under reduced pressure. The solid was washed with *n*-hexane (2 x 20 mL) and then extracted into toluene (20 mL) and filtered. The filtrate was concentrated to half the volume and stored at –20°C to give the product as colourless crystals (0.4 g, 1.1 mmol, 15%). The sample was transferred to the glovebox and stored as a solid at –35 °C. ^{1}H NMR (C_6D_6, 298K,

400 MHz): δ 7.30 (d, *J* = 7.2 4H, *o*-Ph), 7.17 (t, *J* = 7.3, 4H, *m*-Ph), 7.07 (t, *J* = 6.6, 2H, *p*-Ph), 5.91 (s, 10H, *Cp*) ppm. The values agree with the literature report.[78]

3.5.2.1 NMR-scale Catalysis

Catalytic 1,5-COD isomerisation experiment: ^{D}Mg•Zr and ^{D}Zn•10

In a glovebox, 0.009 mmol of bimetallic catalyst was weighed into a 2 mL scintillation vial. The solid was dissolved in 500 μL C_6D_6. Roughly 2-3 mg of ferrocene was added to the vial (as internal standard for quantification). The reaction mixture was transferred to an NMR tube and cycloocta-1,5-diene (0.185 mmol, 20 equiv.) added directly by calibrated pipette. The reactions were heated to 80 °C in an oil bath. The products were confirmed by spiking product mixtures with genuine product. The combined cycloocta-1,3-diene and cyclooctene yield was calculated from ^{1}H NMR spectroscopy *in situ* (C_6D_6). Before the tube was heated to 80 °C, the substrate, cycloocta-1,5-diene, was integrated over the signal δ = 2.21 ppm (8H, 4x{-CH_2-}, m); the combined cycloocta-1,3-diene and cyclooctene yield was based on the integration of their conjoined peaks in the window 2.15–2.03 ppm (both multiplet peaks representing 4 H, 2x{-CH_2-}). Amounts of cycloocta-1,4-diene were calculated based on integration of an alkene proton multiplet resonance at δ = 5.42–5.31 ppm.[79] Cyclooctane was observed as a sharp singlet at δ = 1.49 ppm.[80]

A repeat of this procedure was adapted for making an estimate of *TON*. When all of the initial 1,5-COD was consumed, further equivalents were added to the tube back in the glovebox, before monitoring by ^{1}H NMR and heating was continued. The results are illustrated in Figure 3.18.

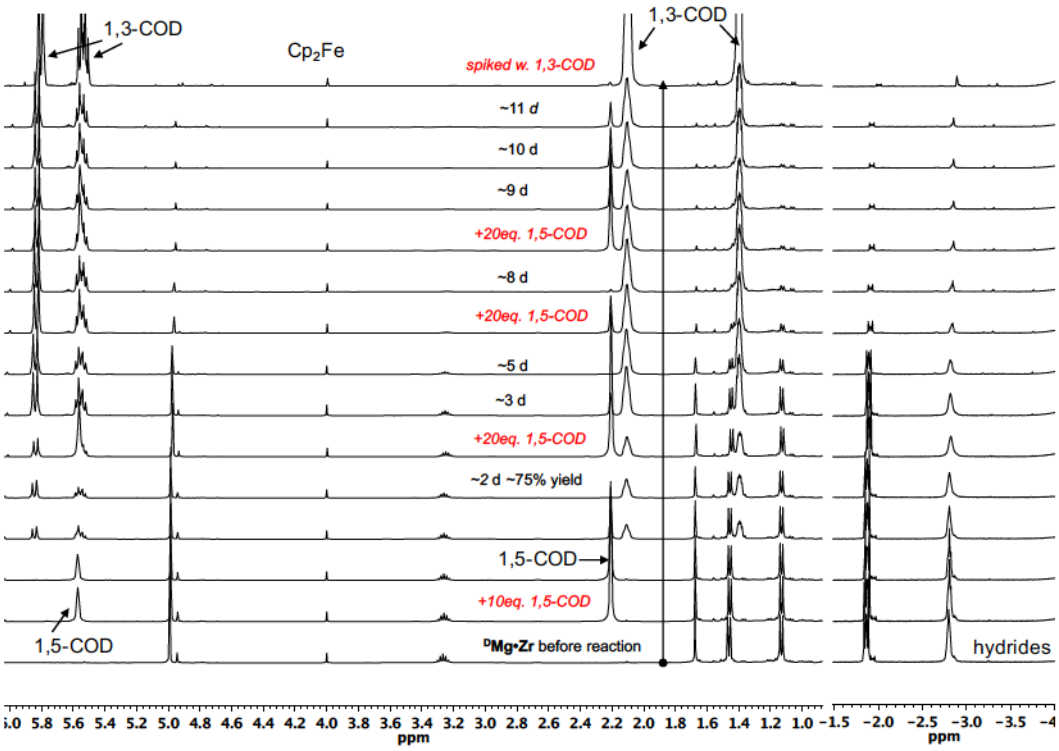


Figure 3.18. ^{1}H NMR stack plot (bottom to top, 293 K, benzene-d_6) of the *TON* estimation for the isomerisation of 1,5- to 1,3-COD by the **^{D}Mg•Zr** catalyst at 80°C.

Catalytic 1,5-COD isomerisation experiment: ^{M}Al•Zr and Zr•Zr

In a glovebox, 500 μL C_6D_6 was transferred to an NMR tube containing 2-3 mg of ferrocene (as internal standard for quantification). The cycloocta-1,5-diene (0.185 mmol, 20 equiv.) was added to the tube by calibrated pipette and a ^{1}H NMR spectrum measured. After returning the NMR tube to the glove box, the required amount of bimetallic (0.005 mmol **Zr•Zr**) was added to the tube. The reaction progress was monitored at 25 °C by ^{1}H NMR spectroscopy. Major products were confirmed by spiking with genuine samples.

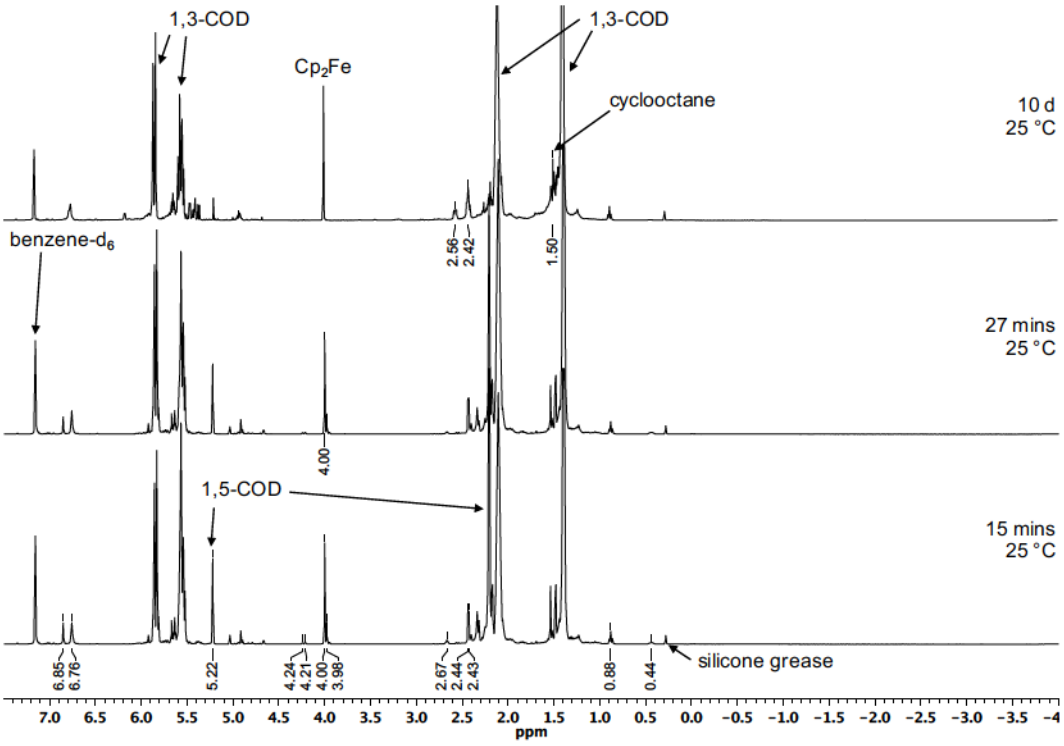


Figure 3.19. Stack plot of ^{1}H NMR data for the reaction of ^{M}**Al•Zr** (5 mol%) with 1,5-COD at 25 °C in benzene-d_6.

3.5.2.2 NMR-scale Reactions

Unless stated otherwise, NMR-scale experiments with yield calculations were carried out by the following general procedure:

In a glovebox, the starting material (yield-determining reactant) was weighed into a 4 mL scintillation vial. The solid was dissolved in 0.5 mL of benzene-d_6, and ferrocene (ca. 2–3 mg) was added to the solution directly by spatula. This mixture was transferred into a J Young NMR tube, and a ^{1}H NMR spectrum collected for the yield calculation purposes. The tube was reopened back inside the glovebox, hydrocarbon reactant added by calibrated pipette, and resealed for the reaction.

Synthesis of ^{D}Mg•10 by Substitution

The starting solution of ^{D}**Zn•10** (20 mg, 0.019 mmol, 1 equiv. in 0.5 mL benzene-d_6) was emptied from the J Young NMR tube into a 4 mL scintillation vial containing weighed ^{D}**2$_2$** (8.5 mg, 0.019 mmol, 1 equiv.). This method of addition was repeated after 48 h of heating at 80°C. Two ^{1}H NMR stack plots of the reaction progress are shown below.

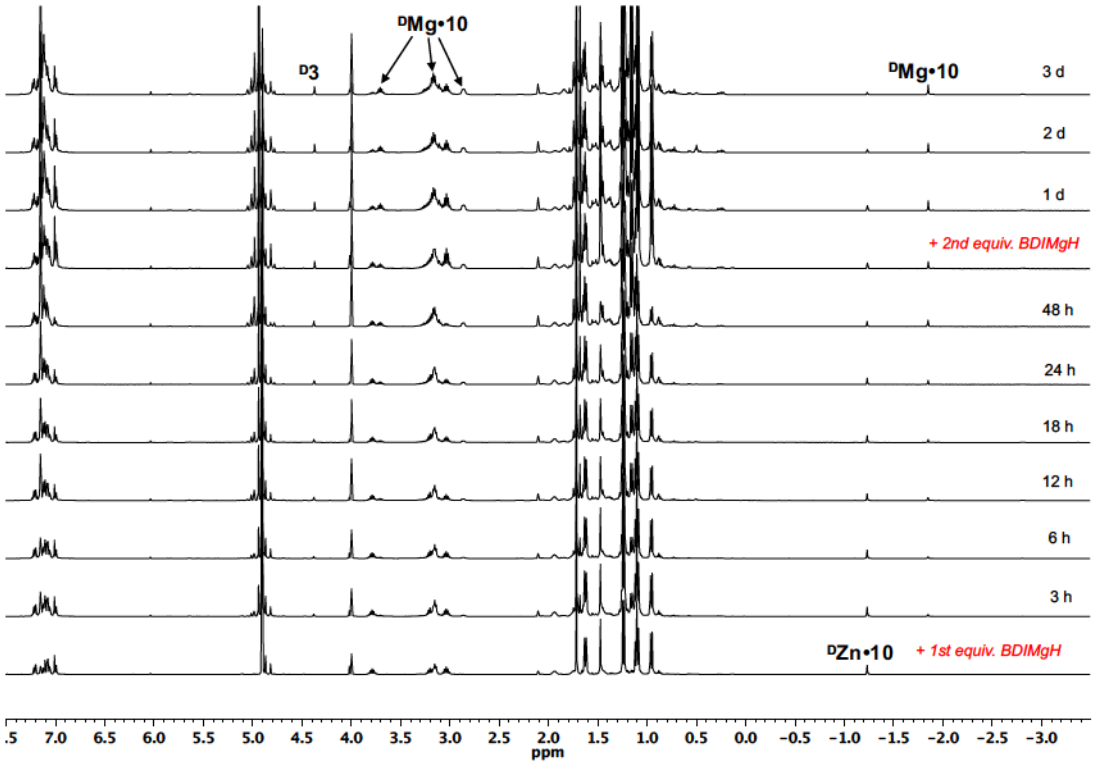


Figure 3.20. Stack plot of ^{1}H NMR data for the heating of ^{D}**Zn•10** at 80°C in the presence of ^{D}**2**$_2$.

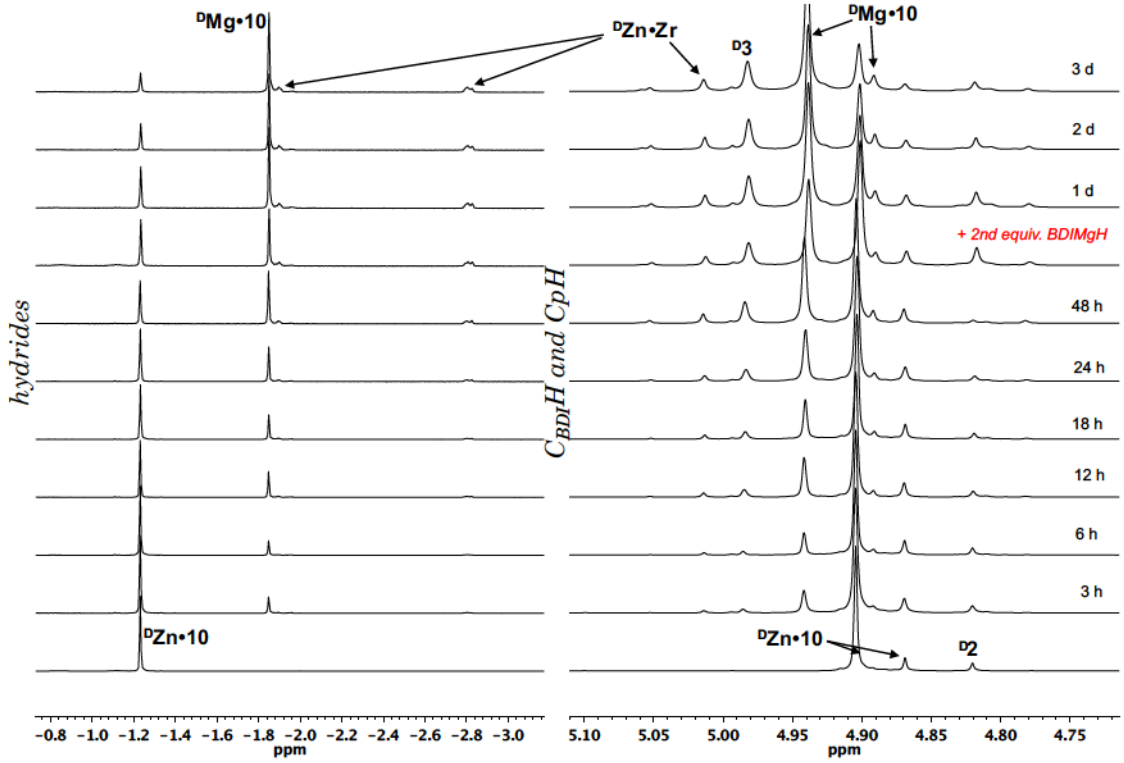


Figure 3.21. Stack plot of ^{1}H NMR spectra (in benzene-d$_6$, 298 K) expansions for the heating of ^{D}**Zn•10** at 80°C in the presence of ^{D}**2**$_2$.

Hydrogenolysis of ^{D}Zn•10

A 0.5 mL benzene-d_6 solution of **^{D}Zn•10** (39 mg, 0.047 mmol) was transferred to a J Young NMR tube by Pasteur pipette, and the tube was sealed and removed from the glovebox. The tube was attached to a vacuum/N_2 manifold, and the solution was freeze-pump-thaw degassed 3 times over. An ^{1}H NMR was taken of the mixture (under an N_2 atmosphere in the tube) before and after this process to check for signs of decomposition from a possible leak in the seal of J Young's tap. The tube was evacuated whilst again frozen, before being reheated to room temperature and dry H_2 (1 atm) released into the headspace. The reaction was heated immediately after H_2 addition (see Scheme 3.4 for results): a 20% yield of [^{Dipp}*BDI*ZnPh] was also returned, judged by the integration of its δ = 5.04 ppm methylylidene resonance. Furthermore, the bridging hydride peaks showed evidence of isotopomers, and therefore involvement of solvolysis.

Kinetics Experiments on ^{D}Zn•10 Production

A stock solution of 94 mg of **^{D}Zn•Zr** in 1 mL benzene-d_6 was made up in a 20 mL scintillation vial. Four 200 μL portions were then withdrawn by calibrated pipette and each injected into a separate J Young NMR tube. A spatula tip of ferrocene (2–3 mg) was dropped into each tube to serve as the ^{1}H NMR internal standard. The solutions were diluted with benzene-d_6**.** The amounts of benzene-d_6 used are collected in Table 3.5. The tubes were sealed and left in the glovebox until the day of the NMR experiment, on which occasion 1,3-COD was added by calibrated pipette. The total volume of every reaction mixture was 0.6 μL, and the concentration of **^{D}Zn•Zr** was 44 mM.

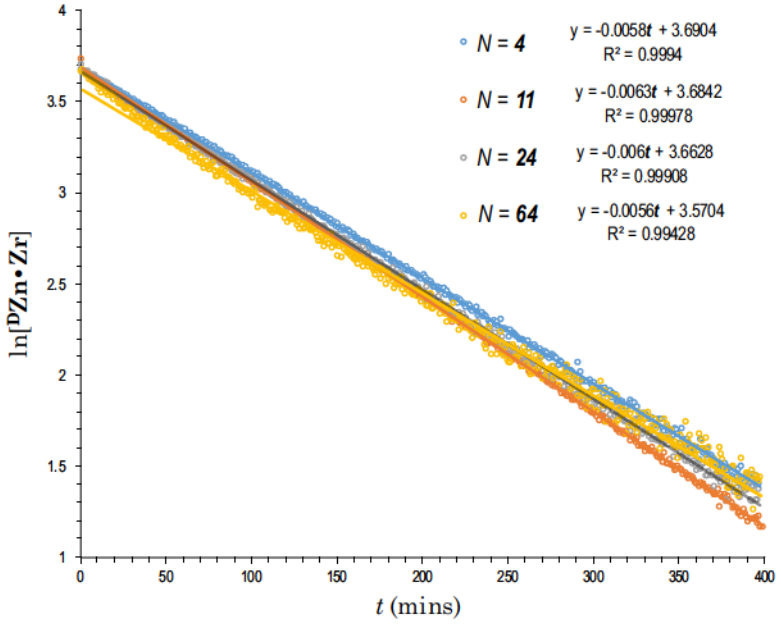
Integrations of the H_μ peak in **^{D}Zn•Zr** (δ = –1.14 (*t*, J = 4.5 Hz) ppm) and **^{D}Zn•10** (δ = –1.22 (*s*) ppm) were followed at high temperature (343–358 K) until at least 87.5% consumption of the former. The cycloocta-1,3-diene:cyclooctene ratio was based on the integration of their respective multiplet peaks at δ = 5.83–5.75 and 5.62–5.57 ppm. No reactivity at room temperature was observed (24 h 25°C), and the tubes were not frozen between the addition of 1,3-COD and the start of the kinetic data. However, all reactions showed a small amount (approximately 5%) of production of **^{D}Zn•10**, seemingly caused by the heating time taken to shim the NMR signals. The ^{1}H NMR experiments were run with 4 scans (-3–9 ppm) per data point. All reactions showed a strange phenomenon in the first few points of in probe ^{1}H NMR data. The initial integrations of the H_μ peak of **^{D}Zn•Zr** were invariably smaller than the values a few points into the experiment. The **^{D}Zn•10** H_μ integration did not suffer from the inverse of this phenomenon *i.e.* greater integrations at the immediate beginning of the reaction than in the following early stages. These data were assumed to be an artefact, and they were not included in the kinetic profile and the analysis. The maximum integration (usually at *t* = 2–4

mins) of this peak was used as the starting point, but the concentration of **^{D}Zn•Zr** was adapted to be <44 mM, based on the amount of **^{D}Zn•10** in the very first real time point.

The significant disagreement between the two measured (80 °C) 11-fold excess k_{obs} values may be due to the different spectrometers used; a 500 MHz machine was used for the relevant order in 1,3-COD run. A 400 MHz machine was used for all other kinetic experiments.

Table 3.5. Amounts used in the kinetic analysis.

	equiv. 1,3-COD	*additional benzene-d_6 (μL)*	*1,3-COD (μL)*	*temp. (°C)*
1,3-COD	4	387	13	80
	11	364	36	80
	24	322	78	80
	64	198	202	80
Eyring	11	364	36	70
	11	364	36	75
	11	364	36	80
	11	364	36	85



Graph 3.4. First-order graphical analysis of the decay of **^{D}Zn•Zr** when reacted with varying excesses of 1,3-COD.

Diene/Alkyne Scope and Controls

^{D}Zn•Zr (20 mg, 0.028 mmol, 1 equiv.) was dissolved in benzene-d_6 (0.5 mL). After taking a pre-reaction ^{1}H NMR spectrum 0.184 mmol (6.5 equiv.) of hydrocarbon substrate were added by calibrated pipette. A ^{1}H NMR spectrum was measured as quickly as possible after mixing of the reactants. In several cases, these spectra showed that the accuracy of the hydrocarbon addition was poor and fewer than 6.5 equiv. has been added. The true excesses of substrate are stated in the relevant schemes.

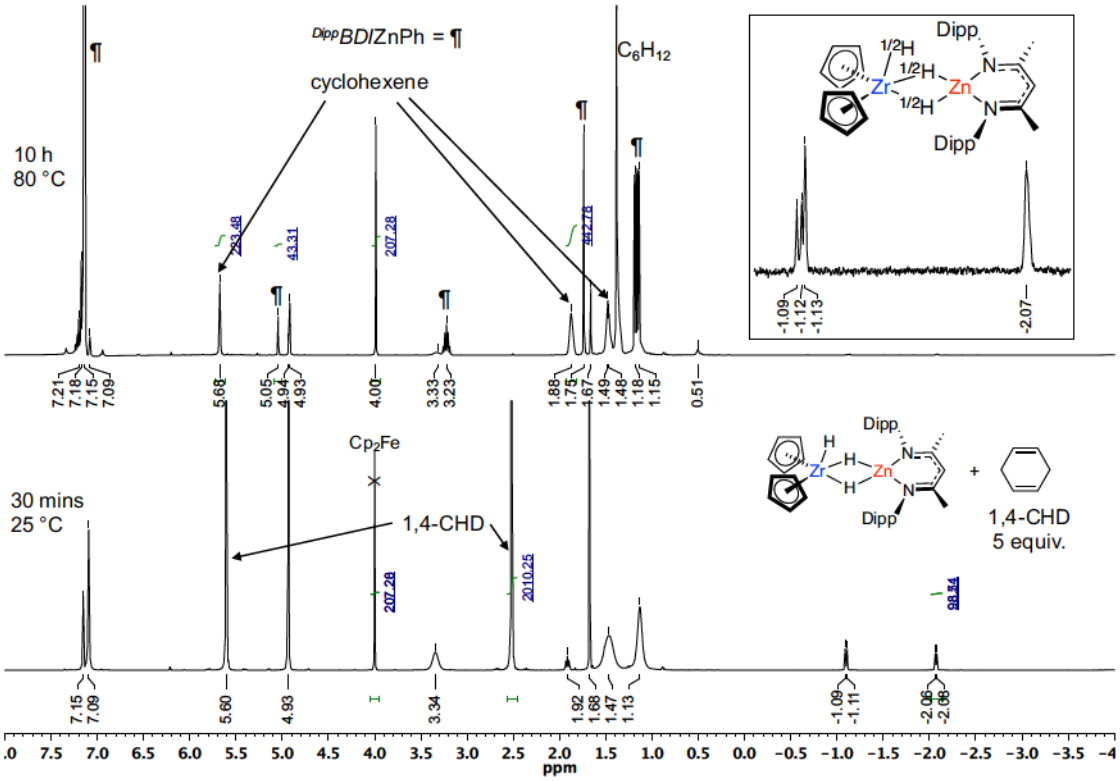


Figure 3.22. ^{1}H NMR (benzene-d_6) stack plot of the 10 h reaction of **^{D}Zn•Zr** with cyclohexa-1,4-diene, including residual bridging hydride signals with putative H/D scrambling (inset).

The cyclohexa-1,3-diene reaction was run for 4 h. Signals for [^{Dipp}*BDI*ZnPh] were checked against those reported in the literature.[81] As a control, it was demonstrated that there is no reactivity between cycloocta-1,5-diene and **^{D}3**. Reactions with octa-1,7-diene and E,E,Z-dodeca-1,5,9-triene are still under investigation. The linear diene may have partly been subject to a known bicyclometallation,[82] but ^{1}H NMR spectra of the crude reaction mixtures are too crowded for meaningful assignment. What can be said is that none but a trace of μ-hydrido complex remains or is formed in either. Insertion chemistry looks to be the dominating and unselective processes at play.

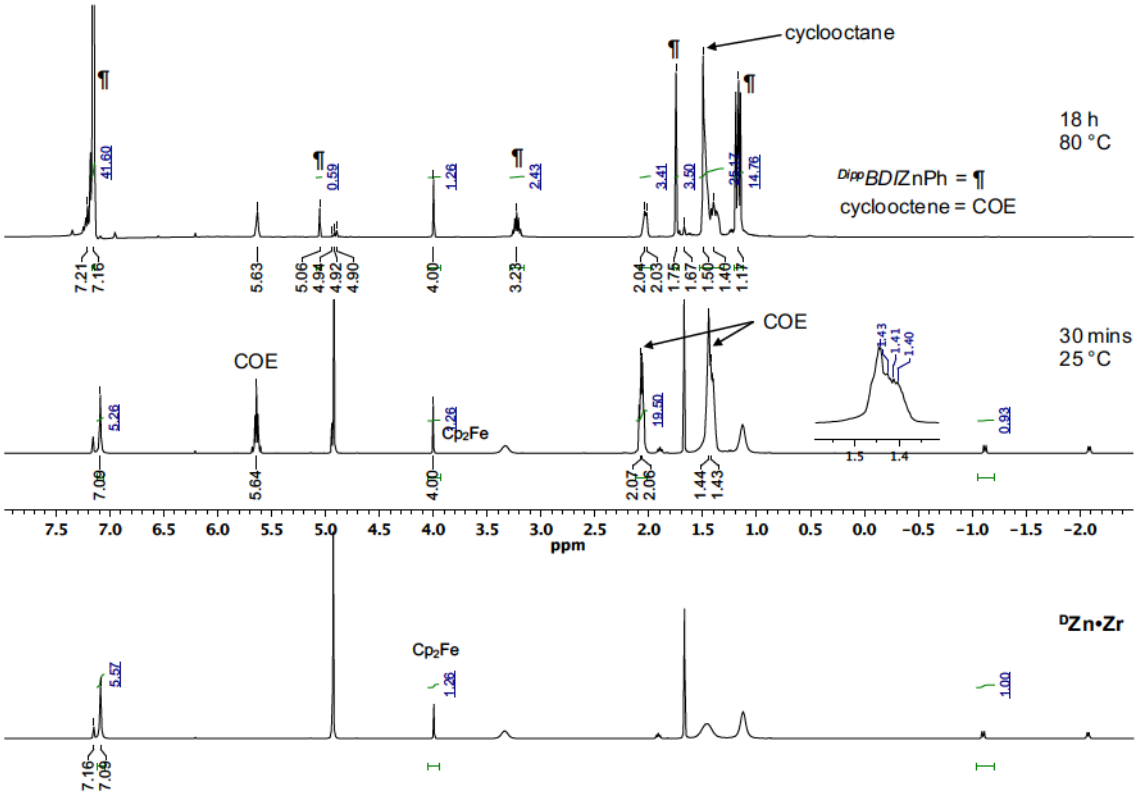


Figure 3.23. ^{1}H NMR (benzene-d_6) stack plot of the reaction of **^{D}Zn•Zr** with cyclooctene.

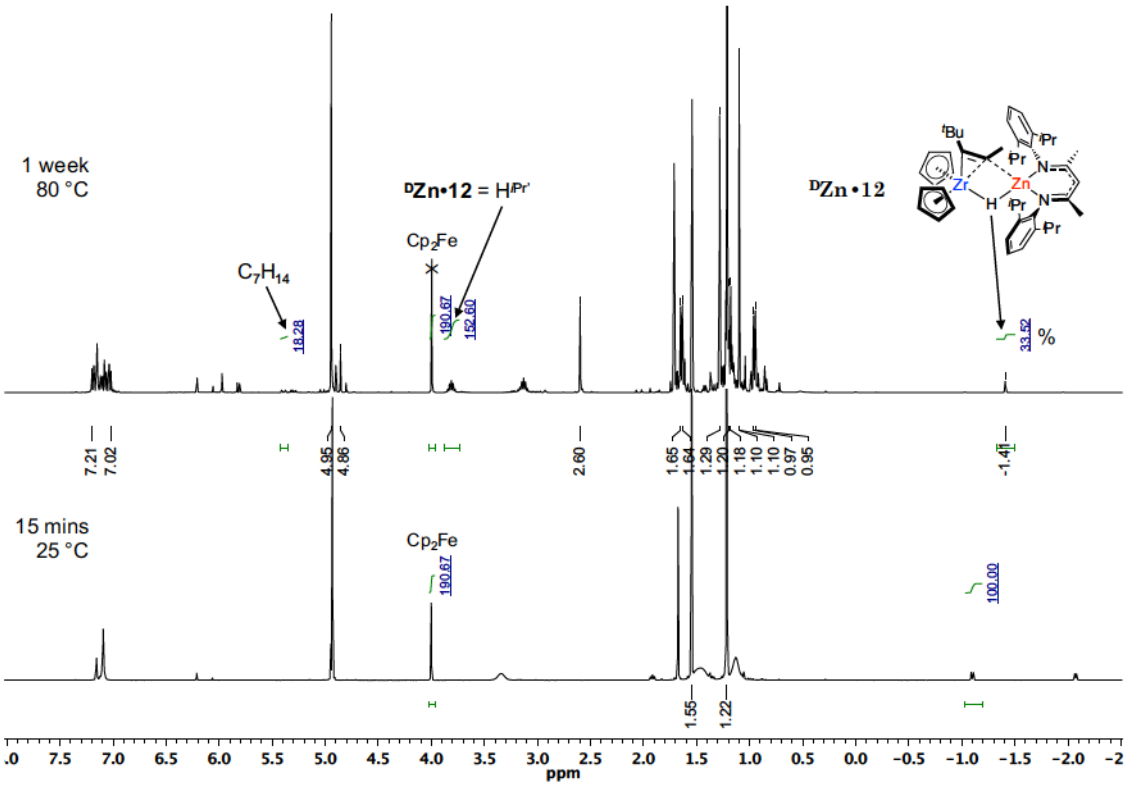


Figure 3.24. ^{1}H NMR (benzene-d_6) stack plot of the reaction of **^{D}Zn•Zr** with 4,4'-dimethylpent-1-yne.

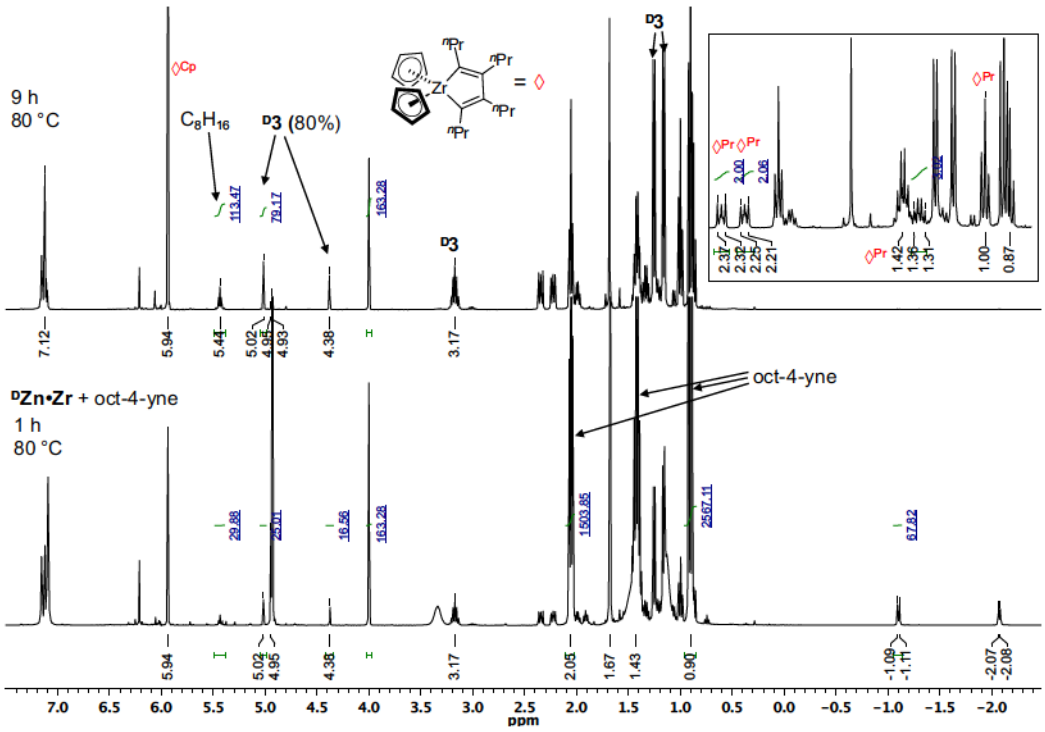


Figure 3.25. Reaction of oct-4-yne with **^{D}Zn•Zr** (in benzene-d_6) to give a putative zirconacyclopentadiene.

Reaction of ^{D}Zn•Zr with PMe$_3$ under Photolysis

Trimethylphosphine (129 μL, 1.937 mmol, 10 equiv.) was added by calibrated pipette to a 0.5 mL of benzene-d_6 solution of ferrocene (ca. 2–3 mg) and 1 equiv. of **^{D}Zn•Zr** in a J Young's NMR tube. The reaction mixture was followed by ^{1}H & ^{31}P NMR, and the data are presented in Figure 3.26 and Figure 3.27 respectively.

Reaction of [Cp$_2$ZrPh$_2$] with ^{D}3 under Photolysis

Zirconocene diphenyl (15 mg, 0.021 mmol, 1 equiv.) was dissolved in 0.5 mL of benzene-d_6 along with ferrocene (ca. 2–3 mg). A ^{1}H NMR spectrum of this pre-reaction mixture was collected for the yield calculation purposes; 20.5 mg of **^{D}3** (0.042 mmol, 1 equiv.) was weighed into a scintillation vial. The solution of [Cp_2ZrPh_2] was emptied onto **^{D}3,** then the reaction mixture was returned to the NMR tube before being subject to photolysis. The desired production of {Cp_2Zr^{II}} (and then a Zr–Zn bonded species) was eclipsed by the ease of the background thermal reaction: [^{Dipp}BDIZnPh] and benzene were produced (50% after 20 min at 25 °C). Photolysis for 2 h darkened the reaction mixture, giving a deep purple solution. By ^{1}H NMR spectroscopy, the background reaction had completed the consumption of the starting materials by this time.

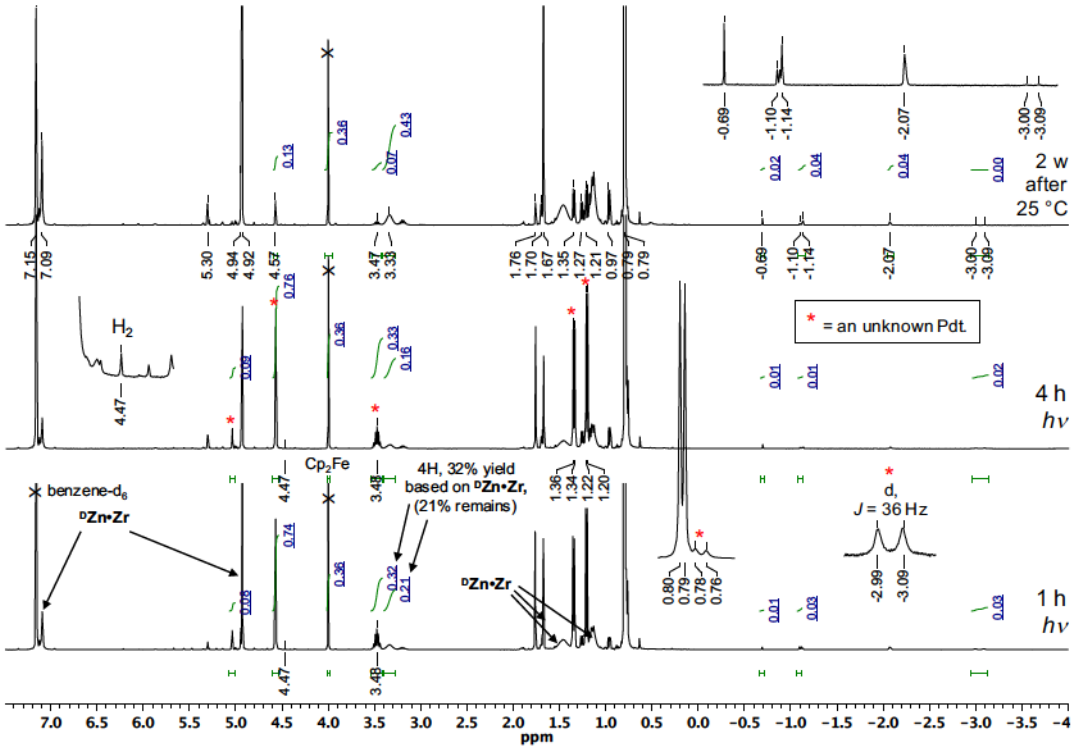


Figure 3.26. A ^{1}H NMR stack plot (benzene-d_6) showing the peaks of the product of photolysis of **^{D}Zn•Zr** in the presence of excess PMe_3, and its subsequent decay under ambient conditions.

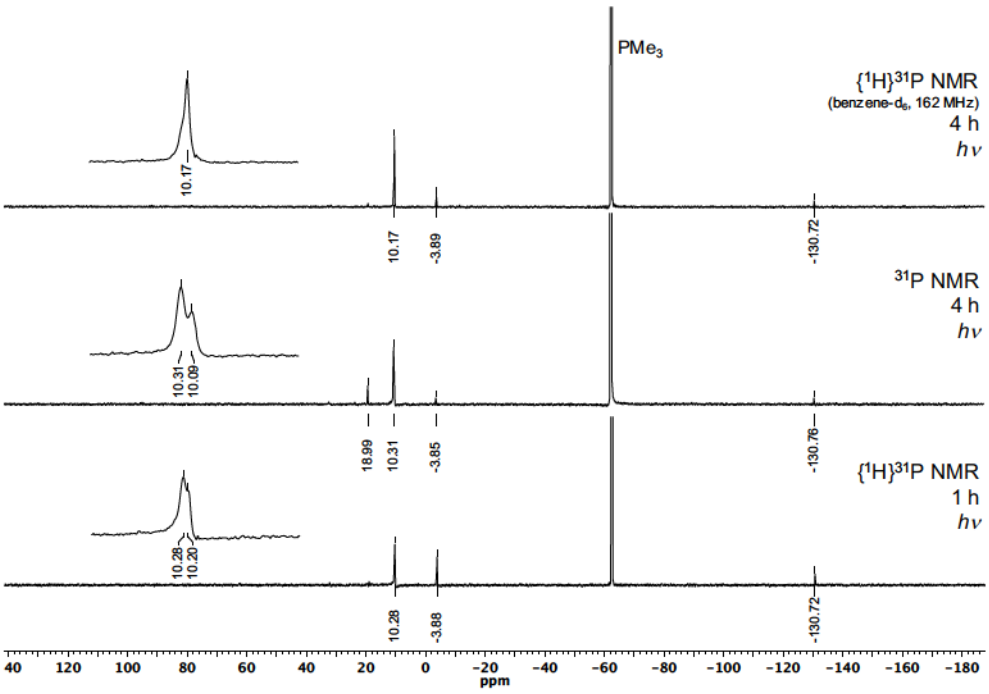


Figure 3.27. The ^{31}P NMR (benzene-d_6) peaks of the non-isolated product of photolysis of **^{D}Zn•Zr** in the presence of excess PMe_3.

3.5.3 DFT Studies

Calculations were conducted in Gaussian09. All minima were confirmed by frequency calculations and solid-state data were used as an input for the atom coordinates. NBO calculations were run using NBO v5.9 within g09. All transition states were confirmed by intrinsic reaction coordinate (IRC) calculations. The relative energies of isomers of C_8H_{12} were calculated using the B3LYP functional and 6,311G+(d,p) basis set, conformation searches were performed manually by initiating calculations from a large number of conformations in g09. Bader analysis was conducted on optimized geometries in the AIMALL package. In all cases the geometries were compared against the solid-state data.

Choice of Functional and Basis Set Combination

A series of functionals (B3LYP, M-062x, ωB97x, ωB97xD) and basis-sets (6,311G+(d,p) / 6,31G+(d,p) / LanL2DZ / SDD) were investigated. Figure 3.28 shows how the geometrical parameters of the metal-metal core were compared in the search for the functional/hybrid basis set combination that matched best the experimental structure. A truncated model of the relevant crystal structure molecule was used as the input. There is little to choose between the ωB97x and ωB97xD functionals, so computational cost was minimised by choice of the former. As a compliment to this benchmarking approach, the non-truncated structures were used for detailed comparison between two dissimilar methods (Figure 3.29). The same method proved to be the best match for the experimental data. It should be noted that the geometrical data around the hydride are not well replicated. However, there is inherent uncertainty in hydride locations by X-ray crystallography. In this instance, both molecules in the unit cell were assessed under the DFT calculation. The optimisations did not converge to the same structural conformation. The separate optimisation results show slight differences in the cyclooctyne ring conformation, but there is negligible Gibbs free energy difference (Figure 3.29).

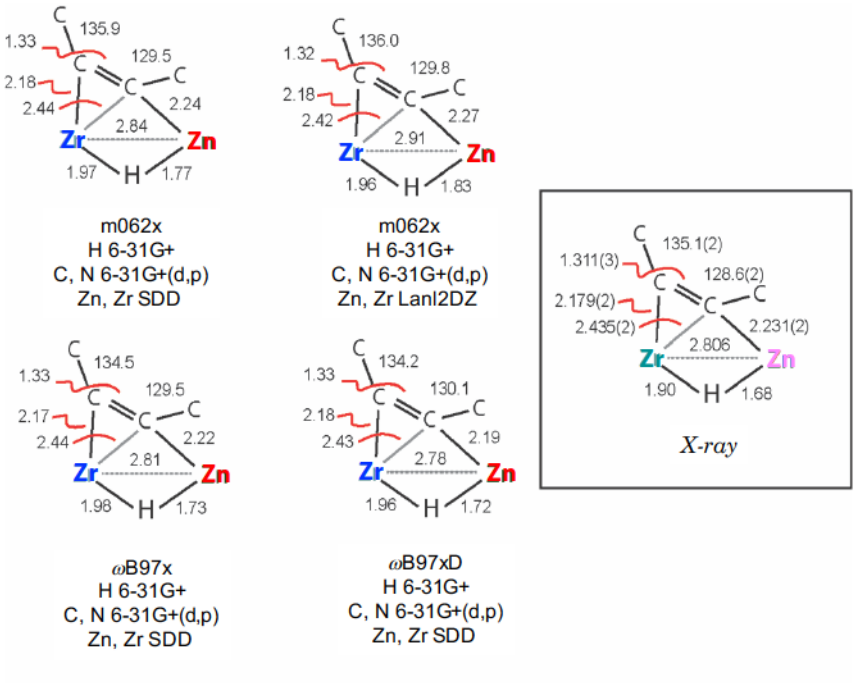


Figure 3.28. Comparison of experimental bond angles and bond lengths of the Zr---Zn core (of molecule B within the unit cell) of ^{D}**Zn•10** against calculated values. A truncated model was used, in which ^{i}Pr groups have been replaced with methyl groups.

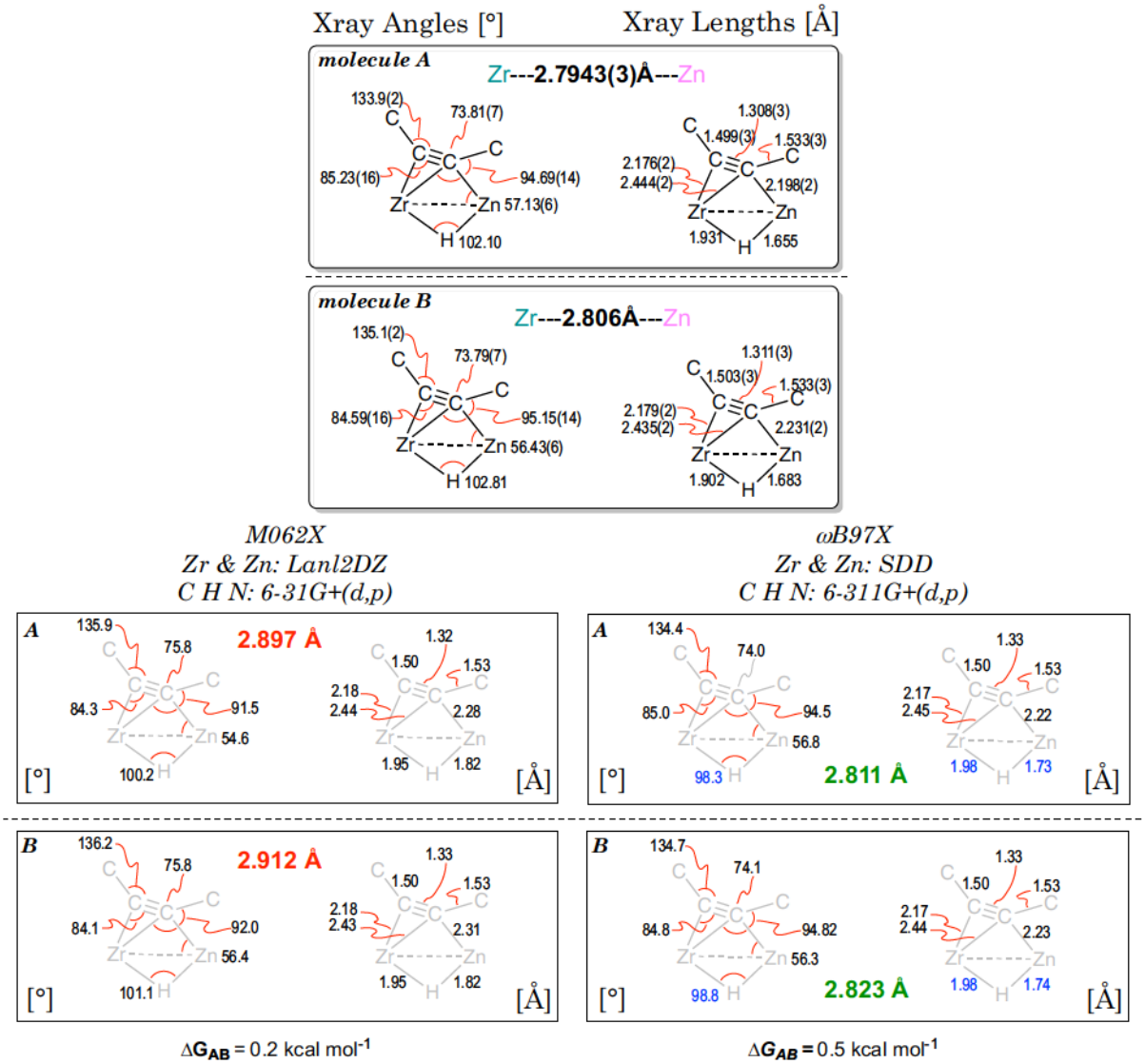


Figure 3.29. Comparison of calculated parameters of ^{D}**Zn•10** using molecule A and B from the X-ray crystallographic data as inputs. No truncations made.

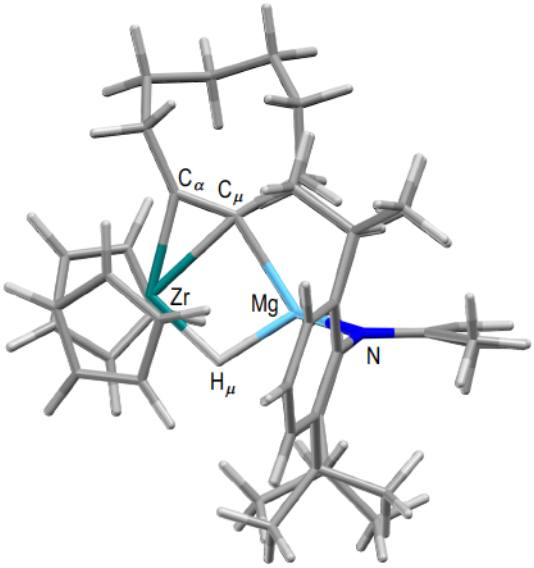


Figure 3.30. Optimised DFT structure of ^{D}**Mg•10**.

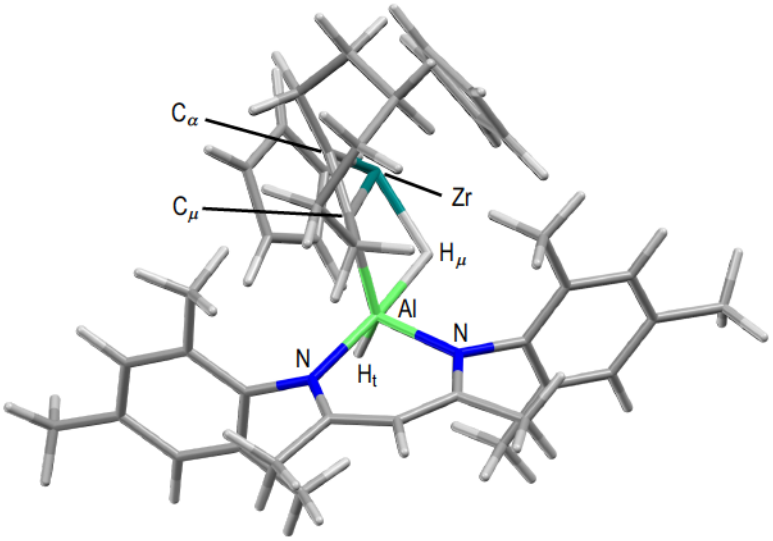


Figure 3.31. Optimised DFT structure of ^{M}**Al•10**, orientated to show the non-planarity of the slipped metallaccyclopropene moiety.

3.5.4 X-ray Crystallography

3.5.4.1 Data and Parameters

X-ray Crystal Structure of ^{D}Zr•10

$C_{47}H_{64}N_2ZnZr$, M = 813.59, monoclinic, $P2_1/c$ (no. 14), a = 16.4692(5), b = 36.5002(10), c = 14.0481(4) Å, β = 103.342(3)°, V = 8216.8(4) Å^3, Z = 8 (two independent molecules), ρ_{calcd} = 1.315 g cm^{-3}, $\mu(Mo_{K\alpha})$ = 0.871 mm^{-1}, T = 173 K, colourless tablets, Agilent Xcalibur 3 E diffractometer; 16152 independent measured reflections (R_{int} = 0.0204), F^2 refinement,

R_1(obs) = 0.0364, wR_2(all) = 0.0919, 12707 independent observed absorption-corrected reflections [$|F_o| > 4\sigma(|F_o|)$, $2\theta_{max}$ = 57°], 955 parameters. CCDC 1454104.

The structure of **^{D}Zr•10** was found to contain two independent complexes, **^{D}Zr•10-A** and **^{D}Zr•10-B**. For each complex the Zr–H–Zn bridging hydrogen atom was located from a ΔF map and refined freely. The standard calculated position for the C2–H hydrogen atom in each complex was found to differ significantly from the observed electron density in the ΔF map, and so these hydrogen atoms were placed in the found positions and then refined freely subject to a C–H distance constraint of 0.950 Å (the distance that would have been used in the standard treatment).

X-ray Crystal Structure of ^{D}Zr•12

$C_{46}H_{64}N_2ZnZr$, M = 801.58, orthorhombic, $P2_12_12_1$, a = 11.9090(3), b = 17.4494(4), c = 19.9943(5) Å, $\alpha = \beta = \gamma = 90°$, V = 4154.89(17) Å^3, Z = 4, ρ_{calcd} = 1.281 g cm^{-3}, $\mu(Mo_{K\alpha})$ = 0.860 mm^{-1}, T = 173 K, colourless blocks, Agilent Xcalibur 3 E diffractometer; 10129 independent measured reflections (R_{int} = 0.0259), F^2 refinement, R_1(obs) = 0.0353, wR_2(all) = 0.0748, 6726 independent observed absorption-corrected reflections [$|F_o| > 4\sigma(|F_o|)$, $2\theta_{max}$ = 57°], 469 parameters.

3.6 REFERENCES

1 E. Larionov, H. Li and C. X. M. Mazet, *Chem. Commun.*, 2014, **50**, 9816–9826.
2 V. C. Gibson, G. Parkin and J. E. Bercaw, *Organometallics*, 1991, **10**, 220–231.
3 H. Hopf, H. Priebe and R. Walsh, *J. Am. Chem. Soc.*, 1980, **102**, 1210–1212.
4 O. V. Ozerov, M. Pink, L. A. Watson and K. G. Caulton, *J. Am. Chem. Soc.*, 2004, **126**, 2105–2113.
5 D. W. Reed, D. R. Polichuk, P. H. Buist, S. J. Ambrose, R. J. Sasata, C. K. Savile, A. R. S. Ross and P. S. Covello, *J. Am. Chem. Soc.*, 2003, **125**, 10635–10640.
6 E. J. Prosen, F. W. Maron and F. D. Rossini, *J. Res. Natl. Bur. Stand.*, 2011, **46**, 106–112.
7 I. Yavari, *J. Mol. Struct.*, 1980, **65**, 169–172.
8 K. J. Daoust, S. M. Hernandez, K. M. Konrad, I. D. Mackie, J. Winstanley and R. P. Johnson, *J. Org. Chem.*, 2006, **71**, 5708–5714.
9 E. Taskinen, K. Nummelin and J. Chattopadhyaya, *Acta Chem. Scand. B*, 1985, **39b**, 791–792.
10 T. Uchida, R. Irie and T. Katsuki, *Synlett*, 1999, 1793–1795.
11 R. Shintani, W.-L. Duan, S. Park and T. Hayashi, *Chem. Commun.*, 2006, 3646–2.
12 K. Hirai, H. Suzuki, Y. Moro-Oka and T. Ikawa, *Tetrahedron Lett.*, 1980, **21**, 3413–3416.
13 M. Shiotsuki, Y. Ura, T. Ito, K. Wada, T. Kondo and T.-A. Mitsudo, *J. Organomet. Chem.*, 2004, **689**, 3168–3172.
14 Z. Wang, Y. Wang and L. Zhang, *J. Am. Chem. Soc.*, 2014, **136**, 8887–8890.
15 K. Mashima, R. Rochat, K. Mashima, K. Yamamoto, M. J. Lopez, H. Nagae and H. Tsurugi, *Chem. Eur. J.*, 2015, **21**, 8112–8120.
16 A. Konig, C. Wagner, M. Bette and D. Steinborn, *Dalton Trans.*, 2012, **41**, 7156–7162.
17 S. M. Coughlan and G. K. Yang, *J. Organomet. Chem.*, 1993, **450**, 151–155.
18 U. Rosenthal, A. Ohff, M. Michalik, H. Görls, V. V. Burlakov and V. B. Shur, *Angew. Chem., Int. Ed.*, 1993, **32**, 1193–1195.
19 A. Ohff, V. V. Burlakov and U. Rosenthal, *J. Mol. Catal. A: Chem.*, 1996, **105**, 103–110.
20 Y. L. Qian, G. S. Li, X. F. Zheng and Y. Z. Huang, *J. Mol. Catal.*, 1993, **78**, L31–L35.
21 S. Biswas, *Comments Inorg. Chem.*, 2015, **35**, 300–330.
22 E. Soriano and I. Fernández, *Chem. Soc. Rev.*, 2014, **43**, 3041–65.
23 V. V. Krivykh, E. S. Taits, P. V. Petrovskii, Y. T. Struchkov and A. I. Yanovskii, *Mendeleev Commun.*, 1991, **1**, 103–104.
24 S. Doherty, J. F. Corrigan, A. J. Carty and E. Sappa, *Adv. Organomet. Chem.*, 1995, **37**, 39–130.
25 A. Wojcicki, *New J. Chem.*, 1994, **18**, 61–68.
26 P. W. Blosser, J. C. Gallucci and A. Wojcicki, *J. Am. Chem. Soc.*, 1993, **115**, 2994–2995.
27 S. Ogoshi, Y. Fukunishi, K. Tsutsumi and H. Kurosawa, *J. Chem. Soc., Chem. Commun.*, 1995, 2485–2486.
28 S. F. Fillery, G. J. Gordon, T. Luker and R. J. Whitby, *Pure Appl. Chem.*, 1997, **69**, 633–638.
29 C. P. Casey and Y. Wang, *Organometallics*, 1992, **11**, 13–15.
30 N. Phadke and M. Findlater, *Organometallics*, 2013, **33**, 16–18.
31 P. H. P. Brinkmann, G. A. Luinstra and A. Saenz, *J. Am. Chem. Soc.*, 1998, **120**, 2854–2861.
32 G. Erker, M. Albrecht, C. Krueger, S. Werner, P. Binger and F. Langhauser, *Organometallics*, 1992, **11**, 3517–3525.
33 M. Albrecht, G. Erker and C. Kruger, *Synlett*, 1993, 441–448.
34 A. Spannenberg, S. Becke, P. Arndt, W. Baumann and U. Rosenthal, *Eur. J. Inorg.*

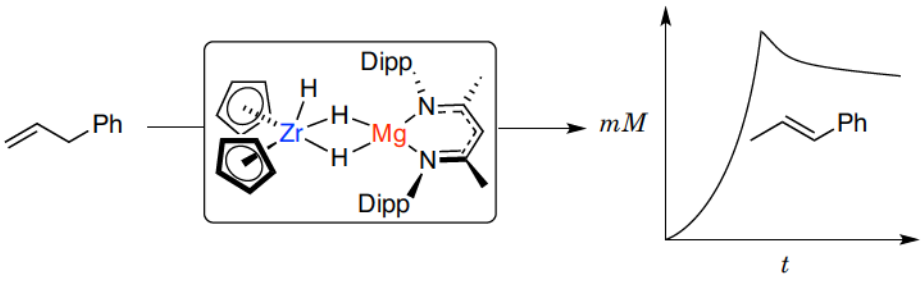
Chem., 2001, 2885–2890.
35 G. Bender, T. Wiegand, H. Eckert, R. Fröhlich, C. G. Daniliuc, C. Mück-Lichtenfeld, S. Ndambuki, T. Ziegler, G. Kehr and G. Erker, *Angew. Chem., Int. Ed.*, 2012, **51**, 8846–8849.
36 S. L. Buchwald, R. T. Lum and J. C. Dewan, *J. Am. Chem. Soc.*, 1986, **108**, 7441–7442.
37 H. Lee, T. Hascall, P. J. Desrosiers and G. Parkin, *J. Am. Chem. Soc.*, 1998, **120**, 5830–5831.
38 S. A. Cohen, P. R. Auburn and J. E. Bercaw, *J. Am. Chem. Soc.*, 1983, **105**, 1136–1143.
39 R. Gleiter, I. Hyla-Kryspin, S. Niu and G. Erker, *Angew. Chem., Int. Ed.*, 1993, **32**, 754–756.
40 A. Wooten, P. J. Carroll, A. G. Maestri and P. J. Walsh, *J. Am. Chem. Soc.*, 2006, **128**, 4624–4631.
41 A. Das, C. Dash, M. A. Celik, M. A. Celik, M. Yousufuddin, G. Frenking and H. V. R. Dias, *Organometallics*, 2013, **32**, 3135–3144.
42 G. Groger, U. Behrens and F. Olbrich, *Organometallics*, 2000, **19**, 3354–3360.
43 A. Das, M. Yousufuddin, C. Dash, M. A. Celik, G. Frenking and H. V. R. Dias, *Angew. Chem., Int. Ed.*, 2012, **51**, 3940–3943.
44 O. V. Ozerov, L. A. Watson, M. Pink and K. G. Caulton, *J. Am. Chem. Soc.*, 2007, **129**, 6003–6016.
45 G. D. Cuny and S. L. Buchwald, *Organometallics*, 1991, **10**, 363–365.
46 S. L. Buchwald, J. C. Huffman and B. T. Watson, *J. Am. Chem. Soc.*, 1986, **108**, 7411–7413.
47 G. Erker, M. Albrecht, S. Werner, M. Noltemeyer and C. Kruger, *Eur. J. Inorg. Chem.*, 1992, **125**, 1953–1956.
48 V. V. Burlakov, W. Baumann, U. Rosenthal, P. Arndt and A. Spannenberg, *Organometallics*, 2004, **23**, 4160–4165.
49 C. McDade and J. E. Bercaw, *J. Organomet. Chem.*, 1985, **279**, 281–315.
50 J. Prust, A. Stasch, W. Zheng, H. W. Roesky, E. Alexopoulos, I. Usón, D. Böhler and T. Schuchardt, *Organometallics*, 2001, **20**, 3825–3828.
51 P. J. Chirik and J. E. Bercaw, *Organometallics*, 2005, **24**, 5407–5423.
52 N. Coles, M. C. J. Harris, R. J. Whitby and J. Blagg, *Organometallics*, 1994, **13**, 190–199.
53 J. M. Davis, R. J. Whitby and A. Jaxa-Chamiec, *Tetrahedron Lett.*, 1994, **35**, 1445–1448.
54 S. L. Buchwald, B. T. Watson and J. C. Huffman, *J. Am. Chem. Soc.*, 1987, **109**, 2544–2546.
55 D. J. Sikora and M. D. Rausch, *J. Organomet. Chem.*, 1984, **276**, 21–37.
56 K. I. Gell and J. Schwartz, *J. Am. Chem. Soc.*, 1981, **103**, 2687–2695.
57 K. I. Gell and J. Schwartz, *J. Am. Chem. Soc.*, 1978, **100**, 3246–3248.
58 F. Taullaj, D. Armstrong, A. J. Lough and U. Fekl, *Polyhedron*, 2016, **108**, 30–35.
59 E. Y. Pankratyev, T. V. Tyumkina, L. V. Parfenova, S. L. Khursan, L. M. Khalilov and U. M. Dzhemilev, *Organometallics*, 2011, **30**, 6078–6089.
60 C. A. Bradley, E. B. Lobkovskii, I. Keresztes and P. J. Chirik, *Organometallics*, 2006, **25**, 2080–2089.
61 M. Yoshifuji, K. I. Gell and J. Schwartz, *J. Organomet. Chem.*, 1978, **153**, C15–C18.
62 G. Erker, G. Kehr and R. Fröhlich, *J. Organomet. Chem.*, 2004, **689**, 4305–4318.
63 C. A. Bradley, I. Keresztes, E. B. Lobkovskii, V. G. Young and P. J. Chirik, *J. Am. Chem. Soc.*, 2004, **126**, 16937–16950.
64 G. Erker, J. L. Petersen, R. Noe and D. Wingbermuhle, *Angew. Chem., Int. Ed.,* 1993, **32**, 1213–1215.
65 J. A. Pool, E. Lobkovsky and P. J. Chirik, *Organometallics*, 2003, **22**, 2797–2805.
66 N. M. Weliange, D. S. McGuinness, M. G. Gardiner and J. Patel, *Dalton Trans.*, 2015, **44**, 20098–20107.

67 R. Choukroun, Y. Raoult and D. Gervais, *J. Organomet. Chem.*, 1990, **391**, 189–194.
68 B. M. Kraft and W. D. Jones, *J. Organomet. Chem.*, 2002, **658**, 132–140.
69 O. Ekkert, A. J. P. White and M. R. Crimmin, *Angew. Chem., Int. Ed.*, 2016, 1–5.
70 L. Fohlmeister, S. Liu, C. Schulten, B. Moubaraki, A. Stasch, J. D. Cashion, K. S. Murray, L. Gagliardi and C. J. Jones, *Angew. Chem., Int. Ed.*, 2012, **51**, 8294–8298.
71 M. Stender, H. Oesen, S. Blaurock and E. Hey Hawkins, *Z. Anorg. Allg. Chem.*, 2001, **627**, 980–984.
72 J. Kopf, H. J. Vollmer and W. Kaminsky, *Cryst. Struct. Commun.*, 1980, **9**, 985.
73 R. D. Broene and S. L. Buchwald, *Science*, 1993, **261**, 1696–1701.
74 E.-I. Negishi, D. R. Swanson and T. Takahashi, *J. Chem. Soc., Chem. Commun.*, 1990, 1254–1255.
75 E. Negishi, F. E. Cederbaum and T. Takahashi, *Tetrahedron Lett.*, 1986.
76 N. Suzuki, M. Hosoya, Y. Ariga and Y. Masuyama, *J. Organomet. Chem.*, 2017, **835**, 39–42.
77 Lu, Y. Qian, Jiaqui and W. Xu, *J. Mol. Catal.*, 1986, **34**, 31–38.
78 K. C. Jantunen, B. L. Scott and J. L. Kiplinger, *J. Alloys Compd.*, 2007, **444-445**, 363–368.
79 R. G. Salomon and N. El Sanadi, *J. Am. Chem. Soc.*, 1975, **97**, 6214–6221.
80 A. K. Cook and M. S. Sanford, *J. Am. Chem. Soc.*, 2015, **137**, 3109–3118.
81 Y. Wang, B. Quillian, C. S. Wannere, P. Wei, P. V. R. Schleyer and G. H. Robinson, *Organometallics*, 2007, **26**, 3054–3056.
82 W. A. Nugent and D. F. Taber, *J. Am. Chem. Soc.*, 1989, **111**, 6435–6437.

"How I long to clear this sordid tale away from my desk."

Leo Tolstoy, Letter to a Friend re: *Anna Karenina*

CHAPTER 4 – (*E*)-Selective Alkene Isomerisation Catalysis with a Magnesium/Zirconium Heterobimetallic Complex



The isomerisation of terminal alkenes to internal positions may be catalysed by ***^{D}Mg•Zr*** *with high* (E)*-selectivity. It is shown that both the catalyst activity and selectivity is dependent on the identity of the main group metal –* ***^{D}Zn•Zr*** *is a comparatively ineffective catalyst. Two selectivity events are important: the alkene:alkane ratio and E:Z ratio. While the active M/Zr catalysts of the series all yield products with high* (E)*-selectivity, the Mg/Zr heterobimetallic complex gives the highest ratios of alkene:alkane across a number of substrates as well as being most consistently successful with total yield. An appreciation of the factors that determine selectivity led to the identification of* ***Zr•Zr*** *as a simple yet efficient alkene isomerisation catalyst at low-loadings. Kinetic profiles betrayed a distinct substrate sensitivity in the catalysis with the Mg/Zr complex: the reaction with allylbenzene revealed an apparent autocatalytic regime, with the* (E)*-alkene becoming incorporated into the catalyst in some way to give an unknown* ***cat****. Future work is required to establish the nature of* ***cat****.*

4.1 Introduction to Alkene Isomerisation

For heterobimetallic complexes containing both main group and transition metals, contemporary approaches with well-defined systems, have long been foreshadowed by additive effects in catalysis. For example, the activation of group 4 metallocenes with methylaluminoxane (MAO) was a key discovery in the development of homogeneous Ziegler-Natta catalysts for alkene polymerisation.[1-4]

In related studies, a handful of group 4 metallocenes have been shown to effect the isomerisation of alkenes. Eisen and co-workers have demonstrated that zirconium and titanium benzamidinate complexes (Figure 4.1, **A**) in combination with an excess of MAO are capable of triggering the isomerisation of terminal alkenes to internal positions.[5,6] While these systems and straightforward Zr^{IV} monohydride catalysts[7-9] have been proposed to proceed by an insertion-elimination mechanism, mechanistically distinct work has attended to low-valent group 4 catalysts and the π-allyl hydride mechanism.[10-12] The latter are generated from the reduction of metallocene dichloride precursors by Mg (Figure 4.1, **B**). Nevertheless, precatalyst complexes combining a group 4 *and* main group metal are, to our knowledge, unknown. A contemporary review of well-defined transition metal hydride catalysts in isomerisations has been compiled by Mazet and co-workers.[13] Highly successful (*E*)-selective catalysts based on late transition metals have been developed by the groups of Grotjahn[14-16] and Trapp.[17]

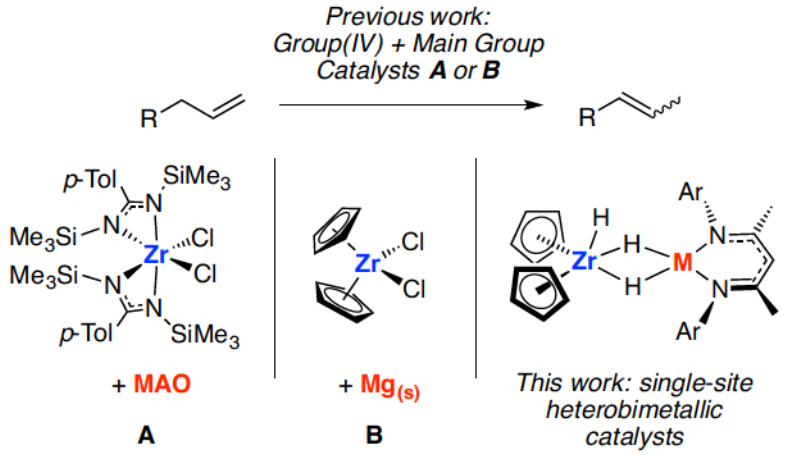


Figure 4.1. Alkene isomerisation catalysed by zirconocene complexes.

Through comparison of the M/Zr series (Figure 4.1), it is shown that, at moderate catalyst loadings (5 mol%), both activity and selectivity are dependent upon the identity of the main group fragment. This 'heterobimetallic effect' predominately influences the alkene:alkane ratio. At lower catalyst loadings the parent complex $[Cp_2Zr(H)(\mu\text{-}H)]_2$ (**Zr•Zr**) is a more efficient

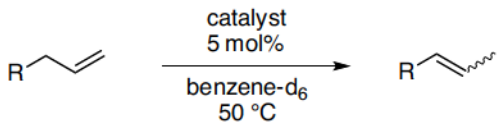
catalyst for alkene isomerisation than any member of the heterobimetallic series. This raises the question of the true nature of the catalytic species in the M/Zr systems.

4.2 RESULTS

4.2.1 Alkene Isomerisation

In attempting to explore the hydrometallation reactivity of ^{D}**Mg•Zr** and ^{D}**Zn•Zr**, their ability to catalytically isomerise terminal alkenes to internal positions was discovered. The results of these experiments are presented in Table 4.1. ^{D}**Mg•Zr** is a selective catalyst for alkene isomerisation giving internal alkenes with the lowest recorded *E*:*Z* selectivity of 12:1. Although ^{M}**Al•Zr** is also an effective catalyst under identical catalyst loadings, the alkene:alkane selectivities are somewhat lower than those recorded for ^{D}**Mg•Zr**. The by-products are the corresponding alkanes formed in approximately 5–10% yield. Catalytic experiments employing ^{D}**Zn•Zr** were slow, resulting in only low conversion over the same timescales as those reported for ^{D}**Mg•Zr**. In combination, these data demonstrate the dependence of catalysis on the presence and the nature of the main group fragment.

Table 4.1. Scope of alkene isomerisation with ^{Ar}**M•Zr** (R = Ar^{X} = 4-XC$_6$H$_4$).

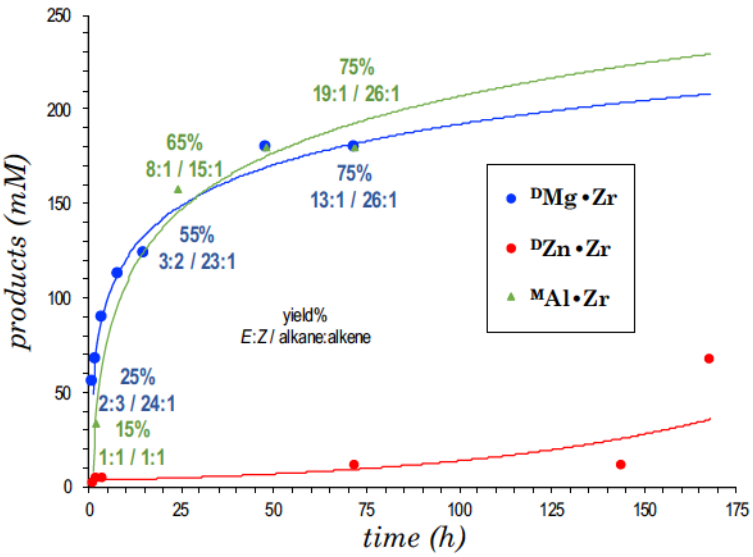


substrate	*catalyst*	*time (h)*	*combined yield (%)*	*E:Z*	*alkene :alkane*
R = Ph	^{D}**Mg•Zr**	24	75	40:1	45:1
	^{M}**Al•Zr**	2	95	99:1	15:1
	^{D}**Zn•Zr**	168	90	64:1	99:1
R = Ar^{OMe}	^{D}**Mg•Zr**[a]	24	80	52:1	48:1
	^{M}**Al•Zr**	4	95	36:1	25:1
R = Ar^{CF_3}	^{D}**Mg•Zr**	24	80	16:1	17:1
	^{M}**Al•Zr**	24	90	20:1	22:1
R = SiMe$_3$	^{D}**Mg•Zr**	72	75	12:1	35:1
	^{M}**Al•Zr**[a]	24	75	22:1	19:1[a]
	^{D}**Zn•Zr**	216	25	3:1	3:1
R = ^{n}Pr	^{D}**Mg•Zr**	48	70	40:10:1[b]	99:1
	^{M}**Al•Zr**[a]	24	95	11:4:3[b]	9:1
	^{D}**Zn•Zr**	168	80	6:1:2[b]	99:1

[a] Reaction conducted at 25 °C. [b] Ratio of 2*E*:2*Z*:3*E*

The differences in catalyst efficiency and selectivity were further underscored by monitoring the isomerisation of allyltrimethylsilane as a function of time (Graph 4.1). While both **^{D}Mg•Zr** and **^{M}Al•Zr** give high ratios of alkene:alkane at high conversion, only the magnesium analogue demonstrates high selectivity over the entire course of the reaction. For both aforementioned catalysts the *E:Z* selectivity is low at low conversions, suggesting that the reactions may be under thermodynamic control with the (*Z*)-alkene slowly isomerising to the (*E*)-alkene as the reaction proceeds.

The limits of the catalysts were explored and the isomerisation of allyltrimethylsilane over 38 h at 50 °C is still observed with 0.5 mol% **^{D}Mg•Zr** giving a 20:1 mixture of *E:Z* of the vinylsilane in 65% yield and only trace amounts of transfer hydrogenation. This experiment allows an estimation of the upper *TON* as 120. Attempts to extend the scope to more hindered or 1,1-disubstituted alkenes met with limited success, and both methylenecyclohexane and 4,4-dimethyl-pent-1-ene failed to isomerise under the catalytic conditions. No alkane products were produced from these substrates either.



Graph 4.1. Catalytic isomerisation of allyltrimethylsilane by ^{R}*BDI*M•**Zr**. Including *E:Z* and alkene:alkane ratios respectively, followed as a function of time. Data trendlines are fitted as a guide only.

Isolation of the heterobimetallic complex is not a prerequisite for catalysis, and a mixture of 5 mol% [Cp_2ZrCl_2] and 7.5 mol% [^{Dipp}*BDI*Mg(μ-H)]$_2$ was effective for the isomerisation of allylbenzene (see Experimental). However, this reaction did not display ^{1}H NMR signals for **^{D}Mg•Zr** at any point during the isomerisation of allylbenzene. There is also no remaining **^{D}Mg•Zr** in the final isomerisation reaction mixtures with the substrates 4-allylanisole and 1-allyl-4-(trifluoromethyl)benzene. As such, the involvement of a well-defined heterobimetallic pre-catalyst in this protocol is unknown. Based on the catalytic activities, the focus of the

following investigation was placed on mechanistic studies of the well-defined **^{D}Mg•Zr** pre-catalyst.

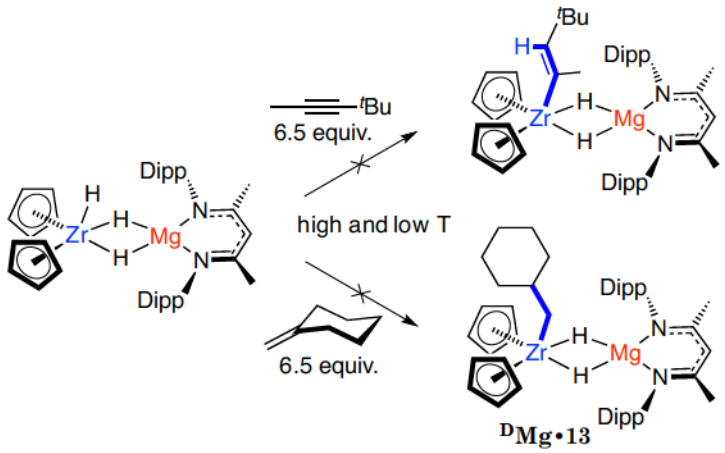
4.2.2 Mechanistic Studies

A series of experiments were undertaken to gain some insight into the mechanism of alkene isomerisation and the origin of alkane by-products. Two widely accepted mechanisms were considered (*viz*. Figure 3.2): an addition-elimination mechanism involving alkene insertion and β-hydride elimination steps, and a redox mechanism involving generation and isomerisation of a π-allyl intermediate.

4.2.2.1 Metal Hydride Insertion-elimination Mechanism

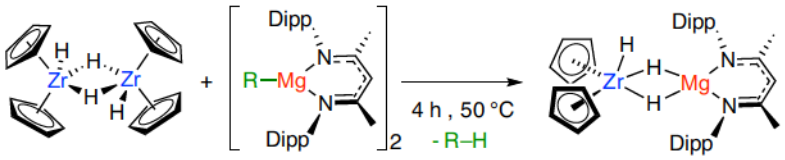
A number of observations are contradictory with a hypothetical addition-elimination pathway: 1) the insertion of methylenecyclohexane, diphenylacetylene, or 2,2-dimethyl-pent-3-yne into the terminal Zr–H bond of **^{D}Mg•Zr** did not proceed at 50 °C despite the last alkyne being an outstanding trapping reagent for $[Cp^*_2ZrH_2]$ (Scheme 4.1);[18] 2) the reaction of $[^{Dipp}BDIMg(\mu\text{-}R)]_2$ (R = $^{n/s}$Bu, $CH_2CH_2CH_2Ph$) with **Zr•Zr** resulted in the formation of **^{D}Mg•Zr** (Table 4.2, entries i and ii), but only trace amounts of alkene products were observed.

Both reactions provide insight into reversible alkene insertion into the terminal Zr–H bond of **^{D}Mg•Zr**. The failure of **^{D}Mg•Zr** to form dihydridoalkyl analogues such as those illustrated in Scheme 4.1 means that hydrometallation by the catalyst is not facile, or at least not thermodynamically downhill. The magnesium alkyl reactions suggest that β-hydride elimination from a zirconium alkyl intermediate is not the major pathway to form **^{D}Mg•Zr**.



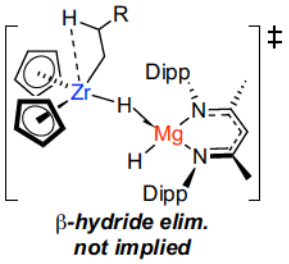
Scheme 4.1. Attempted reactions of **^{D}Mg•Zr** with unsaturated hydrocarbons.

Table 4.2. Formation of ^{D}**Mg•Zr** from magnesium alkyl complexes.

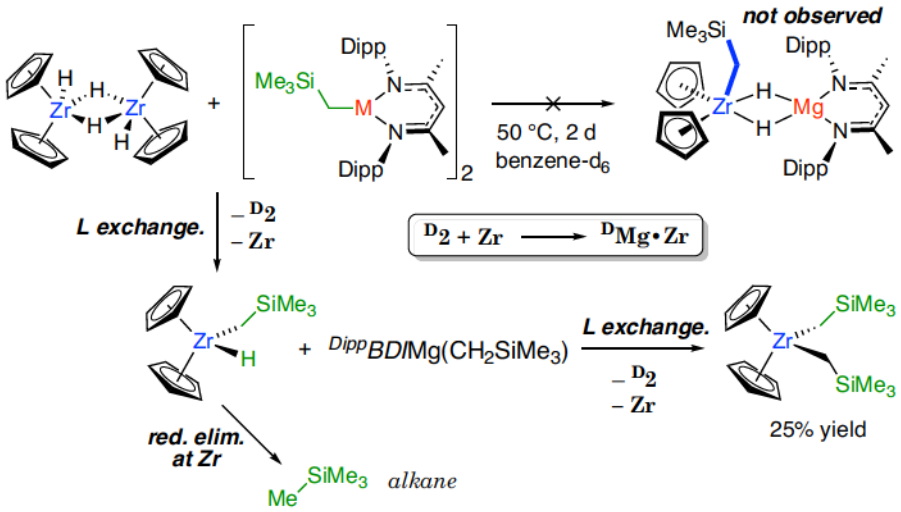


	Mg-alkyl	^{D}**Mg•Zr**	*alkene*	*alkane*
i	R = $CH_2CH_2CH_2Ph$	25%	trace	40%
ii[a]	R = $^{n/s}$Bu	20%	0%	35%[b]
iii	R = CH_2SiMe_3	55%	0%	15%[b]

[a] 9:2 n:sec butyl Magnesium
[b] volatile products, percentages are lower estimates.



Entry iii in Table 4.2 further corroborates these findings. The neosilyl ligand, $(CH_2SiMe_3)^-$, was used for its lack of a β-hydride atom. This way, an alkyl heterobimetallic complex might be trapped in the reaction of [^{Dipp}*BDI*Mg(μ-CH_2SiMe_3)]$_2$ with **Zr•Zr** (Scheme 4.2). Nevertheless, alkane by-products again accompanied formation of the known Mg/Zr complex. After 2 d of heating and complete consumption of [^{Dipp}*BDI*Mg(μ-CH_2SiMe_3)]$_2$, a 50% yield of ^{D}**Mg•Zr** was produced. Also observed was the dialkyl complex [$Cp_2Zr(CH_2SiMe_3)_2$][19] (25% yield after 2 d).



Scheme 4.2. Results and inferred mechanism of the reaction of **Zr•Zr** with [^{Dipp}*BDI*Mg(μ-CH_2SiMe_3)]$_2$.

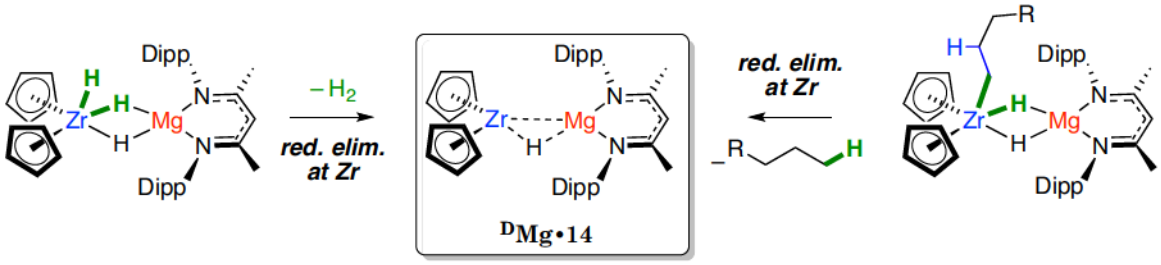
The result of this experiment shows a preference for exchange of the neosilyl and hydride ligands between Mg and Zr. The by-products of the initial ligand exchange form ^{D}**Mg•Zr** (Scheme 4.2, inset). The other Zr centre has collected the neosilyl ligand to become [$Cp_2Zr(CH_2SiMe_3)H$]. The complex is not observed directly, but reductive elimination from the species explains the production of alkane (Me_4Si – Scheme 4.2) as well as [$Cp_2Zr(CH_2SiMe_3)_2$], which arises from the second alkyl/hydride ligand exchange. Thus,

[$Cp_2Zr(CH_2SiMe_3)H$] is unstable with respect to reductive elimination *and* alkyl/hydride ligand exchange, and both processes are apparently in kinetic competition.

An attempt was made to synthesise the related **^{D}Mg•13** (Scheme 4.1) from ligand exchange [$Cp_2Zr(\eta^1$-$CH_2Cy)Cl$][20] (Cy = cyclohexyl) and 2 equiv. **^{D}2$_2$**, but methylcyclohexane was the only assignable major product. In combination, the data intimate that the putative bimetallic dihydridoalkyl analogues of **^{D}Mg•Zr** – a key intermediate in the proposed insertion-elimination pathway – may not be formed under these conditions. Moreover, alkene insertion into a M–H bond of the 18-electron complex **^{D}Mg•Zr** is not thermodynamically favourable (but could be reversible and endergonic).

4.2.2.2 π-Allyl Hydride Mechanism

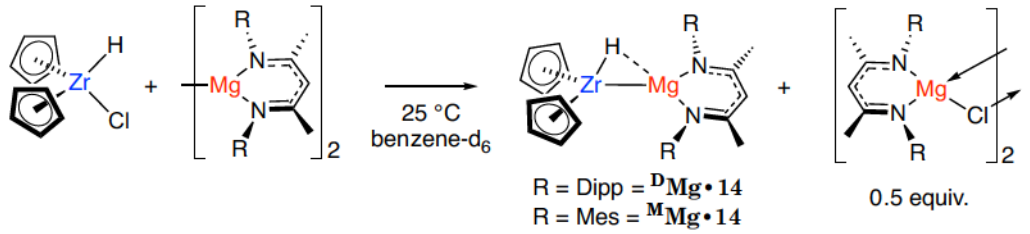
The results in section 4.2.2.1 turned the focus of the investigation towards examining a redox mechanism. A number of experiments have been conducted in order to probe the possibility of a singly hydride-bridged Mg/Zr complex. Such a heterobimetallic complex maybe be formed from reductive elimination of H_2 on Zr,[21] or by insertion of a terminal alkene into Zr–H and reductive elimination of alkane (Scheme 4.3). The former process is unlikely under the thermolytic conditions of catalysis; an intermediate dihydrogen complex would likely deliver exchange between H_t and H_μ, which is not observed in the VT NMR data presented in Chapter 2 (section 2.3.2).



Scheme 4.3. Possible pre-catalyst activation steps, *via* which a singly hydride-bridged Mg/Zr complex (**^{D}Mg•14**) may be formed.

Reduced M/Zr Species

Whilst a reduced heterobimetallic complex has not yet been isolated, some evidence has been collected to suggest that this is achievable. Currently, the task seems most workable by mixing Schwartz' reagent and the low-valent β-diketiminate Mg^{I} complex, [^{Dipp}*BDI*Mg^{I}]$_2$. At 25 °C this leads to production of a major species (structure proposed in Scheme 4.4) with a lone singlet in the bridging hydride region of the ^{1}H NMR spectrum at δ = –1.99 ppm.



Scheme 4.4. Putative production of Zr–H–Mg species through reaction of Schwartz' and Jones' reagents. In the absence of further structural data, the bonding in the {H–Zr–Mg} unit is arbitrarily described.

Use of the ^{Mes}*BDI* ligand led to a hydride signal at δ = –2.21 ppm. The complex (**^{M}Mg•14**) is short-lived, suffering deterioration after 12 h at room temperature. The analogue, **^{D}Mg•14** is much more persistent, and it is the major species in a relatively clean reaction. Possibly due to the larger steric defence of ^{Dipp}*BDI* (*cf.* ^{Mes}*BDI*), it survives for at least 2 weeks (15% yield, Figure 4.2) at room temperature in an NMR tube scale reaction.

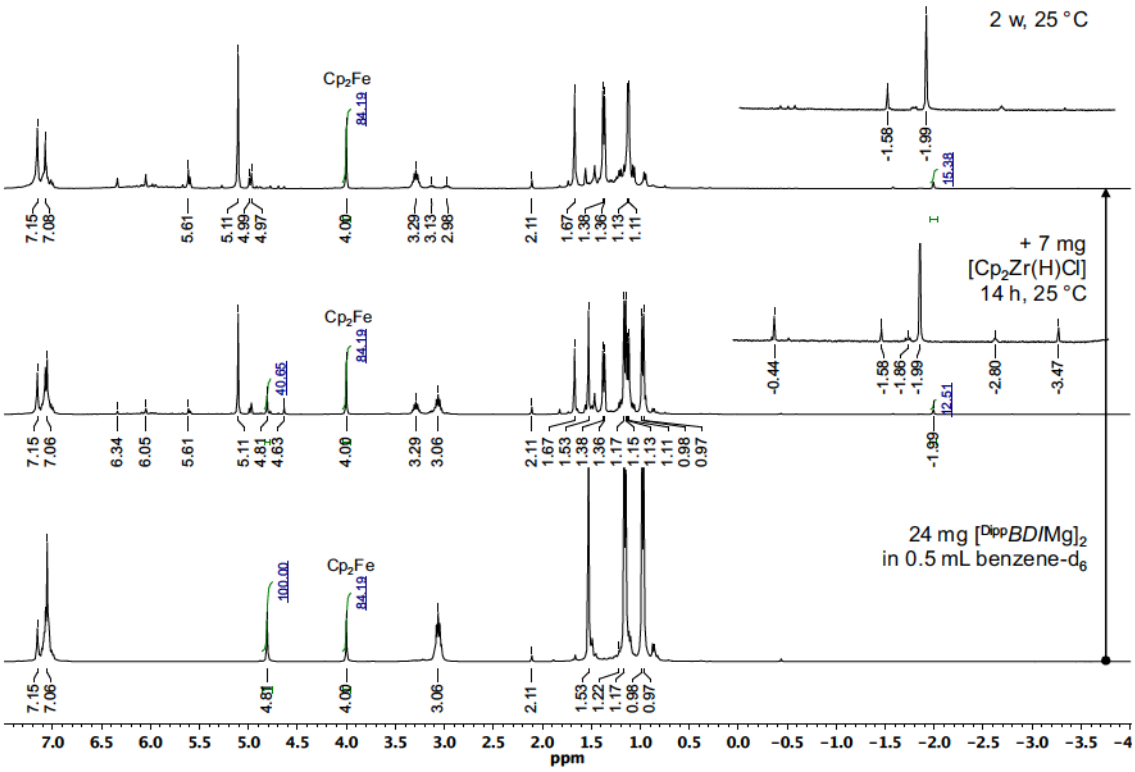


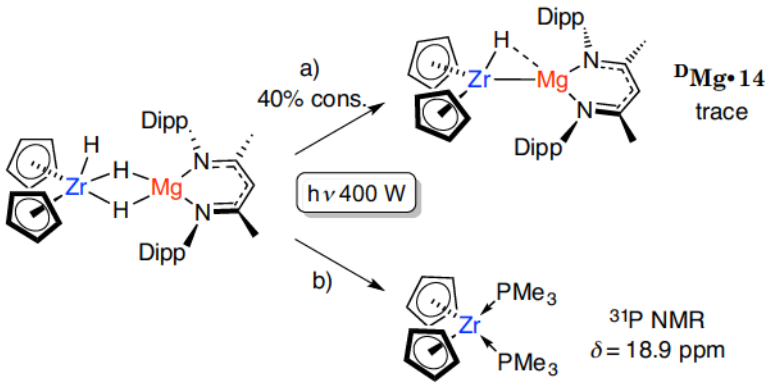
Figure 4.2. Stack plot of selected ^{1}H NMR data for the reaction of [$Cp_2Zr(H)Cl$] with [^{Dipp}*BDI*Mg]$_2$ at room temperature.

The presence of a bridging hydride singlet resonance and the relatively unchanged pattern of the other major peaks (Figure 4.2) are consistent with the proposed structure for **^{D}Mg•14**. Nevertheless, a preparative scale reaction is yet to be successful in the isolation of **^{D}Mg•14**. Material is lost from the mass balance according to ^{1}H NMR, and both reaction mixtures develop a dark red colour. Thus it is presumed paramagnetic Zr^{III} species are by-products.

Interestingly, the hydride resonance and other dominant peaks of **^{D}Mg•14** are also recognised as a transient product in the attempt to synthesise **^{D}Mg•13** (*vide supra* – for spectrum see Figure 4.12 after 1 h 30 mins). This observation may result from reductive elimination of methylcyclohexane from [$Cp_2Zr(CH_2Cy)H$] to give {Cp_2Zr}, and combination of the latter fragment with {**^{D}2**}.

Attempts to trap the low-valent products with phosphine ligands also met with limited success, although the results are less encouraging for synthetic refinement. The reactions are not clean, and none of the procedures tried thus far appears suitable for isolation of a product. There is no reaction on heating **^{D}Mg•Zr** in the presence of excess Ph_2PMe or PMe_3. However, photolysis of **^{D}Mg•Zr** brought about consumption (15% after 6 h, hν 400 W) and a trace of **^{D}Mg•14**. Addition of 5 equiv. PMe_3 to the reaction mixture and a further 6 h photolysis (Scheme 4.5a) brought about another 25% consumption of **^{D}Mg•Zr** and further traces of new species (see Experimental, Figure 4.15); in the ^{1}H NMR a peak relating to the phosphine group appeared at δ = 0.71 ppm (doublet, $^{2}J_{H\text{-}P}$ = 5.1 Hz). The ^{31}P{^{1}H} NMR spectrum showed two trace resonances, δ = +8.5 (present after the initial 6 h photolysis) and –4.4 ppm, with no splitting apparent for either signal.

No free dihydrogen was observed during the reaction. There was no change in the hydride resonance line shape to suggest H/D scrambling as was seen in the case of **^{D}Zn•Zr** photolysis. The reaction mixture stayed homogeneous and developed a light red colour. As with Scheme 4.4, the incomplete mass balance can be explained by formation of one or more paramagnetic species, likely to be heterobi-[22] and mononuclear[23,24] Zr^{III} complexes. These species are likely to give rise to the colour change.



Scheme 4.5. Attempts at synthesis of low-valent species through photolysis in the presence of a) 5 equiv. PMe_3 (in benzene-d_6, 10 h) and b) 5 equiv. PMe_3 and 5 equiv. 3,3-dimethyl-but-1-ene (in benzene, 20 h).

The colour change and the unknown peaks in ^{31}P NMR spectra were also seen when the photolysis experiment (Scheme 4.5b) was run in the presence of the hydrogen trap 3,3-dimethyl-but-1-ene (TBE). Treatment of the heterobimetallic complex with this alkene reagent

does not yield any reaction under thermal conditions (8 h, 80 °C). Use of TBE gives rise to many other signals (see Experimental section, Figure 4.16), including a signal at δ = +18.9 ppm in the ^{31}P NMR spectrum, which is assigned as $[Cp_2Zr(PMe_3)_2]$.[25] This product implies that the $\{Cp_2Zr\}$ fragment is accessible from **^{D}Mg•Zr**, and the several hydride containing products may represent structures in which it is bound by Mg and P ligands. Not present in these reactions is $[Cp_2Zr(H)_2PMe_3]$, whose ^{31}P NMR signal at δ = +11.7 ppm (triplet of dectets) was identified when **Zr•Zr** and the phosphine were mixed at room temperature.

DFT Calculated Reduced M/Zr Species

The structure of the putative **^{D}Mg•14** was calculated (Figure 4.3), and the result was compared against the theoretical Zn analogue. The complexes differ more than any other Mg/Zn comparison elsewhere in the study (*cf.* Chapter 2 and Chapter 3): on the one hand, the metal-metal linkage in **^{D}Mg•14** clearly involves the hydride atom, whereas the hydride atom is a spectator in the Zn/Zr bonding of **^{D}Zn•14**. Complementary input geometries were used for the calculations, which returned the core geometries shown in Figure 4.3 in all cases. The H-M-Zr angles in **^{D}Mg•14** and **^{D}Zn•14** are 43° and 93° respectively. Both structures show an approximate 45° twist of the {Cp-Zr-Cp} axle relative to the β-diketiminate plane. NBO analysis (see Experimental) shows an ate complex description dominates **^{D}Mg•14**, and Zr and Zn are covalently bonded in **^{D}Zn•14** – agreeing with similar comparisons made in Chapter 2.

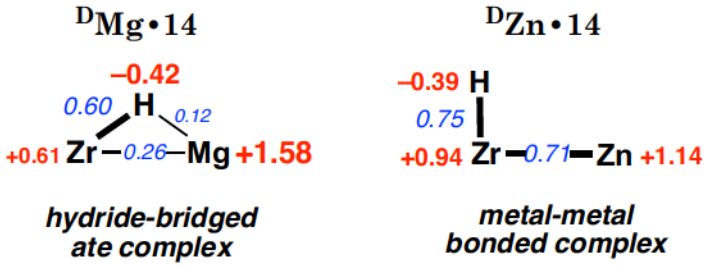


Figure 4.3. NBO analysis of the **^{D}Mg•14** and **^{D}Zn•14** core fragments: NPA charges on atoms (red) and WBIs between atoms (blue).

The free energy of elimination of dihydrogen from the trihydride pre-catalysts was calculated to gauge the relative stability of these complexes. Figure 4.4a displays the results – no transition states have been calculated at this point. Interestingly, **^{D}Mg•14** is 8.1 kcal mol^{-1} *less* stable than **^{D}Zn•14**. Contrastingly, looking at the coordination of but-1-ene to the monohydride complexes (Figure 4.4b), the formation of the Mg/Zr slipped metallacyclopropane (**^{D}Mg•Int^{7}**) is 9.5 kcal mol^{-1} *more* favourable than the Zn/Zr counterpart. (The regiochemistry of the bridging alkene was based on the X-ray structure of **^{D}Zn•12** in Chapter 3.) Even considering just the differences in the **^{D}Mg•14** and **^{D}Zn•14** structures, there is a good chance that the

kinetic barriers surrounding the species will differ significantly with regards to incoming substrate.

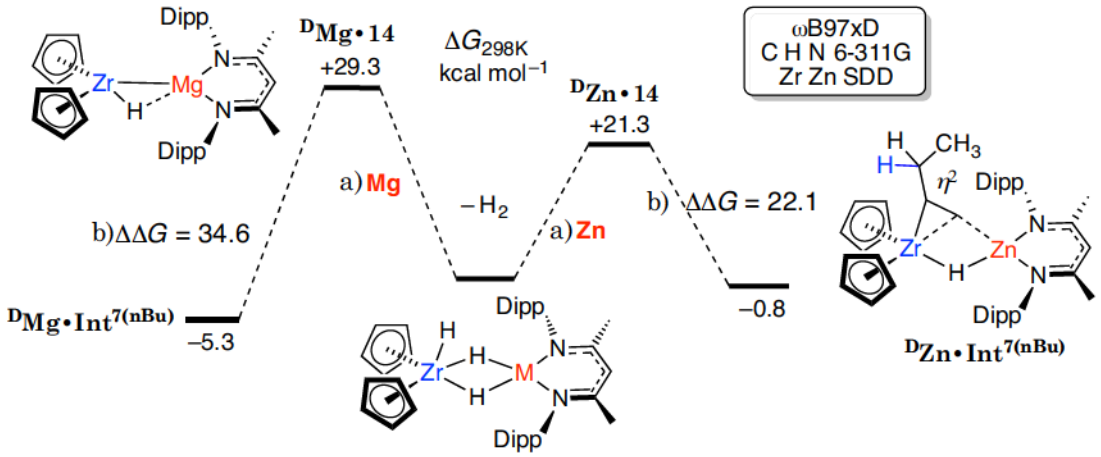


Figure 4.4. Comparison of stabilities of some possibly early mechanism intermediates, M•**14** and M•**Int**^{7} (M = ^{D}**Mg**, ^{D}**Zn**).

4.2.2.3 Monometallic Catalyst and the Origin of Selectivity

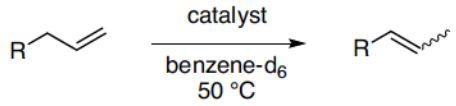
The formation of high quantities of alkane by-products for ^{M}**Al•Zr** can bea explained by an alternative mechanism for pre-catalyst activation for this heterobimetallic complex. Zirconocene dihydrides are established alkene hydrogenation catalysts.[4,26-32] In benzene-d_6 ^{M}**Al•Zr** exists in equilibrium with **Zr•Zr** and ^{M}**1**. The zirconocene dihydride is known to equilibrate with 2 equiv. of monomeric [Cp_2ZrH_2] at 80 °C.[33] Alkene insertion into [Cp_2ZrH_2] would result in the formation of monomeric 16-electron complexes of the form [$Cp_2Zr(H)R$] or [Cp_2ZrR_2]. Studies on alkene insertion into Zr–H bonds (and the microscopic reverse β-hydride elimination) have been carried out by Chirik, Bercaw and co-workers.[18,34] β-Hydride elimination and reductive elimination of alkanes from these species, either in the absence or presence of an external alkene or dihydrogen, is well-established and has been studied in detail.[35-40] Moreover, it has been demonstrated above (see Table 4.2). This reductive elimination explains alkane formation, and it would generate a low-valent zirconocene intermediate, which, based on precedent, should be an active catalyst for alkene isomerisation.[10-12] This hypothesis is consistent with the low ratios of alkene:alkane observed in the initial period of the reaction (Graph 4.1) and suggests that ^{M}**Al•Zr** may simply be acting as a precursor to **Zr•Zr**.

To further explore this hypothesis, **Zr•Zr** was investigated as a catalyst for alkene isomerisation of terminal alkenes at different catalytic loadings. The results of these experiments are presented in Table 4.3. For the isomerisation of allylbenzene catalysed by **Zr•Zr**, at high catalyst loadings (5 mol%) the alkene:alkane ratio is low while at low catalyst loadings (0.5 mol%) this ratio is high. The implication is that catalyst initiation results in transfer

hydrogenation of the alkene and the higher the catalyst loading the greater the quantity of alkane formed. At low loadings **Zr•Zr** is a simple and efficient catalyst for alkene isomerisation, side reactions are avoided, and the catalyst is competitive with synthetically complex group 4 initiators for alkene isomerisation.[5-12]

For comparison, low-loading experiments with **^{D}Mg•Zr** and the three substrates in Table 4.3 were carried out. Overall, the heterobimetallic catalyst shows no great improvement in performance for allyltrimethylsilyl and hexene isomerisation. The selectivity of isomerisation by 1 mol% of **^{D}Mg•Zr** is superior to the 5 mol% runs in Table 4.1. The ^{1}H NMR signals of **^{D}Mg•Zr** remained present throughout. A 1 mol% loading of **^{D}Mg•Zr** was successful in isomerisation of allylbenzene when heated for 100 min at 80°C. Nevertheless, the reaction races to completion giving a remarkable alkene:alkane ratio of 250:1 and a 90% yield. The alkene selectivity is 55:1 *E*:*Z* after consumption of allylbenzene, but drops to 42:1 after further heating of the internal alkenes. Catalysis of 4,4-dimethyl-pent-1-ene isomerisation was not possible at 5 mol% or 1 mol% loading of **Zr•Zr**.

Table 4.3. Alkene isomerisation with **Zr•Zr** at low loadings.



substrate	*catalyst*	*mol%*	*time (h)*	*combined yield (%)*	*E:Z*	*alkene :alkane*
R = Ph	**Zr•Zr**	5	24	15	45:1	9:1
		1	60	90	51:1	26:1
	^{D}Mg•Zr[a]	1	1.5[b]	90	55:1	250:1
R = $SiMe_3$	**Zr•Zr**	0.5	38	75	23:1	35:1
	^{D}Mg•Zr	1	38	65[c]	128:1	61:3
R = ^{n}Pr	**Zr•Zr**	0.5	38	90	16:5:8[d]	30:1
	^{D}Mg•Zr	1	712	>95%	20:1:5[d]	99:1

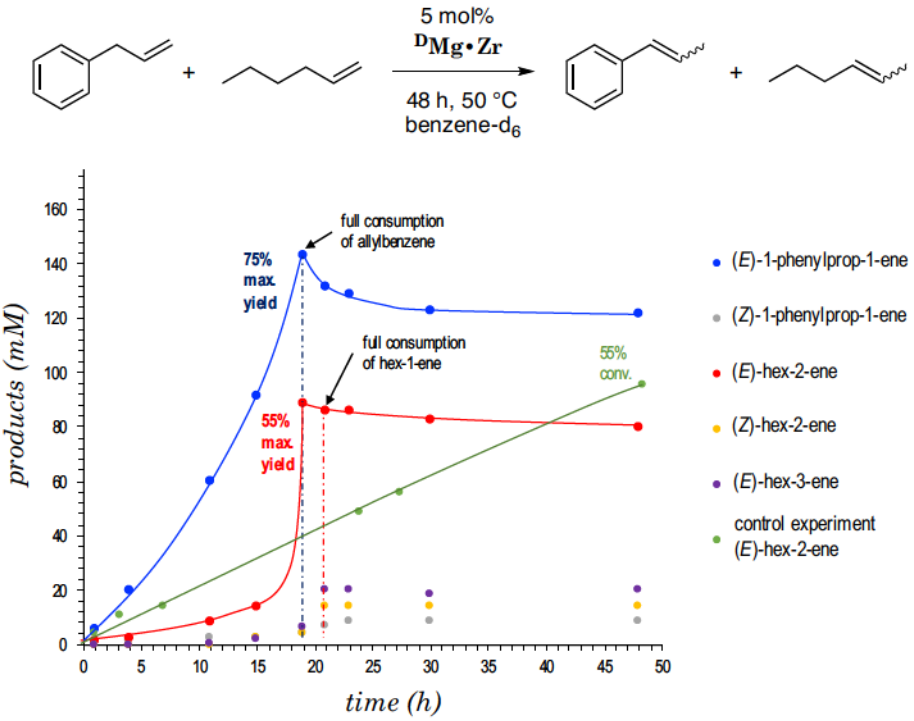
[a] On one occation, catalyst death before any conversion. [b] Reaction temperature of 80 °C was used. [c] Yield could not be increased after 38 h. [d] Ratio of 2*E*:2*Z*:3*E*.

4.2.2.4 Kinetic Analysis for the Mg/Zr Catalyst

Competition Experiment

To further monitor the performance of **^{D}Mg•Zr**, as well as to derive mechanistic arguments for the catalysis, a kinetic analysis was planned. Firstly, two substrates were investigated in a competition experiment. Allylbenzene and hex-1-ene were used for the rough similarity of their reaction times and the clear separation of the crucial ^{1}H NMR resonances used for yield

calculation. Equimolar amounts were added to the same solution of 5 mol% ^{D}**Mg•Zr** (loading with respect to one substrate). The results are illustrated in Graph 4.2. Primarily, the experiment demonstrates the catalyst's preference for conversion of allylbenzene over hex-1-ene. This was perhaps to be expected considering their separate reaction times (in Table 4.1). However, the reaction of hex-1-ene is suppressed before all allylbenzene is consumed (somewhere between 16 and 19 h), around which time it dramatically accelerates and is itself consumed in the next 4 h, some 48 h before the completion of the original experiment quoted in Table 4.1. Moreover, hex-1-ene isomerisation in the absence of allylbenzene (green markers on Graph 4.2) is obviously slower, having only 70% conversion after 48 h. Therefore, a species involved in allylbenzene catalysis is accelerating the hex-1-ene catalysis (once the former is finished).



Graph 4.2. Product distribution *vs.* time for the terminal alkene isomerisation of a mixture of allylbenzene and hex-1-ene by 5 mol% ^{D}**Mg•Zr**. Data trendlines are illustrated as a guide only. Results from an isolated hex-1-ene control experiment are also included.

In Graph 4.2, the curve for (*E*)-1-phenylprop-1-ene is unusual. The rate of production of (*E*)-1-phenylprop-1-ene appears to increase exponentially until the point of full consumption of allylbenzene, then the concentration decays almost as quickly, before plateauing to give a final 60% yield of the (*E*)-isomer. The plot for (*E*)-hex-2-ene hints at the same pattern. The drastic burst in conversion of hex-1-ene prevents the point kinetics method from concluding the true shape of the (*E*)-hex-2-ene curve in Graph 4.2. The minor products of both substrates

grow in after the point at which the maximum yield of the major product has been reached. Their yields are too low to confidently model the plots.

The decay of (*E*)-1-phenylprop-1-ene after a maximum point is reached is partially due to conversion to the (*Z*)-isomer. Yet, there is clearly more going on: the amount of (*Z*)-isomer created does not account for the entire loss in yield of the (*E*)-isomer, 1-phenylpropane is only present in trace amounts, and at the end of the reaction, 30% of the catalyst is still present. A significant amount of substrate mass is unaccounted for, and it is possible that alkene oligomerisation or polymerisation may be occurring at longer reaction times.

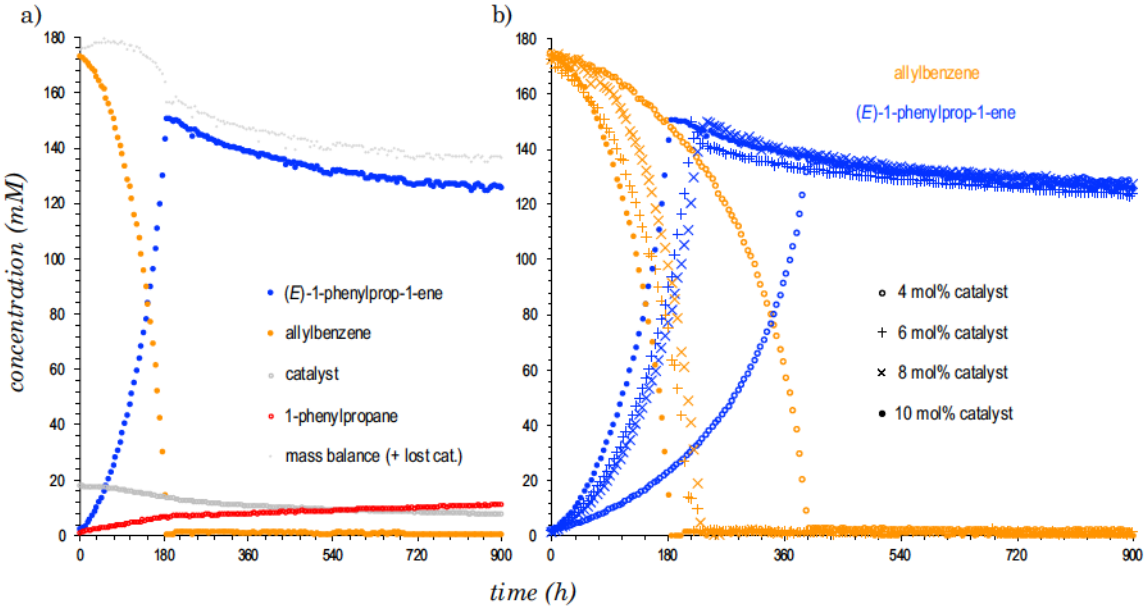
Furthermore, the maximum yield of (*E*)-hex-2-ene also seems to deplete and coincide with small growths in the minor products. To examine this depletion process, an isolated reaction of (*E*)-hex-2-ene with 5 mol% **^{D}Mg•Zr** was conducted. This control experiment found that in isolation the conversion of the major (*E*)-isomer is clearly slower in the competition experiment. The isolated control experiment produced smaller proportions of the minor isomers. It took 1 d of heating at 50 °C to reach a (*E*)-hex-2-ene:(*Z*)-hex-2-ene:(*E*)-hex-3-ene ratio of 18:1:1. This is lower with respect to the minor isomers than the same ratio calculated from Graph 4.2 (approx. 20:5:3). Even a total 4 d heating of the isolated experiment led to an inferior 18:2:1 ratio. The data again suggest that a more active catalyst is generated in the presence of allylbenzene.

Allylbenzene Reaction Profiles

For closer inspection of the unusual reaction profile revealed by the competition experiment, in-probe ^{1}H NMR analysis was used to monitor the isolated isomerisation of the dominant substrate, allylbenzene. The experiments were run at 60 °C to allow for workable reaction times; the general shape of the reaction profiles was the same for 50, 60 and 70 °C runs. The results (*e.g.* Graph 4.3a – 6 mol% catalyst) confirm the suggestion made earlier by Graph 4.2: the maximum of (*E*)-1-phenylprop-1-ene concentration *does* appear to be a cusp.

The accelerating (*E*)-alkene production is stopped abruptly (at 215 min in Graph 4.3a) upon the total consumption of allylbenzene. A *ca.* 3% yield of 1-phenylpropane accumulates during the reaction, and concomitantly, the pre-catalyst (**^{D}Mg•Zr**) concentration drops to 3 mol% of the initial allylbenzene concentration. The yield of the (*Z*)-alkene is not accurately measurable in this experiment, but appears to follow (*E*)-1-phenylprop-1-ene, in a roughly 40:1 proportion across the whole reaction. A plot of the substrate-related mass balance shows strange behaviour (Graph 4.3a, grey diamonds); by the end of the reaction, over 20% of the substrate is missing, even when considering the amount of degraded catalyst (which could form off-cycle metal alkyl species). The kinetic analysis was carried out for a range of catalyst concentrations, and Graph 4.3b shows that the same general profile shape is maintained

between 4–10 mol% loadings. The rate of each run increases with increased **^{D}Mg•Zr** loading (Graph 4.3b).



Graph 4.3. a) The reaction profile for the isomerisation of allylbenzene with 10 mol% loading of **^{D}Mg•Zr**; and b) reaction profiles of the same reaction across a range of four different loadings.

At 2 mol% of **^{D}Mg•Zr**, the reaction failed (see Experimental, Graph 4.5) – with full consumption of the catalyst after around 200 min. The failure of catalysis at these conditions is at odds with the successful 80 °C, 1 mol% **^{D}Mg•Zr** experiment in Table 4.3. Both the 1 and 2 mol% experiments used the same stock solution of catalyst. The death of the catalyst in the 2 mol% experiment may be caused by adventitious air or moisture, but may also be explained by the difference in heating conditions. Repeat experiments are necessary. Should the catalyst death be a persistent condition, then issues with substrate and catalyst purity need to be addressed.

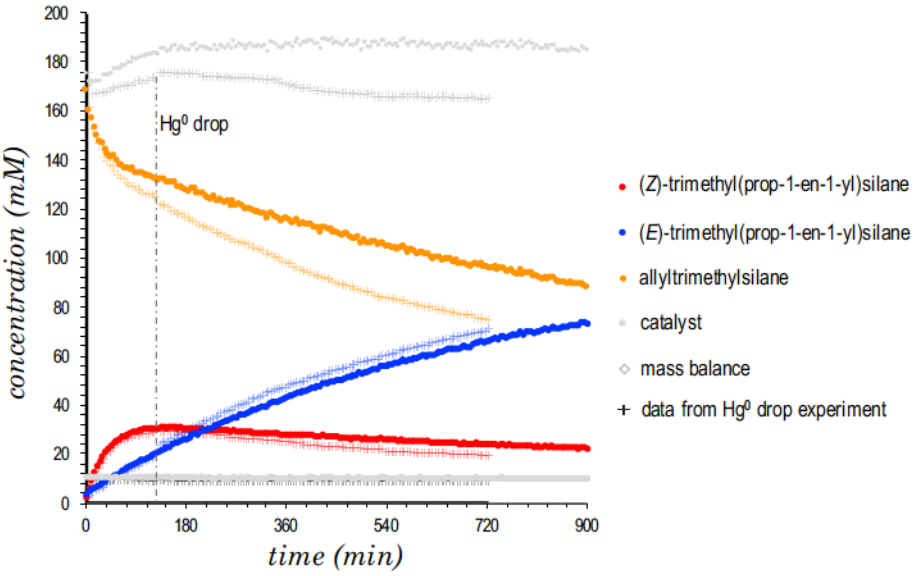
A control experiment was carried out to confirm that the **^{D}Mg•Zr** pre-catalyst does not produce a catalyst simply by thermolysis. The pre-catalyst (6 mol%) was heated for 20 h at 50 °C in benzene-d_6, *before* the addition of the alkene substrate. This pre-heating period was chosen because Graph 4.2 shows that 20 h of heating at 50 °C leads to the maximum acceleration in reaction rate. There is no clear difference in the reaction profiles (see Experimental, Graph 4.7).

Allyltrimethylsilane Reaction Profiles

The unusual shape of the allylbenzene reaction profiles in Graph 4.3 and Graph 4.2 suggested a complexity to the mechanism which was not expected before the kinetic analysis. With this in mind, a further in-probe reaction profile has been measured for comparison: the

isomerisation of allyltrimethylsilane at 60°C (Graph 4.4). The results are markedly different. The decay of the starting material has two regimes. The (*Z*)-isomer is initially produced more than twice as quickly than the (*E*)-isomer, but the former's production subsides after 90 minutes. The (*E*)-alkene begins to dominate after 200 min.

The production of the internal alkenes, and changing relative ratio, is consistent with the previous results of Graph 4.1. As well as the obvious differences in reaction profile, it should be noted that the allytrimethylsilane experiment involves virtually no hydrogenation compared to the allylbenzene analogue. Only trace amounts of trimethylpropylsilane are observed throughout the experiments in Graph 4.4. It also appears that catalyst death is linear and slower in this case. Only around 5% of ^{D}**Mg•Zr** is lost across 955 min.



Graph 4.4. Reaction traces of the ^{D}**Mg•Zr**-catalysed isomerisation of allyltrimethylsilane at 60°C (6 mol% ^{D}**Mg•Zr**). The cross data points (the fainter graphs) are the data from the Hg^0 drop experiment.

As a control for heterogeneous catalysis, the experiment was repeated with the addition of a Hg^0 drop at 120 min (Graph 4.4). The catalysis was not slowed, suggesting the active species is homogeneous. An inhibitive effect of PMe_3 has not been found to be clear cut. The phosphine does not shut down the isomerisation catalysis with ^{D}**Mg•Zr** or **Zr•Zr**, but in-probe kinetic experiments are needed to test for subtle effects on reaction progress (see Future Work, section 4.5).

4.3 DISCUSSION

^{D}Mg•Zr, is a particularly capable alkene isomerisation catalyst for several substrates, compared to its Al and Zn analogues. The study has concentrated on the mechanistic chemistry behind the catalytic success. The key findings support an π-allyl hydride mechanism:

i. **^{D}Mg•Zr** does not show any signs of hydrometallation of several unsaturated probe substrates, effectively ruling out an M–H insertion-elimination mechanism.
ii. The loss of **^{D}Mg•Zr** pre-catalyst during alkene isomerisation is offset by the yield of alkane by-product.
iii. Catalysis by **^{D}Mg•Zr** gives high alkene:alkane selectivity compared to the other pre-catalysts.
iv. The reduced, mono-hydride complex **^{D}Mg•14** is eminently achievable.
v. With allyltrimethylsilane and **^{D}Mg•Zr**, the alkene isomerisation reaction does not use a heterogeneous catalyst.
vi. With allylbenzene and **^{D}Mg•Zr**, the kinetic profile of the reaction shows acceleration in reaction rate throughout.
vii. Once the allylbenzene isomerisation is complete, the mixture shows the ability to drastically accelerate hex-1-ene isomerisation (compared with the rate when isolated **^{D}Mg•Zr** is the pre-catalyst).

4.3.1 Mechanistic Proposal for the Mg/Zr Catalyst

Significantly, the insertion-elimination mechanism for **^{D}Mg•Zr** was all but ruled out early in the study (section 4.2.2.1). The π-allyl hydride mechanism is therefore likely; a simple bimetallic version of this mechanism is proposed in Figure 4.5, with Zr as the active centre. The catalytic cycle begins after transfer hydrogenation of one equivalent of substrate to yield the putative 16-electron Zr catalyst, **^{D}Mg•14**.

4.3.1.1 On-cycle Mechanism

An 18-electron complex results from a second equivalent of terminal alkene substrate entering the coordination sphere of Zr (and potentially Mg). The resulting intermediate, **^{D}Mg•Int^{7}**, is a heterobimetallic alkene adduct, and based on precedent in Chapters 1 & 3 (*i.e.* **1.80** and **^{D}Mg•12**), its feasibility as a slipped metallacyclopropane is strong. From **^{D}Mg•Int^{7}**, allylic C–H activation by a formally d^2 Zr centre allows progression of the isomerisation steps. Harrod and co-workers have demonstrated that zirconocyclopropanes are capable of equilibrating with the corresponding allyl hydride by C–H activation of the allylic position.[23] In

the current case, subsequent η^1- to η^3-rearrangement (**^{D}Mg•Int^{8a}** → **^{D}Mg•Int^{8b}**) followed by reductive elimination would explain catalytic turnover. To circumvent a 20-electron complex, the η^3-configured **^{D}Mg•Int^{8b}** is able to achieve a μ^1 hydride linkage ({Zr–H}→Mg).[41] The high *E:Z* ratio of the alkene products is readily explained by a process that is under thermodynamic control. The (*E*)-isomers of simple alkenes are slightly more stable than the (*Z*)-alkenes based on sterics;[42] the *E*:*Z* ratio increases over the course of the reaction. Graph 4.4 shows how (*Z*)-trimethyl(prop-1-ene-1-yl)silane is kinetically favoured, but is the minor product as the system tends towards equilibrium.

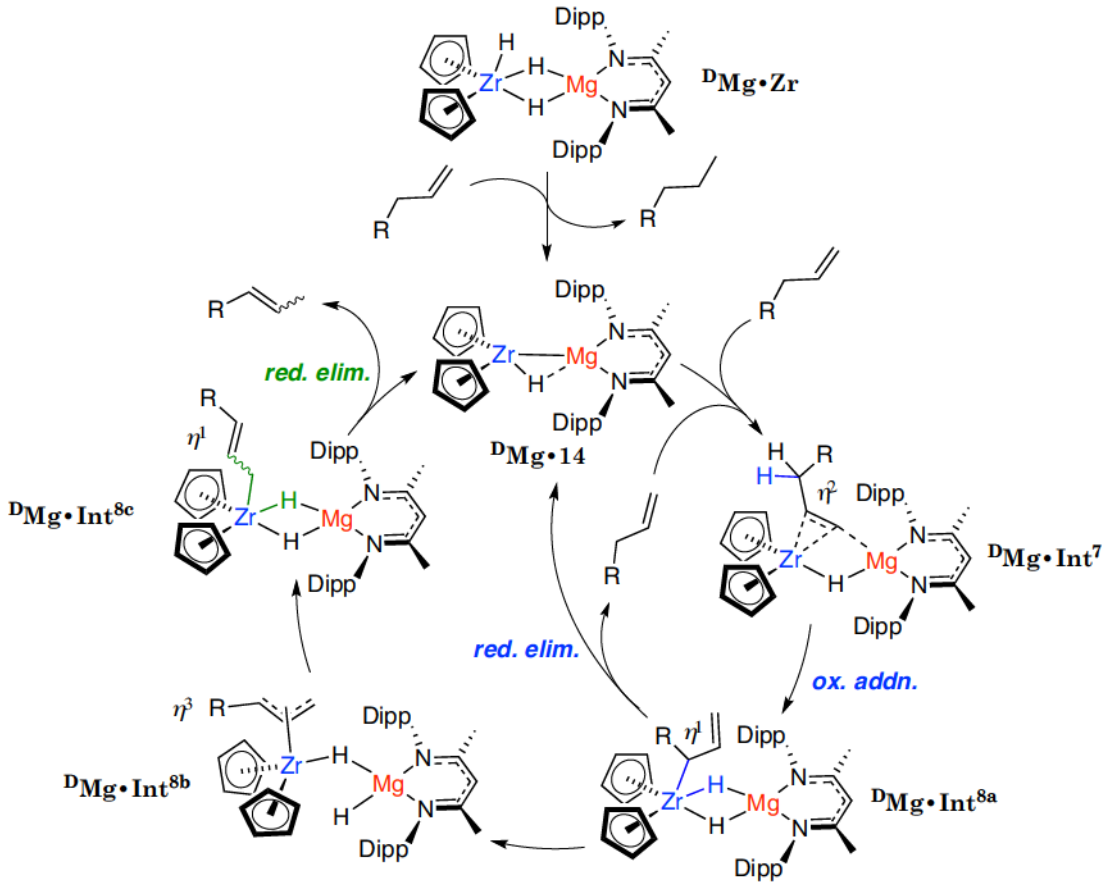
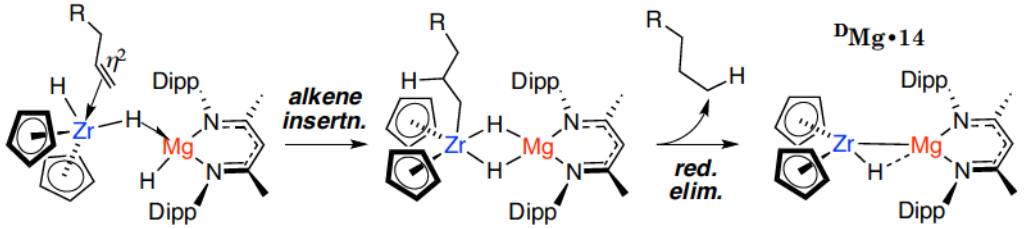


Figure 4.5. A mechanistic possibility for the catalytic isomerisation of alkenes by **^{D}Mg•Zr**.

4.3.1.2 Pre-catalyst Activation

It is proposed that the high alkene:alkane selectivity observed for **^{D}Mg•Zr** is a result of the tightly bound heterobimetallic catalyst not dissociating under the reaction conditions, and therefore not generating **Zr**. The monomeric **Zr** is easily susceptible to the mechanistic steps required for transfer hydrogenation of alkene (and metal reduction).[18,34-40] With the alkene isomerisation at 50 °C, thermal dissociation of **^{D}Mg•Zr** should be virtually non-existent. Chapter 2 shows that **^{D}Mg•Zr** is tighter bound than the Zn analogue. Above, it was unreactive with the zirconocene dihydride trap, 4,4-dimethyl-pent-2-yne (Scheme 4.1) even at 80 °C. At

the same conditions, the alkyne reacts cleanly with ^{D}**Zn•Zr** to give ^{D}**Zn•12** (Scheme 3.9). Therefore, for ^{D}**Mg•Zr** any catalytic mechanism should not be reliant on the dissociation of **Zr** from these pre-catalysts. With this in mind, Scheme 4.6 gives a mechanistic proposal for the activation of ^{D}**Mg•Zr** by terminal alkene.



Scheme 4.6. A plausible coordination of terminal alkene to ^{D}**Mg•Zr** and subsequent steps for the production of the active catalyst, ^{D}**Mg•14**.

The terminal alkene may achieve η^2-coordination to the Zr centre after partial dissociation of the heterobimetallic trihydride complex.[43] Subsequent hydrometallation of the coordinated alkene by Zr–H_t gives an alkyl *bis*-hydrido complex. Reductively elimination from such species has been strongly implied several times during the study (Table 4.2 and section 4.2.2.2). The resulting complex is the 16-electron Zr species ^{D}**Mg•14**.

Alkane products are seen throughout the catalysis experiments, and the yield of alkane compensates for the amount of catalyst lost in all instances. This is nicely illustrated in the composition profile in Graph 4.3a. The pre-catalyst activation would not need to be wholesale: a small amount of activation could generate a very small concentration of the catalyst. This would explain why only the pre-catalyst is observable throughout the reaction.

4.3.2 Autocatalysis

4.3.2.1 Allylbenzene

The exponential acceleration of the allylbenzene reaction is typical of an autocatalytic mechanism.[44] An autocatalytic reaction occurs when the product acts as (or forms a part of) a species that is a catalyst for the product's formation.[45] The product, 1-phenylprop-1-ene, is not able to react with the terminal alkene alone; it would seem that any autocatalysis would go *via* what Blackmond calls a "ligand-accelerated cycle".[45] This is the case in which the product, P (the internal alkene), acts as a ligand in a new organometallic species (*i.e.* P + catalyst → **cat***). The new complex, **cat***, is a far superior catalyst for the formation of P than what went before.

The results of the competition experiment lend support to this theory. The otherwise slow hex-1-ene isomerisation is greatly accelerated after the completion of the allylbenzene isomerisation process (Graph 4.2 – key finding vii.). This suggests that build-up of **cat*** (from

an allylbenzene-related moiety and Mg/Zr) acts as a better catalyst for hex-1-ene isomerisation than **^{D}Mg•Zr**. Additional support is in the kinetic profile for the pre-catalyst, **^{D}Mg•Zr**. Graph 4.3a shows how, as the (*E*)-isomer is being generated from the substrate, the pre-catalyst consumption also accelerates, before slowing to a linear consumption once the maximum concentration of product is reached. Thus, there appears to be a correlation between formation of product and a putative "catalyst → **cat***" process.

Furthermore, a very similar kinetic profile to that of (*E*)-1-phenylprop-1-ene (*e.g.* in Graph 4.3) was exhibited by the product of an autocatalytic reaction reported this year.[46] This profile includes the drop in product concentration after total consumption of substrate. The authors imply that this product depletion stage occurs when autocatalysis stops and the autocatalytic species is freed up to take part in counterproductive processes. The aforementioned pieces of experimental support and the matching of kinetic profiles with literature precedent mean that an autocatalysis explanation is preferred to substrate inhibition. The latter would have to be very pronounced (for some relatively similar substrates) to have such a marked effect.

4.3.2.2 Allyltrimethylsilane

What is more, there is a feature of the data that makes it possible to extend the aforementioned "**cat***" hypothesis for the allylbenzene and the allyltrimethyl isomerisations. It is possible that in the longer runs, a second regime in the catalysis is reached. It may involve the formation of **cat***. As Graph 4.4 tends towards $t = \infty$ the hyperbolic plots suggest a maximum combined yield of around 60% (100 mM). It is therefore strange that the yields of the in-probe kinetics experiments differ from the earlier run (Graph 4.1) by 15%. The point kinetics may fail to capture the step change between two regimes.

It was initially assumed that the waywardness of the 15 h time-point in Graph 4.1 was due to measurement error – but now we see that this may not be the case. At t = 15 h, the experiment in Graph 4.1 shows 55% combined yield and a 3:2 ratio of *E*:*Z* products. This is in fair agreement with the final time-point of the in-probe kinetics results (Graph 4.4 – 60 °C, 15 h, 56% yield, 16:5 *E*:*Z*). The boost in yield between 15 and 50 h, may arise from the generation of **cat*** (possibly an allyltrimethylsilane analogue). Repeats, and a lengthened in-probe kinetics experiment will resolve the issue.

4.3.2.3 Origin of Autocatalyst

For a plausible **cat***, incorporation of the alkene product as a ligand would probably not be tolerated by a (Mg/Zr) bimetallic complex (see Scheme 4.1 and Table 4.2). The coordination number would be prohibitively high for the species to be a catalyst. To generate an active site, it may be suggested that there is decomposition of the Mg/Zr heterobimetallic species presented in Figure 4.5. Therefore, the true catalyst might be something like the mononuclear

Int[8a]. With terminal hydrides, the alkyl complexes (in Figure 4.6) are theoretically capable of catalysing the isomerisation of another equivalent of incoming allylbenzene *via* an insertion-elimination pathway.

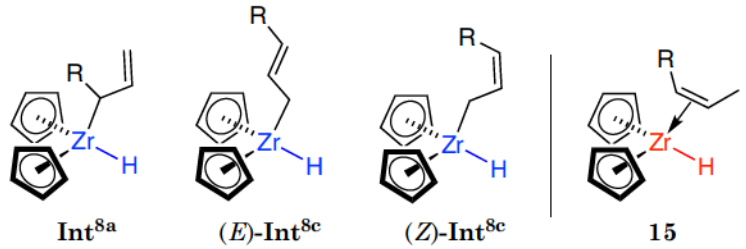


Figure 4.6. Candidates for the role of **cat*** in the terminal alkene isomerisations by **[D]Mg•Zr**.

The selected isomers of **Int**[8] are included as candidates for **cat*** to make the point that they have a free coordination site and may have varying reactivity, if only due to sterics. The generalised alkene complex, **15**, is related to the M/Zr slipped metallacyclopropanes and **[D]Mg•Int**[7]. A formal hydrogen atom transfer (HAT) from the {**[D]2**} fragment to the Zr^{IV} alkene complex would give a Zr^{III} hydride species. The latter is theoretically capable of alkene isomerisation by the insertion-elimination mechanism.

When the substrate is allylbenzene (*i.e.* R = Ph), it could be the case that this substrate accelerates the decomposition pathway towards **cat***, the true catalyst. Indeed, this acceleration would be to the extent that **cat*** operates from the beginning of the kinetics, supposedly not the case with the allyltrimethylsilane system. We must contemplate trivial factors which could explain the complex behaviour of the catalysis – factors such as the involvement of impurity in the material. One such theory has already been covered in section 4.2.2.4, *viz.* the exponential build-up or destruction of a key impurity in **[D]Mg•Zr**, which leads to **cat*** and increase of the rate. The *allylbenzene* sample could just as likely harbour trace impurities, and these could be the root of the substrate sensitivity.

4.3.3 General Mechanistic Summary

The loosely bound **[M]Al•Zr** and **Zr•Zr** are both able to generate **Zr** and thus **14** after subsequent transfer hydrogenation of 1 equiv. alkene (section 4.2.2.3). Until future studies, it is assumed that **14** operates as the active species in these systems. Under the catalytic conditions, **[D]Mg•Zr** and **[D]Zn•Zr** cannot generate appreciable concentrations of **Zr**. It has been shown above that the Mg/Zr pre-catalyst may undergo activation to give a reduced species (**[D]Mg•14**).The reason for catalytic activity with **[D]Mg•Zr** but not **[D]Zn•Zr** may lie in a difference in the impurity profiles of the pre-catalysts. Controls for involvement of the impurities should be carried out before launching exploration into the mechanism(s) by DFT analysis (primarily).

4.4 Conclusion

In summary, ^{D}**Mg•Zr** is an active and selective catalyst for internalisation of a range of terminal alkenes, controlling both the alkene:alkane and *E*:*Z* ratio even at low loadings. Catalysis *via* the zinc analogue is found to be reliant upon long (> 3 d) initiation periods to trigger the breakdown of the pre-catalyst. Disappearance of the pre-catalyst is also seen for ^{M}**Al•Zr** and **Zr•Zr** reactions with the terminal alkenes. This leads to smaller alkene:alkane ratios, which is not the case for the Zn/Zr system. As a result, lower loadings (by an order of magnitude) were trialled for **Zr•Zr,** with much success: improved yields and improved alkene:alkene and *E*:*Z* selectivities are achieved.

For ^{D}**Mg•Zr,** an insertion-elimination mechanism is ruled out by the pre-catalyst's complete reluctance to react with methylenecyclohexane, diphenylacetylene, or 2,2-dimethyl-pent-3-yne. Additionally, introduction of several β-diketiminato magnesium alkyl complexes to $[Cp_2Zr(H)(\mu\text{-}H)]_2$ fails to generate a supposed intermediate for an insertion-elimination mechanism: dihydridoalkyl analogues of ^{D}**Mg•Zr** are not observed, neither are any alkene products that might be expected from β-hydride elimination in these species. Therefore, a π-allyl hydride mechanism is expected; ^{D}**Mg•Zr** can be reduced to a related monohydrido complex (^{D}**Mg•14**) which is catalytically operative. The monohydrido complex is accessible (according to ^{1}H NMR) from $[^{Dipp}BDI Mg^{I}]_2$ and Schwartz' reagent.

Kinetic profiling of the allylbenzene reaction with ^{D}**Mg•Zr** gives unexpected results. The isomerisation accelerates up until completion. This is thought to be due to build-up of a new catalytic species, **cat***, which requires the internal alkene product for its formation. In a competition experiment, the rate of hex-1-ene isomerisation is greatly accelerated after the **cat*** finishes its action on allylbenzene. Hence, it appears that when **cat*** is created in an ^{D}**Mg•Zr**/allylbenzene system, it outstrips the standard Mg/Zr catalyst.

4.5 FUTURE WORK

4.5.1 ^{D}Mg•Zr & ^{D}Mg•14

There are several ways to explore the viability of the **^{D}Mg•14** catalytic route before turning to DFT work. Simply in terms of collecting more information, the allyltrimethylsilane isomerisation can be used to advance a customary kinetic analysis – *i.e.* derivation of the order of the reaction in catalyst and in alkene, as well as the kinetic parameters. This analysis should hold for the first 24 h of experiment at least, before the possible regime change. With these kinetic experiments, PMe_3 could be explored as a catalytic inhibitor – it has been used as an inhibitor previously for alkene hydrogenation by a Zr-containing heterobimetallic complex.[47] There is a chance that an inhibitor may stymie the putative change in catalytic regime. In other additive trials, repeats of the mercury drop experiment might show that it actually accelerates the reaction (Graph 4.4).

There is more scope for the synthesis and characterisation of **^{D}Mg•14**. Schwartz and Gell's preparations of $[Cp_2Zr^{II}(L)_2]$ compounds[36] from $[Cp_2ZrH(CH_2Cy)]$ can be adapted for introduction of the {Mg–H} ligand. Furthermore, if PMe_3 does inhibit the initial catalysis, then spectroscopic signals for **^{D}Mg•14**•PMe_3 may be found. The latter is possibly synthesised independently by introduction of PMe_3 to the reaction in Scheme 4.4. (A encouraging DFT calculation gives the ΔG_{298K} of this trapping as –8.1 kcal mol^{-1}.) Overall, it would be encouraging if **^{D}Mg•14** were catalytically competent.

Finally, what has not yet been emphasised is the particularly odd difference in reactivity between the Si/C analogues allyltrimethylsilane and 4,4-dimethyl-pent-1-ene (*i.e.* allyl-TMS *vs.* allyl-^{t}Bu). The eventual mechanistic solution will need to include a step which is prohibited by the difference between allyltrimethylsilane and 4,4-dimethyl-pent-1-ene: the shorter length of the C4–C2 compared with the Si–C bond for example. However, more trivially, the hydrocarbon may be lacking a trace impurity that is contained in the silane, and this possibility should also be analysed.

4.5.2 Experimental Issues

Monitoring yields through ^{1}H NMR spectroscopy has been difficult, with resonances at similar frequencies and busy reaction mixtures. Gas chromatography will be a good way to crosscheck the current method. Hopefully, this will bring about an understanding of the imperfect mass balance results (seen in section 4.2.2.4). The possibility of paramagnetic species in the catalytic mixtures might also be mitigated by use of electron paramagnetic resonance. There are experiments (mentioned in the Results and Discussion) which can be

repeated or extended, and will clear up **cat*** issues. For example, is the allylbenzene isomerisation really intolerant of low loading of **^{D}Mg•Zr** – is this temperature related?

*4.5.3 Existence and Identity of cat**

4.5.3.1 Synthesis of cat* Candidates

The allylbenzene/**^{D}Mg•Zr** results imply that the system contains an excellent catalyst (at least in terms of *TOF*) and certainly one that would be notable if it could be isolated and used generally. Future studies could focus on trying to prepare **cat*** independently. Synthesis of (*E*)-**Int^{8c}** and (*Z*)-**Int^{8c}** (Figure 4.6) should be attempted, with subsequent trialling of the products as catalysts for terminal alkene isomerisation. When reacted with hex-1-ene, we can expect a catalytic rate similar to that in Graph 4.2, if the species is indeed **cat***. A cruder relation of this control experiment is to react **Zr•Zr** stoichiometrically with allylbenzene, before isolation of the organometallic species by removal of the volatiles *in vacuo*. The material can then be tried as an alkene isomerisation catalyst.

Further ideas for possible **cat*** are shown in Figure 4.7 and are taken from work by Gervais and co-workers,[9,48] and Schwartz and co-workers.[49] The Gervais papers relate to alkene isomerisation, and structures such as those below were found in reaction mixtures unexpectedly. The Zr^{IV}-Zr^{II} complex is inspired by a phosphinomethyl-bridged counterpart for which a bimetallic 1,3-COD hydrogenation mechanism was proposed.[9] Both complexes are possible from zirconocene hydride and alkene mixtures. The Schwartz motif comes from insertion of the alkenyl ligand on Zr into a main group hydride bond. Aluminium alkyl versions were made (using μ-Cl), but {^{Dipp}*BDI*Mg} variations have a chance of success. Indeed, hydrometallation of the C=C bond in (*Z*)-**Int^{8c}** could viably give something similar.

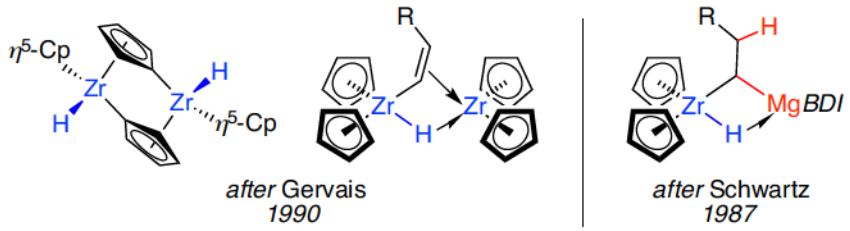
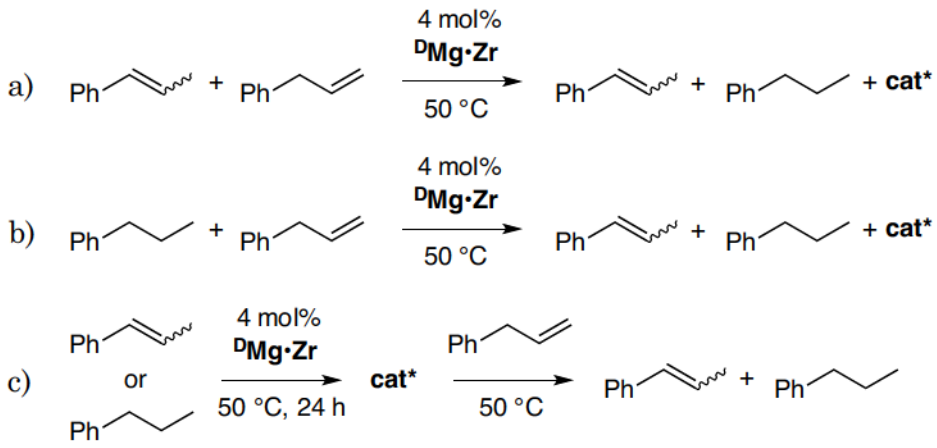


Figure 4.7. Possible **cat*** structures taken from work by Gervais[9,48,] and Schwartz.[49]

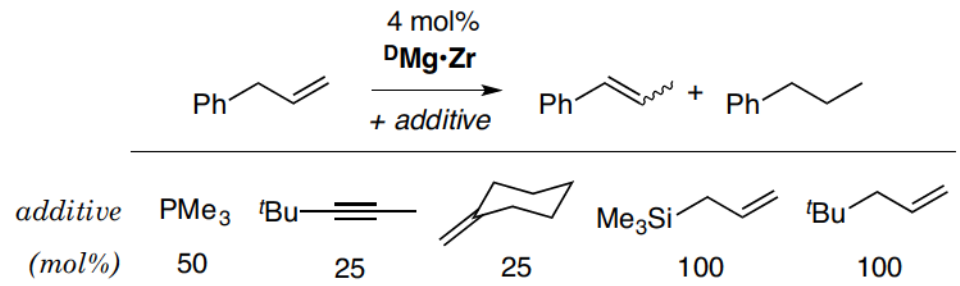
In regard to the allylbenzene reaction, **cat*** generation *in situ* may be accelerated (Scheme 4.7). By using the products as an additive (1:1 with allylbenzene) or a pre-treatment (as in the reported experiment of pre-heating the mixture), it can be seen if these products change the kinetics of allylbenzene conversion and the pre-catalyst consumption. This should therefore point towards the identity of **cat***. The same trials may be run with **Zr•Zr** pre-catalyst.



Scheme 4.7. The use of internal alkene or relevant alkane as additive or c) pre-treatment in order to generate **cat***.

4.5.3.2 DMg•Zr/Allylbenzene: controls and traps for cat*

Inhibition experiments could be investigated with the goal of identifying reagents that selectively inhibit **cat***. A simple starting point may be to work on the best possible purification of the substrate and the pre-catalyst; the kinetic profiles for their reaction can then be compared to that of the more impure original. If impurities effect **cat***, then differences are to be expected.



Scheme 4.8. Planned inhibition and competition experiments for terminal alkene isomerisation catalysed by **DMg•Zr**.

There is then recourse to inhibit the isomerisation by additives (Scheme 4.8). As mentioned earlier, PMe_3 will be a good general starting point. In the past, it too has highlighted the role of trace impurities as active catalysts.[47] An inhibitor designed for a mononuclear zirconocene species, but not a bimetallic species (like **DMg•14**), should give a telling result if the autocatalysis is due to something like **Int**[8c]. A selective inhibitor might be methylenecyclohexane, a trap for hydrido-zirconocene species but apparently inert with regards to **DMg•Zr** (Scheme 4.1). This rationale can be used for separate reactions using different pre-catalysts – *e.g.* if PMe_3 inhibits catalysis by **Zr•Zr** *but not* **DMg•Zr** there will be something to be learnt.

Use of allyltrimethysilane and 4,4-dimethyl-pent-1-ene as 100 mol% additives means these are competition experiments (Scheme 4.8). The results of their reactivity can be expected to be different, just how the kinetics of hex-1-ene were changed so much by the ^{D}**Mg•Zr**/allylbenzene mixture. Successful isomerisation of the otherwise recalcitrant 4,4-dimethyl-pent-1-ene would be particularly telling.

The complementary approach to highlighting presence of **cat*** is to make use of it once it has been generated. Instead of adding something to the reaction mixture, the product mixture can be concentrated, the volatiles removed, and the organometallics – supposedly containing **cat*** – used as the pre-catalyst for other alkene isomerisations. The kinetics of each experiment should be compared.

4.5.3.3 Al and Zn Systems

Measuring kinetic profiles of terminal alkene isomerisations with the non-Mg/Zr systems may find further examples of catalytic regime changes or autocatalysis. The vacuum transfer procedure – to look at organometallic reaction components – can be used to assess species in the activated Al/Zr and Zn/Zr systems, and the Mg/Zr systems where pre-catalyst has been consumed. Isolation and/or identification of candidates found in the crude reaction concentrates will then allow testing of individual complexes for catalytic competency.

4.6 EXPERIMENTAL

4.6.1 General

All manipulations were carried out using standard Schlenk-line and glovebox techniques under an inert atmosphere of argon or dinitogen. A MBraun Labmaster glovebox was employed, operating at <0.1 ppm O_2 and <0.1 ppm H_2O. Solvents were dried over activated alumina from an SPS (solvent purification system) based upon the Grubbs design and degassed before use. Glassware was dried for 12 h at 120 °C prior to use. Benzene-d_6 was stored over molecular sieves and distilled prior to use. NMR-scale reactions were conducted in J. Young's tap tubes and prepared in a glovebox. All heating mentioned was done using silicone oil baths. ^{1}H, ^{13}C, and ^{31}P NMR spectra were obtained on BRUKER 400 MHz or 500 MHz machines unless otherwise stated. ^{1}H NMR peak intensities are derived against an internal standard peak (^{1}H $\underline{Cp}_2$Fe, δ = 4.00 ppm) with values quoted in ppm. Data was processed using the MestReNova software. Elemental analyses were carried out by Stephen Boyer at London Metropolitan Univeristy.

4.6.2 Preparative-Scale Synthesis

[^{Dipp}*BDI*Mg(μ-$^{n/s}$Bu)]$_2$ was synthesised according to literature precedent.[50]

[^{Dipp}BDIMg(μ-CH$_2$SiMe$_3$)]$_2$

In a glovebox, the ligand ^{Dipp}*BDI*H (2 g, 4.78 mmol, 1 equiv.) and [KN(SiMe$_3$)$_2$] (0.95g, 4.78 mmol, 1 equiv.) were weighed out and transferred to a Schlenk flask. Dry toluene (10 mL) was added and the flask sealed and removed from the glovebox. The reaction mixture was stirred overnight and the solvent removed *in vacuo*. The crude product was dissolved in Et_2O (20 mL), and 5.3 mL of [Me_3SiCH_2MgCl] (1M in Et_2O, 5.25 mmol, 1.1 equiv.) was added at 0 °C *via* syringe. An instant precipitation occurred. The reaction mixture was stirred overnight and the solvent was removed under reduced pressure. The crude solid was extracted into hexane (30 mL) and concentrated to induce crystallisation, which occurred at 25 °C and was furthered by storage at -20 °C. The solid obtained, colourless and crystalline, was found to be the etherate of the title compound[51] by ^{1}H NMR. A portion of the 0.89 g yield was heated at 90 °C under dynamic vacuum for 1 h, giving [^{Dipp}*BDI*Mg(μ-CH_2SiMe_3)]$_2$ as a colourless powder. ^{1}H NMR (400 MHz, benzene-d_6, 298 K) δ –1.43 (s, MgCH_2), –0.16 (s, 9H, Si(CH_3)$_3$), 1.13, (d, 12H, $^3J_{H-H}$ = 6.9, CHMe_2), 1.29 (d, 12H, $^3J_{H-H}$ = 6.9, CHMe_2), 1.65 (s, 6H, (NCMe)$_2$), 3.13 (hept., 4H, $^3J_{H-H}$ = 6.9, CHMe$_2$), 4.93 (s, 1H, (NC)$_2$CH), 7.12–7.10 (m, 6H, H_{Aryl}). Due to the sensitivity of the complex, repeated attempts to acquire satisfactory CHN analysis have failed.

*[^{Dipp}BDI*Mg(μ-(CH$_2$)$_3$Ph)]$_2$*

In a glovebox, the ligand ^{Dipp}*BDI*H (2.0 g, 4.78 mmol, 1 equiv.) and [KN(SiMe$_3$)$_2$] (0.95 g, 4.78 mmol, 1 equiv.) were weighed out and transferred to a Schlenk flask. Dry toluene (10 mL) was added and the flask sealed and removed from the glovebox. The reaction mixture was stirred overnight and the solvent removed under vacuum. The crude product was dissolved in Et_2O (20 mL) and an Et_2O solution of [Ph(CH$_2$)$_3$MgBr], freshly prepared from the addition of Ph(CH$_2$)$_3$Br (0.73 mL, 4.78 mmol, 1 equiv.) to magnesium (0.138 g, 5.7 mmol, 1.2 equiv.),[52] was added via filter cannula. The reaction mixture was stirred overnight, the solvent removed and the crude extracted into *n*-hexane (30 mL) and then filtered to remove KBr. The clear light yellow solution was then concentrated to approx. 5 mL to give colourless crystals at 25 °C. The product was isolated and purified by two further recrystallisations from *n*-hexane (3 mL) at -35 °C to give [^{Dipp}*BDI*Mg(μ-(CH$_2$)$_3$Ph)] as colourless crystals in un-optimised yield (0.107 g, 0.19 mmol, 4 %). ^{1}H NMR (400 MHz, benzene-d$_6$, 298 K) δ -0.16 (dd, 2H, $^3J_{H\text{-}H}$ = 8.0 Hz, 7.9 Hz, C*H*$_2$), 1.17 (d, $^3J_{H\text{-}H}$ = 6.9 Hz, 6H, CH*Me*$_2$), 1.29 (d, $^3J_{H\text{-}H}$ = 6.9 Hz, 6H, CH*Me*$_2$), 1.68 (m, 2H, C*H*$_2$), 1.71 (s, 6H, (NC*Me*)$_2$), 2.33 (dd, 2H, $^3J_{H\text{-}H}$ = 8.0, 7.9 Hz, C*H*$_2$), 3.14 (hept, 4H, $^3J_{H\text{-}H}$ = 6.9 Hz, CMe*H*Me'), 4.97 (s, 1H, (NC)$_2$*CH*), 7.03–7.22 (m, H$_{Aryl}$) ppm. ^{13}C NMR (100 MHz, benzene-d$_6$, 298 K) δ 6.1 (*C*H$_2$), 23.5 ((NC*Me*)$_2$), 23.6 (C*Me*HMe'), 24.7 (CMeH*Me'*), 28.6 (CMeHMe'), 31.3 (*C*H$_2$), 44.8 (*C*H$_2$), 95.3 ((NC)$_2$CH), 124.1 (Ar), 125.1 (Ar), 125.9 (Ar), 128.0 (Ar), 128.8 (Ar), 141.9 (q), 144.0 (q), 144.5 (q), 169.2 (*C*=N) ppm. Elemental Analysis: calculated for C$_{38}$H$_{52}$MgN$_2$: C, 81.34; H, 9.34; N, 4.99. Found C, 81.24; H, 9.46; N, 4.99.

*[^{Dipp}BDI*Mg(μ-O(CH$_2$)$_3$Ph)]$_2$*

During a recrystallisation of crude [^{Dipp}*BDI*Mg(μ-(CH$_2$)$_3$Ph)]$_2$ in the above procedure, the alkoxide title compound was unintentionally produced. Upon filtered transfer of a near-saturated solution of crude [^{Dipp}*BDI*Mg(μ-(CH$_2$)$_3$Ph)]$_2$ in *n*-hexane to a new Schlenk flask, a colourless precipitate began to come out of solution on a large scale. Cooling at 0 then –20 °C encouraged further precipitation. The supernatant solution was partly removed by filtration, and a single crystal diffraction experiment corroborated NMR characterisation of [^{Dipp}*BDI*MgO(μ-(CH$_2$)$_3$Ph)]$_2$. The colourless crystalline solid was dried *in vacuo* and isolated as a 0.89 g yield – 20% based on a synthesis from 3.2 g of ^{Dipp}*BDI*H. ^{1}H NMR (400 MHz, benzene-d$_6$, 298 K) δ0.31 (dd, 3H, $^3J_{H\text{-}H}$ = 6.9 Hz, CH*Me*$_2$) 1.06 (d, $^3J_{H\text{-}H}$ = 6.9 Hz, 3H, CH*Me*$_2$), 1.18 (d, $^3J_{H\text{-}H}$ = 6.9 Hz, 3H, CH*Me*$_2$), 1.35 (d, $^3J_{H\text{-}H}$ = 6.9 Hz, 3H, CH*Me*$_2$), 1.41 (s, 6H, (NC*Me*)$_2$), 1.90–1.99 (m, 2H, *CH*$_2$), 2.55 (t, 2H, $^3J_{H\text{-}H}$ = 7.5 Hz, C*H*$_2$), 2.97 (hept, 4H, $^3J_{H\text{-}H}$ = 6.9 Hz, C*H*Me$_2$), 3.38 (hept, 4H, $^3J_{H\text{-}H}$ = 6.9 Hz, CM*H*Me$_2$), 3.60–3.65 (m, 2H, C*H*$_2$), 4.68 (s, 1H, (NC)$_2$*CH*), 7.02–7.22 (m, H$_{Aryl}$) ppm. ^{13}C NMR (100 MHz, benzene-d$_6$, 298 K) δ23.5 (CH*Me*$_2$), 23.6 (CH*Me*$_2$), 24.1 (CH*Me*$_2$), 24.7 ((NC*Me*)$_2$), 25.4 (CH*Me*$_2$), 27.9 (*C*HMe$_2$), 29.2 (*C*HMe$_2$),

32.8 (CH_2), 37.4 (CH_2), 64.1 (CH_2), 95.3 ($(NC)_2CH$), 123.5 (Ar), 124.1 (Ar), 125.5 (Ar), 128.3 (Ar), 128.5 (Ar), 141.8 (q), 142.5 (q), 143.7 (q), 147.3 (q), 169.1 (C=N) ppm. Elemental Analysis: calculated for $C_{38}H_{52}MgN_2O$: C, 79.08; H, 9.08; N, 4.85; found: C, 79.04; H, 9.15; N, 4.96.

The product is presumably a result of the unwanted presence of O_2 in the system at some point during the work-up of the alkyl complex. This hypothesis is supported by studies on O_2 insertion into Mg–R, particularly by Parkin *et al.*[53] and very recently by Lewiński and co-workers.[53] The latter work has examined the mechanism of an almost identical transformation of [^{Dipp}*BDI*MgCH$_2$Ph]$_2$ into [^{Dipp}*BDI*Mg(μ-OCH$_2$Ph)]$_2$ in the presence of dry air.

4.6.3 NMR-Scale Reactions

4.6.3.1 Catalyic Experiments (for Table 4.1)

In a glovebox, 0.005 mmol of bimetallic catalyst was weighed into a 2mL scintillation vial. The solid was dissolved in 0.5 mL benzene-d_6. Roughly 2-3 mg of ferrocene was added to the vial (as internal standard for quantification). The reaction mixture was transferred to an NMR tube and alkene (0.102 mmol, 20 equiv.) added directly by calibrated pipette. The reactions were heated to 50 °C in an oil bath. The major products were confirmed by spiking product mixtures with genuine sample. In the cases where this was not possible, assignment of stereochemistry was made based on comparison to previously reported chemical shifts and/or olefinic $^3J_{H-H}$ values.

The yields were calculated from ^{1}H NMR spectroscopy *in situ*. For each substrate, the salient shifts and coupling constants are listed below this paragraph. Before the tube was heated to 50 °C, the alkene substrate was integrated over the most isolated signal in the ^{1}H NMR spectrum. This starting material resonance was also chosen on the basis that a peak in a similar region would be integrated for the major product yield; (in some cases) alkene region peaks did not give integration values consistent with alkyl region peaks. Whilst taking this effective "t = 0" time-point, it was noticed that some reactions were willing to operate at room temperature. These reactions are marked in Table 4.1.

Organic compound (= not confirmed with genuine sample):*
δ peak integrated for yield [ppm, benzene-d_6], reference of literature report used for confirmation (by δ in benzene-d_6, or $^3J_{trans/cis}$ in the case of a different solvent).

Allylbenzene: δ 3.17 (d, 2H, $^3J_{H-H}$ = 6.7 Hz, CH_2)
(*E*)-1-Phenylprop-1-ene: δ 1.64 (dd, 3H, J_{H-H} = 6.6, 1.7 Hz, CH_3)[54]

(*Z*)-1-Phenylprop-1-ene*: δ 1.70 (dd, 3H, $J_{H\text{-}H}$ = 7.2, 1.9 Hz, CH_3)[55]

1-Phenylpropane*: δ 0.83 (t, 3H, $^3J_{H\text{-}H}$ = 7.4 Hz, CH_3), or otherwise: δ 2.43 (t, 3H, $^3J_{H\text{-}H}$ = 7.4 Hz, CH_2)[56]

4-Allylanisole: δ 3.18 (d, 2H, $^3J_{H\text{-}H}$ = 6.6 Hz, CH_2)

Trans-anethole: δ 1.70 (d, 3H, $J_{H\text{-}H}$ = 6.7, 1.7 Hz, CH_3), 6.32 (dq, 1H $J_{H\text{-}H}$ = 15.8, 1.7 Hz)

Cis-anethole*: δ 1.77 (d, 3H, $J_{H\text{-}H}$ = 7.2, 1.9 Hz, CH_3)[57]

4-Propylanisole*: δ 0.86 (t, 3H, $^3J_{H\text{-}H}$ = 7.3 Hz, CH_3)[58]

1-Allyl-4-(trifluoromethyl)benzene: δ 2.98 (d, 2H, $^3J_{H\text{-}H}$ = 6.7 Hz, CH_2)

(*E*)-1-(Prop-1-enyl)-4-(trifluoromethyl)benzene*: δ 1.57 (dd, 3H, $^3J_{H\text{-}H}$ = 6.6, 1.5 Hz, CH_3), 6.07 ($^3J_{trans}$ = 15.9 Hz, $^4J_{H\text{–}H}$ = 1.8 Hz, Ar–C*H*=)

(*E*)-1-(Prop-1-enyl)-4-(trifluoromethyl)benzene*: δ 1.54 (m, 3H, 1.9 Hz, CH_3), resonance not clear for $^3J_{cis}$.

1-Propyl-4-(trifluoromethyl)benzene*: δ 0.73 (t, 3H, $^3J_{H\text{-}H}$ = 7.3 Hz, CH_3).

Ratios tentative because of peak overlaps. In an ^{19}F NMR of the 1-Allyl-4-(trifluoromethyl)benzene experiment, the signal for [^{Dipp}*BDI*Mg(μ-F)]$_2$ is collected, suggesting activation of a C–F bond by a metal complex.

Allyltrimethylsilane: δ -0.03 (s, 9H, $Si(CH_3)_3$)

(*E*)-trimethyl(prop-1-en-1-yl)silane*: δ 0.09 (s, 9H, $Si(CH_3)_3$),[59]

5.68 (dq, 1H, $^3J_{trans}$ = 18.4 Hz, $^4J_{H\text{–}H}$ = 1.7 Hz, C*H*CHMe),[59] 1.66 (dd, 3H, $^4J_{H\text{–}H}$ = 1.7 Hz, CHC*H*$_3$)

(*Z*)-trimethyl(prop-1-en-1-yl)silane*: δ 0.15 (s, 9H, $Si(CH_3)_3$),[59]

5.59 (dq, 1H, $^3J_{cis}$ = 14.0 Hz, $^4J_{H\text{–}H}$ = 1.5 Hz, C*H*CHMe), 1.66 (dd, 3H, $^4J_{H\text{–}H}$ = 1.5 Hz, CHC*H*$_3$)

Trimethylpropylsilane*: δ -0.01 (s, 9H, $Si(CH_3)_3$), 0.86 (t, 3H, $^3J_{H\text{-}H}$ = 6.0 Hz, CH_2CH_3)

(*E*)-hex-1-ene: δ 1.95 (q, 2H, $^3J_{H\text{-}H}$ = 6.9 Hz, CH_2)

(*E*)-hex-2-ene: δ 1.59 (d, 3H, $^3J_{H\text{-}H}$ = 4.0 Hz, CH_3)

(*Z*)-hex-2-ene: δ 1.53 (d, 3H, $^3J_{H\text{-}H}$ = 5.7 Hz, CH_3)

(*E*)-hex-3-ene: δ 0.94 (t, 6H, $^3J_{H\text{-}H}$ = 7.4 Hz, 2{CH_3})

Yield estimated from: total integration of the upfield CH_3 triplets for *all* products minus the integration of the downfield vinylic methyl peaks of the alkene products, leaving a value for $\int(\text{-}CH_3)_2$ in hexane and (*E*)-hex-3-ene, which was halved and recombined with the integration of the vinylic methyls.

4,4-Dimethyl-pent-1-ene: δ 0.85 (s, 9H, $C_q(CH_3)_3$)

(*E*)-4,4-Dimethyl-pent-2-ene*: δ 1.60 (dd, 3H, $^4J_{H\text{–}H}$ = 6.3, 1.5 Hz, CHC*H*$_3$),

5.47 (m, 1H, $^3J_{trans}$ = 15.2 Hz) 5.32 (m, 1H, $^4J_{H\text{–}H}$ = 6.3, C*H*CH$_3$)

(*Z*)-4,4-Dimethyl-pent-2-ene*: *no peaks clearly assignable*

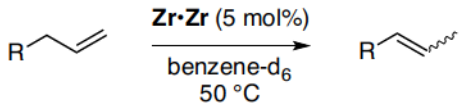
4,4-Dimethylpentane*: δ 0.85–0.88 (m, 3H, CH_3)

Low Catalyst Loading Experiments (for Table 4.3)

Experiments were carried out according to the general NMR scale reaction procedure, however, whilst the millimoles of catalyst was kept the same as in the 5 mol% loading experiments, greater quantities of terminal alkene were used in 0.6 mL of benzene-d_6: 0.495 mmol for 1 mol% reactions, 0.984 mmol for the 0.5 mol% reactions.

Results of Catalysis with 5 mol% Zr•Zr

Table 4.4. Results for terminal alkene isomerisation experiments using 5 mol% of **Zr•Zr**, not included in the Results section.



substrate	*time (h)*	*combined yield (%)*	*E:Z*	*alkene :alkane*
R = Ar^{OMe}	4[a]	90	26:1	9:1
R = Ar^{CF_3}	24	70	20:1	12:1
R = $SiMe_3$	15	65	33:2	35:1

[b]Reaction run at 25 °C.

Competition Experiment (Graph 4.2)

The general catalytic procedure was followed, with 20 equiv. of each alkene substrate added to the catalyst solution. An initial room temperature NMR showed that there was slightly more allylbenzene than hex-1-ene in the starting mixture. Assuming perfect addition of the less volatile allylbenzene, a correction was made before starting the reaction. A further 2.7 μL of hex-2-ene was added, and the NMR showed very good parity between the relative concentrations of the two substrates. The yields were measured (as best as possible) using integration over the regions illustrated in Figure 4.8. The quantity of hexane cannot be calculated because of trace hexane in the catalyst sample.

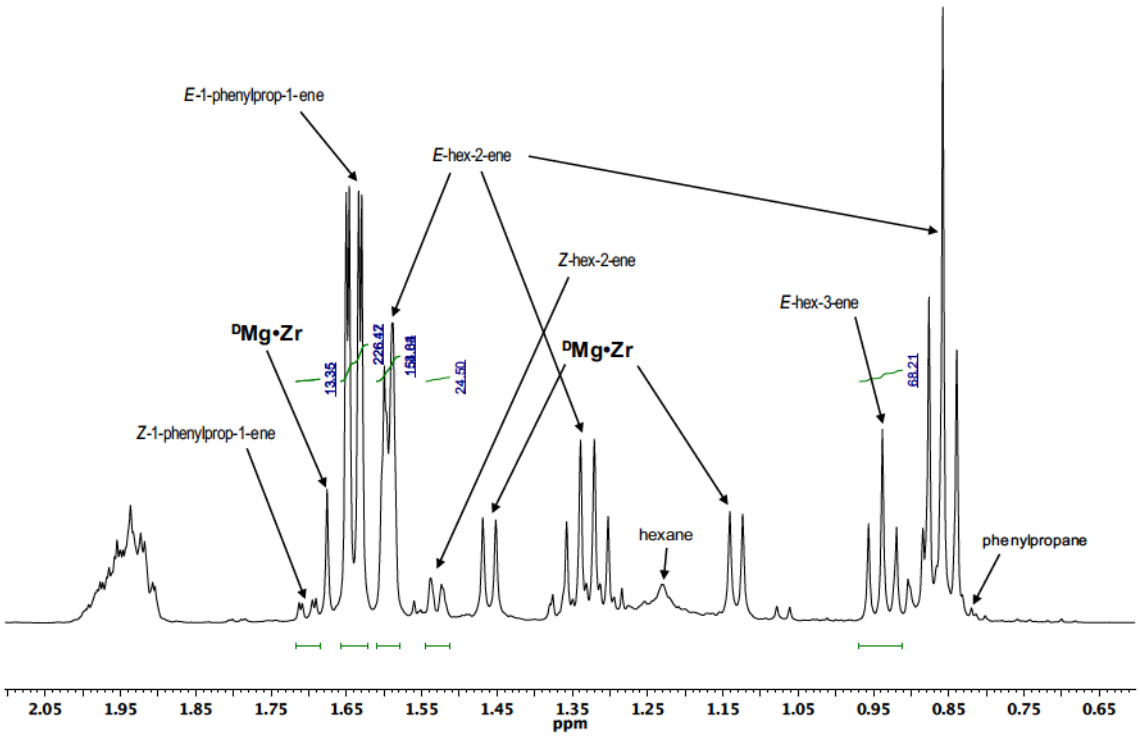
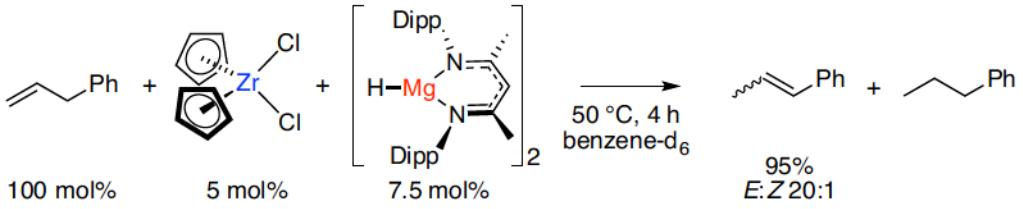


Figure 4.8. The ^{1}H NMR spectrum (benzene-d_6) between 0.60–2.10 ppm after 23 h of the competition experiment at 50 °C.

*Allylbenzene Isomerisation Catalysed by a [Cp_2ZrCl_2] and [^{Dipp}BDI*Mg*(μ-H)]$_2$ mixture*

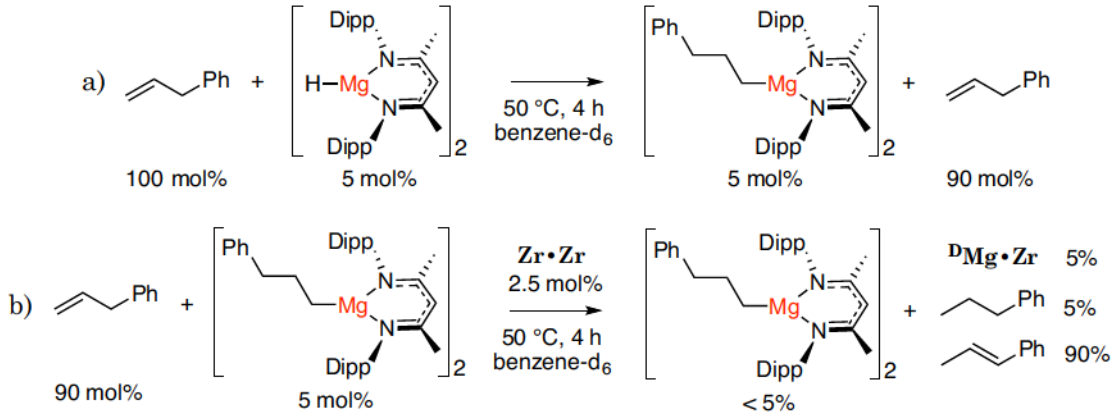
With the aim of forming the catalyst *in situ*, 5 mol% [Cp_2ZrCl_2] and 7.5 mol% [^{Dipp}*BDI*Mg(μ-H)]$_2$ were used – *i.e.* a 1:3 ratio of chloride:hydride in order to allow for complete conversion to ^{D}**Mg•Zr**. A 0.5 mL benzene-d_6 solution of 13.6 mg of ^{D}**2$_2$** (1.5 equiv., 0.031 mmol) was made in a 4 mL scintillation vial. The solution was transferred to an NMR tube. Ferrocene with (2–3 mg) was added by spatula. The yield calculation was calibrated by measurement of a ^{1}H NMR spectrum at this point. Back inside the glovebox, the NMR tube was re-opened and the remaining reactants added: 3 mg [Cp_2ZrCl_2] (1 equiv., 0.010 mmol) and 27.1 mL allylbenzene (20 equiv., 0.021 mmol) were added in quick succession. The former was dropped into the tube by spatula, and the latter was added by mechanical pipette. The tube was sealed and heated at 50 °C.



Scheme 4.9. Allylbenzene isomerisation catalysed by a [Cp_2ZrCl_2] and [^{Dipp}*BDI*Mg(μ-H)]$_2$ mixture

The mixture was effective for the isomerisation of allylbenzene (95% yield of alkenes, 20:1 {*E*:*Z*}) in 4 h at 50 °C. However, this reaction did not display ^{1}H NMR signals for ^{D}**Mg•Zr** at any point during the isomerisation of allylbenzene. The yield for this experiment is 20% greater than with the ^{D}**Mg•Zr** pre-catalyst (Table 4.1), and the stereoselectivity is only half as good.

Allylbenzene Isomerisation Catalysed by a Mg-alkyl and Zr•Zr Mixture



Scheme 4.10. Allylbenzene isomerisation catalysed by a [^{Dipp}*BDI*Mg(μ-H)]$_2$ and **Zr•Zr** mixture.

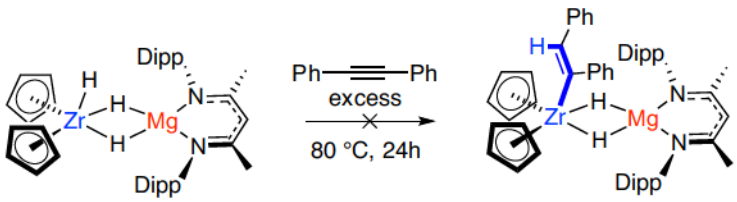
A starting solution of $^{D}\mathbf{2_2}$ (5.4 mg, 0.006 mmol) was made of 0.5 mL benzene-d_6 in a 4 mL scintillation vial. Allylbenzene (16.1 μL, 0.122 mmol) was added to this solution of $^{D}\mathbf{2_2}$. The latter does not independently catalyse the isomerisation of allylbenzene (Scheme 4.10a). After 4 h at 50 °C, all $^{D}\mathbf{2_2}$ was consumed; 1 equiv. of alkene had been quantitatively inserted into the main group hydride bond. This was confirmed by comparison of the NMR to a genuine sample of [^{Dipp}BDIMg{μ-$(CH_2)_3$Ph}]$_2$ (section 4.6.1).

To the opened J Young's tube containing the product mixture from Scheme 4.10a, 0.5 equiv. **Zr•Zr** (2.3 mg, 0.006 mmol) was then added *via* spatula. The tube was resealed, and the progress of the reaction (at 50 °C) monitored by ^{1}H NMR. Yields (Scheme 4.10b) are measured from the starting solution of $^{D}\mathbf{2_2}$ and allylbenzene (based on the vinylic CH_2 resonance of the latter at 3.18 ppm). The (*Z*)-isomer yield was indeterminable due to peak overlap; relative peak hights allowed estimation of the *E*:*Z* ratio as 20:1.

4.6.3.2 Mechanistic Controls

Reactions of ^{D}Mg•Zr with alkenes and alkynes

^{D}**Mg•Zr** (10 mg, 0.015 mmol) was dissolved in benzene-d_6 (0.5 mL). After taking a ^{1}H NMR spectrum, 0.184 mmol (6.5 equiv.) of the hydrocarbon substrate (methylenecyclohexane, diphenylacetylene, 4,4-dimethylpent-2-yne) was added by calibrated pipette. A ^{1}H NMR spectrum was measured as quickly as possible after mixing of the reactants. The reaction mixtures were heated at 50 °C and then 80 °C for over 4 h. No reaction was seen.



Scheme 4.11. Failed reaction between diphenylacetylene and ^{D}**Mg•Zr**.

In the case of the methylenecyclohexane substrate, the reaction was repeated in 0.5 mL toluene-d_8 and variable temperature ^{1}H NMR spectra were taken at –30 °C and +50 °C to check for an equilibrium between starting materials and insertion products at these temperatures.[20] No such change nor any other change was observed in the spectrum, aside from the known VT NMR phenomena (Chapter 2).

Reaction of Mg-alkyls with Zr•Zr

The relevant [^{Dipp}*BDI*MgR]$_2$ complex (10 mg, R = {$(CH_2)_2$Ph}, $^{n/s}$Bu, {CH_2SiMe_3}) was dissolved in benzene-d_6 (0.5 mL). Ferrocene (2–3 mg) was also added. After taking a ^{1}H NMR spectrum 1 equiv. of **Zr•Zr** was added; the desired amount, was weighed into a 4 mL scintillation vial

and the reaction mixture poured on to the solid. The mixture was returned to the J Young's NMR tube, sealed, and immediately subjected to heating at 50 °C. Hydrocarbon product yields and ratios seemed to stabilise after roughly 4 h in each case. To aid assignment of products, a vacuum transfer work-up was carried out on the product mixtures of the $[^{Dipp}BDI\text{Mg}\{(CH_2)_2\text{Ph}\}]_2$ and $[^{Dipp}BDI\text{Mg}(^{n/s}\text{Bu})]_2$ experiments. The assignments of reductive elimination products were made based upon previous reports (*vide supra*). The β-hydride elimination product (*E*)-but-2-ene – signals at δ 1.57 and 5.47 ppm – was not observed.[60] In the instance of $[^{Dipp}BDI\text{MgCH}_2\text{SiMe}_3]_2$ the by-products $(Me_3Si)_4C$ and $[Cp_2Zr(CH_2SiMe_3)_2]$ were confirmed against work by Mulvey and Klett *et al.*[61] and Meijboom[19] respectively.

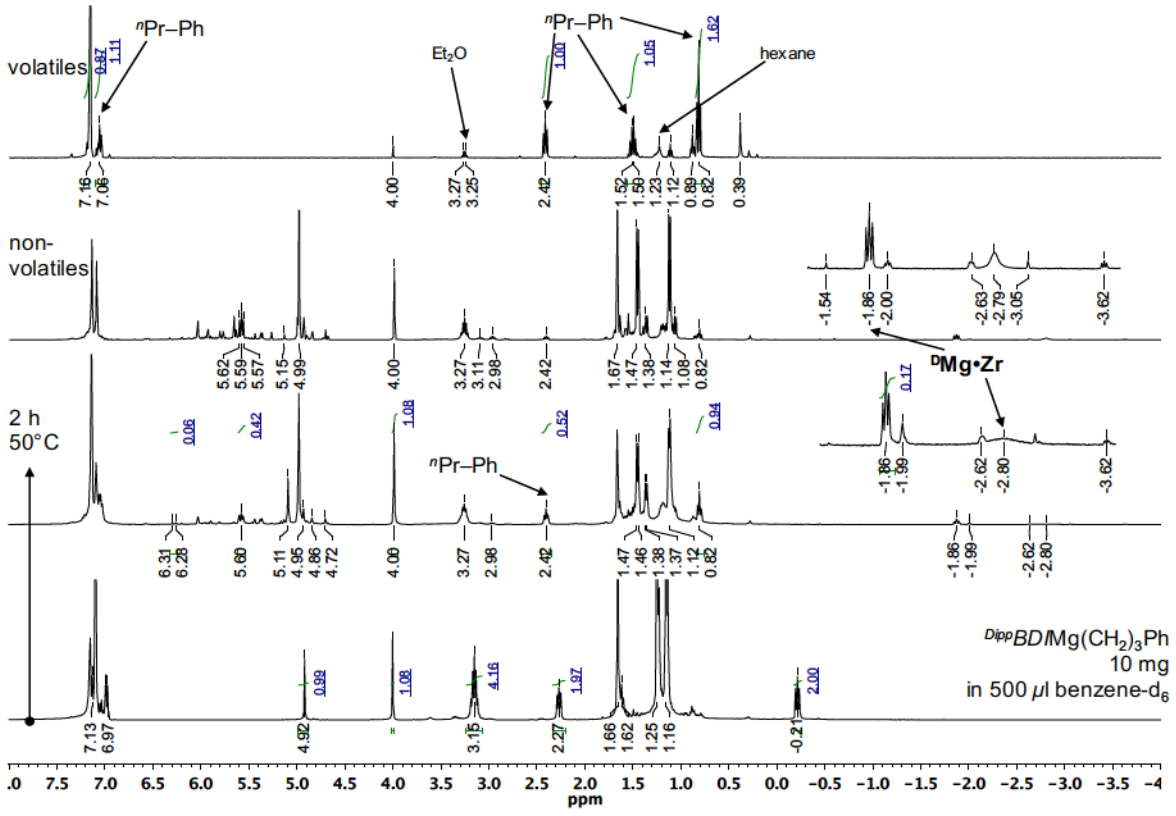


Figure 4.9. Stack plot of ^{1}H NMR data for the reaction of $[^{Dipp}BDI\text{Mg}\{\mu\text{-}(CH_2)_2\text{Ph}\}]_2$ with **Zr•Zr**, also showing (top) the separation the product mixture by vacuum transfer (benzene-d_6).

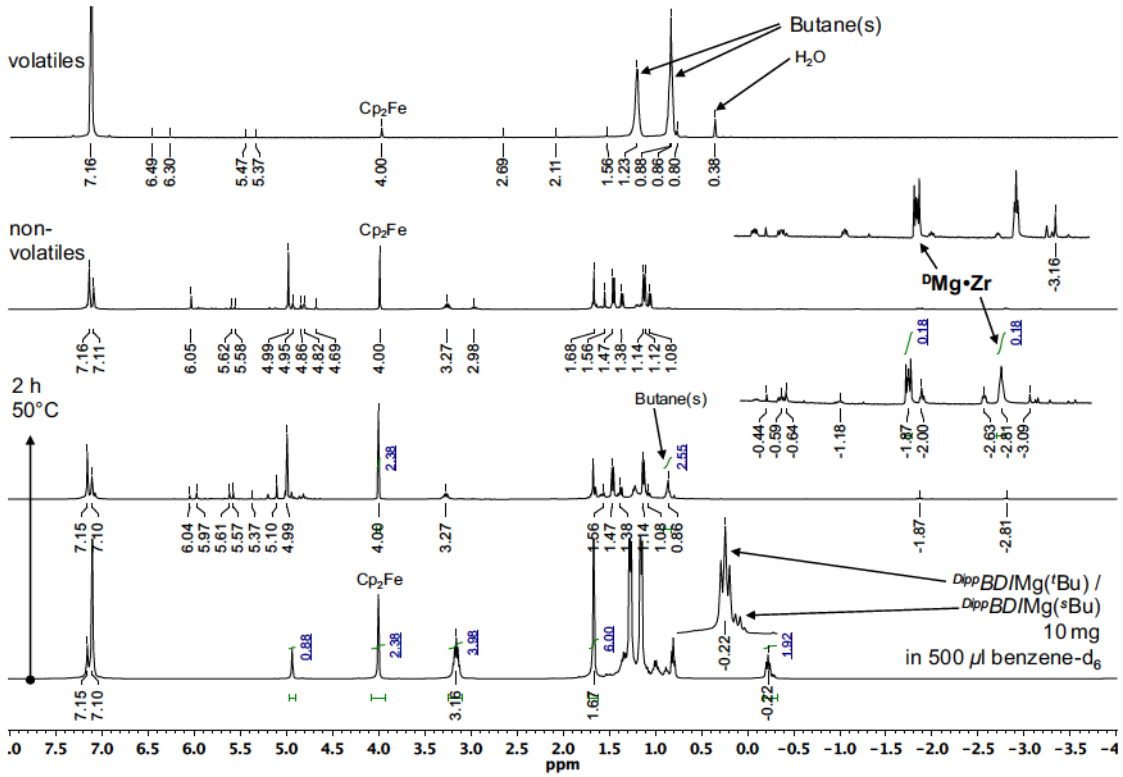


Figure 4.10. Stack plot of ^{1}H NMR data for the reaction of [^{Dipp}*BDI*Mg(μ-$^{n/s}$Bu)$_2$] with **Zr•Zr**, also showing (top) the separation the product mixture by vacuum transfer (benzene-d$_6$).

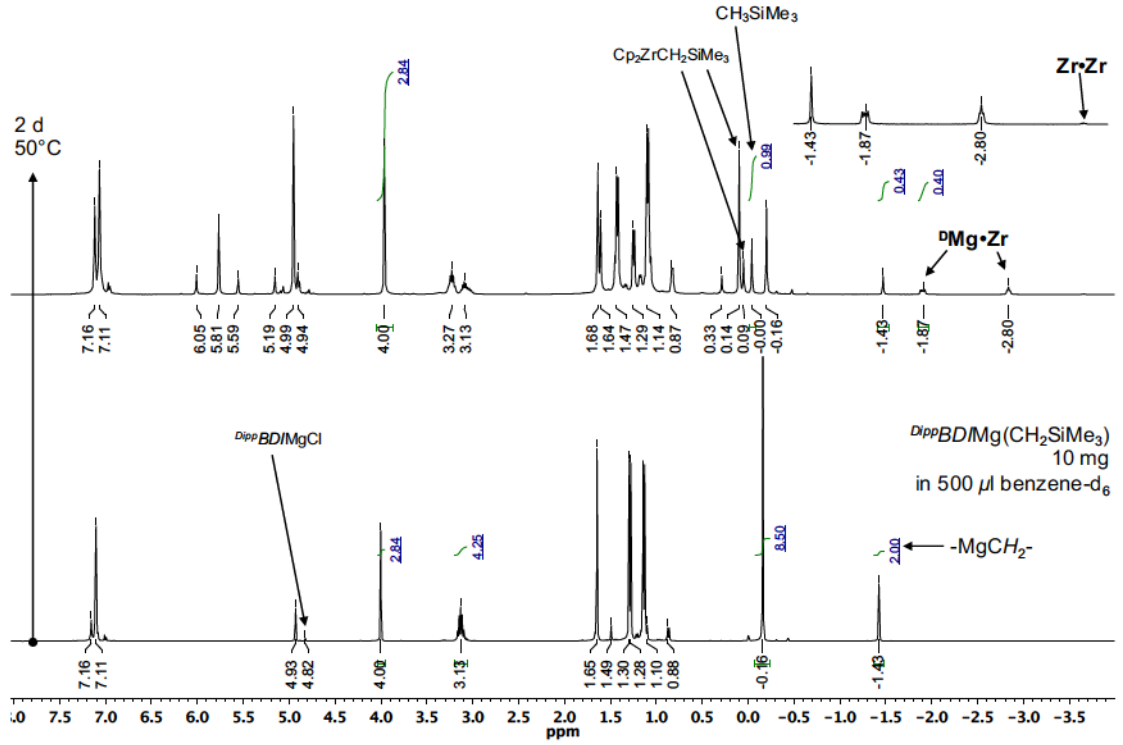
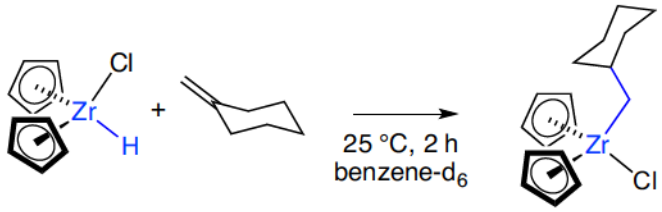


Figure 4.11. Stack plot of ^{1}H NMR data for the reaction of [^{Dipp}*BDI*Mg(μ-CH$_2$SiMe$_3$)]$_2$ with **Zr•Zr**.

In situ *generation of [Cp₂Zr(η¹-CH₂Cy)Cl]*

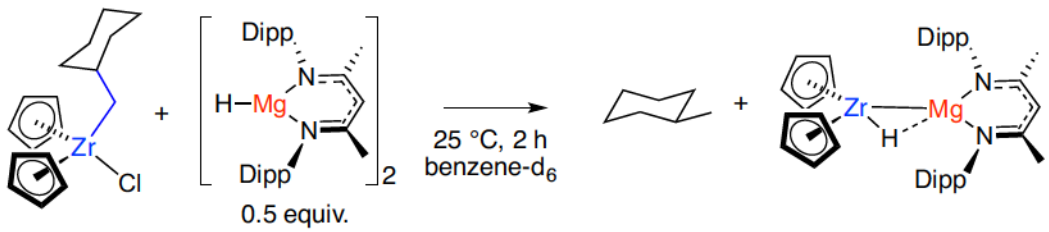
In a glovebox, Schwartz' reagent (31 mg, 0.113 mmol, 1 equiv.) was slurried in 0.5 mL benzene-d_6. The slurry was removed from the 4 mL scintillation vial and given to a J Young's NMR tube *via* pipette. Methylenecyclohexane (14 μL, 0.113 mmol., 1 equiv.) was added to the NMR tube by calibrated pipette, and the reaction mixture was left at room temperature. The ^{1}H NMR resonances of [$Cp_2Zr(\eta^1$-$CH_2Cy)Cl$] were identifiable in a spectrum taken after 90 mins,[20] and the appearance of the spectrum did not change over a week at room temperature. Methylenecyclohexane (bought, dried and freeze-pump-thawed) contained *ca.* 5% 1-methylcyclohexane (Figure 4.12 and Figure 4.13).



Scheme 4.12. Synthesis of [$Cp_2Zr(\eta^1$-$CH_2Cy)Cl$] from Schwartz' reagent.

Reaction of [Cp₂Zr(η¹-CH₂Cy)Cl] with ^{D}**2₂**

The NMR tube containing freshly prepared [$Cp_2Zr(\eta^1$-$CH_2Cy)Cl$] (Scheme 4.12) was returned to the glovebox and emptied into a 20 mL scintillation vial and a further 0.5 mL benzene-d_6 was added to the reaction solution, which was clear and a pale yellow colour. A 0.5 mL aliquot of the reaction mixture was then removed and added to a scintillation vial containing 50 mg (0.114 mmol, 1 equiv.) of ^{D}**2₂** and 0.5 mL of benzene-d_6. Not all ^{D}**2₂** could be dissolved. This reaction mixture was then halved; 0.5 mL was added to a J Young's NMR tube *via* calibrated pipette.



Scheme 4.13. Reaction of [$Cp_2Zr(\eta^1$-$CH_2Cy)Cl$] with ^{D}**2₂**.

The reaction of Zr reagent with Mg hydride was followed by ^{1}H NMR at room temperature (top two spectra in Figure 4.12 and Figure 4.13). Both the mixture in the NMR tube and the remaining mixture in the scintillation vial developed a brown-black hue accompanied by white/brown sediment. The original solution of [$Cp_2Zr(\eta^1$-CH_2{cyclohexyl}$)Cl$] remained a pale yellow solution. After 1 month, this latter solution had fostered crystal growth, for which a single

crystal X-ray diffraction experiment was run. Unfortunately, the structure resolved was that of [{Cp_2ZrCl}$_2$O] (see Figure 4.18) owing to decomposition.

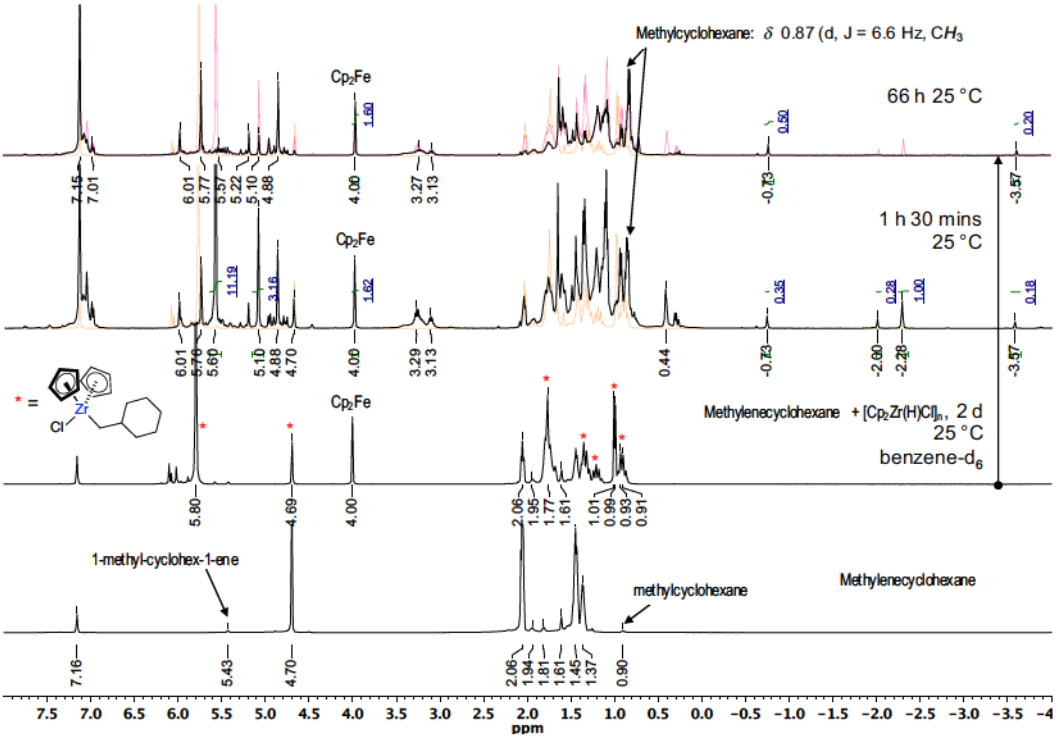


Figure 4.12. Stack plot of selected ^{1}H NMR data for the reaction of [$Cp_2Zr(\eta^1$-CH_2{cyclohexyl}$)Cl$] with $^{D}\mathbf{2_2}$ at room temperature. Preceding spectra remain superimposed as coloured traces underneath.

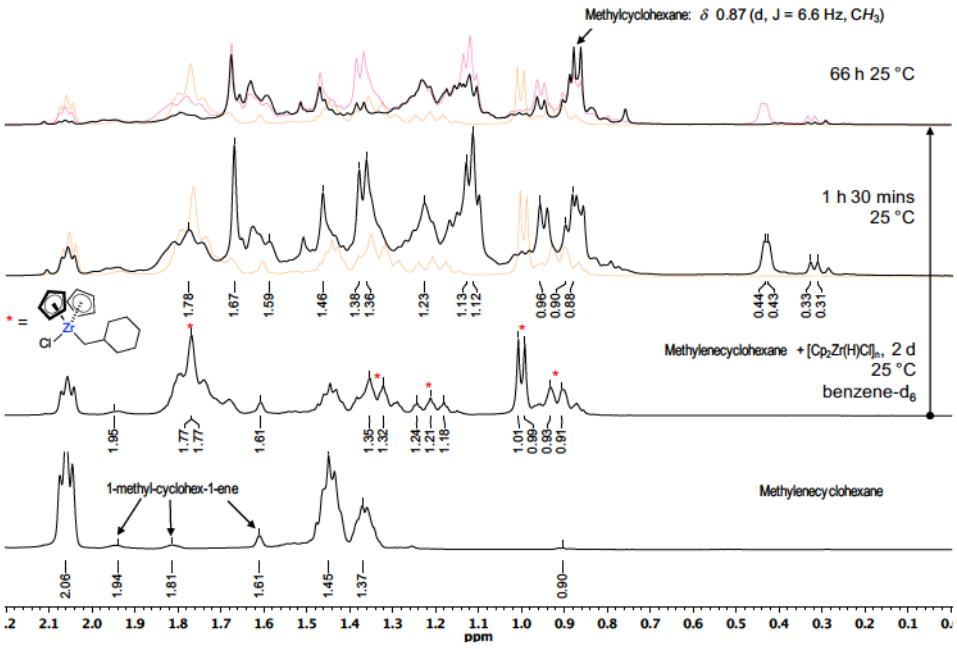


Figure 4.13. Expanded alkyl region stack plot of selected ^{1}H NMR data for the reaction of [$Cp_2Zr(\eta^1$-CH_2{cyclohexyl}$)Cl$] with $^{D}\mathbf{2_2}$ at room temperature. Preceding spectra remain superimposed as coloured traces underneath.

Reactions of Mg^{I} dimers with $[Cp_2Zr(Cl)H]$

The solid $[\{^{R}BDIMg^{I}\}_2]$ (R = Dipp, 24 mg, 0.012 mmol; R = Mes, 8.3 mg, 0.027 mmol) was weighed into a 4 mL scintillation vial. The solid was dissolved in 0.5 mL of benzene-d_6, and ferrocene (ca. 2–3 mg) was added to the solution directly by spatula. This mixture was transferred into a J Young's NMR tube, and a ^{1}H NMR spectrum collected for the yield calculation purposes. The tube was reopened back inside the glovebox, and Schwartz' reagent (1 equiv.) was added *via* spatula, and resealed for the reaction (see Figure 4.2 in the main text, and Figure 4.14 below).

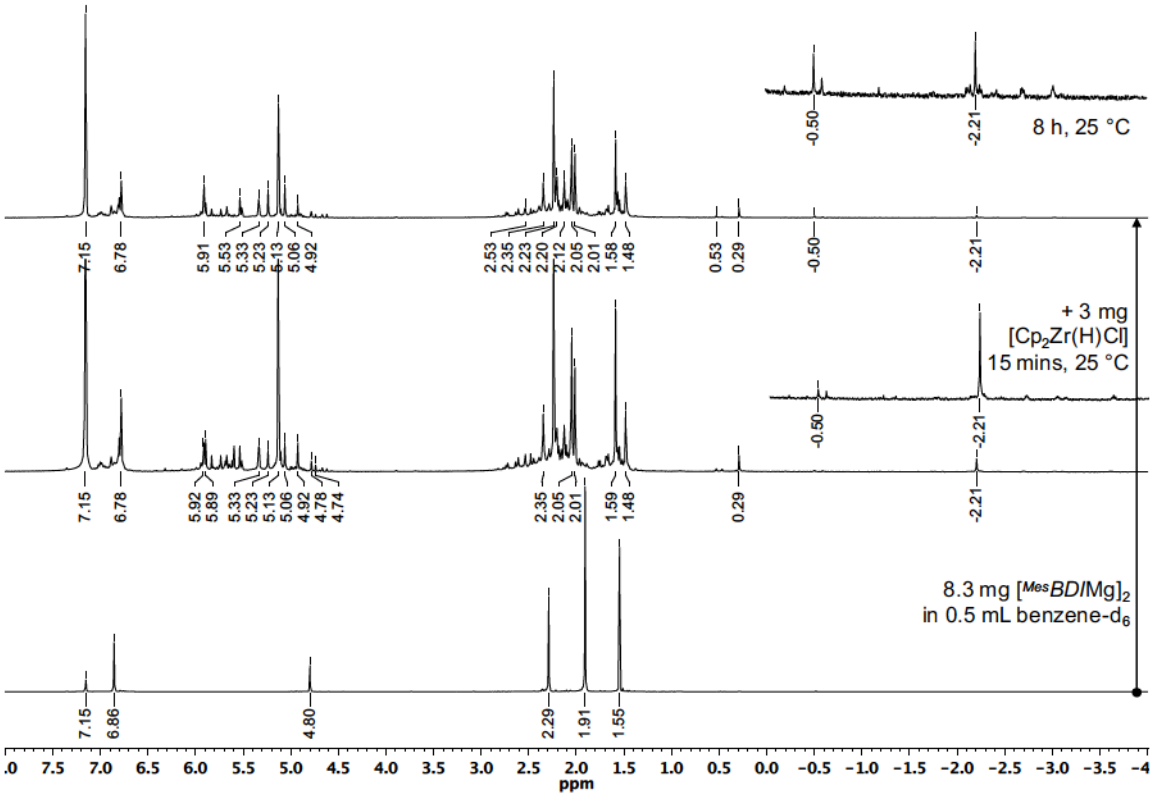


Figure 4.14. Stack plot of selected ^{1}H NMR data for the reaction of $[Cp_2Zr(H)Cl]$ with $[^{Mes}BDIMg]_2$ at room temperature.

Photolysis of ^{D}Mg•Zr

A 0.5 mL benzene-d_6 solution of 23 mg of **^{D}Mg•Zr** (0.035 mmol) was prepared in a 4 mL scintillation vial by addition of the solvent to the solid complex. Ferrocene (ca. 2–3 mg) was added to the solution directly by spatula. This mixture was transferred into a J Young's NMR tube, and a ^{1}H NMR spectrum collected for the yield calculation purposes. After 6 h of photolysis (400 W – Figure 4.15) the tube was reopened back inside the glovebox, and PMe_3 (10 equiv., 36 μL) was added by mechanical pipette.

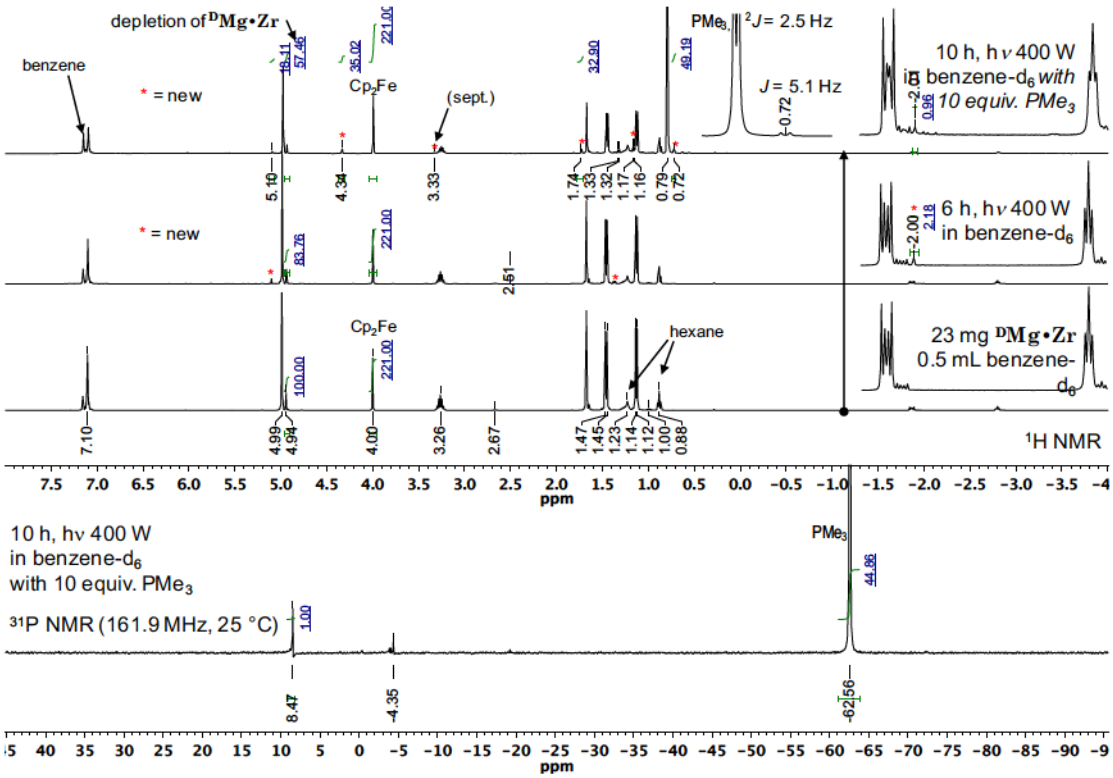


Figure 4.15. Stack plot of selected NMR data for the photolysis of **^{D}Mg•Zr** at room temperature. Trimethylphosphine was added after 6 h of photolysis.

Photolysis of ^{D}Mg•Zr in the Presence of 3,3-dimethyl-but-1-ene and PMe$_3$

Proteobenzene (0.5 mL) was added to 23 mg of **^{D}Mg•Zr** (0.035 mmol) in a 4 mL scintillation vial. This mixture was transferred into a J Young's NMR tube. Subsequently, both TBE (3,3-dimethyl-but-1-ene, 7.5 equiv., 33 μL) and PMe_3 (10 equiv., 36 μL) were added using a mechanical pipette before the NMR tube was sealed and the photolysis (400 W) commenced. Figure 4.16 shows ^{1}H and ^{31}P spectra after the photolysis. The spectra shown were measured when the photolysis was stopped and the volatile species removed *in vacuo* before re-dissolving the reaction mixture in benzene-d_6.

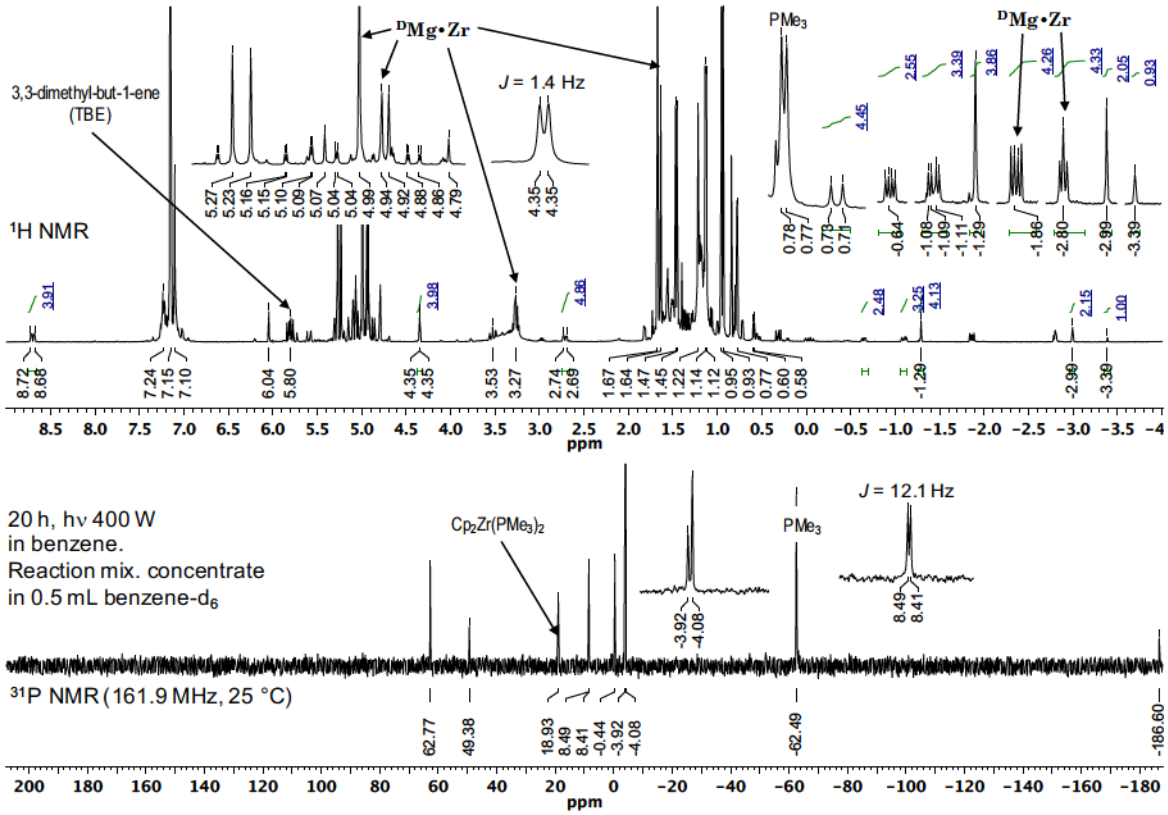


Figure 4.16. NMR spectra for the concentrate of the reaction mixture after photolysis of **^{D}Mg•Zr** at room temperature in the presence of TBE and PMe_3.

4.6.3.3 Kinetics of Alkene Isomerisation Catalysis

Table 4.5. Amounts used in the kinetic analysis of terminal alkene isomerisation catalysis.

^{D}Mg•Zr *mol%*	*stock soln. taken (μL)*	*additional benzene-d_6 (μL)*	*alkene (μL)*
4	36	464	12
6	54	446	12
8	72	428	12
10	86	414	12
6	51	449	14 [a]

[a] alkene = allyltrimethylsilane

A stock solution of 41 mg of **^{D}Mg•Zr** in 0.6 mL benzene-d_6 was made up in a 20 mL scintillation vial. Portions of the catalyst solution (see Table 4.5) were then withdrawn by calibrated pipette and each injected into a separate J Young's NMR tube. A spatula tip of ferrocene (2–3 mg) was dropped into each tube to serve as the ^{1}H NMR internal standard. The solutions were diluted with benzene-d_6. The amounts of benzene-d_6 used are collected in Table 4.5. The tubes were sealed and left in the glovebox until the day of the NMR experiment, on which

occasion neat alkene was added by calibrated pipette. The volume of every reaction mixture was 0.6 μL, and the concentration of alkene was 175 mM. The tubes were frozen at –79 °C, and a dummy alkene solution was used to for the shimming of the ^{1}H NMR spectrum before the catalyst-containing tube was inserted into the machine.

A 500 MHz machine was used for all kinetic experiments to give a clearer peak separation. The ^{1}H NMR experiments were run with 20 scans (–3—9 ppm) per data point, with a data point every 5 minutes. For allylbenzene, partial peak overlap at the high temperature (due to in-probe monitoring), meant that the integral regions employed in the regular catalysis (*vide supra*) could not be used. Use of the alkene proton resonances (below) led to a phenomenon whereby the major product was apparently produced in a >100% yield. Checking against relative integrations of partially measurable CH_2 and CH_3 resonances in the starting material and product showed that the inflated yield was an artefact of using the integrals of the peaks in the alkene region.

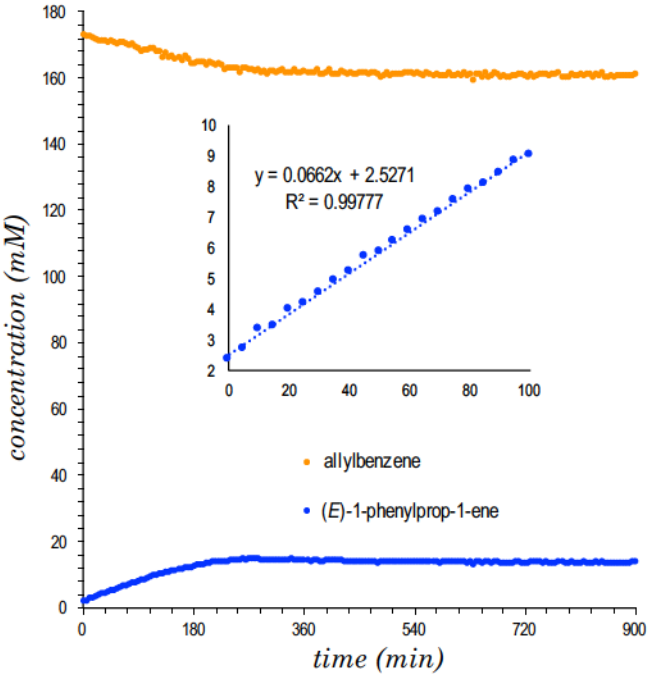
The yields were hence recalibrated manually: the alkene peak integral of the starting material in the first time point was set as 99% of the substrate mass (allowing 1% for the trace amounts of product already visible in the same spectrum). Then, using the original non-kinetics results in Table 4.1 were used to normalise the kinetics data. The full sequence of (*E*)-isomer %yield values (as measured from the alkene signal integral) were manipulated together until the %yield value at the time point relevant to Table 4.1 matched.

Allylbenzene: δ 5.77–5.88 (m, 1H, $PhCH_2$–C*H*=CH_2)
(*E*)-1-Phenylprop-1-ene: δ 5.95–6.04 (dq, 1H, $J_{H\text{-}H}$ = 15.7, 6.6 Hz, C*H*CH_3)[54]
(*Z*)-1-Phenylprop-1-ene: δ 5.56–5.64 (dq, 1H, $J_{H\text{-}H}$ = 11.1, 7.6 Hz, C*H*CH_3)[55]
1-Phenylpropane: δ 0.80–0.84 (t, 3H, $^3J_{H\text{-}H}$ = 7.3 Hz, CH_3)[56]

Allyltrimethylsilane: δ –0.03 (s, 9H, $Si(CH_3)_3$)
(*E*)-trimethyl(prop-1-en-1-yl)silane*: δ 0.09 (s, 9H, $Si(CH_3)_3$),[59]
(*Z*)-trimethyl(prop-1-en-1-yl)silane*: δ 0.15 (s, 9H, $Si(CH_3)_3$),[59]
Trimethylpropylsilane*: δ –0.01 (s, 9H, $Si(CH_3)_3$), 0.97 (t, 3H, $^3J_{H\text{-}H}$ = 7.2 Hz, CH_3)

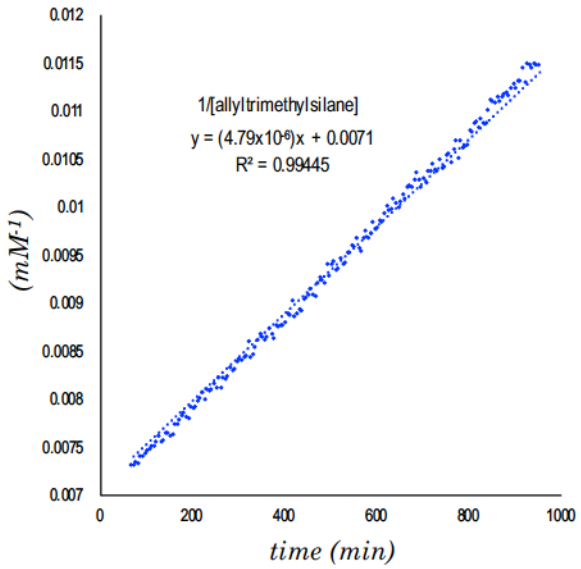
The reaction profile of the 2 mol% loading experiment (Graph 4.5) shows full consumption of the catalyst after around 200 min. Initial slow allylbenzene isomerisation eventually stops after 290 min, with just a 15% yield of the (*E*)-alkene, trace (*Z*)-isomer, and 2% yield of 1-phenylpropane. After this, (*E*)-1-phenylprop-1-ene decays slightly, falling slowly to 14% yield over the next 10 hours. Before catalyst death, the decay of the starting material is apparently

zero-order. The zero-order rate constant for (*E*)-1-phenylprop-1-ene production in the first 100 min is 0.066 ± 0.001 mM min^{-1}.

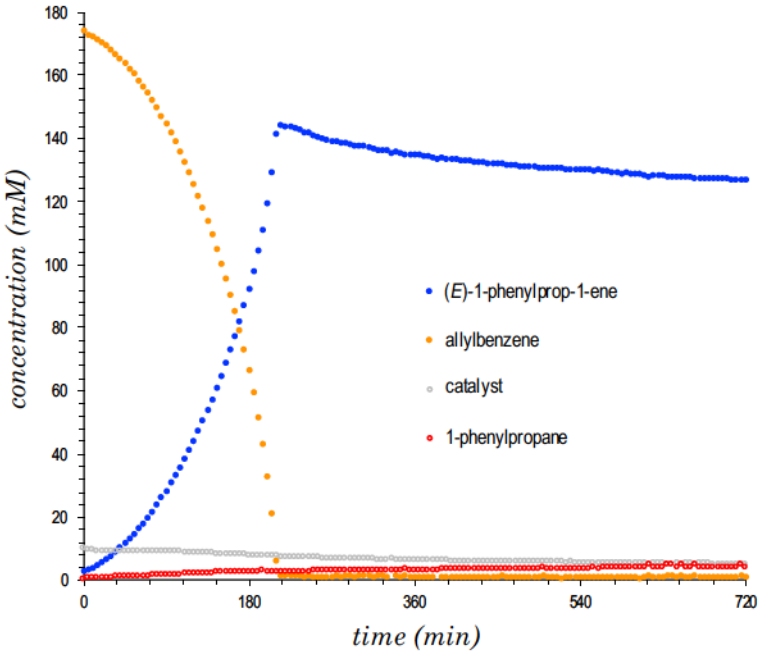


Graph 4.5. Reaction profile of the attempted isomerisation of allylbenzene by 2 mol% ^{D}**Mg•Zr**, and inset, the calculation of the zero-order rate constant for the first 100 min of (*E*)-1-Phenylprop-1-ene production.

After 70 min at 60 °C, decay of allyltrimethylsilane settles on a second-order rate constant of 4.79 ± 0.02 nM^{-1} min^{-1} in its isomerisation by 6 mol% ^{D}**Mg•Zr** (Graph 4.6).



Graph 4.6. Calculation of the second-order rate constant for the main domain of allyltrimethylsilane production, between 70–955 min at 60 °C.



Graph 4.7. Reaction profile of the isomerisation of allylbenzene by 6 mol% ^{D}**Mg•Zr**, after 20 h heating of the pre-catalyst at 50 °C in solution.

4.6.4 X-ray Crystallography

[^{Dipp}BDIMgO(CH$_2$)$_3$Ph]$_2$

$C_{76}H_{104}Mg_2N_4O_2$, M = 1154.25, Orthorhombic, $P2_12_12_1$, a = 13.09627(7), b = 22.75715(11), c = 22.79193(13) Å, $\alpha = \beta = \gamma = 90°$, V = 6792.77(6) Å^3, Z = 4, ρ_{calcd} = 1.129 g cm^{-3}, $\mu(Cu_{K\alpha})$ = 0.673 mm^{-1}, T = 173 K, colourless blocks, Agilent Xcalibur PX Ultra A, 1.54184 Å; 13327 independent measured reflections (R_{int} = 0.0222), F^2 refinement, R_1(obs) = 0.0294, wR_2(all) = 0.0776, 13327 independent observed absorption-corrected reflections [$|F_o| > 4\sigma(|F_o|)$, $2\theta_{max}$ = = 57°], 777 parameters.

The structure does not depart significantly from what would be expected based upon the structure of [^{Dipp}*BDI*MgOCH$_2$Ph]$_2$.[62] Selected bond lengths [Å] and angles [°]: Mg(1)–O(30) 1.9688(13) Å, Mg(1)–O(70) 1.9722(13) Å, Mg(2)–O(30) 1.9681(13) Å, Mg(1)–O(70) 1.9790(13) Å, Mg(1)---Mg(2) 3.0057(7), O(30)–C(31) 1.404(2) Å; O(70)–Mg(1)–O(30) 80.76(5)°, O(70)–Mg(1)–N(1) 116.68(6)°, O(30)–Mg(1)–N(1) 124.82(6)°, O(70)–Mg(1)–N(3) 129.07(6)°, O(30)–Mg(2)–N(43) 121.56(6)°, O(70)–Mg(2)–N(43) 120.82(6)°, O(30)–Mg(2)–N(41) 122.40(6)°, O(70)–Mg(2)–N(41) 123.09(6)°.

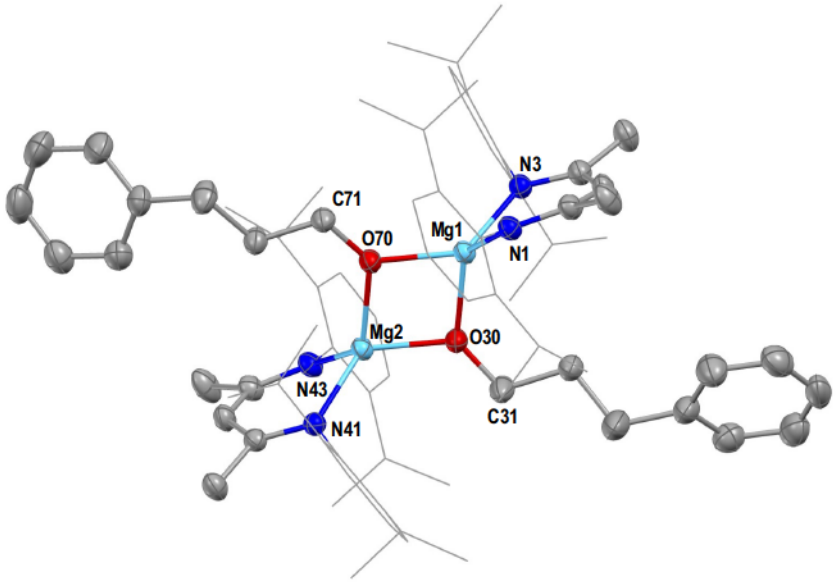


Figure 4.17. Crystal structure of [^{Dipp}*BDI*MgO(CH$_2$)$_3$Ph]$_2$ – 50% probability ellipsoids, H atoms omitted for clarity.

[{Cp$_2$Zr(Cl)}$_2$O]

$C_{38}H_{52}MgN_2O$, M = 607.81, triclinic, P -1 (no. 2), a = 9.7617(5), b = 11.7378(5), c = 12.3893(8) Å, α = 109.692(5)°, β = 106.691(5)°, γ = 100.656(4)°, V = 1216.18(12) Å^3, Z = 2, ρ_{calcd} = 1.660 g cm^{-3}, μ(Mo$_{K\alpha}$) = 1.093 mm^{-1}, T = 173 K, colourless blocks, Agilent Xcalibur 3 E diffractometer; 4778 independent measured reflections (R_{int} = 0.0200), F^2 refinement, R_1(obs) = 0.0318, wR_2(all) = 0.0646, 3977 independent observed absorption-corrected reflections [$|F_o| > 4\sigma(|F_o|)$, $2\theta_{max}$ = 57°], 296 parameters.

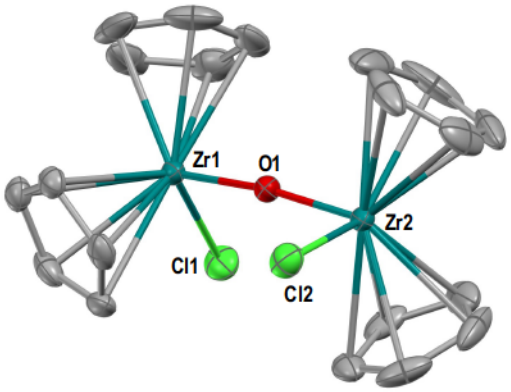


Figure 4.18. Crystal structure of [{Cp$_2$Zr(Cl)}$_2$O] – 50% probability ellipsoids, H atoms omitted fro clarity. Selected bond lengths [Å] and angles [°]: Zr(1)–O(1) 1.957(2) Å, Zr(1)–Cl(1) 2.4736(9) Å; O(1)–Zr(1)–Cl(1) 98.37(6)°, Zr(2)–O(1)–Zr(1) 172.99(11)°.

4.6.5 DFT Studies

Aside from the difference in hydride ligation, the two computed complexes in Figure 4.3 agree with the conclusions and similar comparisons made in Chapter 2. An ate complex character dominates ^{D}**Mg•14**, and Zr and Zn are covalently bonded. The WBI of 0.71 between the two metals nearly matches that for Zr–H (WBI = 0.75). The Zr–Mg covalent bond is much weaker (WBI = 0.26); it is strongly polarised towards Zr, being 87% Zr and 13% Mg according to NBO analysis. The polarisation in Zr–Zn is weaker – the difference in the charges on Zr in ^{D}**Zn•14** and ^{D}**Mg•14** is $\Delta q_{\{Zn-Mg\}}$ = 0.33 – and there is a much larger NBO contribution from the main group atom (38% Zn). There are significant donor-acceptor hydride-bridging interactions for the Mg complex only. The Zr–H bond donates into the Zr–Mg antibonding orbital (38 kcal mol^{-1}) and the Zr–Mg bond donates back into the Zr–H antibonding orbital (21 kcal mol^{-1}).

4.7 REFERENCES

1 C. J. Harlan, S. G. Bott and A. R. Barron, *J. Chem. Soc., Dalton Trans.*, 1997, 637–642.
2 S. M. Baldwin, J. E. Bercaw and H.-H. Brintzinger, *J. Am. Chem. Soc.*, 2008, **130**, 17423–17433.
3 A. R. Siedle, R. A. Newmark, J. N. Schroepfer and P. A. Lyon, *Organometallics*, 1991, **10**, 400–404.
4 P. C. Wailes, A. P. Bell and H. Weigold, *J. Organomet. Chem.*, 1972, **43**, C29–C31.
5 C. Averbuj and M. S. Eisen, *J. Am. Chem. Soc.*, 1999, **121**, 8755–8759.
6 E. Shaviv, M. Botoshansky and M. S. Eisen, *J. Organomet. Chem.*, 2003, **683**, 165–180.
7 C. E. Petrisor, L. M. Frutos, O. Castaño, M. E. G. Mosquera, E. Royo and T. Cuenca, *Dalton Trans.*, 2008, **3**, 2670–2673.
8 G. Chahboun, C. E. Petrisor, E. Gómez-Bengoa, E. Royo and T. Cuenca, *Eur. J. Inorg. Chem.*, 2009, 1514–1520.
9 Y. Raoult, R. Choukroun, M. Basso-Bert and D. Gervais, *J. Mol. Catal.*, 1992, **72**, 47–58.
10 S. A. Rao, S. Achyutha Rao and M. Periasamy, *J. Organomet. Chem.*, 1988, **342**, 15–20.
11 A. Ohff, V. V. Burlakov and U. Rosenthal, *J. Mol. Catal. A: Chem.*, 1996, **105**, 103–110.
12 Lu, Y. Qian, Jiaqui and W. Xu, *J. Mol. Catal.*, 1986, **34**, 31–38.
13 E. Larionov, H. Li and C. X. M. Mazet, *Chem. Commun.*, 2014, **50**, 9816–9826.
14 C. R. Larsen and D. B. Grotjahn, *J. Am. Chem. Soc.*, 2012, **134**, 10357–10360.
15 G. Erdogan and D. B. Grotjahn, *Org. Lett.*, 2014, **16**, 2818–2821.
16 C. R. Larsen and D. B. Grotjahn, *Top. Catal.*, 2010, **53**, 1015–1018.
17 M. J. Spallek, S. Stockinger, R. Goddard and O. Trapp, *Adv. Synth. Catal.*, 2012, **354**, 1466–1480.
18 P. J. Chirik and J. E. Bercaw, *Organometallics*, 2005, **24**, 5407–5423.
19 R. Meijboom, *J. Organomet. Chem.*, 2010, **695**, 2277–2280.
20 J. Schwartz, K. I. Gell, B. Posin and G. M. Williams, *J. Am. Chem. Soc.*, 1982, **104**, 1846–1855.
21 H.-H. Brintzinger, *J. Organomet. Chem.*, 1979, **171**, 337–344.
22 M. Horacek, P. Štěpnička, J. Kubišta, K. Fejfarová, R. Gyepes and K. Mach, *Organometallics*, 2003, **22**, 861–869.
23 V. K. Dioumaev and J. F. Harrod, *Organometallics*, 1997, **16**, 2798–2807.
24 R. Choukroun and D. Gervais, *J. Chem. Soc., Chem. Commun.*, 1985, 224–225.
25 K. McNeill and R. G. Bergman, *J. Am. Chem. Soc.*, 1999, **121**, 8260–8269.
26 T. Takahashi, N. Suzuki, M. Kageyama, Y. Nitto, E. Negishi, M. Saburi and E.-I. Negishi, *Chem. Lett.*, 1991, **20**, 1579–1582.
27 L. A. Paquette, M. R. Sivik, E. I. Bzowej and K. J. Stanton, *Organometallics*, 1995, **14**, 4865–4878.
28 S. Couturier and B. Gautheron, *J. Organomet. Chem.*, 1978, **157**, C61–C63.
29 P. C. Wailes, A. P. Bell and H. Weigold, *J. Organomet. Chem.*, 1972, **43**, C32–C34.
30 R. Waymouth and P. Pino, *J. Am. Chem. Soc.*, 1990, **112**, 4911–4914.
31 D. H. Appella and S. L. Buchwald, *J. Am. Chem. Soc.*, 1999, **121**, 4916–4917.
32 M. F. Sloan, A. S. Matlack and D. S. Breslow, *J. Am. Chem. Soc.*, 1963, **85**, 4014–4018.
33 D. G. Bickley, N. Hao, P. Bougeard, B. G. Sayer, R. C. Burns and M. J. McGlinchey, *J. Organomet. Chem.*, 1983, **246**, 257–268.
34 J. E. Bercaw, J. A. Labinger, M. W. Day and P. J. Chirik, *J. Am. Chem. Soc.*, 1999, **121**, 10308–10317.
35 J. E. Bercaw, D. R. McAlister, D. R. McAlister and D. K. Erwin, *J. Am. Chem. Soc.*, 1978, **100**, 5966–5968.

36 K. I. Gell and J. Schwartz, *J. Am. Chem. Soc.*, 1981, **103**, 2687–2695.
37 K. I. Gell and J. Schwartz, *J. Am. Chem. Soc.*, 1978, **100**, 3246–3248.
38 B. M Kraft and W. D. Jones, *J. Am. Chem. Soc.*, 2002, **124**, 8681–8689.
39 Jaime A Pool, E. B. Lobkovsky and P. J. Chirik, *J. Am. Chem. Soc.*, 2003, **125**, 2241–2251.
40 E. B. Lobkovsky, P. J. Chirik, W. H. Bernskoetter and J. A. Pool, *Organometallics*, 2006, **25**, 1092–1100.
41 E. Y. Pankratyev, T. V. Tyumkina, L. V. Parfenova, S. L. Khursan, L. M. Khalilov and U. M. Dzhemilev, *Organometallics*, 2011, **30**, 6078–6089.
42 R. W. Hoffmann, *Chem. Rev.*, 1989, **89**, 1841–1860.
43 E. Y. Pankratyev, T. V. Tyumkina, L. V. Parfenova, S. L. Khursan, L. M. Khalilov and U. M. Dzhemilev, *Organometallics*, 2011, **30**, 6078–6089.
44 P. Muller, *Pure Appl. Chem.*, 1994, **66**, 1077–1184.
45 D. G. Blackmond, *Angew. Chem.*, 2009, **121**, 392–396.
46 M. Sankaralingam, Y.-M. Lee, W. Nam and S. Fukuzumi, *Inorg. Chem.*, 2017, **56**, 5096–5104.
47 A. M. Baranger and R. G. Bergman, *J. Am. Chem. Soc.*, 1994, **116**, 3822–3835.
48 R. Choukroun, Y. Raoult and D. Gervais, *J. Organomet. Chem.*, 1990, **391**, 189–194.
49 F. M. Hartner, S. M. Clift, J. Schwartz and T. H. Tulip, *Organometallics*, 1987, **6**, 1346–1350.
50 A. P. Dove, V. C. Gibson, P. Hormnirun, E. L. Marshall, J. Segal, A. J. P. White and D. J. Williams, *Dalton Trans.*, 2003, 3088–3097.
51 X. H. Wei, M. P. Coles, P. B. Hitchcock and M. F. Lappert, *Z. Anorg. Allg. Chem.*, 2011, **637**, 1807–1813.
52 M. L. H. Green and M. Wagner, *J. Chem. Soc., Dalton Trans.*, 1996, 2467–2473.
53 T. Pietrzak, T. Pietrzak, M. Kubisiak, I. Justyniak, I. Justyniak, M. Kubisiak, K. Zelga, E. Bojarski, E. Tratkiewicz, Z. Ochal and J. Lewiński, *Chem. Eur. J.*, 2016, **22**, 17776–17783.
54 B. J. Ireland, B. T. Dobigny and D. E. Fogg, *ACS Catal.*, 2015, **5**, 4690–4698.
55 J. Hong, Z. Li, Z. Chen, L. Weng, X. Zhou and L. Zhang, *Dalton Trans.*, 2016, **45**, 6641–6649.
56 Y. Wang, W. Chen, Z. Lu, Z. H. Li and H. Wang, *Angew. Chem., Int. Ed.*, 2013, **52**, 7496–7499.
57 Z.-M. Wang, X.-L. Sang, C.-M. Che and J. Chen, *Tetrahedron Lett.*, 2014, **55**, 1736–1739.
58 C. E. Hartmann, V. Jurčík, O. Songis and C. S. J. Cazin, *Chem. Commun.*, 2013, **49**, 1005–1007.
59 E. A. Austin and C. P. Casey, *J. Am. Chem. Soc.*, 1988, **110**, 7106–7113.
60 E. Abinet, D. Martin, S. Standfuss, H. Kulinna, T. P. Spaniol and J. Okuda, *Chem. Eur. J.*, 2011, **17**, 15014–15026.
61 A. R. Kennedy, J. Klett, R. E. Mulvey, S. Newton and D. S. Wright, *Chem. Commun.*, 2008, 308–310.
62 P. J. Bailey, R. A. Coxall, C. M. Dick, S. Fabre, L. C. Henderson, C. Herber, S. T. Liddle, D. Loroño González, A. Parkin and S. Parsons, *Chem. Eur. J.*, 2003, **9**, 4820–4828.

"When we are not sure, we are alive."

Graham Greene

5 – SUPPORTING INFORMATION

5.1 DFT DATA

Compound ^{D}Mg•Zr
ωB97xD 6-311G / SDD
ZPE= -1874.074421
E= -1874.028861
H= -1874.027916
G= -1874.152121
Lowest Energy vibrations = 14.1, 18.0, 42.9 cm^{-1}

Compound ^{M}Mg•Zr
ωB97xD 6-311G / SDD
ZPE= -1638.446953
E= -1638.408102
H= -1638.407158
G= -1638.517092
Lowest Energy vibrations = 25.6, 25.9, 47.0 cm^{-1}

Compound ^{D}Zn•Zr
ωB97xD 6-311G / SDD
ZPE= -1901.127286
E= -1901.081785
H= -1901.080840
G= -1901.203849
Lowest Energy vibrations = 18.4, 20.1, 46.0 cm^{-1}

Compound ^{M}Zn•Zr
ωB97xD 6-311G / SDD
ZPE= -1665.502781
E= -1665.463601
H= -1665.462657
G= -1665.573355
Lowest Energy vibrations = 23.1, 24.3, 46.8 cm^{-1}

Compound ^{M}Al•Zr
ωB97xD 6-311G / SDD
ZPE= -1681.371463
E= -1681.332701
H= -1681.331757
G= -1681.440771
Lowest Energy vibrations = 24.9, 32.1, 35.7 cm^{-1}

Compound ^{D}Al•Zr
ωB97xD 6-311G / SDD
ZPE= -1916.997985
E= -1916.952961
H= -1916.952017
G= -1917.072535
Lowest Energy vibrations = 27.0, 28.9, 39.2 cm^{-1}

Compound $^{D}2_2$
ωB97xD 6-311G / SDD
ZPE= -2877.971627
E= -2877.901697
H= -2877.900753
G= -2878.072677
Lowest Energy vibrations = 20.9, 25.4, 32.0 cm^{-1}

Compound $^{D}2$
ωB97xD 6-311G / SDD
ZPE= -1438.957696
E= -1438.921982
H= -1438.921038
G= -1439.026572
Lowest Energy vibrations = 13.1, 20.1, 42.9 cm^{-1}

Compound $^{M}2_2$
ωB97xD 6-311G / SDD
ZPE= -2406.725791
E= -2406.669096
H= -2406.668152
G= -2406.815526
Lowest Energy vibrations = 11.0, 23.2, 25.7 cm^{-1}

Compound $^{M}2$
ωB97xD 6-311G / SDD
ZPE= -1203.329870
E= -1203.301485
H= -1203.300541
G= -1203.388796
Lowest Energy vibrations = 10.8, 30.3, 34.1 cm^{-1}

Compound $^{D}3$
ωB97xD 6-311G / SDD
ZPE= -1466.022499
E= -1465.986746
H= -1465.985802
G= -1466.091296
Lowest Energy vibrations = 15.4, 18.4, 34.3 cm^{-1}

Compound $^{M}3$
ωB97xD 6-311G / SDD
ZPE= -1230.393688
E= -1230.364783
H= -1230.363839
G= -1230.454211
Lowest Energy vibrations = 11.2, 33.5, 35.1 cm^{-1}

Compound $^{M}1$
ωB97xD 6-311G / SDD
ZPE= -1246.283223
E= -1246.254972
H= -1246.254028
G= -1246.341648
Lowest Energy vibrations = 16.1, 36.4, 37.8 cm^{-1}

Compound $^{D}1$
ωB97xD 6-311G / SDD
ZPE= -1481.909669
E= -1481.874638
H= -1481.873694
G= -1481.974823
Lowest Energy vibrations = 17.1, 28.7, 41.9 cm^{-1}

Compound Zr•Zr
ωB97xD 6-311G / SDD
ZPE= -870.142939
E= -870.122296
H= -870.122296
G= -870.192189
Lowest Energy vibrations = 30.5, 54.4, 70.8 cm^{-1}

Compound Zr
ωB97xD 6-311G / SDD
ZPE= -435.039179
E= -435.028848
H= -435.027904
G= -435.075791
Lowest Energy vibrations = 45.8, 57.4, 122.3 cm^{-1}

Cyclooctyne
B3LYP / 6-311G
ZPE = -311.907271
E = -311.899441
H = -311.898497
G = -311.939077
Lowest Energy vibrations = 152.0, 214.1. 353.0 cm^{-1}

1,2-Cyclooctadiene
B3LYP / 6-311G
ZPE = -311.910979
E = -311.903332
H = -311.902388
G = -311.942439
Lowest Energy vibrations = 207.8, 267.4. 299.2 cm^{-1}

1,3-Cyclooctadiene
B3LYP / 6-311G
ZPE = -311.945741
E = -311.938371
H = -311.937427
G = -311.976916
Lowest Energy vibrations = 227.5 248.2. 357.8 cm^{-1}

1,4-Cyclooctadiene
B3LYP / 6-311G
ZPE = -311.938067
E = -311.930453
H = -311.929509
G = -311.971413
Lowest Energy vibrations = 14.1, 336.8, 360.7 cm^{-1}

1,5-Cyclooctadiene
B3LYP / 6-311G
ZPE = -311.937397
E = -311.929943
H = -311.928999
G = -311.968904
Lowest Energy vibrations = 121.1, 323.5, 336.1 cm^{-1}

Compound ^{D}Zn•10, Molecule A
ωB97x / 6-311G / SDD
ZPE = -2211.744639
E= -2211.691672
H= -2211.690728
G= -2211.827310
Lowest Energy vibrations = 32.8, 36.1, 43.2 cm^{-1}

Compound ^{D}Zn•10, Molecule B
ωB97x 6-311G / SDD
ZPE= -2211.744294
E= -2211.690880
H= -2211.689936
G= -2211.828099
Lowest Energy vibrations = 31.8, 36.8, 42.5 cm^{-1}

Compound ^{D}Mg•10
ωB97x 6-311G / SDD
ZPE= -2184.704812
E= -2184.651790
H= -2184.650846
G= -2184.788592
Lowest Energy vibrations = 30.8, 32.0, 37.1 cm^{-1}

Compound ^{M}Al•10
ωB97x 6-311G / SDD
ZPE= -1991.978072
E= -1991.931931
H= -1991.930987
G= -1992.054507
Lowest Energy vibrations = 27.6, 32.8, 35.9 cm^{-1}

Cyclooctyne
ωB97x 6-311G
ZPE= -311.715528
E= -311.708129
H= -311.707185
G= -311.746793
Lowest Energy vibrations = 141.3, 194.4, 220.1 cm^{-1}

Cycloocta-1,3-diene
ωB97x 6-311G
ZPE= -311.759415
E= -311.752354
H= -311.751410
G= -311.790313
Lowest Energy vibrations = 176.4, 188.5, 256.0 cm^{-1}

Cyclooctene
ωB97x 6-311G
ZPE= -312.961193
E= -312.953767
H= -312.952823
G= -312.992451
Lowest Energy vibrations = 164.6, 182.3, 245.7 cm^{-1}

Compound Zr
ωB97x 6-311G / SDD
ZPE= -435.032332
E= -435.021804
H= -435.020860
G= -435.070001
Lowest Energy vibrations = 36.1, 41.5, 117.7 cm^{-1}

Compound Int^{3}
ωB97x 6-311G/ SDD
ZPE= -745.609443
E= -745.591837
H= -745.590892
G= -745.654437
Lowest Energy vibrations = 49.9, 63.8, 76.6 cm^{-1}

Compound Int^4
ωB97x 6-311G / SDD
ZPE= -745.583325
E= -745.565294
H= -745.564350
G= -745.629338
Lowest Energy vibrations = 31.7, 54.4, 64.6 cm^{-1}

Compound Int^5
ωB97x 6-311G / SDD
ZPE= -745.624253
E= -745.606381
H= -745.605437
G= -745.670699
Lowest Energy vibrations = 35.3, 48.6, 53.4 cm^{-1}

Compound Int^6
ωB97x 6-311G / SDD
ZPE= -745.581807
E= -745.563358
H= -745.562414
G= -745.631214
Lowest Energy vibrations = 8.4, 37.8, 47.8 cm^{-1}

Compound 10
ωB97x 6-311G
ZPE= -745.635045
E= -745.617063
H= -745.616119
G= -745.682846
Lowest Energy vibrations = 22.3, 30.1, 45.5 cm^{-1}

Compound ^{D}Mg•14
ωB97xD 6-311G
ZPE= -1872.854211
E= -1872.808774
H= -1872.807830
G= -1872.930949
Lowest Energy vibrations = 23.5, 26.6, 42.4 cm^{-1}

Compound ^{D}Zn•14
ωB97xD 6-311G
ZPE= -1899.917957
E= -1899.872169
H= -1899.871225
G= -1899.995328
Lowest Energy vibrations = 25.4, 27.3, 36.5 cm^{-1}

Compound ^{D}Mg•14•PMe_3
ωB97xD 6-311G
ZPE= -2333.805196
E= -2333.752621
H= -2333.751677
G= -2333.888065
Lowest Energy vibrations = 20.4, 34.1, 36.6 cm^{-1}

Compound ^{D}Mg•Int$^{7(n\text{-}Bu)}$
ωB97xD 6-311G
ZPE= -2029.985179
E= -2029.934658
H= -2029.933713
G= -2030.066774
Lowest Energy vibrations = 25.5, 28.0, 36.7 cm^{-1}

Compound ^{D}Zn•Int$^{7(n\text{-}Bu)}$
ωB97xD 6-311G
ZPE= -2057.032142
E= -2056.982104
H= -2056.981160
G= -2057.111316
Lowest Energy vibrations = 26.9, 34.4, 45.2 cm^{-1}

Transition States

Structure [^{D}Mg-η^1-Zr]‡
ωB97xD 6-311G / SDD
ZPE= -1874.048179
E= -1874.001797
H= -1874.000853
G= -1874.128803
Lowest Energy vibrations = -399.5, 15.8, 24.6 cm^{-1}

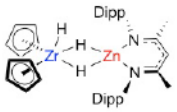
Structure [^{D}Zn-η^1-Zr]‡
ωB97xD 6-311G / SDD
ZPE= -1901.103644
E= -1901.056831
H= -1901.055887
G= -1901.184815
Lowest Energy vibrations = -286.6, 10.2, 25.7 cm^{-1}

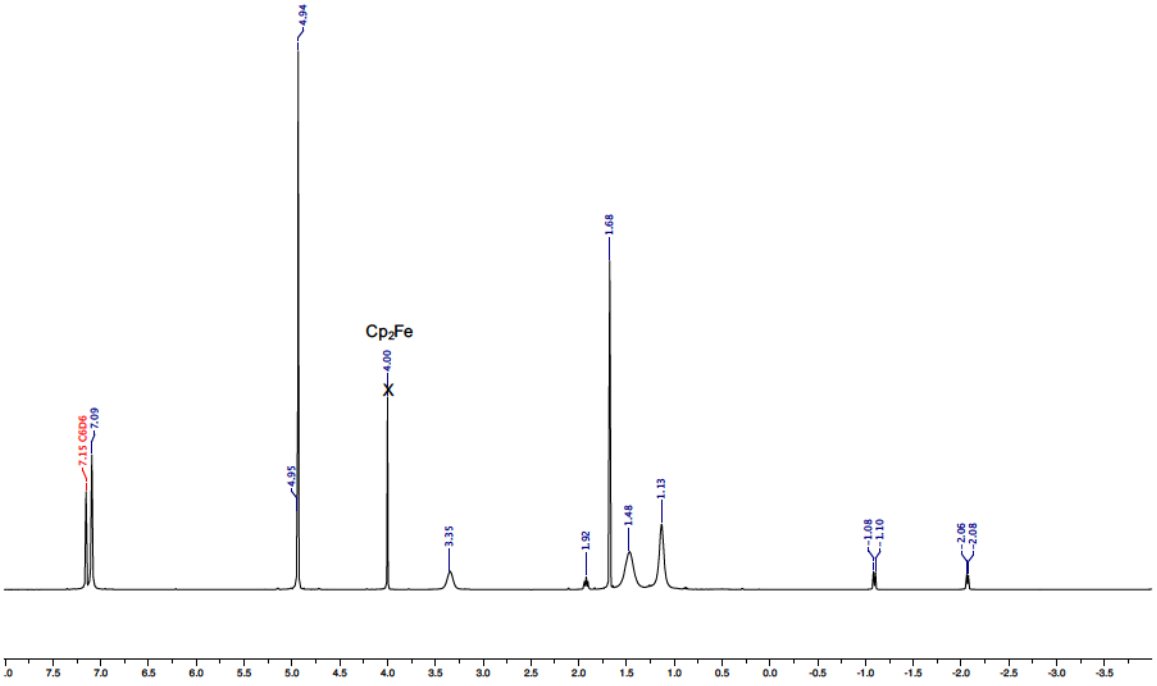
Structure TS$^{3–4}$
ωB97x 6-311G / SDD
ZPE= -745.579444
E= -745.562147
H= -745.561203
G= -745.623920
Lowest Energy vibrations = -26.6, 56.7, 58.7 cm^{-1}

Compound TS$^{5–6}$
ωB97x 6-311G / SDD
ZPE= -312.961193
E= -312.953767
H= -312.952823
G= -312.992451
Lowest Energy vibrations = -797.3, 38.0, 66.6

5.2 NMR DATA

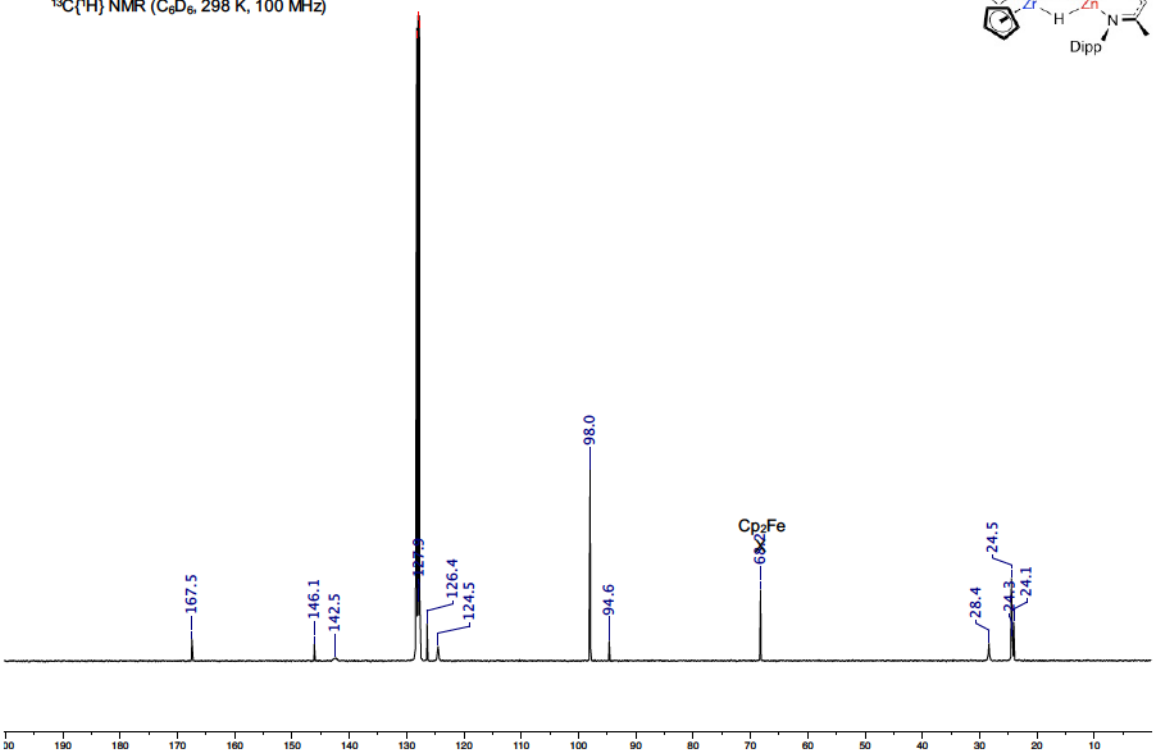
^{1}H NMR (C_6D_6, 298 K, 400 MHz)

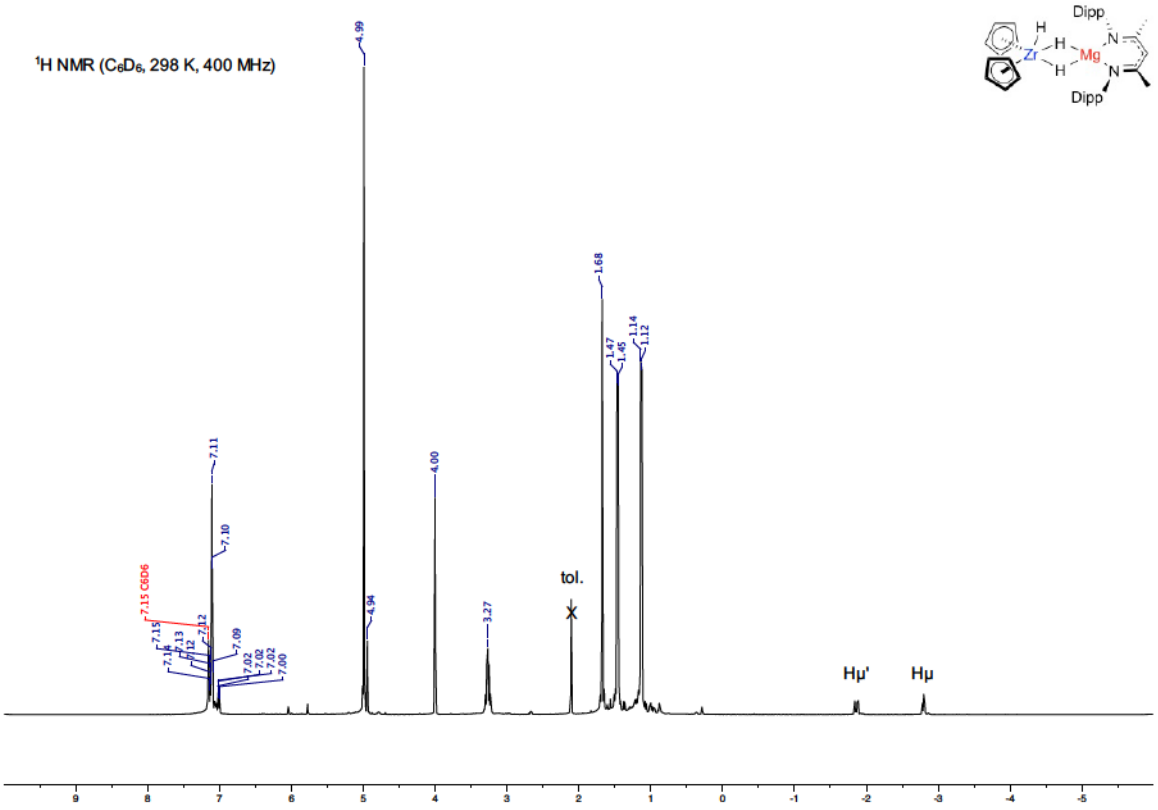


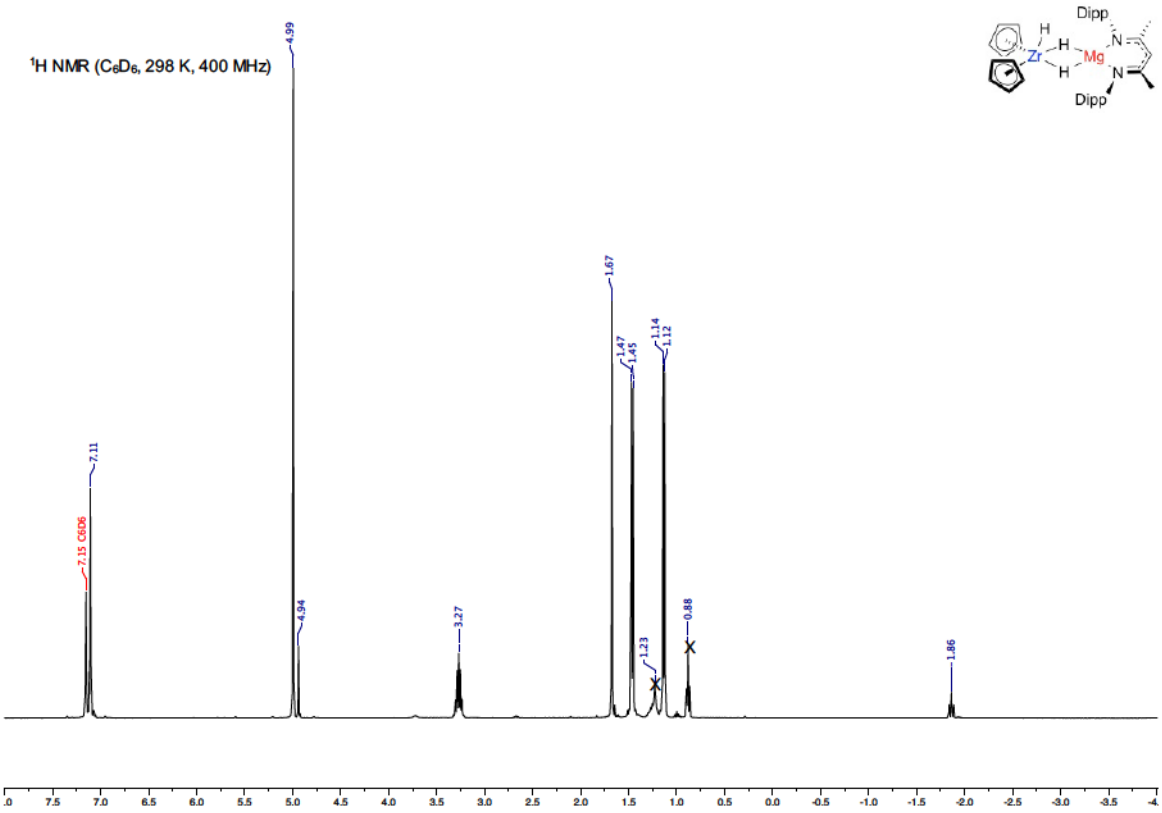


^{13}C{^{1}H} NMR (C_6D_6, 298 K, 100 MHz)

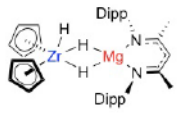




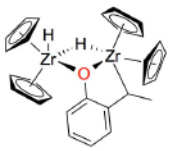

^{1}H NMR (C_6D_6, 298 K, 400 MHz)
Dipp
H
Zr
H
H
Mg
N
N
Dipp
4.99
1.68
1.47
1.45
1.14
1.12
7.11
4.00
7.10
7.15 C6D6
tol.
4.94
3.27
7.15
7.13
7.12
7.12
7.09
7.02
7.02
7.02
7.00
Hμ'
Hμ
9
8
7
6
5
4
3
2
1
0
-1
-2
-3
-4
-5


^{1}H NMR (C_6D_6, 298 K, 400 MHz)
Dipp
H
Zr
H
H
Mg
N
N
Dipp
4.99
1.67
1.47
1.45
1.14
1.12
7.11
7.15 C6D6
4.94
3.27
1.23
0.88
1.86
7.5
7.0
6.5
6.0
5.5
5.0
4.5
4.0
3.5
3.0
2.5
2.0
1.5
1.0
0.5
0.0
-0.5
-1.0
-1.5
-2.0
-2.5
-3.0
-3.5

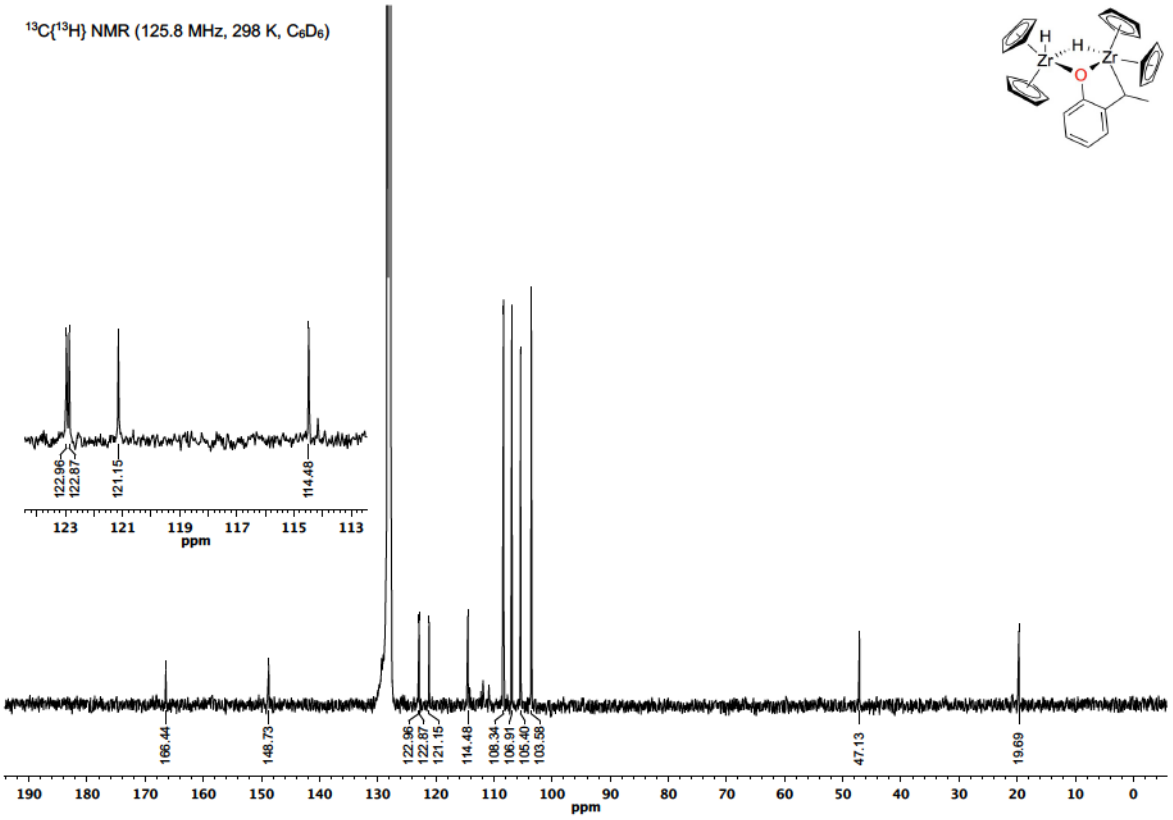
$^{13}C\{^{1}H\}$ NMR (C_6D_6, 298 K, 125.8 MHz)



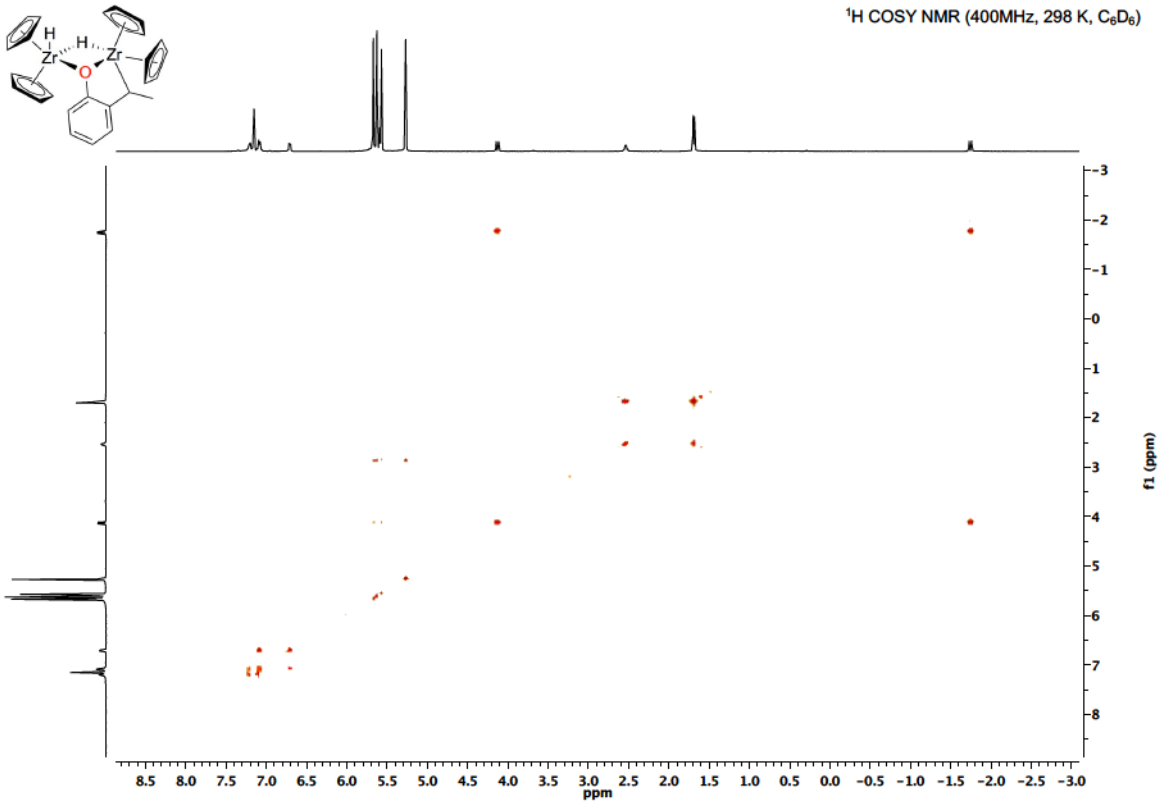
^{1}H NMR (400MHz, 298 K, C_6D_6)

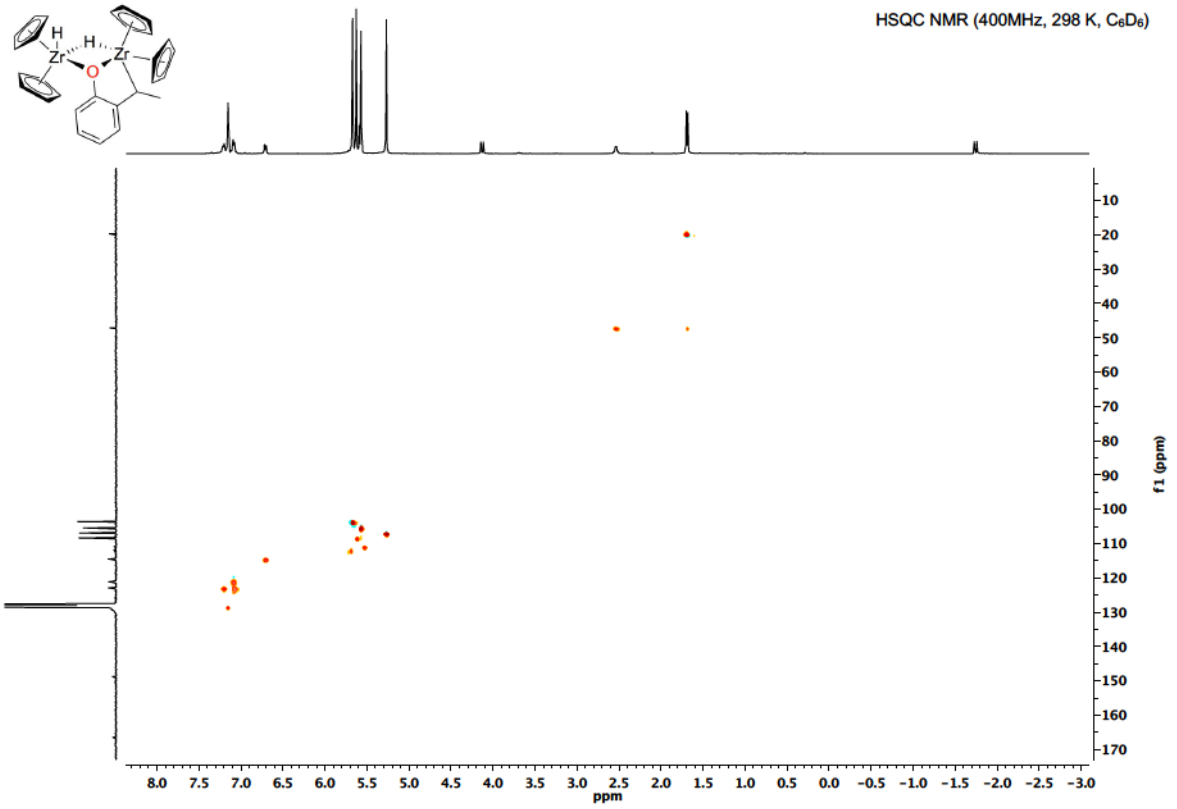


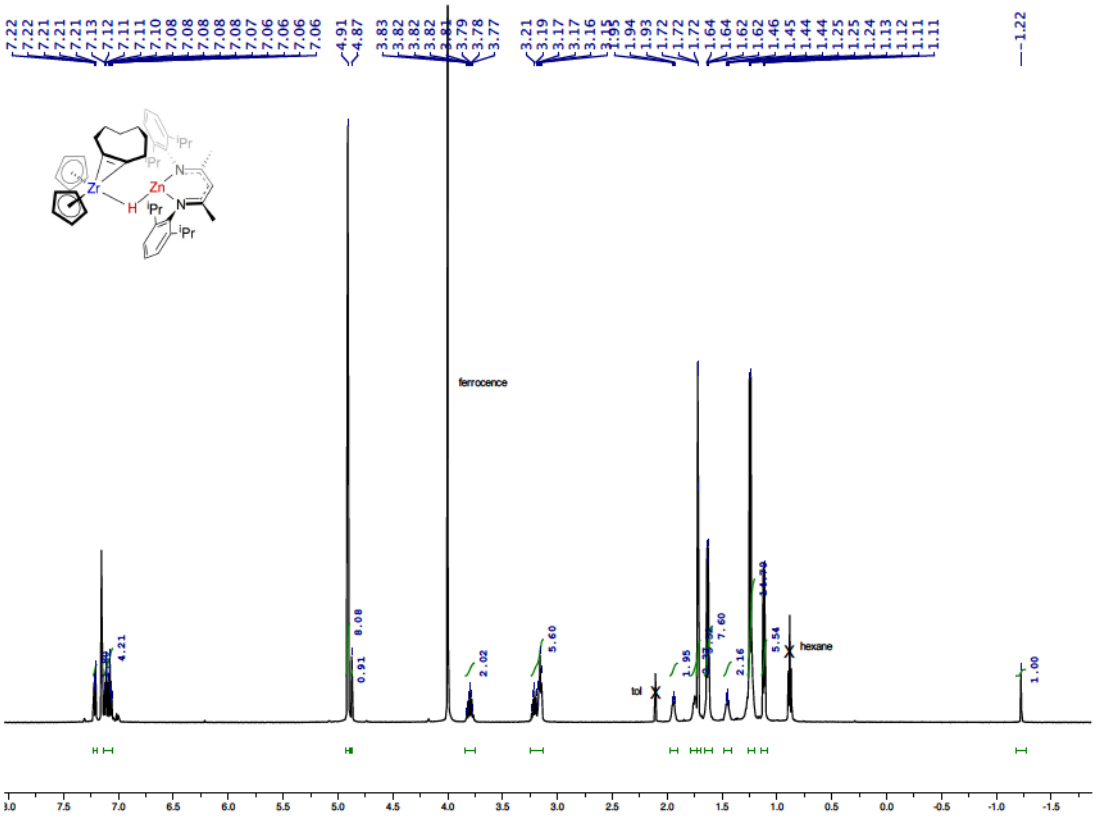
$^{13}C\{^{1}H\}$ NMR (125.8 MHz, 298 K, C_6D_6)

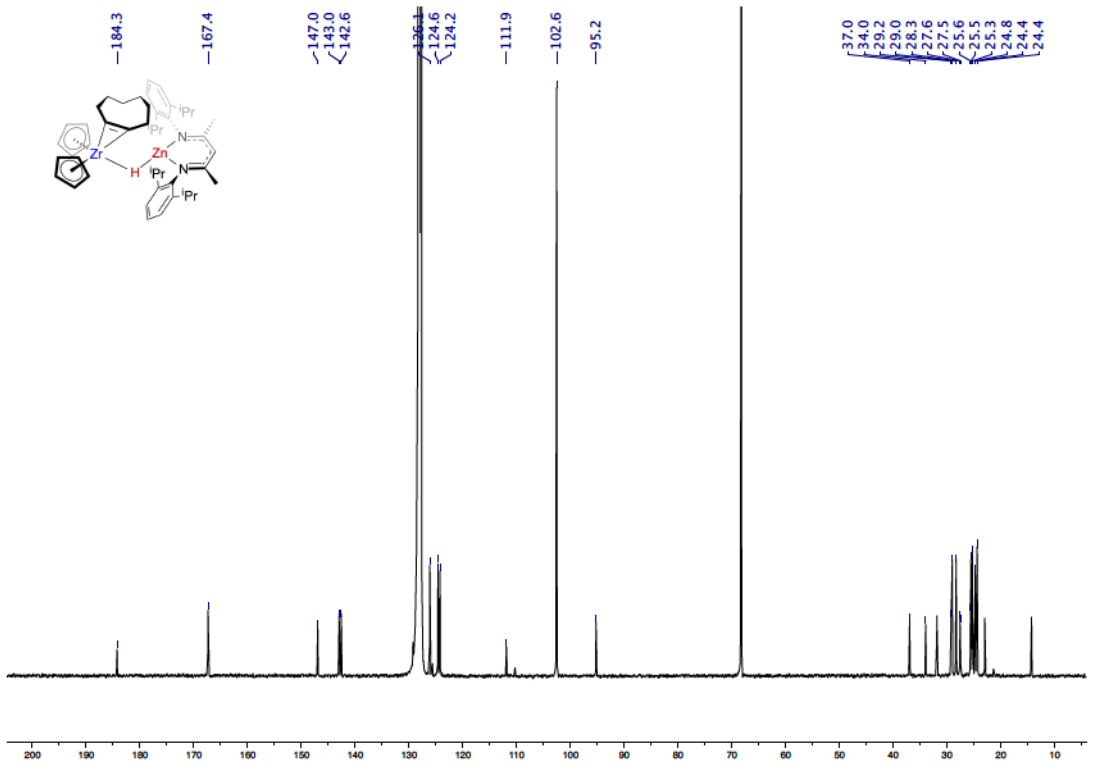


^{1}H COSY NMR (400MHz, 298 K, C_6D_6)




HSQC NMR (400MHz, 298 K, C6D6)
H
Zr
H
Zr
O
f1 (ppm)
ppm


ferrocence
tol
hexane



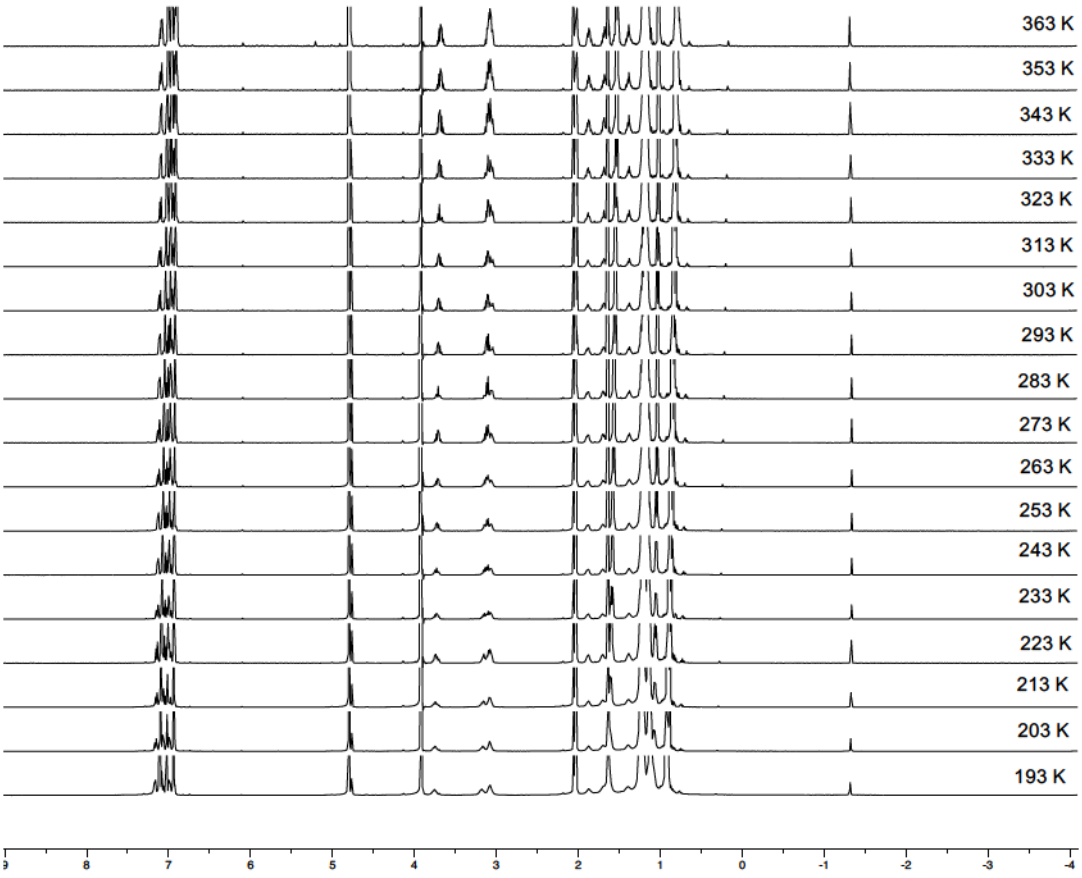
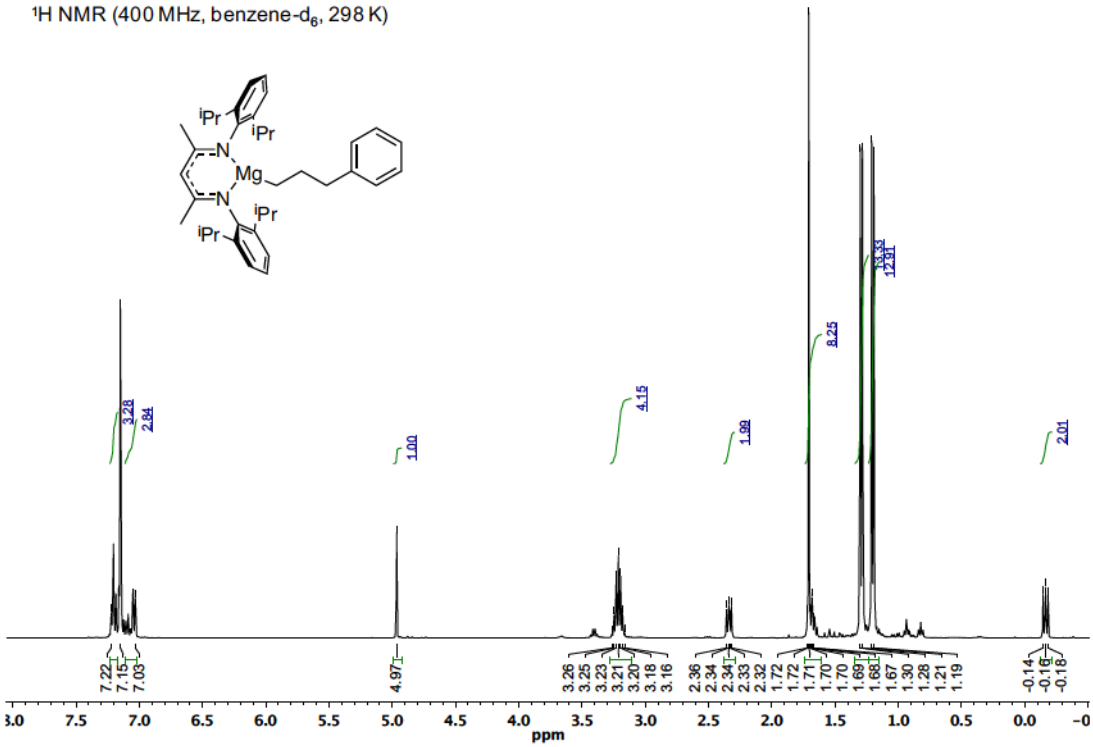
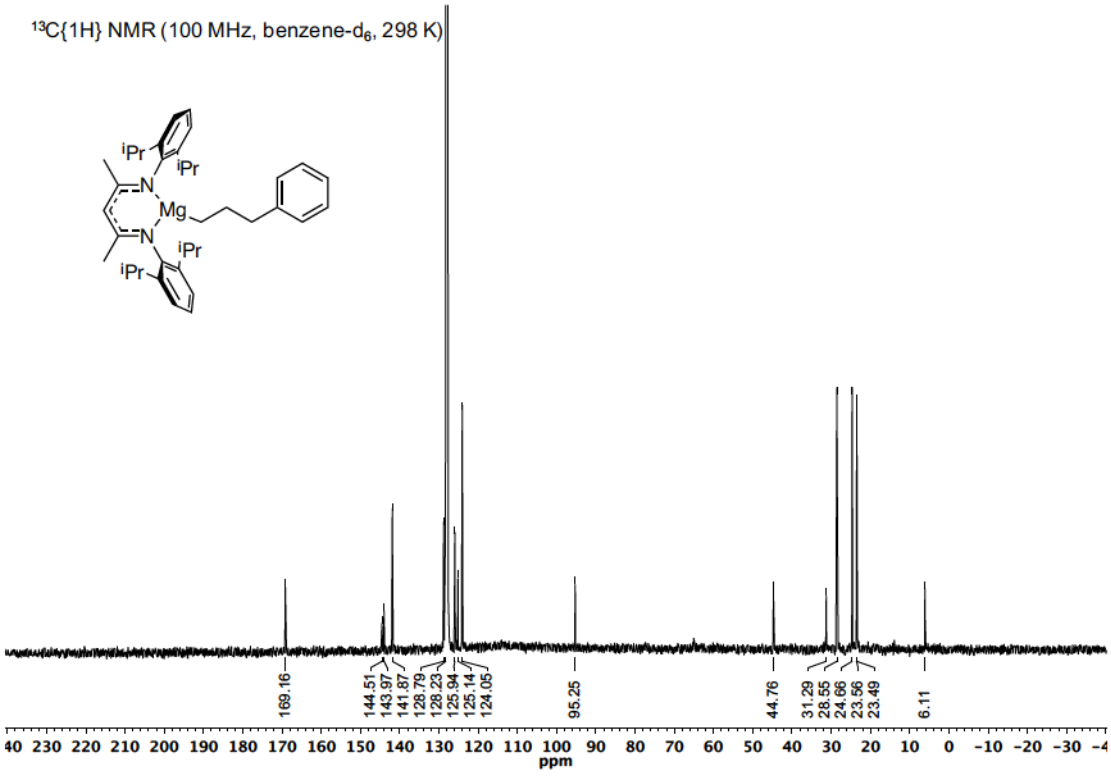


Figure 5.1. VT NMR data on **1** 193 to 363 K in toluene-d_8: VT NMR data in toluene-d_8 revealed that **1** retains its integrity in solution, undergoing little or no change across the 193 to 353 K temperature range.

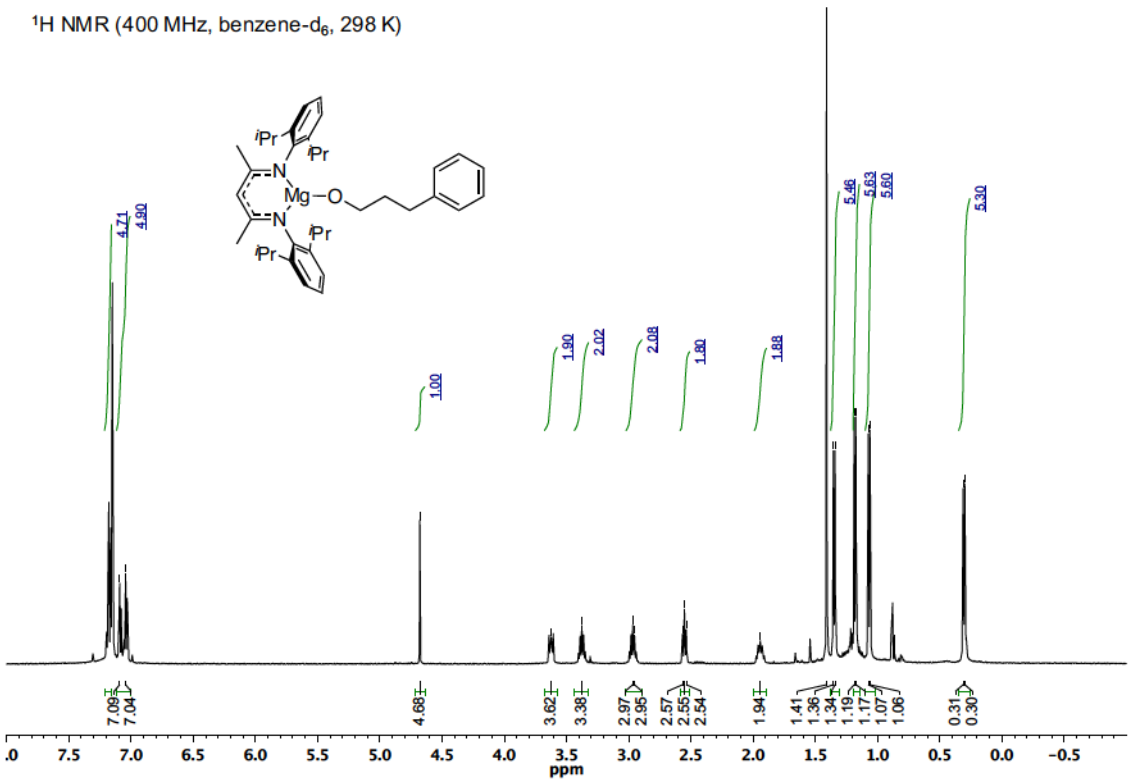
^{1}H NMR (400 MHz, benzene-d_6, 298 K)



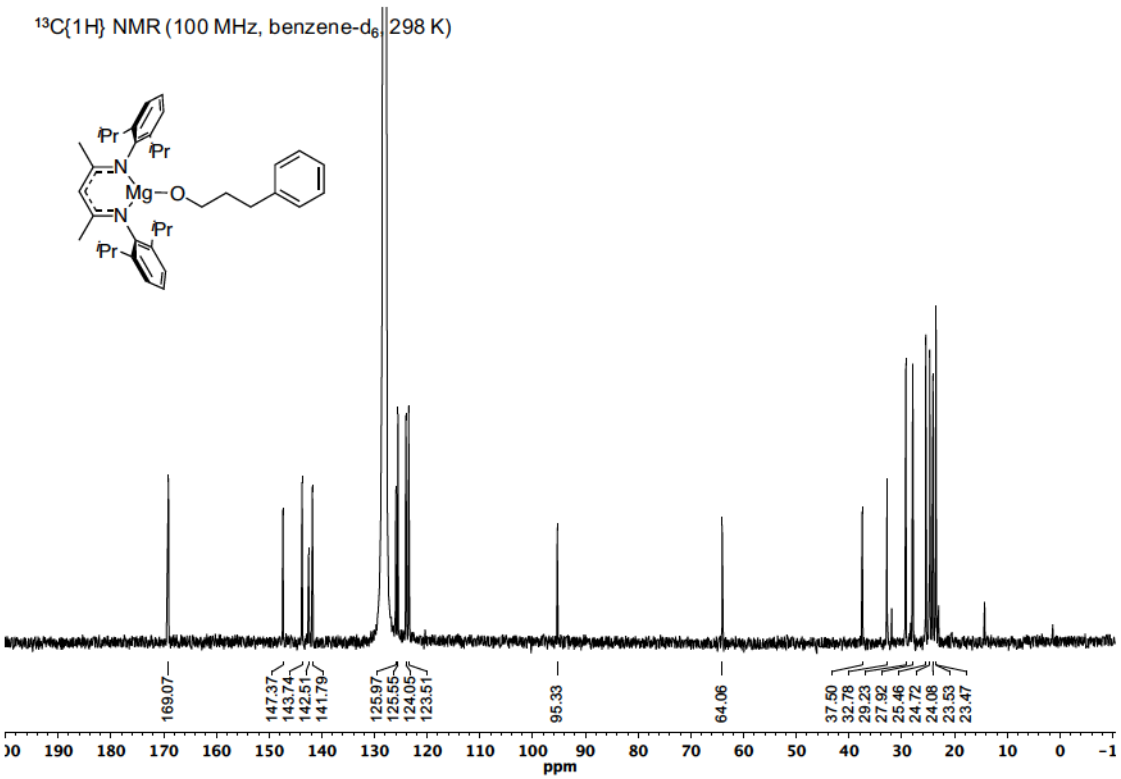
^{13}C{1H} NMR (100 MHz, benzene-d_6, 298 K)



^{1}H NMR (400 MHz, benzene-d_6, 298 K)



^{13}C{1H} NMR (100 MHz, benzene-d_6, 298 K)



^{1}H NMR (400 MHz, benzene-d_6, 298 K)

